



University of Kentucky  
UKnowledge

---

Theses and Dissertations--Physics and  
Astronomy

Physics and Astronomy

---


2017

## A MEASUREMENT OF THE PARITY VIOLATING ASYMMETRY IN THE NEUTRON CAPTURE ON $^3\text{He}$ AT SNS

Md Latiful Kabir

*University of Kentucky*, [siplukabir@gmail.com](mailto:siplukabir@gmail.com)

Author ORCID Identifier:

 <https://orcid.org/0000-0003-2142-5166>

Digital Object Identifier: <https://doi.org/10.13023/ETD.2017.291>

[Right click to open a feedback form in a new tab to let us know how this document benefits you.](#)

---

### Recommended Citation

Kabir, Md Latiful, "A MEASUREMENT OF THE PARITY VIOLATING ASYMMETRY IN THE NEUTRON CAPTURE ON  $^3\text{He}$  AT SNS" (2017). *Theses and Dissertations--Physics and Astronomy*. 45. [https://uknowledge.uky.edu/physastron\\_etds/45](https://uknowledge.uky.edu/physastron_etds/45)

This Doctoral Dissertation is brought to you for free and open access by the Physics and Astronomy at UKnowledge. It has been accepted for inclusion in Theses and Dissertations--Physics and Astronomy by an authorized administrator of UKnowledge. For more information, please contact [UKnowledge@lsv.uky.edu](mailto:UKnowledge@lsv.uky.edu).

## **STUDENT AGREEMENT:**

I represent that my thesis or dissertation and abstract are my original work. Proper attribution has been given to all outside sources. I understand that I am solely responsible for obtaining any needed copyright permissions. I have obtained needed written permission statement(s) from the owner(s) of each third-party copyrighted matter to be included in my work, allowing electronic distribution (if such use is not permitted by the fair use doctrine) which will be submitted to UKnowledge as Additional File.

I hereby grant to The University of Kentucky and its agents the irrevocable, non-exclusive, and royalty-free license to archive and make accessible my work in whole or in part in all forms of media, now or hereafter known. I agree that the document mentioned above may be made available immediately for worldwide access unless an embargo applies.

I retain all other ownership rights to the copyright of my work. I also retain the right to use in future works (such as articles or books) all or part of my work. I understand that I am free to register the copyright to my work.

## **REVIEW, APPROVAL AND ACCEPTANCE**

The document mentioned above has been reviewed and accepted by the student's advisor, on behalf of the advisory committee, and by the Director of Graduate Studies (DGS), on behalf of the program; we verify that this is the final, approved version of the student's thesis including all changes required by the advisory committee. The undersigned agree to abide by the statements above.

Md Latiful Kabir, Student

Dr. Chris Crawford, Major Professor

Dr. Chris Crawford, Director of Graduate Studies

A MEASUREMENT OF THE PARITY VIOLATING  
ASYMMETRY IN THE NEUTRON CAPTURE ON  $^3\text{He}$   
AT SNS

---

DISSERTATION

---

A dissertation submitted in partial fulfillment of the  
requirements for the degree of Doctor of Philosophy in the  
College of Arts and Sciences at the  
University of Kentucky

By  
Md Latiful Kabir  
Lexington, Kentucky

Director: Dr. Chris Crawford, Professor of Physics  
Lexington, Kentucky 2017

Copyright © Md Latiful Kabir 2017

## ABSTRACT OF DISSERTATION

### A MEASUREMENT OF THE PARITY VIOLATING ASYMMETRY IN THE NEUTRON CAPTURE ON $^3\text{He}$ AT SNS

Weak nucleon nucleon couplings are largely unknown because of the involved theoretical and experimental challenges. Theoretically the topic is difficult due to the non-perturbative nature of the strong interaction, which makes calculations of the couplings challenging. Experimentally, the topic is difficult given that 1) the observables are determined by ratios between strong couplings and weak couplings which differ in size by seven orders of magnitude, and 2) theoretically clean and predictable measurements are almost always restricted to simple systems that do not allow for effects that enhance the size of the asymmetry. However parity violation (PV) can be used to separate out the weak part and thus studies of PV in hadronic systems could offer a unique probe of nucleon structure. The n- $^3\text{He}$  experiment at the Spallation Neutron Source was performed to measure the parity violating asymmetry of the recoil proton momentum  $\vec{k}_p$  with respect to the neutron spin  $\vec{\sigma}_n$  in the reaction  $\bar{n} + ^3\text{He} \rightarrow \text{p} + \text{T} + 764 \text{ keV}$ . This asymmetry is sensitive to the isospin-conserving and isospin-changing ( $\Delta I = 0, 1, 2$ ) parts of the Hadronic Weak Interaction (HWI), and is expected to be small ( $\sim 10^{-7}$ ). The goal of this experiment was to determine this PV asymmetry with a statistical sensitivity of  $2 \times 10^{-8}$ . We also measured the parity even nuclear asymmetry proportional to  $\vec{k}_p \cdot \vec{\sigma}_n \times \vec{k}_n$  for the first time for verification of nuclear theory in both observables and for confirmation of the sensitivity of our experiment to the parity violating asymmetry.

KEYWORDS: Parity violation, Hadronic Weak Interaction, Spallation Neutron, Asymmetry,  $^3\text{He}$  Ion Chamber

Md Latiful Kabir

---

Date: July 19th, 2017

---

A MEASUREMENT OF THE PARITY VIOLATING  
ASYMMETRY IN THE NEUTRON CAPTURE ON  $^3\text{He}$   
AT SNS

By  
Md Latiful Kabir

Dr. Chris Crawford

---

Director of Dissertation

Dr. Chris Crawford

---

Director of Graduate Studies

Date: July 19th, 2017

---

Dedicated to ...

My parents, wife, daughter and all family members who did the real work.

## ACKNOWLEDGEMENTS

I would like to express my gratitude to my advisor Chris Crawford for supervising me throughout my research, showing me the approach of doing research and all the other support. I want to appreciate my advisor's extended time for me very late after hour, over the weekend or even while on travel/vacation. I also appreciate his patience to teach me and the time he spent to drive down to ORNL to supervise me.

I was very fortunate to have Seppo Penttila, David Bowman and Vince Cianciolo as my local advisors during my stay at ORNL. It was their ideas, discussions and support that helped me finish this work. I also acknowledge and thank Geoffrey Greene and Nadia Fomin for their support and contributions.

I consulted David Blyth and Chad Gillis on numerous occasions and they had always been very generous in giving thoughts and input. I learned a lot interacting with them.

I acknowledge the hard work by Mark McCrea and Chris Hayes for ion chamber and RFSF, respectively. I want to thank Paul Mueller, Michael Gericke, Rob Mahurin, Irakli Garishvili, Chris Coppola, John Calarco, Eric Plemons, Ivan Novikov, Josh Hamblen, Carlos Olguin, Libertad Barron, Jack Thomison, Aaron Sprow, Noah Birge, Mae Scott (in random order) for their contributions. The experiment was a collaborative work. It would not be possible without the contribution from each member of the collaboration.

Many thanks to Chris Crawford, Seppo Penttila, Aaron Sprow and Mark McCrea

for proof reading my thesis. I also acknowledge the feedback by the members of the thesis committee.

Raza Sufian, Mirza Rafiul Islam, Jon Demidio, Nilanjan Roy, Diptarka Das, Nandita Raha, Syed Uddin made my time in the grad school pleasant.

Finally, my wife Nahid and my daughter Liyana sacrificed a lot more than I did. I cannot just express their sacrifices and support in words. My wife and my family members in Bangladesh were more willing to see this accomplished. They were my main source of inspiration to finish this work.

This work was funded by the U.S. Department of Energy.



# TABLE OF CONTENTS

Acknowledgements	iii
List of tables	viii
List of figures	ix
1 Motivation, theoretical framework & observables	1
1.1 Parity violation as the probe of HWI . . . . .	2
1.2 Existing theoretical framework . . . . .	4
1.3 Relating coupling constants to observables . . . . .	8
1.4 Existing data . . . . .	9
1.5 Outlook for the current experiment . . . . .	10
1.6 The n- <sup>3</sup> He Experiment . . . . .	12
1.6.1 Experimental observable . . . . .	12
1.6.2 Experimental Setup . . . . .	13
1.6.3 Modes of operation . . . . .	15
2 Neutron beam and the time of flight choppers	16
2.1 Spallation neutron source . . . . .	16
2.1.1 Neutron flux from the SNS . . . . .	17
2.2 Time of flight choppers . . . . .	19
2.2.1 Maximizing the RFSF efficiency . . . . .	19
2.2.2 Neutrons mixing . . . . .	19
2.3 Chopper optimization . . . . .	20
2.3.1 The model . . . . .	20
2.3.2 Producing 60 Hz spectrum . . . . .	27
2.3.3 Test for the model . . . . .	28
2.3.4 Optimization outcome . . . . .	30
2.4 Chopped beam profile . . . . .	33
2.4.1 Dropped pulses . . . . .	33
2.4.2 Construction of the image pulse . . . . .	34
2.4.3 Neutron beam spatial profile . . . . .	37
2.4.4 Beam collimation . . . . .	39
3 Spin flipper & Detector	41

3.1	Radio frequency spin flipper (RFSF)	41
3.1.1	RFSF working principle	42
3.1.2	1/t ramp for the RF field amplitude	45
3.1.3	$^3\text{He}$ transmission polarimetry	47
3.2	Ion Chamber / Detector	48
3.2.1	Target chamber interior structure	49
3.2.2	Signal from the ion chamber	51
4	Readout electronics	54
4.1	Preamplifier	54
4.2	Data acquisition system	56
4.2.1	The DAQ modules	56
4.2.2	ADC characteristics	59
4.2.3	Resynchronization and jitter	62
4.2.4	Event length, dead time and file size	64
4.2.5	The data file structure	65
4.2.6	ADC count to volt conversion and time bin	68
4.3	Wire map and the network	68
4.4	Processed and compressed data file	70
4.5	The n- $^3\text{He}$ analysis tools	72
4.6	Instrumental asymmetry	73
5	Simulation	76
5.1	Geometry factors	76
5.2	Simulation toolkit	78
5.3	Geometry and materials	79
5.4	Physics list	81
5.5	Primary particles: Neutron beam profile	82
5.5.1	Neutron energy distribution	82
5.5.2	Neutron spatial profile	86
5.6	Validation of the simulation	88
5.6.1	The conservation of energy	88
5.6.2	Cross section comparison	89
5.6.3	Energy dependence of the cross section	90
5.6.4	The stopping power and ionization curve	92
5.6.5	The energy range relationship	96
5.6.6	The angular distribution of tracks	97
5.6.7	Comparison of yield	97
5.6.8	Comparison with beam scan data	99
5.7	Outcome from the simulation	102
6	Data analysis	103
6.1	Data analysis method	103
6.1.1	Asymmetry definition	103
6.1.2	Data selection	108

6.1.3	Background subtraction . . . . .	109
6.1.4	Beam fluctuations . . . . .	109
6.1.5	False asymmetry . . . . .	113
6.2	Parity conserving (LR) asymmetry . . . . .	114
6.3	Correction for correlation . . . . .	119
6.3.1	Correlation correction by direct inversion of the covariance matrix	121
6.3.2	Correlation correction by diagonalizing the covariance matrix .	122
6.3.3	Data reduction . . . . .	125
6.3.4	Correlation corrected LR asymmetry . . . . .	126
6.4	Parity violating (UD) asymmetry . . . . .	133
6.5	Systematic effects . . . . .	140
7	Results & discussion	148
	Appendices	153
A	List of n- <sup>3</sup> He parameters	154
B	Spin flipper	155
B.1	Time evolution of $\mu_z$ . . . . .	155
C	Simulation	158
C.1	M1 signal window . . . . .	158
D	Data analysis	160
D.1	Parity conserving asymmetry . . . . .	160
D.2	Parity violating asymmetry . . . . .	163
	Bibliography	167
	Vita	171

## LIST OF TABLES

1.1	Reasonable ranges and best values for the DDH coupling constants . . . . .	6
1.2	Prediction for the five PV low energy constants . . . . .	7
1.3	Measured observables in terms of DDH coupling constants . . . . .	8
4.1	Content of the branch “ <i>asym</i> ” in the summary file . . . . .	71
4.2	The major functionalities in the n- <sup>3</sup> He analysis tools . . . . .	73
6.1	The batch numbers and corresponding run ranges of the LR data set . . . . .	114
6.2	LR asymmetries from all the batches . . . . .	129
6.3	All the batches and corresponding run ranges for the UD dataset. . . . .	133
6.4	UD asymmetries from all the batches . . . . .	136
6.5	List of the systematic effects [68, 69]. . . . .	147
7.1	The relationship between LECs $\Lambda$ , DDH and Girlanda coefficients . . . . .	151

## LIST OF FIGURES

1.1	a. Fermi's 4-point interaction. b. Weak interaction in SM . . . . .	3
1.2	The structure of weak interaction is defined by parity violation. . . . .	3
1.3	Exchange particles for different interactions. . . . .	4
1.4	Meson exchange model . . . . .	5
1.5	Constraints for the coupling constants from different experiments . . . . .	10
1.6	PV in nuclear and few-body systems . . . . .	11
1.7	The n- <sup>3</sup> He reaction. . . . .	12
1.8	The experimental setup for the n- <sup>3</sup> He experiment . . . . .	13
1.9	CAD model for the beamline 13 (FnPB). . . . .	14
1.10	CAD model for the experimental setup. . . . .	14
1.11	The experimental setup for the parity violating UD mode . . . . .	15
1.12	The experimental setup for the parity conserving LR mode. . . . .	15
2.1	Different components of the spallation neutron source at ORNL. . . . .	17
2.2	Unchopped 1Hz spectrum from the SNS . . . . .	18
2.3	Neutron spectra from the SNS as a function of wavelength . . . . .	18
2.4	A single neutron pulse and neutrons mixing from different frames . . . . .	19
2.5	The effect of the use of a single chopper and two choppers . . . . .	20
2.6	Chopper geometry . . . . .	21
2.7	The angles with the lower and upper corner of the guide . . . . .	22
2.8	A triangular opening part of the guide. . . . .	22
2.9	A trapezoidal part of the guide . . . . .	23
2.10	The open area of the guide as a function of $\phi$ . . . . .	24
2.11	Plot for the transmission as a function of the time of flight. . . . .	25
2.12	Plot for the transmission as a function of the time of flight . . . . .	26
2.13	Plot for the transmission of chopper-1 and chopper-2 . . . . .	26
2.14	Unchopped (top) and chopped (bottom) 1 Hz spectrum . . . . .	27
2.15	Recipe of producing 60 Hz spectrum from 1 Hz . . . . .	27
2.16	Folding 1 Hz spectrum to produce 60 Hz spectrum . . . . .	28
2.17	Fit for the folded 60 Hz model spectrum with the experimental spectrum. . . . .	28
2.18	Fit for the folded 60 Hz model spectrum with the experimental spectrum. . . . .	29
2.19	Three parameters contour plot with FOM . . . . .	30
2.20	High resolution plot zooming the optimum FOM region. . . . .	31
2.21	Chopper window for optimized chopper phases . . . . .	31
2.22	Chopper window for optimized chopper phases . . . . .	31
2.23	RFSF window with optimal chopper phases . . . . .	32

2.24	The M1 signal as a function of the TOF . . . . .	33
2.25	Dropped pulse in the pulse train . . . . .	34
2.26	The image pulse generated using the dropped pulse . . . . .	35
2.27	The wrap around in the image pulse . . . . .	35
2.28	The image (surrogate) pulses . . . . .	36
2.29	Image pulses with contribution from wrap around and injection flash . . . . .	37
2.30	Upstream beam profile from the scan . . . . .	38
2.31	Downstream beam profile from the scan . . . . .	38
2.32	Beam collimator with beam centroid . . . . .	39
3.1	The spin flipper interior and housing [59] . . . . .	41
3.2	Field lines for cosine theta coil and double cosine theta coil . . . . .	42
3.3	The situation in the rotating frame . . . . .	44
3.4	The RFSF current vs neutron time of flight . . . . .	46
3.5	Spin flip ratio for different guide field values at fixed $\omega_0$ . . . . .	46
3.6	Average neutron beam polarization from the polarimetry measurements . . . . .	47
3.7	Average spin flipper efficiency from the polarimetry measurements . . . . .	48
3.8	The n- <sup>3</sup> He ion chamber . . . . .	48
3.9	The signal and high voltage planes . . . . .	49
3.10	2D view for the signal and high voltage wires . . . . .	50
3.11	Creation and collection of ion pairs along the proton and triton tracks . . . . .	51
3.12	The ionization curve for proton and triton inside <sup>3</sup> He . . . . .	52
4.1	The preamplifier attached to the ion chamber . . . . .	54
4.2	The preamp circuit diagram . . . . .	55
4.3	The ADCs used for the n- <sup>3</sup> He experiments . . . . .	57
4.4	ADS1278 block diagram . . . . .	58
4.5	Analog input front-end circuit of the DAQ . . . . .	59
4.6	Distribution for bare ADC signal . . . . .	59
4.7	ADC noise at different sampling rate . . . . .	60
4.8	Autocorrelation plot for the ADC noise data . . . . .	61
4.9	Rise time measurement with DAQ running at 128 kHz . . . . .	61
4.10	The test of the averaging feature of the DAQ . . . . .	62
4.11	Test signal for testing resynchronization of the ADC . . . . .	63
4.12	Jitter from the intercepts. . . . .	63
4.13	Jitter from the intercepts. Projection of Fig. 4.12 on <i>y</i> -axis . . . . .	64
4.14	Data file structure for the detector data . . . . .	66
4.15	Content of the header for the detector data . . . . .	67
4.16	Data file structure (after processing) for the M1 and RFSF signals . . . . .	67
4.17	Content of the header (M1 and RFSF data) . . . . .	67
4.18	Signal wire to ADC channel map . . . . .	69
4.19	The network diagram of the n- <sup>3</sup> He experiment . . . . .	70
4.20	Setup for the instrumental asymmetry measurement . . . . .	74
4.21	Signal used for the instrumental asymmetry measurement . . . . .	74
4.22	Instrumental asymmetry from one of the channels . . . . .	75

4.23	Instrumental asymmetry from different channels . . . . .	75
5.1	Intuitive distribution of geometric factors inside the chamber . . . . .	78
5.2	A basic simulation process flow in the Geant4 . . . . .	79
5.3	A simplified geometry of the setup . . . . .	80
5.4	Propagating the unconvoluted M1 signal at the detector position . . . . .	83
5.5	Unconvoluted M1 signal at the detector position . . . . .	84
5.6	Corrected unconvoluted M1 signal at the detector position . . . . .	85
5.7	Generated neutron energy distribution . . . . .	86
5.8	Neutron position distribution on the $xy$ plane . . . . .	87
5.9	Example of simulated capture events (2D view) inside the chamber . . . . .	87
5.10	Initial kinetic energy of proton and triton in the simulation . . . . .	89
5.11	Capture cross section from the simulation with pencil beam . . . . .	90
5.12	ENDF vs Geant4 cross section comparison for different thermal energies . . . . .	91
5.13	$\frac{1}{\sqrt{E}}$ dependence of crsoss section form the simulation . . . . .	91
5.14	Proton stopping power as a function of the kinetic energy . . . . .	94
5.15	Triton stopping power as a function of the kinetic energy . . . . .	95
5.16	The ionization curve . . . . .	95
5.17	The energy-range relationship . . . . .	96
5.18	Proton momentum angular distribution from the simulation . . . . .	97
5.19	Triton momentum angular distribution from the simulation . . . . .	97
5.20	Yield distribution: simulation vs data . . . . .	98
5.21	Comparison of yield distribution: simulation vs data . . . . .	98
5.22	Yield distribution from run# 37990: simulation vs data . . . . .	99
5.23	Comparison of yield distribution from run# 37990: simulation vs data . . . . .	99
5.24	Yield distribution from run# 38000: simulation vs data . . . . .	100
5.25	Comparison of yield distribution from run# 38000: simulation vs data . . . . .	100
5.26	Yield distribution from run# 38006: simulation vs data . . . . .	101
5.27	Comparison of yield distribution from run# 38006: simulation vs data . . . . .	101
5.28	The distribution of the geometry factors for all the signal wires . . . . .	102
5.29	The geometry factors with errors . . . . .	102
6.1	The TOF window used for the anymmetry extraction . . . . .	108
6.2	The pulses excluded from the analysis . . . . .	109
6.3	Pedestal measured from the dropped pulse . . . . .	110
6.4	The M1 asymmetry from the UD data . . . . .	111
6.5	The M1 asymmetry from the LR data . . . . .	112
6.6	The M1 signal variation as a function of distance from dropped pulse . . . . .	112
6.7	Slow drift from image pulse . . . . .	113
6.8	Different batch groups and beam power for the LR runs . . . . .	114
6.9	The LR raw asymmetry from the layer number 1, wire 1 . . . . .	115
6.10	Raw asymmetry from the entire LR data set: Group $\mathcal{A}$ vs Group $\mathcal{B}$ . . . . .	115
6.11	Raw asymmetry from the entire LR data set: Group $\mathcal{A}$ + Group $\mathcal{B}$ . . . . .	116
6.12	The LR physics asymmetry (uncorrected) from batch $2\mathcal{A}$ . . . . .	117
6.13	The LR physics asymmetry (uncorrected) from batch $2\mathcal{B}$ . . . . .	117

6.14	The LR physics asymmetry (uncorrected) from batch $2\mathcal{A} + 2\mathcal{B}$ . . . . .	118
6.15	Raw asymmetry correlation between wires . . . . .	119
6.16	Physics asymmetry correlation between wires . . . . .	121
6.17	Two approaches of the data reduction process. . . . .	126
6.18	The transformation matrix $S$ and the eigenvector . . . . .	127
6.19	The eigenvalues for the LR batch 2 data . . . . .	128
6.20	Fit for the correlation corrected physics asymmetry for the LR batch 2	129
6.21	LR physics asymmetries (corrected) from all the batches . . . . .	130
6.22	LR physics asymmetries from different batches for layer-1, wire-4 . . .	130
6.23	Physics asymmetry for each wire from the fit . . . . .	131
6.24	Chi square distribution for the fits . . . . .	131
6.25	Fit for the correlation-corrected physics asymmetry . . . . .	132
6.26	Average proton beam power distribution for the UD dataset . . . . .	134
6.27	Distribution of the UD raw asymmetry from layer-1, wire-1 . . . . .	134
6.28	The UD physics asymmetry (uncorrected) for batch-2 . . . . .	135
6.29	The UD physics asymmetry (corrected) for batch 2 . . . . .	135
6.30	UD physics asymmetries (corrected) from all the batches . . . . .	137
6.31	Physics asymmetry for wire 1 from all the batches . . . . .	138
6.32	Chi square distribution from the fits . . . . .	138
6.33	The UD physics asymmetry (corrected) from the fit . . . . .	139
6.34	Detector asymmetries . . . . .	141
6.35	The wire asymmetry and M1 asymmetry with no beam . . . . .	142
6.36	The correlation between the wire asymmetry and M1 asymmetry. . .	142
6.37	M1 asymmetry as a function of the run number (all LR and UD runs).	143
6.38	UD raw asymmetry from layer-1, wire-1 as a function of the run number.	143
6.39	Correlation between UD raw asymmetry with M1 . . . . .	144
6.40	Pressure optimization in the simulation . . . . .	145
6.41	Optimization of collimation width and beam centroid . . . . .	145
7.1	Contribution of the $n$ - $^3\text{He}$ experiment to the coupling constants . . .	149
7.2	The $n$ - $^3\text{He}$ result on the DDH plot . . . . .	150
7.3	Constraints on the leading order large- $N_c$ solutions . . . . .	152
B.1	Field components in rotating frame . . . . .	156
D.1	Fit with covariance for LR batch-2 data . . . . .	160
D.2	LR asymmetry considering all the runs in as a single batch . . . . .	161
D.3	LR physics asymmetry using average wire asymmetry from the fit . .	161
D.4	LR asymmetry (corrected) considering all the runs in a single batch .	162
D.5	Raw asymmetry (UD) correlation between wires . . . . .	163
D.6	Physics asymmetry correlation between wires from UD batch-1 data .	164
D.7	The transformation matrix $S$ for UD batch-2 data . . . . .	164
D.8	The eigenvalues from UD batch-2 data . . . . .	165
D.9	UD physics asymmetry (corrected) for batch 2 using alternative fitting.	165
D.10	UD physics asymmetry calculated using average wire asymmetry . . .	166



D.11 UD physics asymmetry considering all the runs in a single batch . . . 166

# Chapter 1

## Motivation, theoretical framework & observables

---

There are a number of unsolved experimental and theoretical puzzles involving the Hadronic Weak Interaction (HWI) of baryons. In particular, we have not found a way to simultaneously account for both the parity conserving P-wave and parity violating (PV) S-wave decay amplitudes in the case of hyperon non-leptonic decays. The PV asymmetries associated with the radiative decays of hyperons are surprisingly large. SU(3) flavor symmetry indicates that, in the limit of degenerate u, d and s-quarks, these asymmetries are expected to be zero. Using the mass splitting between the strange and two light quarks, we expect the asymmetries to be on the order of  $m_s/M_B \sim 0.15$ , where  $M_B \sim 1$  GeV is the typical hyperon mass. But the measured asymmetries, from the available experiments, turned out to be four to five times larger in magnitude. Also, the well-known  $\Delta I = 1/2$  rule that summarizes the observed dominance of the  $I = 1/2$  channel over the  $I = 3/2$  channel in strangeness changing nonleptonic decays remains unclear, mostly because the existing symmetry does not favor either channel. Thus, the QCD symmetries and the relevant physical scales do not provide a satisfactory explanation for the observed properties of the  $\Delta S = 1$  HWI [10]. In this sense, consideration of the  $\Delta S = 0$  HWI, which has not been fully explored and for which the strange quark plays a relatively minor role, is important. The goal of studying the  $\Delta S = 0$  HWI with hadronic and nuclear PV is to help determine the degree to which the symmetries of QCD characterize the HWI and to shed light on the long standing puzzles in the  $\Delta S = 1$  sector. Thus, in the theoretical formulation of this problem, one tries to make the contact with the underlying SM as transparent as possible keeping the hadronic model and nuclear structure unchanged.

In various models or formulations, the HWI is characterized by 6 different couplings. In the DDH (meson exchange) model[7], the couplings are  $h_\pi^1$ ,  $h_\rho^0$ ,  $h_\rho^1$ ,  $h_\rho^2$ ,  $h_\omega^0$ , and  $h_\omega^1$ , labeled according to the meson exchanged and change in isospin  $\Delta I$  at the vertex. In effective field theories, the couplings are replaced by contact interactions with appropriate operators. However, under certain approximations, one can relate these

couplings to each other [21]. The determination of the weak NN interaction coupling constants through measurement of various hadronic PV observables is an essential test of the underlying model and our understanding of the interaction. Ideally we would like to test self-consistency of the underlying framework by over constraining the extraction of couplings with more measurements of observables than needed for a simple extraction of couplings.

The n-<sup>3</sup>He experiment is part of a series of experiments needed to provide a self-consistent description of the HWI by extracting the nucleon-nucleon coupling constants in combination with other two-body and few-body experiments.

## 1.1 Parity violation as the probe of HWI

---

Parity refers to the behavior of a system under spatial inversion, i.e. behavior under the mathematical transformation  $\vec{r} \rightarrow -\vec{r}$ . Momentum, being proportional to velocity, also changes sign under parity:  $\vec{p} \rightarrow -\vec{p}$ , but angular momentum, being an axial vector, does not:  $\vec{L} = \vec{r} \times \vec{p} \rightarrow -\vec{r} \times -\vec{p} = +\vec{L}$ . Likewise, spin is invariant under parity.

Prior to 1956 it was taken for granted that the laws of physics are parity invariant. But in 1956, the “tau-theta puzzle” led Lee and Yang to wonder whether there had been any experimental test of this assumption [1]. They concluded that in the case of the weak interaction, experimental data neither confirmed nor refuted parity invariance. They proposed a test which was carried out independently later that year by Wu [2] and Lederman [3] to settle the issue. In the famous Wu experiment she observed parity violation in the beta decay of <sup>60</sup>Co nuclei [2]



The search for parity violation in nuclear systems started just after the revolutionary discovery of parity violation in the above beta decay in 1957. The first search was carried out by by Tanner [4]. However the first persuasive result was obtained by Lobashov and others in 1967 [5] who were able to find a  $-6 \pm 1 \times 10^{-6}$  signal among the much larger parity-conserving strong background in radiative neutron capture from <sup>181</sup>Ta. At that time this was consistent with the prediction by Feynman and Gell-Mann [6] that there should an intermediate vector particle in the weak interaction as it is right now in the standard model (opposed to what Fermi proposed in the original paper of beta decay).

Even though PV has been discovered and is consistent with a left-handed W exchange boson, hadronic parity violation experiments are still relevant. From a theoretical point of view, for example at the quark and lepton level, it defines the structure of the weak interaction. Similarly, we can get the structure of the nucleon-nucleon interaction by studying parity violation in the nuclear system.

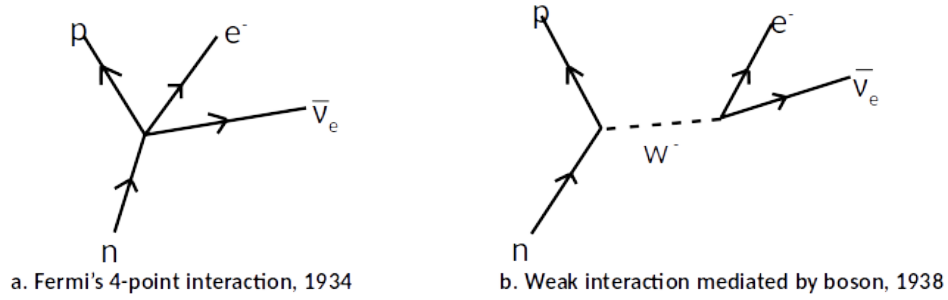


Figure 1.1: a. Fermi's 4-point interaction. b. Weak interaction in SM

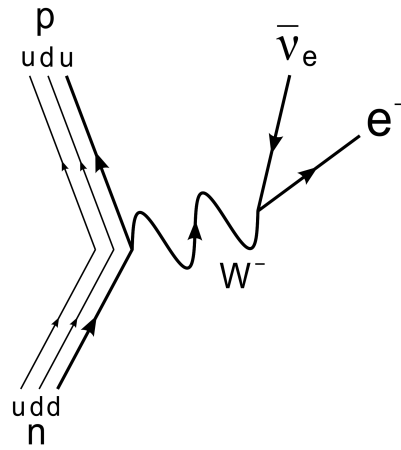


Figure 1.2: The structure of weak interaction is defined by parity violation.

$$\mathcal{H} = \mathcal{H}_{\text{strong}} + \mathcal{H}_{\text{weak}}$$

From the experimental point of view, it is a very powerful tool because of the fact that strong interaction is even under parity while weak interaction is odd. So while the strong interaction dominates the weak interaction by several order of magnitude ( $\frac{e^2}{M_W^2} / \frac{g^2}{m_\pi^2} \approx 10^{-7}$ ), we can use parity violation to isolate out the weak contribution from the strong one.

The hadronic weak interaction manifests itself in parity-violating phenomena both in the two-nucleon system and in nuclei.

Experimentally, we look for a parity violating signal by examining a scalar correlation which is odd under parity, such as correlation between spin and momentum:  $\vec{\sigma} \cdot \vec{p}$ .

## 1.2 Existing theoretical framework

In Standard Model (SM), the structure of low-energy  $\Delta S = 0$  HWI is described by the Hamiltonian [10]

$$\mathcal{H}_{\text{HWI}}^{\Delta S=0} = \frac{G_F}{\sqrt{2}} \left( J_\lambda^{CC\dagger} J^{\lambda CC} + \frac{1}{2} J_\lambda^{NC\dagger} J^{\lambda NC} \right), \quad (1.1)$$

where  $G_F$  is the Fermi constant and  $J_\lambda^{CC}$  and  $J_\lambda^{NC}$  are the weak charged and neutral currents, respectively. The main challenge here is finding the correct effective interaction  $\mathcal{H}_{\text{HWI}}^{\Delta S=0 \text{ eff}}$  ( $N, \pi, \Delta$ ) that best describes the hadronic manifestation of  $\mathcal{H}_{\text{HWI}}^{\Delta S=0}$ . This is because  $J_\lambda^{CC}$  transforms as a doublet under strong isospin while  $J_\lambda^{NC}$  has  $I = 0$  and  $I = 1$  components, and the current-current products in  $\mathcal{H}_{\text{HWI}}^{\Delta S=0}$  contain terms that transform as isoscalars, isovectors and isotensors. As a result,  $\mathcal{H}_{\text{HWI}}^{\Delta S=0 \text{ eff}}$  must contain the most general set of operators having the same isospin properties.

There are several approaches to modeling or formulating the hadronic weak interaction by introducing effective coupling unlike the coupling used in elementary particles, where the interactions are through mediators like vector bosons in weak interactions.

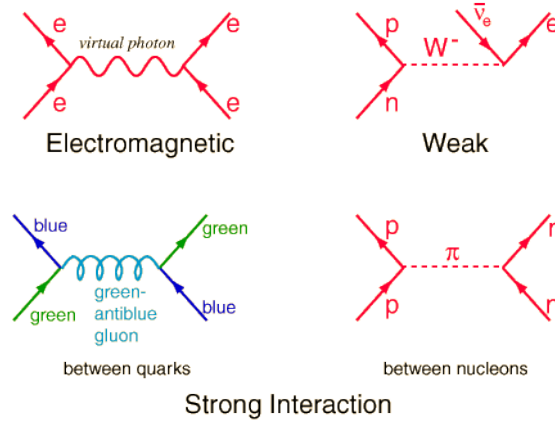


Figure 1.3: Exchange particles for different interactions.

Among all the theoretical frameworks, the most classical one is the meson exchange model, also known as the DDH model, named after B. Desplanques, J. F. Donoghue and B. R. Holstein [7, 9]. In this meson exchange model, the strength of the HWI is specified by coupling constants at the vertex where an exchange meson is emitted or absorbed. The strong Hamiltonian related to the DDH potential is given by [21]

$$\begin{aligned} \mathcal{H}_{st} = & ig_{\pi NN} \bar{N} \gamma_5 \vec{\tau} \cdot \vec{\pi} N + g_\rho \bar{N} \left( \gamma_\mu + i \frac{\chi_V}{2M} \sigma_{\mu\nu} k^\nu \right) \vec{\tau} \cdot \vec{\rho}^\mu N \\ & + g_\omega \bar{N} \left( \gamma_\mu + i \frac{\chi_S}{2M} \sigma_{\mu\nu} k^\nu \right) \omega^\mu N, \end{aligned} \quad (1.2)$$

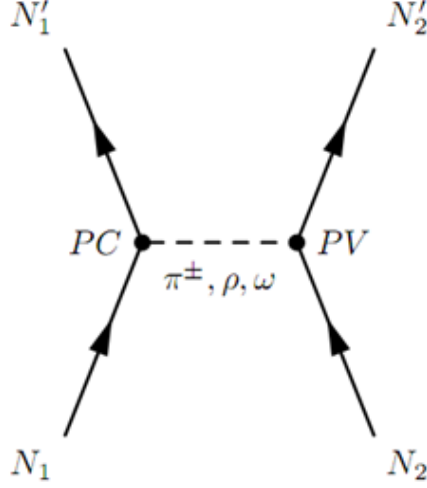


Figure 1.4: Meson exchange model

where  $\vec{\sigma}$  and  $\vec{\tau}$  are Pauli matrices for spin and isospin,  $\vec{\pi}$ ,  $\vec{\rho}$  and  $\vec{\omega}$  are the pseudo and vector meson quantized fields. The weak vertices are written in terms of the seven phenomenological couplings mentioned earlier [21]

$$\begin{aligned}
 \mathcal{H}_{wk} = & \frac{h_{\pi}^1}{\sqrt{2}} \bar{N} (\vec{\tau} \times \vec{\pi})_z N \\
 & + \bar{N} \left( h_{\rho}^0 \vec{\tau} \cdot \vec{\rho}^{\mu} + h_{\rho}^1 \rho_z^{\mu} + \frac{h_{\rho}^2}{2\sqrt{6}} (3\tau_z \rho_z^{\mu} - \vec{\tau} \cdot \vec{\rho}^{\mu}) \right) \gamma_{\mu} \gamma_5 N \\
 & + \bar{N} (h_{\omega}^0 \omega^{\mu} + h_{\omega}^1 \tau_z \omega^{\mu}) \gamma_{\mu} \gamma_5 N - h_{\rho}^{1'} \bar{N} (\vec{\tau} \times \vec{\rho}^{\mu})_z \frac{\sigma_{\mu\nu} k^{\nu}}{2m_N} \gamma_5 N.
 \end{aligned} \tag{1.3}$$

The potential  $V_{DDH}^{PV}$ , is generated by the meson exchange diagram of Fig. 1.4, where one meson-nucleon vertex is parity conserving and the other is parity violating. A fourier transform of the Eqs. 1.2 and 1.3 gives the coordinate-space DDH potential

[10, 21]

$$\begin{aligned}
V_{DDH}^{PV}(\vec{r}) = & i \frac{h_\pi^1 g_A m_N}{\sqrt{2} F_\pi} \left( \frac{\vec{\tau}_1 \times \vec{\tau}_2}{2} \right)_3 (\vec{\sigma}_1 + \vec{\sigma}_2) \cdot \left[ \frac{\vec{p}_1 - \vec{p}_2}{2m_N}, w_\pi(r) \right] \\
& - g_\rho \left( h_\rho^0 \tau_1 \cdot \tau_2 + h_\rho^1 \left( \frac{\vec{\tau}_1 + \vec{\tau}_2}{2} \right)_3 + h_\rho^2 \frac{(3\tau_1^3 \tau_2^3 - \tau_1 \cdot \tau_2)}{2\sqrt{6}} \right) \\
& \left( (\vec{\sigma}_1 - \vec{\sigma}_2) \cdot \left\{ \frac{\vec{p}_1 - \vec{p}_2}{2m_N}, w_\rho(r) \right\} + i(1 + \chi_\rho) \vec{\sigma}_1 \times \vec{\sigma}_2 \cdot \left[ \frac{\vec{p}_1 - \vec{p}_2}{2m_N}, w_\rho(r) \right] \right) \\
& - g_\omega \left( h_\omega^0 + h_\omega^1 \left( \frac{\vec{\tau}_1 + \vec{\tau}_2}{2} \right)_3 \right) \\
& \left( (\vec{\sigma}_1 - \vec{\sigma}_2) \cdot \left\{ \frac{\vec{p}_1 - \vec{p}_2}{2m_N}, w_\omega(r) \right\} + i(1 + \chi_\omega) \vec{\sigma}_1 \times \vec{\sigma}_2 \cdot \left[ \frac{\vec{p}_1 - \vec{p}_2}{2m_N}, w_\omega(r) \right] \right) \\
& - (g_\omega h_\omega^1 - g_\rho h_\rho^1) \left( \frac{\vec{\tau}_1 - \vec{\tau}_2}{2} \right)_3 (\vec{\sigma}_1 + \vec{\sigma}_2) \cdot \left\{ \frac{\vec{p}_1 - \vec{p}_2}{2m_N}, w_\rho(r) \right\} \\
& - g_\rho h_\rho^1 i \left( \frac{\vec{\tau}_1 \times \vec{\tau}_2}{2} \right)_3 (\vec{\sigma}_1 + \vec{\sigma}_2) \cdot \left[ \frac{\vec{p}_1 - \vec{p}_2}{2m_N}, w_\rho(r) \right],
\end{aligned} \tag{1.4}$$

where  $\vec{p}_i = -i\vec{\nabla}_i$ , and  $\vec{\nabla}_i$  is the gradient with respect to the coordinate  $\vec{x}_i$  of the  $i$ -th nucleon,  $r = |\vec{x}_1 - \vec{x}_2|$  is the separation between the two nucleons,

$$w_i(r) = \frac{e^{-m_i r}}{4\pi r} \tag{1.5}$$

is the standard Yukawa potential. Various observables are sensitive to distinct linear combinations of  $h_M^i$

$$V_{PV} = \sum_{M=\pi,\rho,\omega} \sum_{\Delta I=0,1,2} h_M^{\Delta I} V_M^{\Delta I}. \tag{1.6}$$

The DDH reasonable ranges and best values are given in Table 1.1.

PV coupling	DDH range	DDH best value
$h_\pi^1$	$0 \rightarrow 30$	+12
$h_\rho^0$	$30 \rightarrow -81$	-30
$h_\rho^1$	$-1 \rightarrow 0$	-0.5
$h_\rho^2$	$-20 \rightarrow -29$	-25
$h_\omega^0$	$15 \rightarrow -27$	-5
$h_\omega^1$	$-5 \rightarrow -2$	-3

Table 1.1: Theoretical reasonable ranges and best values for the PV meson-nucleon couplings  $h_M^i$  from DDH[7, 10, 69]. All values are quoted in units of  $g_\pi = 3.8 \times 10^{-8}$ .

For the HWI, the relatively newer and modern approach is to use effective field theory. The EFTs are written in the language of nucleons, since matching to quark-level QCD

calculation is not possible at present. Various versions of this approach are: pionless EFT (EFT  $\not{\pi}$ ), chiral EFT ( $\chi$ PT), heavy baryon chiral perturbation theory (HB $\chi$ PT), etc. [12]. Here, we consider the pionless EFT developed by Holstein, Ramsey-Musolf, van Kolck, Zhu and Maekawa [11]. In this model independent effective field theory, nucleon nucleon potentials are expressed in terms of 12 parameters, whose linear combinations give us 5 low energy coupling constants (LEC) [10]

$$\lambda_t, \lambda_s^{I=0,1,2}, \rho_t. \quad (1.7)$$

It is possible to obtain the expressions for  $\rho_t, \lambda_t$  and  $\lambda_s^{0,1,2}$  expressed in terms of DDH coupling constants and then to employ the DDH best values and reasonable ranges for the PV meson-nucleon couplings to obtain the predictions for the PV LECs listed in Table 1.2. In this sense, the meson exchange model and effective field theory are actually equivalent to each other.

PV LEC	DDH best	DDH range
$m_N \rho_t$	0.05	0.07 $\rightarrow$ 0.03
$m_N \lambda_t$	0.84	-1.00 $\rightarrow$ 2.48
$m_n \lambda_s^0$	3.82	-4.86 $\rightarrow$ 11.7
$m_N \lambda_s^1$	0.37	0.64 $\rightarrow$ 0.21
$m_N \lambda_s^2$	2.72	2.17 $\rightarrow$ 3.15

Table 1.2: Prediction for the five PV low energy constants (LECs) characterizing hadronic PV in the pionless EFT [10]. All values are quoted in units of  $g_\pi = 3.8 \times 10^{-8}$ .

Another promising approach is the lattice QCD. The first lattice calculation of hadronic parity violation, was performed by J. Wasem [17], who determined the PV  $\pi N$  coupling

$$h_{\pi NN}^{(1),\text{con}} = (1.099 \pm 0.505_{-0.064}^{+0.058}) \times 10^{-7}. \quad (1.8)$$

The first uncertainty is statistical and the second one systematics, and the superscript “con” indicates contribution from connected diagrams only. This value is consistent with the DDH range for  $h_{\pi NN}^{(1)}$  and the values determined in other calculations, as well as the current experimental bounds [17]. The application of lattice QCD to nuclear physics problems is relatively new and continues to be a very active area of research. It has the potential to predict the relevant couplings at the level of Standard Model degrees of freedom, establishing a direct link to the well-tested weak quark-quark interactions. More on lattice QCD approach for hadronic parity violation can be found in Refs. [15, 16, 17].



### 1.3 Relating coupling constants to observables

In general, the parity violating asymmetry in a measurement can be expressed as a linear combination of the coupling constants

$$A = C_\pi^1 h_\pi + C_\rho^0 h_\rho^0 + C_\rho^1 h_\rho^1 + C_\rho^2 h_\rho^2 + C_\omega^0 h_\omega^0 + C_\omega^1 h_\omega^1, \quad (1.9)$$

where the coefficients  $C$  are estimated for each observable using nuclear wave functions and operators for the observables.

In simple systems, for example two-body reactions  $\vec{n} + p \rightarrow d + \gamma$ , the calculation involves considering the initial state  $|i\rangle$ , the final state  $|f\rangle$  and then calculating the matrix elements of the amplitude  $\langle i|V_{PV}|f\rangle$ , where the potential is chosen from the DDH model or EFT under consideration. For the  $\vec{n} + p \rightarrow d + \gamma$  reaction, the sensitivity coefficients are [27, 46]

$$A_\gamma = -0.107h_\pi^1 - 0.001h_\rho^1 - 0.004h_\omega^1. \quad (1.10)$$

In few-body systems, calculations are done with quasi-exact nonperturbative strong interaction methods. Faddeev-Yakubovsky methods and variational methods in hyperspherical harmonic bases have been applied to the  $A = 4$  system. For  $\vec{n} + {}^3\text{He} \rightarrow \text{p} + \text{T}$ , M. Viviani *et al.* reported the sensitivities [30]

$$A_p = -0.1853 h_\pi^1 - 0.0380 h_\rho^0 + 0.0230 h_\rho^1 - 0.0011 h_\rho^2 - 0.0231 h_\omega^0 + 0.0500 h_\omega^1. \quad (1.11)$$

Hyperspherical harmonics and quantum Monte Carlo methods are used for  $A = 5$  systems, such as the spin rotation of polarized neutrons in helium [30, 31]. Table 1.3 shows the sensitivity of observables from different processes to the DDH coupling constants, together with the experimental asymmetry, if available. Details of these experimental results are discussed in the next section.

Process	Observable	Expt( $\times 10^{-7}$ )	$h_\pi^1$	$h_\rho^0$	$h_\rho^1$	$h_\rho^2$	$h_\omega^0$	$h_\omega^1$
$\vec{n} + \text{p} \rightarrow \text{d} + \gamma$	$A_\gamma \equiv \vec{\sigma}_n \cdot \vec{k}_\gamma$	$-1.2 \pm 2.1$	-0.11		-0.001			-0.004
$\vec{n} + \text{d} \rightarrow \text{t} + \gamma$	$A_\gamma \equiv \vec{\sigma}_n \cdot \vec{k}_\gamma$	$42 \pm 38$	0.69	-0.33	0.99	0.05	-0.22	-0.05
$\vec{n} + {}^3\text{He} \rightarrow \text{p} + \text{T}$	$A_p \equiv \vec{\sigma}_n \cdot \vec{k}_p$	–	-0.185	-0.038	0.023	-0.0011	-0.023	0.050
$\vec{n} + {}^4\text{He} \rightarrow \text{n} + {}^4\text{He}$	$\phi_{\text{PV}}$	$1.7 \pm 9.2$	-0.97	-0.32	0.11		-0.22	0.22
$\vec{p} + \text{p} \rightarrow \text{p} + \text{p}$ (13.6 MeV)	$A_L \equiv \vec{\sigma}_p \cdot \vec{k}_p$	$-0.93 \pm 0.21$		0.042	0.042	0.017	0.046	0.046
$\vec{p} + \text{p} \rightarrow \text{p} + \text{p}$ (45 MeV)	$A_L \equiv \vec{\sigma}_p \cdot \vec{k}_p$	$-1.57 \pm 0.23$		0.074	0.074	0.032	0.067	0.067
$\vec{p} + \text{p} \rightarrow \text{p} + \text{p}$ (221 MeV)	$A_L \equiv \vec{\sigma}_p \cdot \vec{k}_p$	$0.84 \pm 0.34$		-0.03	-0.03	-0.012		
$\vec{p} + {}^4\text{He} \rightarrow \text{p} + {}^4\text{He}$	$A_L$	$-3.34 \pm 0.93$	-0.34	0.14	0.047		0.059	0.059
${}^{18}\text{F}$ decay	$P_\gamma$	$1200 \pm 3680$	4385		-492			-833
${}^{19}\text{F}$ decay	$A_\gamma$	$-740 \pm 190$	-94.2	34.1	-10.2		19.4	-16.9

Table 1.3: Expressing observables in terms of DDH coupling constants [47]. Details of the reactions and experimental results are explained in the next section.

## 1.4 Existing data

---

To understand the current situation in this field, we take a look of the existing data. Following is the summary of existing results [21].

Two-body results: The proton-proton scattering [25] was measured at different energies. The correlation  $A_L \equiv \vec{\sigma}_p \cdot \vec{k}_p$  was measured in each case for the longitudinally polarized proton from unpolarized proton target. At 13.6 MeV,  $A_L$  was measured to be  $(-0.93 \pm 0.20 \pm 0.05) \times 10^{-7}$  [22] and at 15 MeV it was found to be  $(-1.7 \pm 0.8) \times 10^{-7}$  [23] by groups from Bonn and Los Alamos. The PSI group measured  $A_L = (-1.57 \pm 0.23) \times 10^{-7}$  at 45 MeV [24]. TRIUMF measured it  $(+0.84 \pm 0.34) \times 10^{-7}$  at a medium energy of 221 MeV [25]. The investigation of the polarized neutron capture on the para hydrogen target ( $n + p \rightarrow d + \gamma$ ) has completed several generations. In this case the correlation between the neutron spin and photon direction  $A_\gamma(\vec{n}p)$  was measured. In 1977 it was measured to be  $(0.6 \pm 2.1) \times 10^{-7}$  at Grenoble. [26]. The NPDGamma experiment at LANL measured [27]

$$A_\gamma(\vec{n}p)|_{\text{LANL}} = (-1.2 \pm 1.9 \pm 0.2) \times 10^{-7}. \quad (1.12)$$

The second generation of the LANL measurement, relocated at the SNS with the goal of higher precision, is now preparing the publication of the result. At the Leningrad reactor, the circular polarization of photons, emitted by the protons captured on the unpolarized thermal neutrons, was measured to be  $P_\gamma(np) = (1.8 \pm 1.8) \times 10^{-7}$  [28, 29].

Few-body results: The asymmetry from the scattering of longitudinally polarized protons from  $^4\text{He}$  target was measured to be  $A_L(\vec{p}\alpha; 46 \text{ MeV}) = (-3.3 \pm 0.9) \times 10^{-7}$  by the PSI experiment [32]. A spin rotation of transversely polarized neutrons was at NIST with  $^4\text{He}$  as the target. The measurement found  $\frac{d\phi^{m\alpha}}{dz} = (1.7 \pm 9.1 \pm 1.4) \times 10^{-7} \text{ rad/m}$  [33]. Longitudinally polarized protons scattering on deuterium target was reported to produce an asymmetry of  $A_L(\vec{p}d; 15 \text{ MeV}) = (-0.35 \pm 0.85) \times 10^{-7}$  [34].

Measurements with many-body enhancement: Measurements with many-body systems provided larger PV signal because of the many-body enhancement. Groups from CalTech/Seattle, Florence, Mainz, Queens independently reported the measurements from the circular polarization of photons emitted in the decay of the  $J^P, I = 0^-, 1.081 \text{ MeV}$  excited state of  $^{18}\text{F}$  to the  $J^P, I = 0^+, 0$  ground state to be  $-7 \pm 20, 3 \pm 6, -10 \pm 18$  and  $2 \pm 6$  (all in units of  $10^{-4}$ ) respectively [35, 36, 37, 38]. Similar photon asymmetries from  $^{19}\text{F}$  were measured to be  $A_\gamma = (-8.5 \pm 2.6) \times 10^{-5}$  (Seattle group) and  $A_\gamma = (-6.8 \pm 1.8) \times 10^{-5}$  (Mainz group) [39, 40]. Limits on the anapole moment of  $^{205}\text{Tl}$  came from the measurements [43, 44] with values  $\kappa_{\text{tot}}(^{205}\text{Tl}) = 0.29 \pm 0.40$  (Seattle) and  $\kappa_{\text{tot}}(^{205}\text{Tl}) = -0.08 \pm 0.40$  (Oxford). Similar measurement for  $^{133}\text{Cs}$  [45] reported a value of  $\kappa_{\text{tot}}(^{133}\text{Cs}) = 0.112 \pm 0.016$ .

Fig. 1.5 shows the constraints imposed on the coupling constants by different reactions or experiments. The red \* shows the best value as predicted by the DDH model.

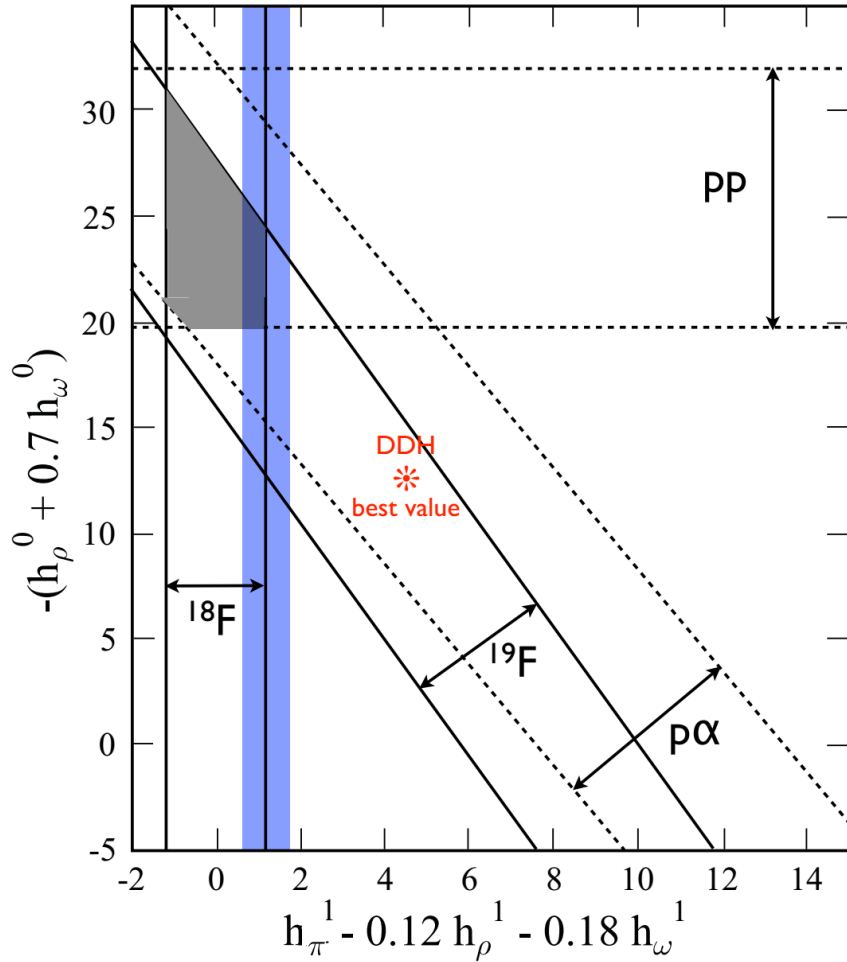


Figure 1.5: Constraints for the coupling constants (in units of  $10^{-7}$ ) from different experiments. Also shown DDH best value. Blue vertical band indicates the recent lattice QCD estimate. The gray shaded area is consistent with all experiments. This plot is from Ref.[21].

## 1.5 Outlook for the current experiment

In any of the hadronic theories, the coupling constants have to be determined experimentally. On one side we have complicated systems like  $^{18}\text{F}$ ,  $^{181}\text{Ta}$ ,  $^{41}\text{K}$ , which give larger PV asymmetries because of many body enhancement. However the nuclear structure for these many-body systems is not well understood. On the other side, theoretically clean and predictable measurements are restricted to simple systems—two body or few body systems. But these simple systems are limited in number and do not allow for effects that enhance the size of the asymmetry. In these systems we embrace the challenge of measuring very small PV asymmetry, overcoming this challenge by employing better experimental design and technological developments. This motivated a program of HWI experiments in few-nucleon systems: p-p, n-p, p- $\alpha$ ,

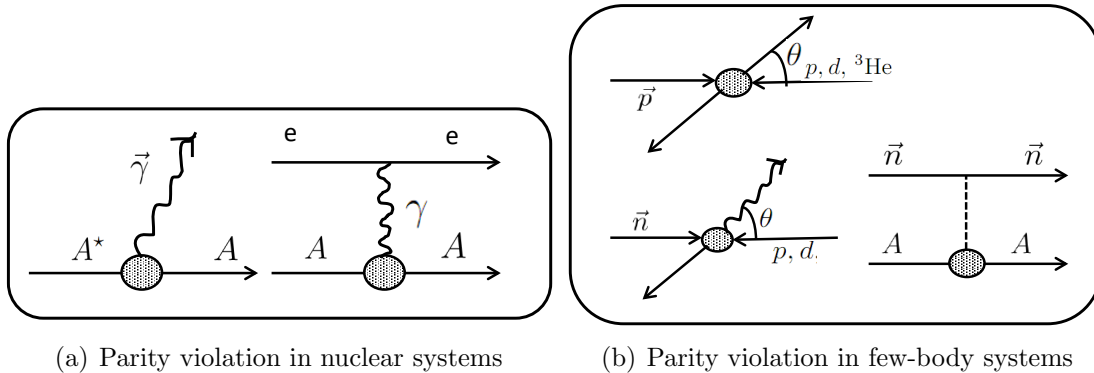


Figure 1.6: PV in nuclear and few-body systems

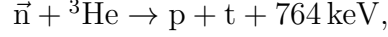
$n$ - $^3\text{He}$ ,  $n$ - $\alpha$  etc. For such few-body systems the parity-violating observables can be reliably calculated in terms of low-energy hadronic weak coupling constants which are accessible from effective field theory or lattice QCD. Different hadronic nuclear reactions have varying sensitivity to each coupling. The goal of HWI program is to measure enough different reactions to resolve each of the coupling constants.

The NPDGamma and  $n$ - $^3\text{He}$  experiments are an important part of this active program to measure the hadronic weak interaction coupling constants, relying on hadronic parity violation to isolate the weak component of the hadronic interaction.

## 1.6 The n-<sup>3</sup>He Experiment

---

The n-<sup>3</sup>He experiment is a high precision measurement of the parity violating proton asymmetry in the reaction



where the incident polarized neutron reacts with the <sup>3</sup>He target nucleus to produce a back-to-back proton and triton. We are interested in the asymmetry of the recoil proton with respect to the spin of the neutron.

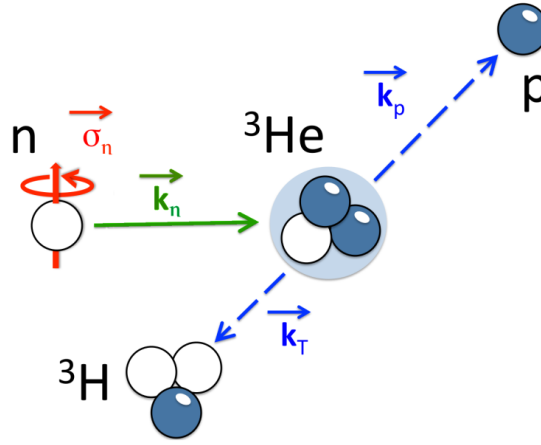


Figure 1.7: The n-<sup>3</sup>He reaction: Polarized neutron hitting helium produces proton and triton. The daughter products carry the energy as the kinetic energy. To conserve momentum, the proton and triton follow opposite directions.

### 1.6.1 Experimental observable

The PV asymmetry involves the correlation between the spin of the neutron, shown in red in Fig. 1.7 and Eq. 1.13, and the momentum of the outgoing proton, shown in blue.

$$\sigma = \sigma_0 \left[ 1 + \vec{\sigma}_n \cdot \vec{k}_p A_{pv} + (\vec{k}_n \times \vec{\sigma}_n) \cdot \vec{k}_p A_{pc} \right] \quad (1.13)$$

Eq. 1.13 has a parity conserving part  $A_{pc}$  and a parity violating part  $A_{pv}$ . The spin of the neutron follows the magnetic field, in the vertical direction ( $\hat{y}$ ), and the neutron momentum is downstream in the ( $\hat{z}$ ) direction. We orient our detector in two different orientations for sensitivity to one of the asymmetries at a time: (a) up-down (UD) mode with wires in individual planes aligned in a vertical row, along ( $\hat{y}$ ) for sensitivity to the PV asymmetry, or (b) left-right (LR) mode with the wires

aligned in a horizontal row, along  $(\hat{x})$  for sensitivity to the PC asymmetry. The PV asymmetry is the main physics result of this measurement, but we also measure the parity conserving asymmetry to confirm the nuclear wave calculations, verify the sensitivity of our experiment, and estimate PC mixing into the much smaller PV asymmetry. The PV asymmetry is expected to be extremely small, on the order of  $10^{-7}$ . Our goal is to measure this asymmetry to a precision of  $2 \times 10^{-8}$ .

## 1.6.2 Experimental Setup

Fig. 1.8 shows the experimental setup for the  $n$ - $^3\text{He}$  experiment at the Fundamental Neutron Physics Beam (FnPB), beamline 13 (BL13) [61] of the Spallation Neutron Source (SNS) at Oak Ridge National Laboratory (ORNL). From the left to right in Fig. 1.8, there is the 60 Hz pulsed neutron beam in the neutron guide and a neutron beam intensity monitor (M1). The neutrons then pass through a super mirror polarizer[60] and then through a radio frequency spin flipper (RFSF) which rotates the neutron spin axis by  $180^\circ$  when the RFSF is turned on. Finally, after passing through the collimator, the neutrons impinge on the helium ion chamber, which acts as both the target and detector. A 10 Gauss holding field preserves the neutron spin. We measure the spin asymmetry between the “spin-up” (RFSF off) and “spin-down” (RFSF on) states to extract  $A_{\text{pv}}$  or  $A_{\text{pc}}$  in mode (a) or (b), respectively.

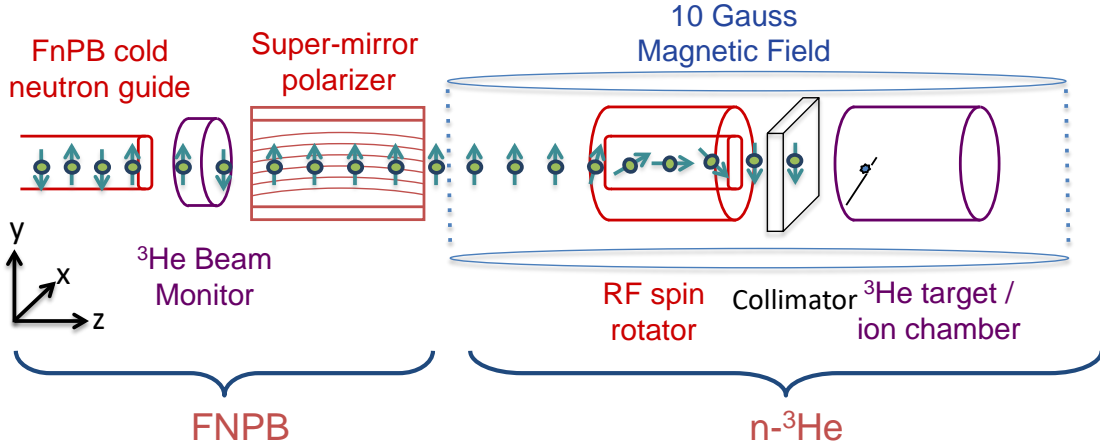


Figure 1.8: The experimental setup for the  $n$ - $^3\text{He}$  experiment. The signal wire orientation inside the ion chamber depends on the mode of operation, which is depicted in the next section.

Fig. 1.10 shows a CAD model of the FnpB/BL13 where the experiment was performed. Fig. 1.10 shows a CAD model of the experimental setup [54].

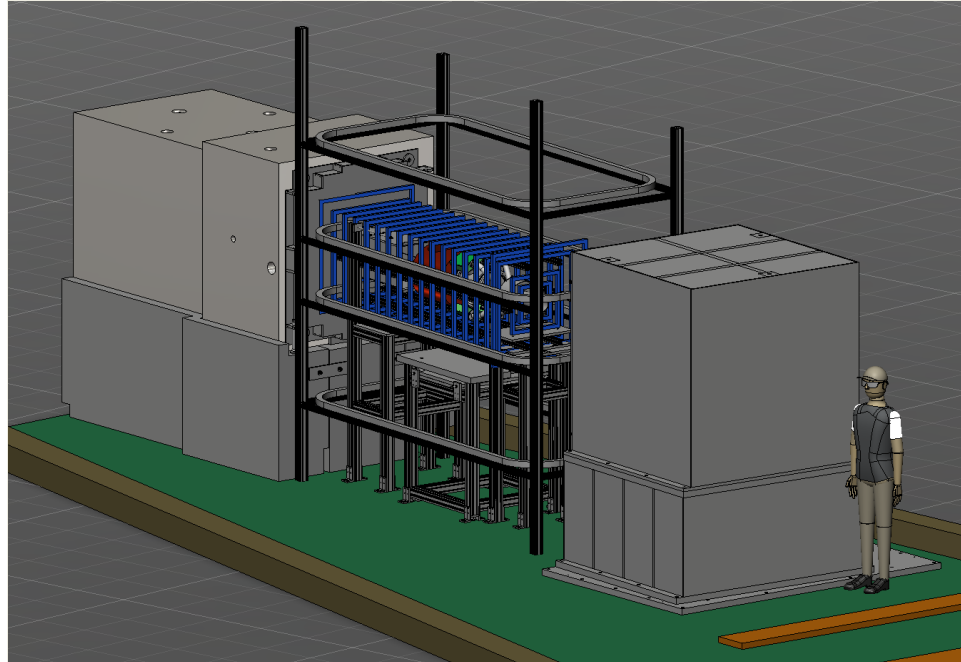


Figure 1.9: CAD model for the beamline 13 (FnPB) where the experiment was performed.

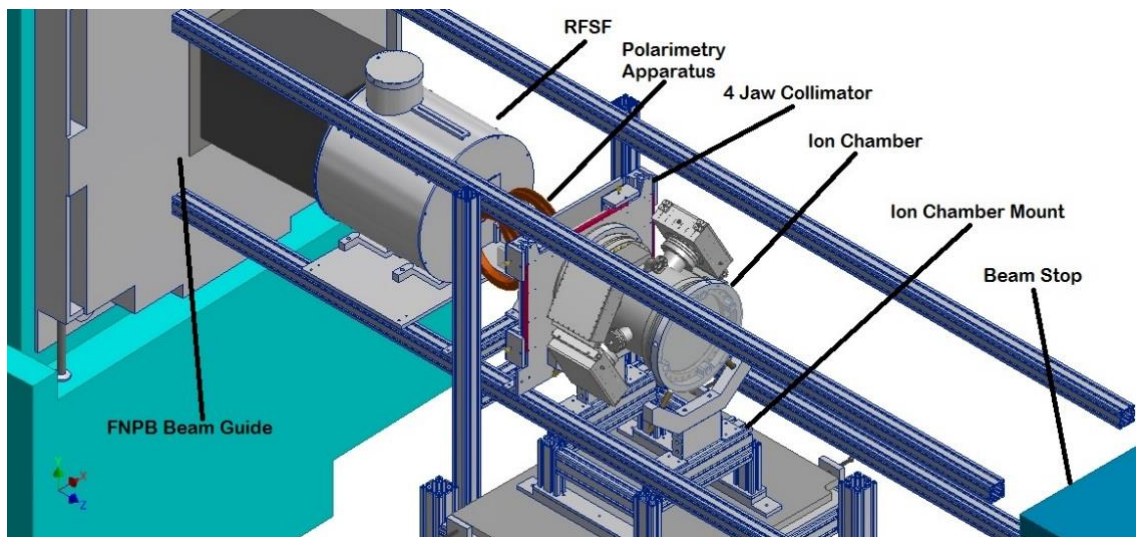


Figure 1.10: CAD model for the experimental setup. Figure courtesy of Eric Plemons [54].

### 1.6.3 Modes of operation

#### Parity violating mode (UD mode)

As we explained above, Fig. 1.11 shows orientation of the detector with the sense wire planes horizontally aligned, in up-down mode for sensitivity to  $A_{pv}$ .

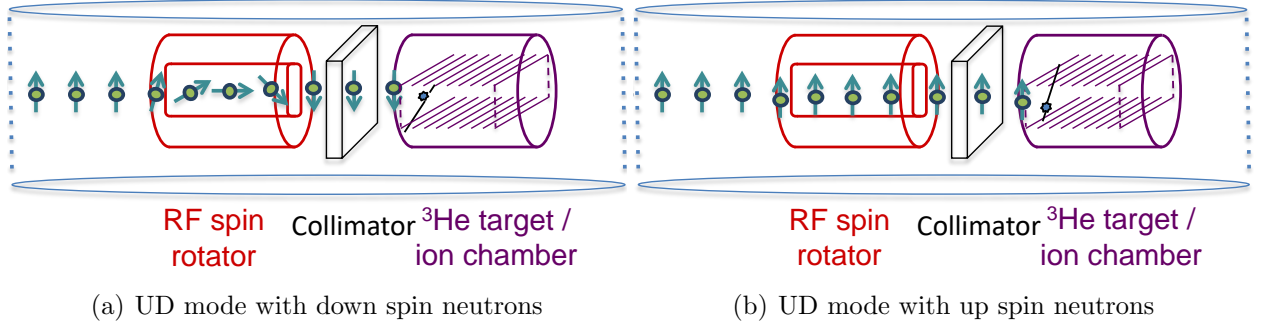


Figure 1.11: The experimental setup for the parity violating UD mode

#### Parity conserving mode (LR mode)

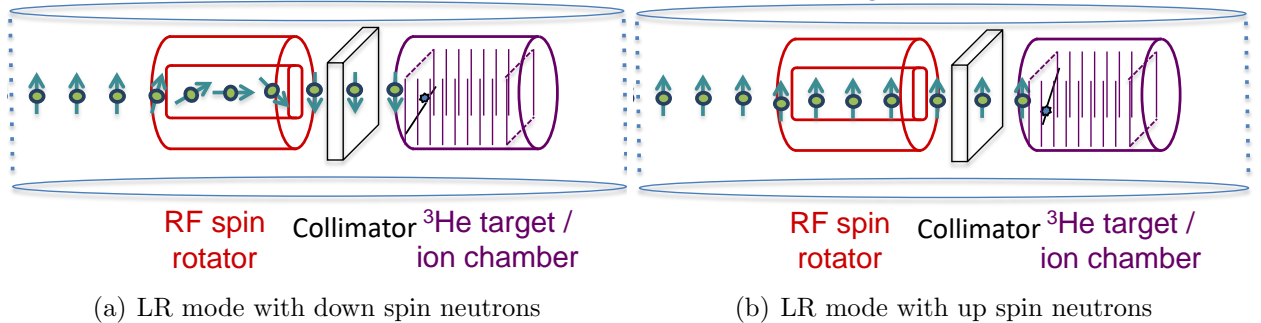


Figure 1.12: The experimental setup for the parity conserving LR mode.

Fig. 1.12 shows the experimental set-up for the parity conserving (left-right) mode. In this orientation of the detector, the sense wires are vertically aligned. In the two modes we measure the asymmetry in the signal of individual sense wires for the neutron spin up versus spin down. 95% of the total data were collected for the UD asymmetry, while the other 5% were for the LR asymmetry. The LR data were taken early in the experiment and then again at the end.



## Chapter 2

# Neutron beam and the time of flight choppers

---

The experiment uses pulsed thermal (cold) neutrons as the incident beam. Much of the experimental design and analysis methods depend on the characteristics of neutron beam. So, here we focus on the spallation neutron source, neutron beam temporal and spatial profile and the time of flight choppers.

### 2.1 Spallation neutron source

---

The n-<sup>3</sup>He experiment was carried out at the Spallation Neutron Source (SNS) facility at Oak Ridge National Laboratory (ORNL) using the 60 Hz pulsed neutron beam from the SNS.

Fig. 2.1 shows different components of the SNS. An ion source at the front end of the accelerator produces negatively charged hydrogen ions ( $H^-$ , one proton orbited by two electrons). The SNS uses a cesium-enhanced, RF-driven multi-cusp ion source to provide a 65 keV  $H^-$  beam at 60 Hz with a pulse length of up to 1 ms. The normal conducting linac consists of six drift tube linac tanks, which bring the  $H^-$  beam up to 86.8 MeV, and four coupled cavity linac structures, which supply additional acceleration to bring the energy to 185.6 MeV. This is followed by a superconducting linac consisting of 11 medium-beta ( $\beta = 0.61$ ) cryomodules each contain 3 cavities and provide 10.1 MV/m, bringing  $H^-$  ions up to an energy of 379 MeV. The high-beta cryomodules (consisting of 4 cavities) are designed to provide up to 15.9 MV/m resulting in a maximum proton energy of 1.3 GeV [61]. The ions pass through a thin foil of carbon or diamond, which strips both electrons off each ion, converting it to a proton [61]. The protons pass into a ring-shaped structure, a proton accumulator ring, where proton pulses from the accelerator are accumulated and shaped to short “bunches” of 700 ns long in base. The 1 GeV proton pulse strikes the liquid mercury spallation target. The MeV neutrons from the spallation process are mod-

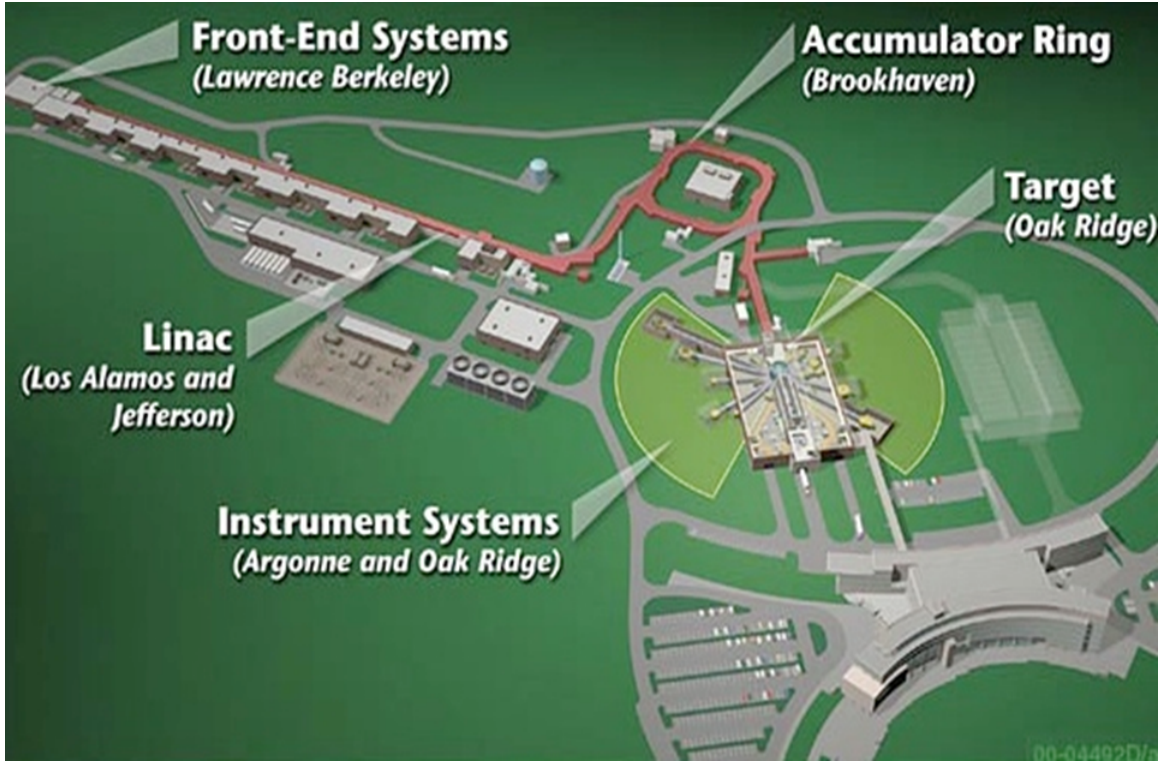


Figure 2.1: Different components of the spallation neutron source at ORNL. The lab name in the parenthesis indicates the facility contributing in the construction of the component.

erated by liquid hydrogen and then guided through 18 beamlines to a wide variety of neutron scattering instruments. Details of the SNS and the BL13 can be found in Ref. [61].

There are compelling reasons for carrying out the  $n$ - $^3\text{He}$  experiment at pulsed neutron source over conventional CW reactor neutron source. The pulsed nature of the beam provides an accurate neutron time of flight information, allowing determination of the neutron energy. Systematic effects can be studied by their energy dependence. Also, the pulsed beam allows an effective use of a resonant RF spin flipper, eliminating the  $\vec{\mu} \cdot \nabla B$  force on the neutrons, which would accelerate the neutrons in a spin-dependent manner, inducing a false asymmetry [64].

### 2.1.1 Neutron flux from the SNS

Fig. 2.2 shows the SNS neutron spectrum taken in special operating mode at 1 Hz (before modification to the DAQ timings) to record the low energy tail of the pulse. In the normal 60 Hz operating mode, individual pulses overlap on top of the previous tail, increasing the average neutron flux. Fig. 2.3 depicts the pulse train, also before modification of the chopper and DAQ timing.

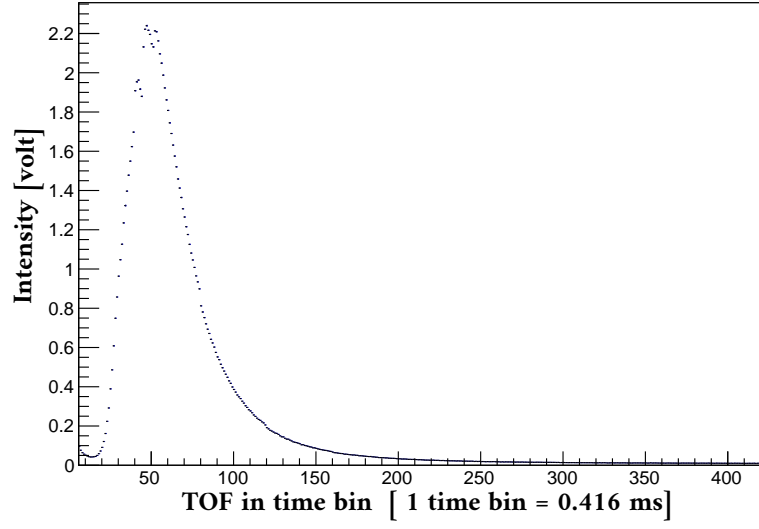


Figure 2.2: Unchopped 1Hz spectrum from the SNS. The TOF does not include the delay. Data taken during the commissioning period of the NPDGamma experiment has been used to make the plot.

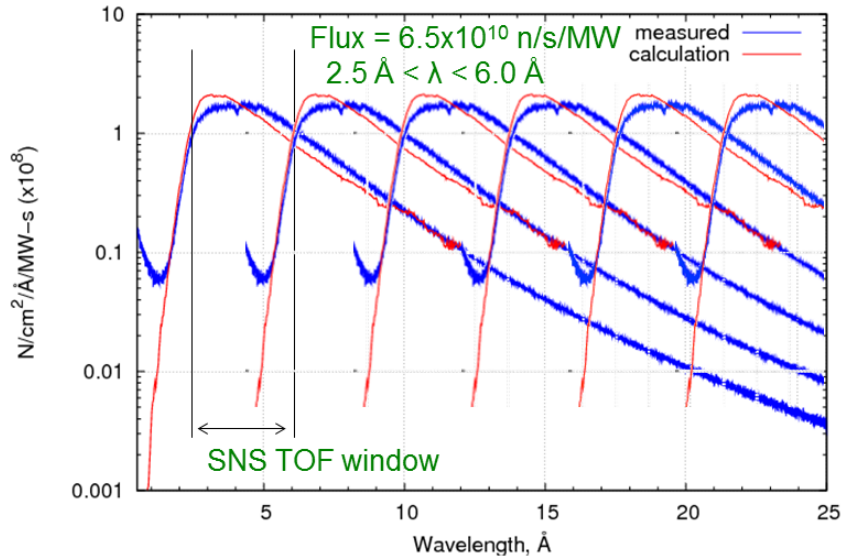


Figure 2.3: Neutron spectrum from the SNS as a function of wavelength. The red one is calculated using McStas and blue line is the measured one. The first vertical lines indicate optimal TOF window. Here  $2.5\text{\AA} < \lambda < 6.0\text{\AA}$  is the naive SNS TOF window. Figure courtesy of Elise Tang.

## 2.2 Time of flight choppers

The experiment uses two time of flight frame definition choppers along the beamline to allow optimal neutron time of flight (TOF) window. The choppers are needed for the experiment to maximize the spin flipper efficiency and minimize the mixing of neutrons of different energies as explained below.

### 2.2.1 Maximizing the RFSF efficiency

The 60 Hz pulsed cold neutrons can be characterized either by wavelength, velocity, energy or time of flight. Two step spin sequence  $\uparrow\downarrow$  is used to form the asymmetry. Moreover runs are separated in groups based on the spin states on dropped pulses to reduce the instrumental systematics. A radio frequency spin flipper is used to flip spin pulse by pulse using NMR technique. We have to tune the amplitude of the RFSF to the specific velocity of the neutrons, which can be done for only one frame of neutron wavelengths at any time. Thus it is necessary to chop out neutrons in all other frames.

### 2.2.2 Neutrons mixing

A single neutron pulse has neutrons of different velocities. Fast neutrons will reach the target first while slower neutrons will have longer time of flight as shown in Fig. 2.4(a). Slower neutrons from any pulse mix with neutrons of subsequent pulses as shown in Fig. 2.4(b). This mixing of neutrons from different frames makes neutron energy information ambiguous.

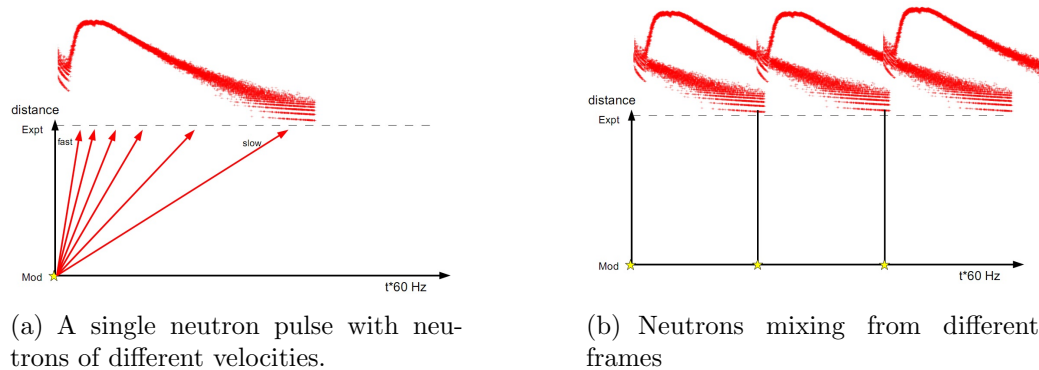


Figure 2.4: a) A single neutron pulse and b) Neutrons mixing from different frames. Figure courtesy of Elise Tang.

The use of one chopper can prevent neutron mixing of two adjacent pulses. But still there will be mixing because of “wraparound”: neutrons so slow the chopper closes

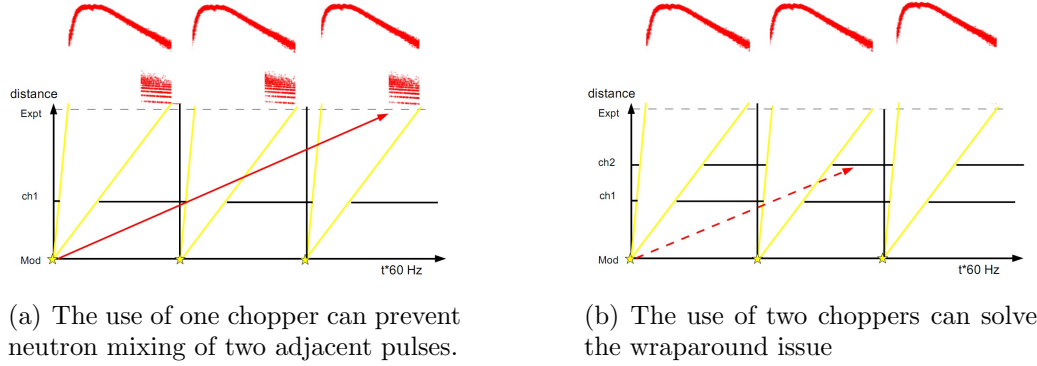


Figure 2.5: The effect of the use of a) single chopper and b) two choppers in removing neutron mixing. Figure courtesy of Elise Tang.

and opens again before they reach the chopper. The use of another chopper can block the wraparound neutrons. Thus the use of two choppers along the neutron beam guide solves any neutron mixing issue.

## 2.3 Chopper optimization

It is a challenge to come up with appropriate chopper settings that give the most optimal TOF window. The optimal TOF window should ensure high neutron flux but fulfill other requirements. To address the issue we do the chopper optimization analysis, where we use a model spectrum and an analytical chopper. This enables us to optimize the choppers by varying chopper location, opening angle and opening phases to get desired neutron flux. For analytical chopper we use the work of Rob Mahurib *et al.* in Ref [48], but we take a different approach for the model spectrum and optimization. This analysis uses NPDGamma data to model the neutron spectrum.

### 2.3.1 The model

We at first rephrase the problem and define the figure of merit. We need to use two choppers to allow neutrons of the desired velocity (wavelength/energy) range, remove wraparound neutrons, maximize SF efficiency and minimize depolarization. But to achieve the desired high precision measurement it is also necessary to get high neutron flux in addition to perfect polarization. This is because the precision in the asymmetry can be related as

$$\delta A = \frac{\sigma_d}{P\sqrt{N}}, \quad (2.1)$$

where  $N$  is the number of neutrons,  $P$  is the polarization on capture,  $\sigma_d$  = the detector efficiency.

Since these (chopping out neutrons and maximizing the flux) requirements are contradictory, we need to find an optimal condition. Considering the effect of the number of neutrons and the polarization in the precision of the measurement we can define our figure of merit (FOM) as follows:

$$FOM = NP^2. \quad (2.2)$$

To find the most optimal operating conditions for the choppers, we construct a model spectrum using an analytical chopper which enables us to optimize the choppers by varying chopper location ( $x$ ), opening angle ( $\theta$ ) and opening phase ( $f_0$ ) to get the maximum FOM.

### Chopper geometry

For the  $n\text{-}^3\text{He}$  experiment, the chopper is a rotating aluminum disk coated everywhere with a gadolinium (Gd) paint except for a slice with opening angle,  $\theta = 2\pi\omega$ . Thus the chopper can absorb a part of the neutron pulse. The disk rotates with the same frequency as the accelerator repetition rate.

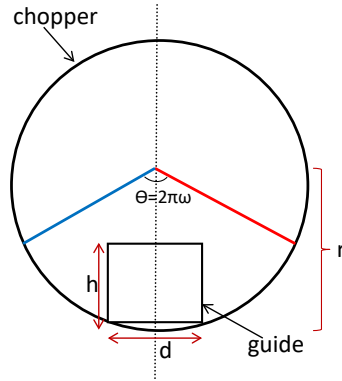


Figure 2.6: Chopper geometry

### Analysis

For the sake of our analysis we consider a chopper with a position  $x$ , an open fraction  $\omega$ , a frequency  $\nu=60$  Hz, time period  $T$ , an opening time  $f_0$ , closing time  $f_c$ , inner crossing time  $t_1$ , outer crossing time  $t_2$ , cross-sectional area of the guide  $h \times d$ . The distance from the bottom of the guide to the center of the chopper disk is  $r$ .

The angle at which the opening edge of the chopper window is at the lower corner of the guide is  $\phi_1$ . The angle at which the opening edge of the chopper window is at the upper corner of the guide is  $\phi_2$  as shown in Fig. 2.7.

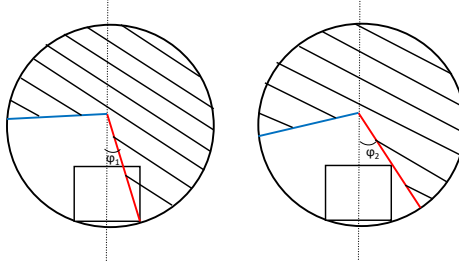


Figure 2.7: The angles between the opening edge of the chopper and the lower and upper corner of the guide

Expressing  $\phi_1$  and  $\phi_2$  in terms of  $r$ ,  $d$  and  $h$ :

$$\tan \phi_1 = \frac{d}{2r},$$

$$\tan \phi_2 = \frac{d/2}{r-h}.$$

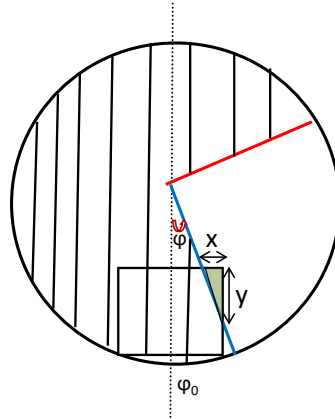


Figure 2.8: A triangular opening part of the guide.

From Fig. 2.8, expression for the area of the triangular part of the guide is

$$A_{tri}(\phi) = \frac{xy}{2} = \frac{\tan |\phi|}{2} \left( \frac{d/2}{\tan |\phi|} - (r-h) \right)^2. \quad (2.3)$$

We can easily check that  $A_{tri}(\phi_2) = 0$  as desired and

$$A_{tri}(\phi_1) = \frac{h^2 d}{4r}. \quad (2.4)$$

From Fig. 2.9, the area of a trapezoid between  $\phi_0 = 0$  and  $\phi$  is

$$A_{trap}(\phi) = h(r - h/2) \tan \phi$$

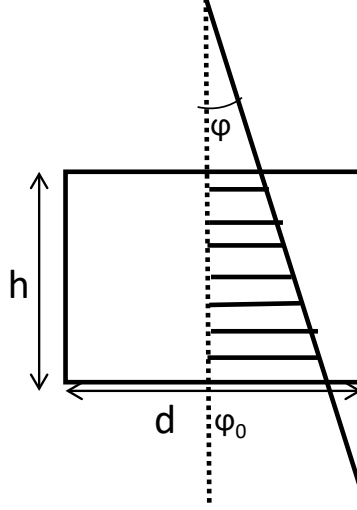


Figure 2.9: A trapezoidal part of the guide

We note that the triangular part  $A_{tri}(\phi)$  is nearly quadratic and for trapezoidal part  $A_{trap}(\phi)$  is nearly linear in  $\phi$ .

For the n-<sup>3</sup>He experiment,  $h = 12$  cm,  $d = 10$  cm,  $r = 29.5$  cm, thus

$$\tan \phi_1 = \frac{d}{2r} \text{ gives } \phi_1 = 0.1679 \text{ rad,}$$

$$\tan \phi_2 = \frac{d/2}{r - h} \text{ gives } \phi_2 = 0.2783 \text{ rad.}$$

Also

$$t_1 = \frac{\phi_1}{2\pi\nu} = 0.445 \text{ ms,}$$

$$t_2 = \frac{\phi_2}{2\pi\nu} = 0.738 \text{ ms.}$$

For any angle  $\phi$  of the open/closed boundary, the open area of the guide becomes [48]:

$$A(\phi) = \begin{cases} 0 & \text{when } \phi < -\phi_2 \\ A_{tri}(\phi) & \text{when } -\phi_2 < \phi < -\phi_1 \\ hd/2 + A_{trap}(\phi) & \text{when } -\phi_1 < \phi < \phi_1 \\ hd - A_{tri}(\phi) & \text{when } \phi_1 < \phi < \phi_2 \\ hd & \text{when } \phi_2 < \phi \end{cases} \quad (2.5)$$

where  $A_{tri}(\phi)$  and  $A_{trap}(\phi)$  are given by the previous expressions.

Now if we plot  $A(\phi)$  we get the open area of the guide as a function of  $\phi$  that looks as shown in Fig. 2.10.



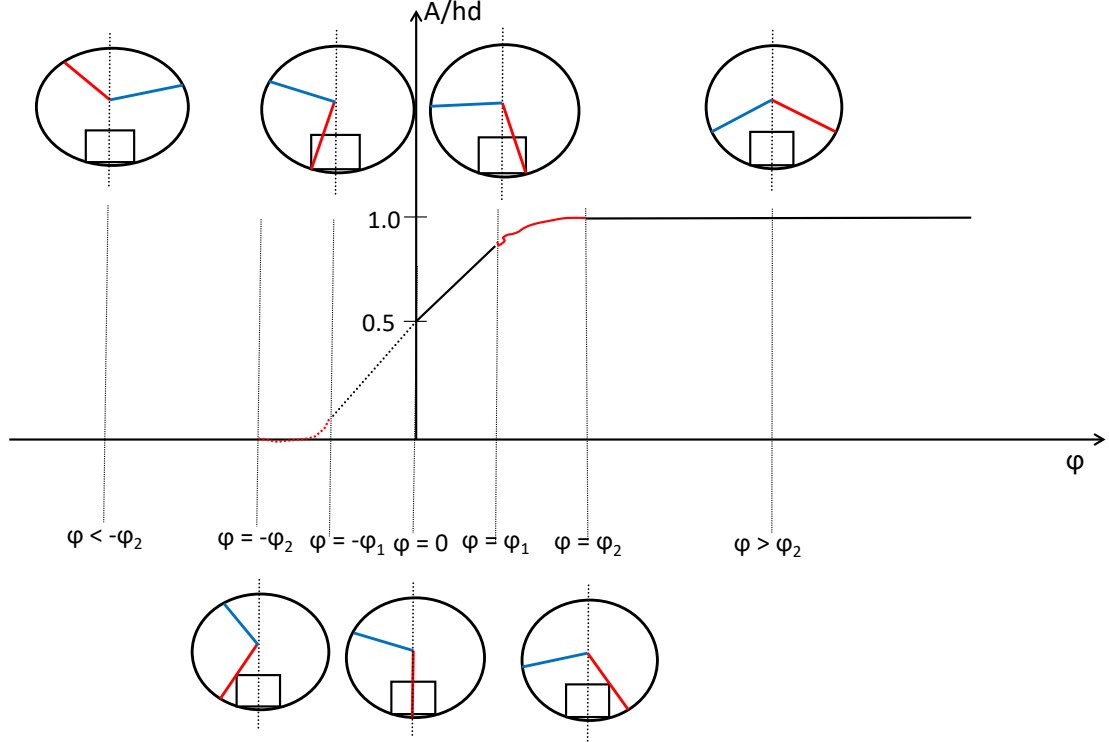


Figure 2.10: The open area of the guide as a function of  $\phi$ . The triangular part  $A_{tri}(\phi)$  which is quadratic in  $\phi$  is indicated by the red color. The slant linear part is for the trapezoidal part. The horizontal linear part is for when the guide is completely blocked or open

In the plot, the triangular part  $A_{tri}(\phi)$  which is quadratic in  $\phi$  is indicated by the red color. The slant linear part is for the trapezoidal part. The horizontal linear part is for when the guide is completely blocked or open.

Thus we have constructed the ramping-up part of a periodic chopper function. Next we want to complete the ramping down part and express it in term of the beam monitor time since our experimental spectrum is in beam monitor time.

To express in term of beam monitor time and introduce the phase, we define  $\tau_x \equiv \tau \cdot x/L - f_0$  to be the time between the chopper's most recent opening and the neutron's arrival at it, then the chopper's transmission can be written as [48]

$$T(\tau) = \begin{cases} A(2\pi\nu \cdot \tau_x)/hd, & 0 \leq \tau_x \leq T\omega - t_2 \\ A(2\pi\nu \cdot (\omega T - \tau_x))/hd, & T\omega - t_2 \leq \tau_x \leq T - t_2 \\ A(2\pi\nu \cdot (\tau_x - T))/hd, & T - t_2 \leq \tau_x \leq T \end{cases} \quad (2.6)$$

In the expression for  $T(\tau)$ , the first condition just replaces our previous function  $A(\phi)$  expressed in beam monitor time. The second and third conditions just complete the full cycle by utilizing the fact that the function is periodic and symmetric (i.e. the chopper edges can be interchanged) so the ramping-down can be constructed by

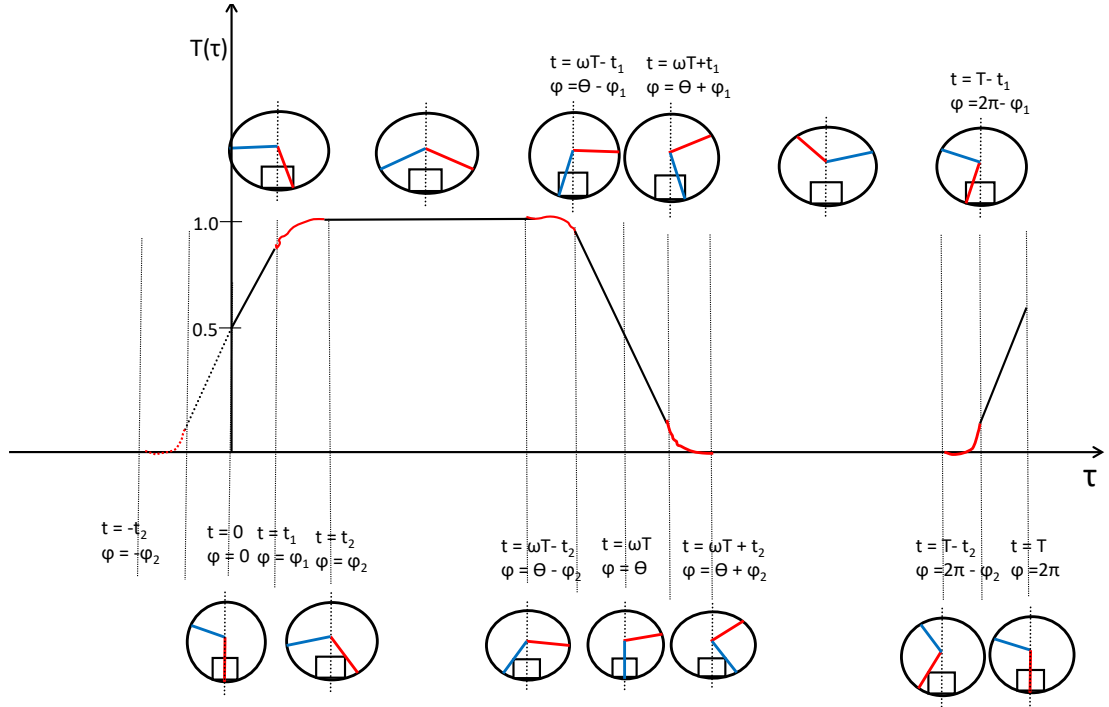


Figure 2.11: Plot for the transmission as a function of the time of flight.

shifting the time appropriately in our first expression. Fig. 2.11 show the transmission as a function of  $\tau$ .

We use the expression for transmission  $T(\tau)$  as our chopper function. In our chopper function the three adjustable parameters are:

- The chopper location ( $x$ )
- Chopper opening angle ( $\theta = 2\pi\omega$ ) and
- Opening phase ( $f_0$ )

Now if we keep repeating our chopper function over periods we get the plot in Fig. 2.12 for the chopper function for any arbitrary beam monitor time. For two choppers the resultant transmission is given by just the product of the two transmissions. This is illustrated in Fig. 2.13.

We note that the plot for the transmission as a function of time of flight has some features. It has a different periodicity than the chopper itself, i.e. period is stretched by a factor of  $L/x$ . The chopper closer to the moderator (here chopper 1) has a larger time period. Again chopper 2 has sharper ramping up and down compared to chopper 1. This means that the opening or closing time is larger for chopper 1 which is closer to the moderator but further from target.

We can now apply the chopper function to 1 Hz spectrum. In Fig. 2.14 we applied the chopper transmission function (resultant of two choppers) to 1 Hz spectrum. The

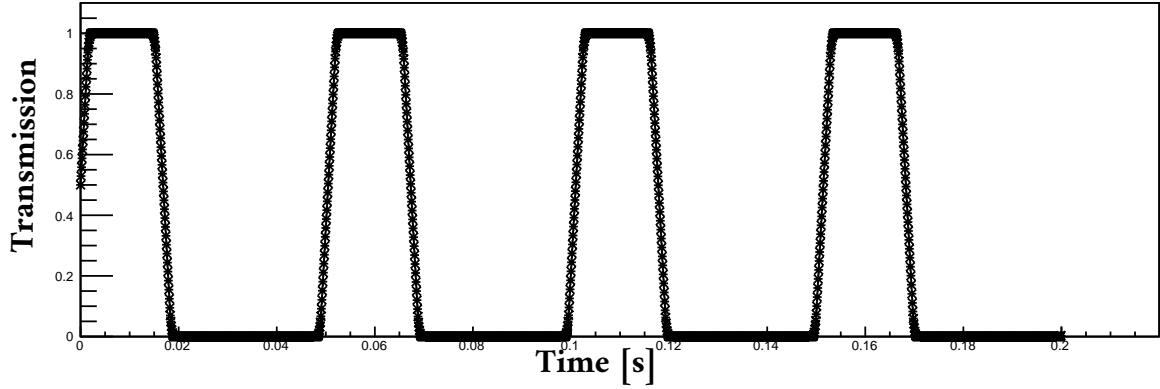


Figure 2.12: Plot for the transmission as a function of the time of flight

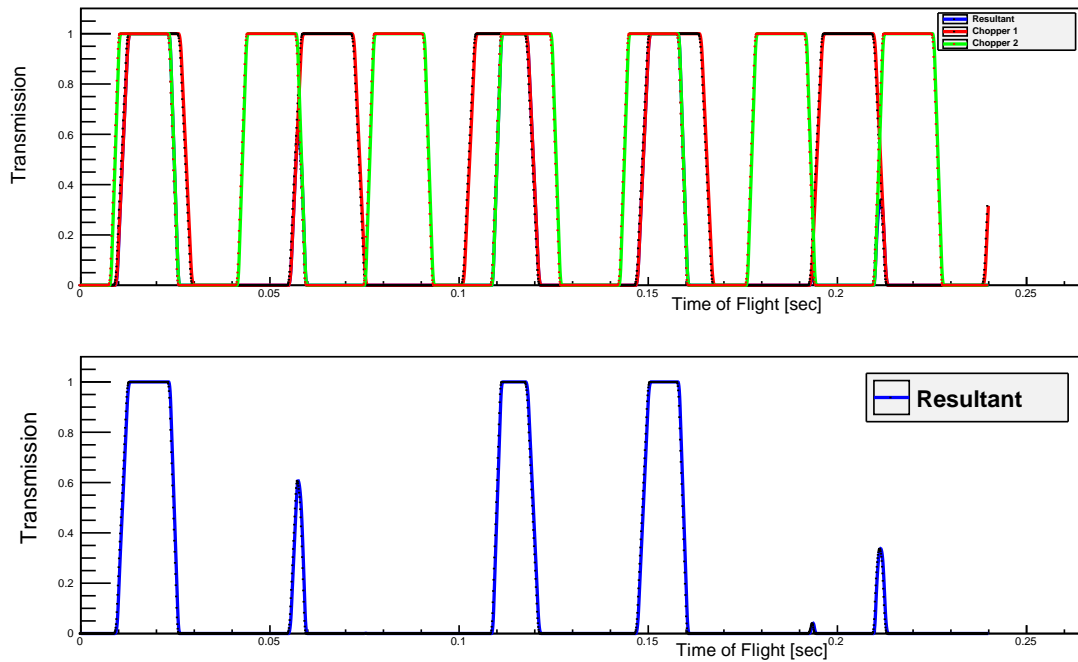


Figure 2.13: The upper one is a simultaneous plot for the transmission of chopper-1 (closer to the moderator) and chopper-2 (further from the moderator). The lower one is the resultant transmission of the two choppers.

top plot is the unchopped 1 Hz spectrum and the bottom one is the result of the application of two choppers. We note that, while the top plot has normal scale for vertical axis, the bottom plot is shown with log scale.

So we have a setup which allows adjusting chopper parameters to get any desired window of the spectrum.

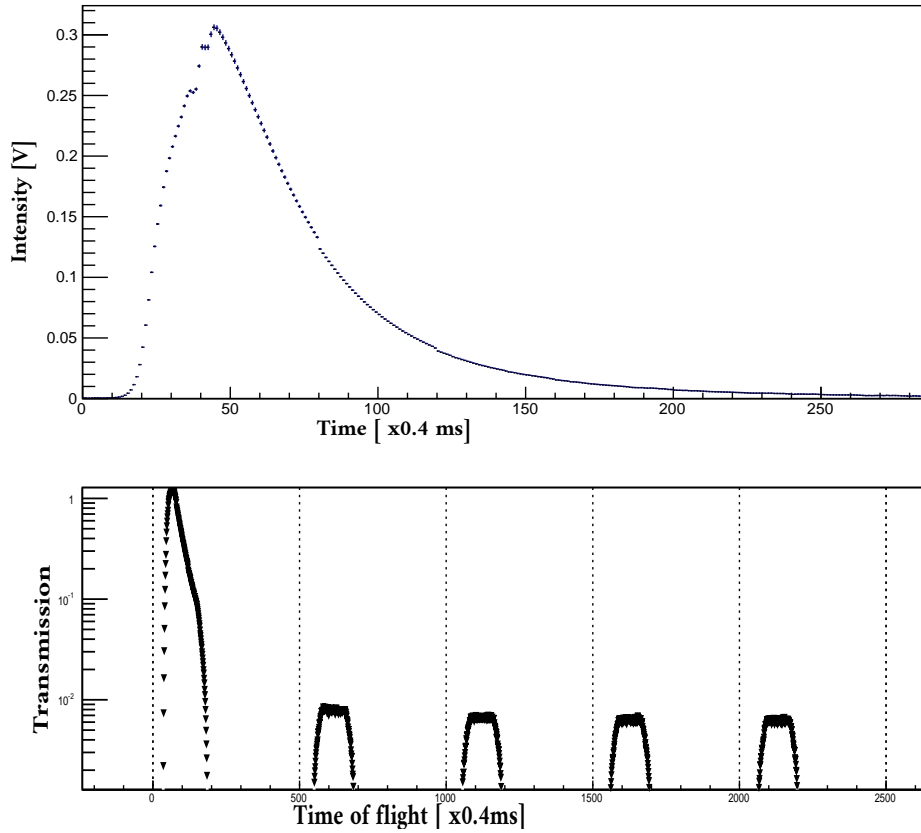


Figure 2.14: Unchopped (top) and chopped (bottom) 1 Hz spectrum

### 2.3.2 Producing 60 Hz spectrum

The experiment uses 60 Hz spectrum. We can use our chopped 1 Hz spectrum to produce 60 Hz spectrum. To do that we split 1 Hz chopped spectrum at each 40 time of flight bins (16.66 ms). Then we add all the pieces to get folded spectrum which is equivalent to 60 Hz spectrum.

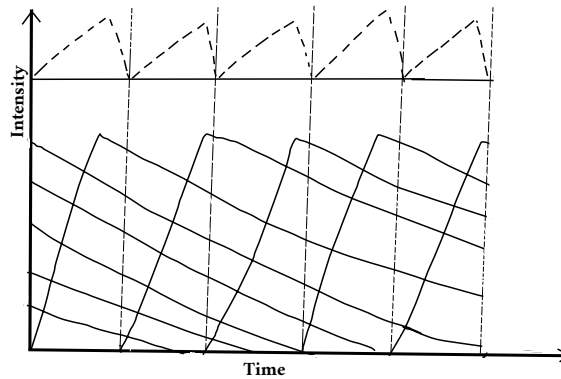


Figure 2.15: A cartoon to illustrate the recipe of producing 60 Hz spectrum from 1 Hz.

The recipe is illustrated in Fig. 2.15 and the spectrum obtained following the recipe is shown in Fig. 2.16.

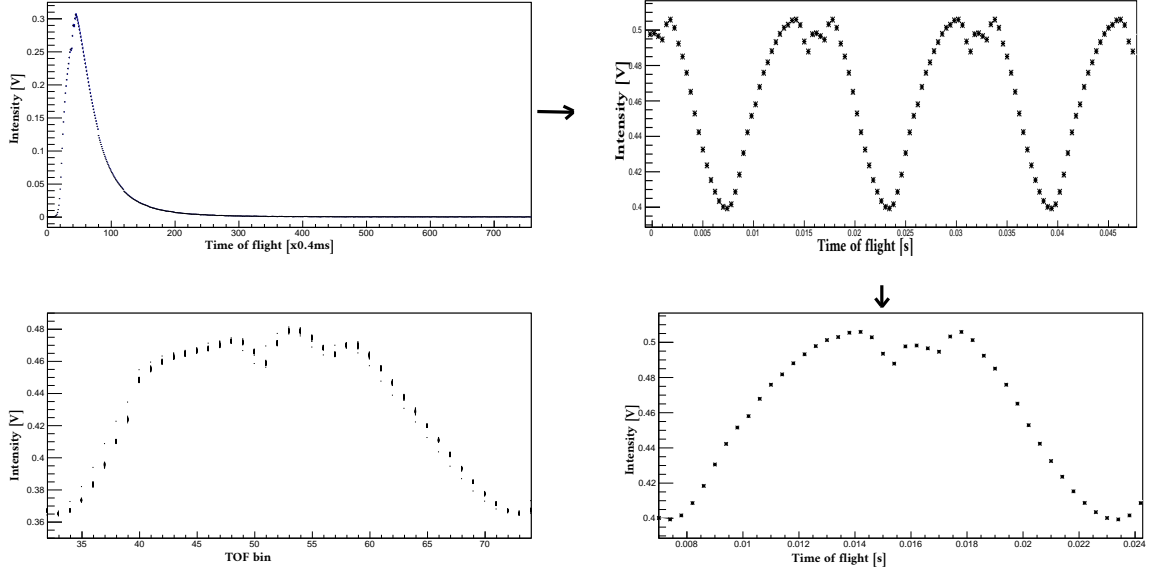


Figure 2.16: 1 Hz spectrum can be folded to produce 60 Hz spectrum. Lower right plot is folded 60 Hz and lower left plot is the experimental 60 Hz spectrum.

### 2.3.3 Test for the model

We are now in a position to compare our model spectrum with experimental one. Out of the three monitors in the experiment we use monitor-1 data for the fitting and comparison. For the  $n\text{-}^3\text{He}$  experiment, for chopper-1 the open fraction is  $\omega=0.3664$  and for chopper-2 it is 0.4639 ; for chopper-1,  $x/L = 0.363036$  and for chopper-2  $x/L = 0.495049$ . In our fitting we look for the phase that minimizes the chi square.

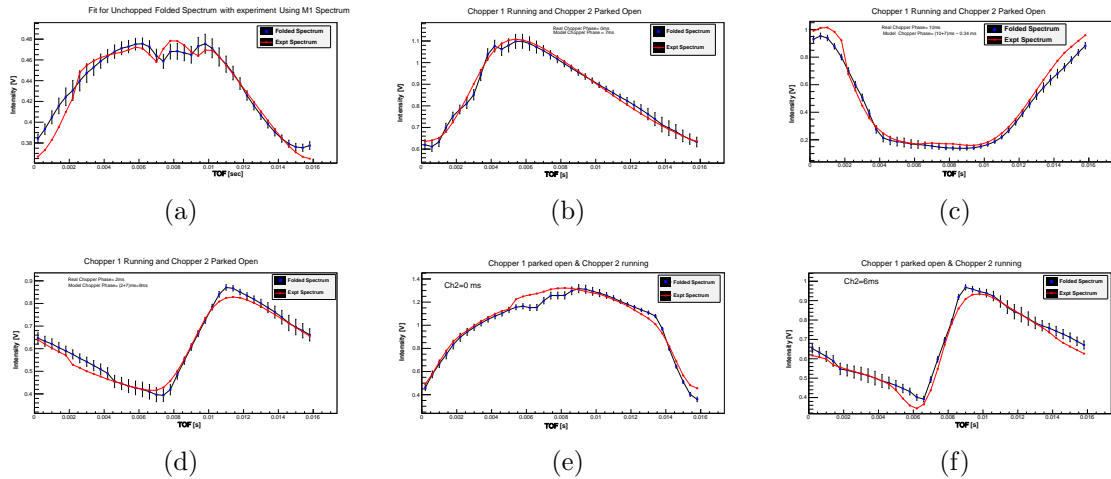


Figure 2.17: Fit for the folded 60 Hz model spectrum with the experimental spectrum.

At first we fit for chopper-1 running and chopper-2 parked open. Then we fit for chopper-2 running and chopper-1 parked open. This process gives us a constant off-set for our model choppers. In Fig. 2.17: (a) is a fit for unchopped folded model spectrum with unchopped experimental one. Fig. 2.17:(b)-(d) are the fitting of model spectrum with experiment for different phases of chopper-1 where chopper-2 is parked open. Fig. 2.17:(e)-(f) are the fitting of model spectrum with experimental for different phases of chopper-2 when chopper-1 is parked open. Next, we do fitting with both choppers running and check the consistency of the constant off-set for the phases.

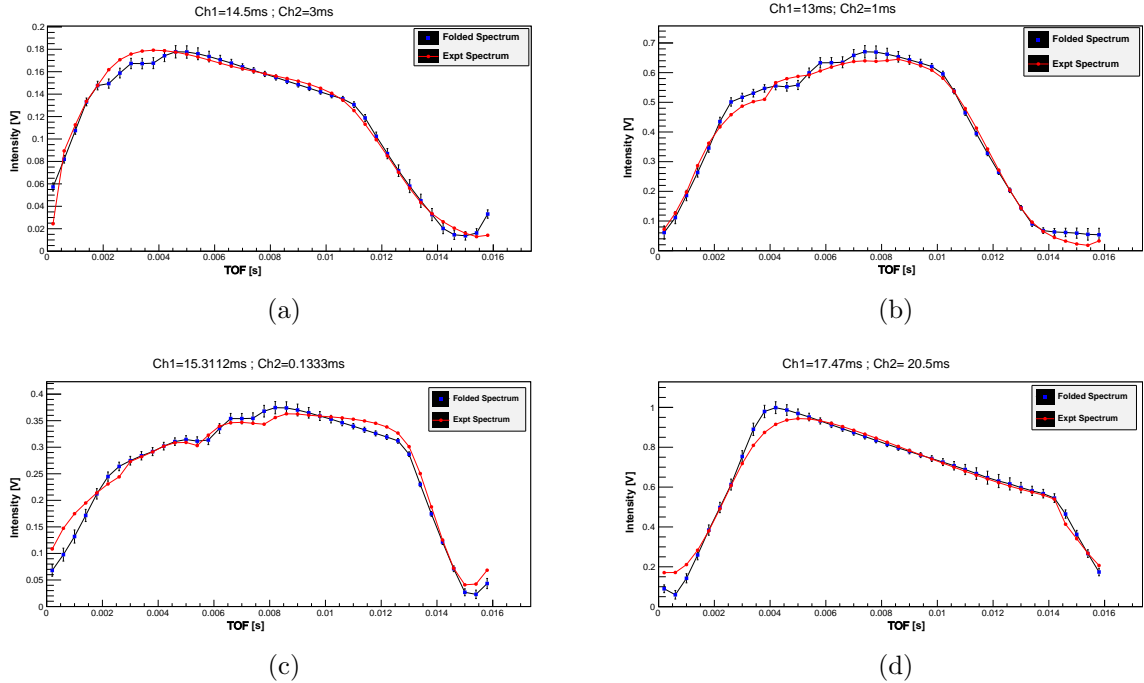


Figure 2.18: Fit for the folded 60 Hz model spectrum with the experimental spectrum.

In Fig. 2.18: (a)-(d) are the fitting of model spectrum with experimental when both of the two choppers are running. In (a) chopper-1 phase = 14.5 ms, chopper-2 phase = 3 ms; (b) chopper-1 phase = 13 ms, chopper-2 phase = 1 ms; (c) chopper-1 phase = 15.3112 ms, chopper-2 phase = 0.1333 ms; (d) chopper-1 phase = 17.47 ms  $\sim$  0.81 ms, chopper-2 phase = 20.5 ms  $\sim$  3.84 ms.

We see that, with the constant phase off-set between the model chopper and the real chopper, the model spectrum fairly agrees with the experimental spectrum.

### 2.3.4 Optimization outcome

The fitting process shows that-

the constant offset of model chopper-1 phase from real chopper-1 = 5.6 ms,

the constant offset of model chopper-2 phase from real chopper-2 =  $(4.2 \pm 0.5)$  ms.

Fig. 2.19 shows a 2-d contour plot with FOM as a function of chopper-1 phase and chopper-2 phase. Here the color represents FOM along third axis.

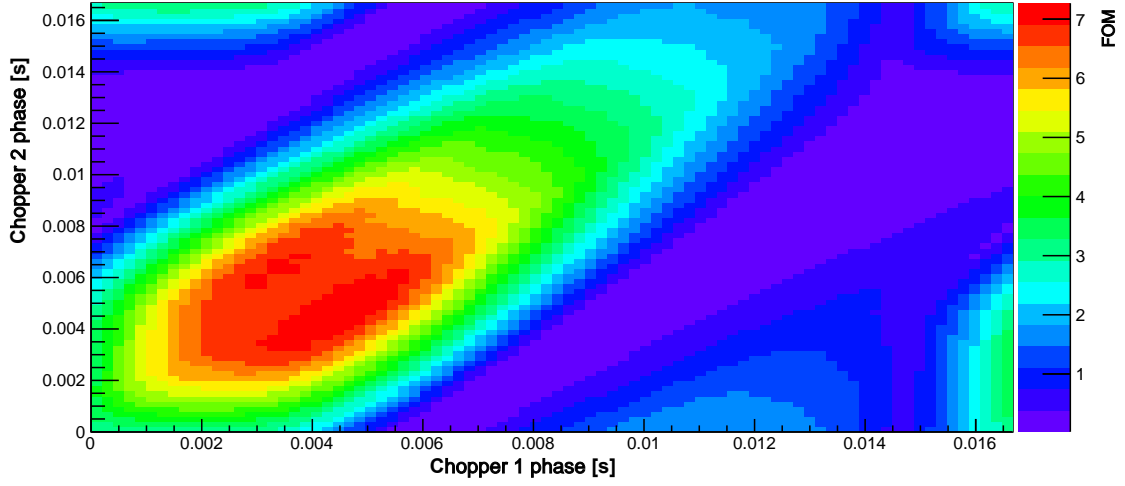


Figure 2.19: Three parameters contour plot with chopper-1 phase, chopper-2 phase and FOM. Here the color represents FOM along the third axis.

The maximum FOM is achieved around the region of model chopper-1 phase = 4 ms chopper-2 phase = 4.5 ms. Converting these setting to real chopper phases, we find that the following chopper phases (in terms of real chopper phases) are the most optimal solutions –

Chopper-1 phase:  $(4 - 5.6)$  ms  $\sim$  15.06 ms.

Chopper-2 phase:  $(4.5 - 4.2)$  ms = 0.3 ms.

Zooming the optimum FOM portion of Fig. 2.19, we find two distinct regions with maximum FOM as shown in Fig(2.20). The two distinct regions can be understood by the fact that the two choppers can be interchanged for ramping up and ramping down to give nearly two similar windows. To check this we go back to our chopper function and plot the transmission for two different points chosen from the two distinct regions. We chose one point from the lower region where chopper-1 phase = 4.1224 ms, chopper-2 phase = 4.31559 ms and another point from upper region where chopper-1 phase = 2.86128 ms, chopper-2 phase = 5.73136 ms. Fig. 2.21 shows the transmission for both of the choppers for these settings.

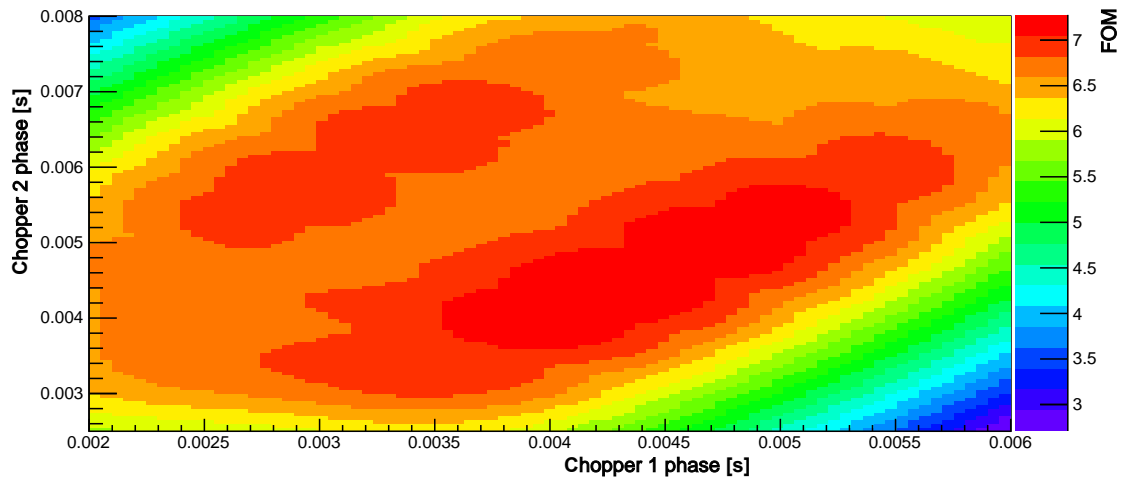


Figure 2.20: High resolution plot zooming the optimum FOM region.

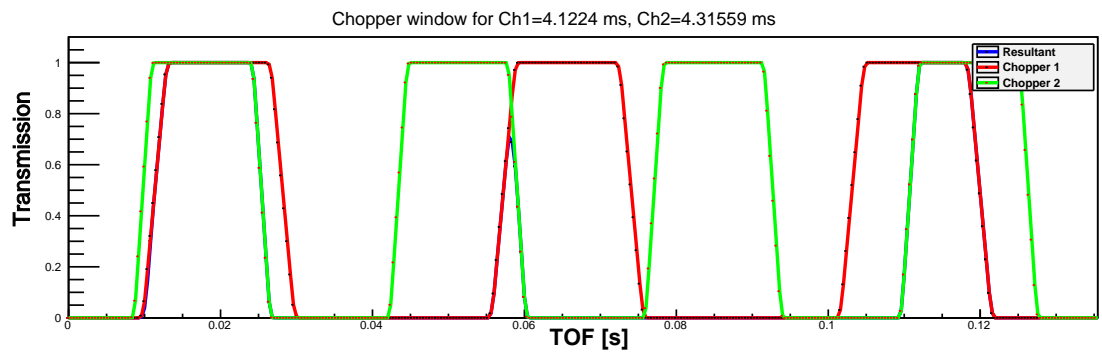


Figure 2.21: Chopper window for chopper-1 phase = 4.1224 ms, chopper-2 phase = 4.31559 ms. The values are in terms of model choppers phases.

Fig. 2.22 is the transmission plot with chopper-1 phase = 2.86128 ms, chopper-2 phase = 5.73136 ms. We see that the the ramping up and ramping down part of the two choppers are indeed interchanged giving nearly similar window.

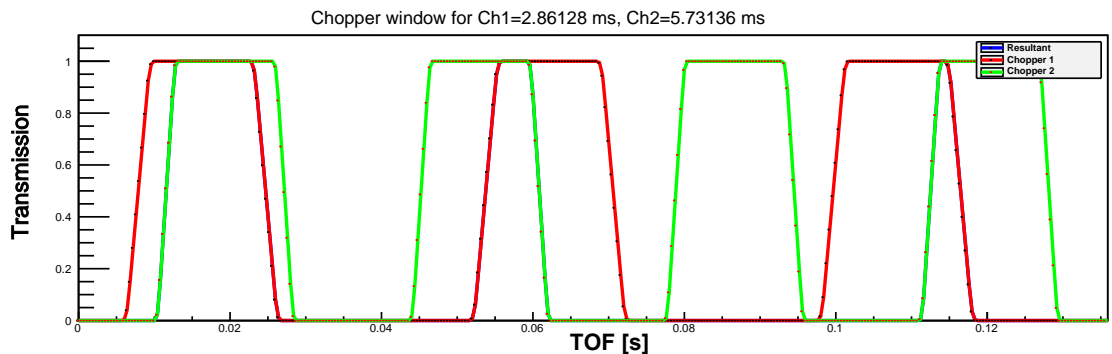


Figure 2.22: Chopper window for chopper-1 phase = 2.86128 ms, chopper-2 phase = 5.73136 ms. Values are in model chopper phases.



To identify the spin flipper window we show on a single plot the chopped spectrum and the spectrum with perfect polarization (NP spectrum). We do this for model chopper-1 = 4.1224 ms, chopper-2 = 4.31559 ms phases. This shows that the spin flipper start-up time is 12 ms.

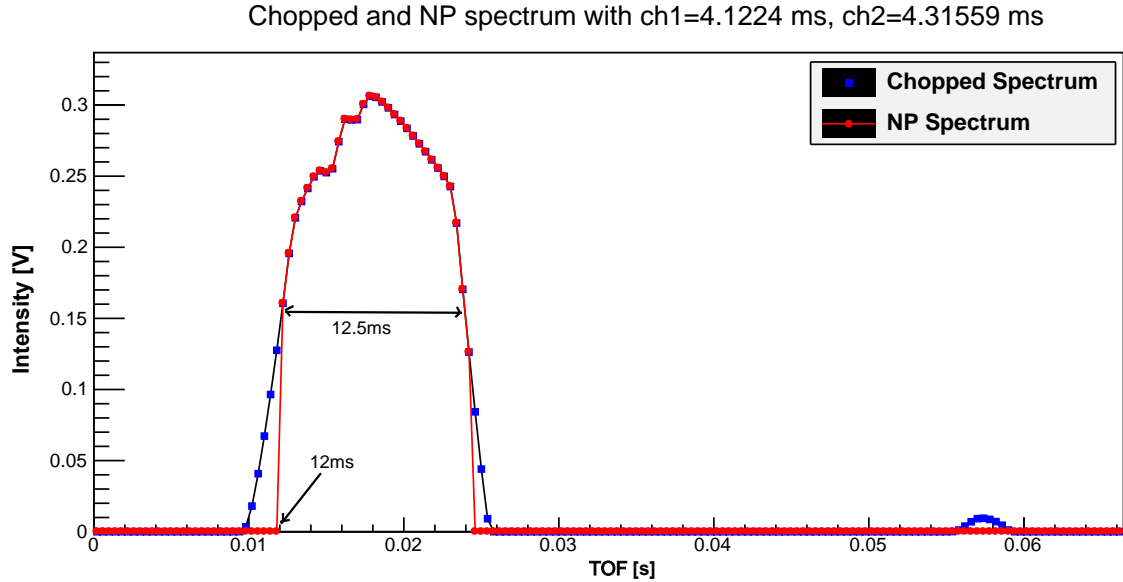


Figure 2.23: Chopped and NP spectrum for chopper-1 phase = 4.122 ms, chopper-2 phase = 4.31559 ms setting. NP indicates spectrum with perfect polarization. Optimal RFSF window is indicated.

In summarizing our analysis on the chopper optimization, we have a model with adjustable parameters – chopper location( $x$ ), opening angle( $\theta$ ) and opening phase( $f_0$ ). The model can successfully predict neutron spectrum and FOM. The model can be used for tuning the chopper phases of the experiment to get the most optimal TOF window.

## 2.4 Chopped beam profile

---

Fig. 2.24 shows the neutron beam TOF spectrum with the n-<sup>3</sup>He chopper setting. In this section we discuss the chopped beam characteristics.

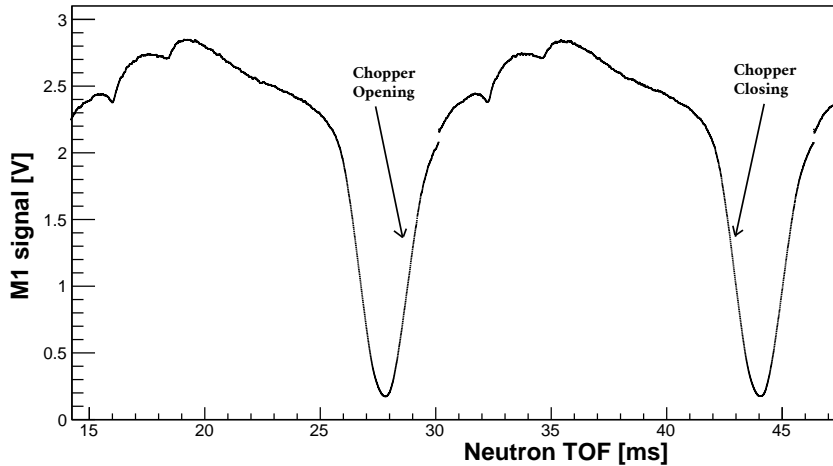


Figure 2.24: The M1 signal as a function of the TOF showing the chopped beam profile. Along  $x$ -axis is the TOF with the  $T_0$  delay included.

### 2.4.1 Dropped pulses

The accelerator intentionally drops one pulse in every 600 pulses for diagnostic purposes. In section 6.1.3 we show that these dropped pulses are advantageous to get the background. However from the analysis perspective this means that we need to understand all the consequences of the dropped pulses in our data.

The other uses of dropped pulse, we will encounter, are – construction of image pulse (explained in the next section), forming pulse sequence with 600 pulses per sequence and separating the dataset based on the RFSF state during the regularly dropped pulse (used in data analysis).

Fig. 2.25 shows the monitor-1 (M1) signal with the dropped pulse. In Fig. 2.25 on the dropped pulse we see the bump of wrap around neutrons from the earlier pulse. And the missing wrap around from the dropped pulse shows up in the 3rd pulse from dropped pulse. In addition to regularly dropped pulses we also have irregular dropped pulses in the data.

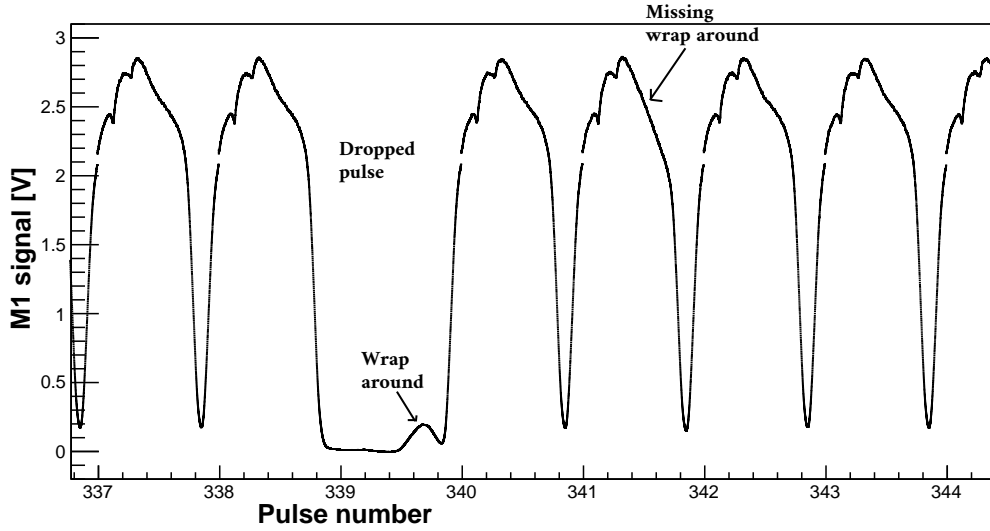


Figure 2.25: Dropped pulse in the pulse train

### 2.4.2 Construction of the image pulse

The signal that we get from M1 (for example in Fig. 2.24 or 2.25) or the detector, represents the convoluted signal, i.e. the resultant of neutrons from main pulse and wraparound neutrons. But the detector interacts with the neutrons individually. To fully understand the constituents of the convoluted signal, we use dropped pulse to get unconvoluted signals. We call this unconvoluted signals the image pulse or surrogate pulse.

To construct the image pulse, we consider a sequence of 600 pulses with the first pulse being the regular dropped pulse which is the only dropped pulse in that sequence. Now at first we construct average pulse signal out of those 600 pulses. We take sum over all the 600 pulses in the sequence and we divide by 599 to get the average pulse signal  $I_{ave}$ . Next we subtract this average pulse from each of the pulses of the 600 sequence. To get a positive value, we can also subtract the other way i.e.  $I_{ave} - I_i$ . After subtracting, we are left with the image pulse. For this analysis we used the processed data file (DST) explained in section 4.4. Fig. 2.26 shows the image pulse. We see the first wrap around shows up in the third window.

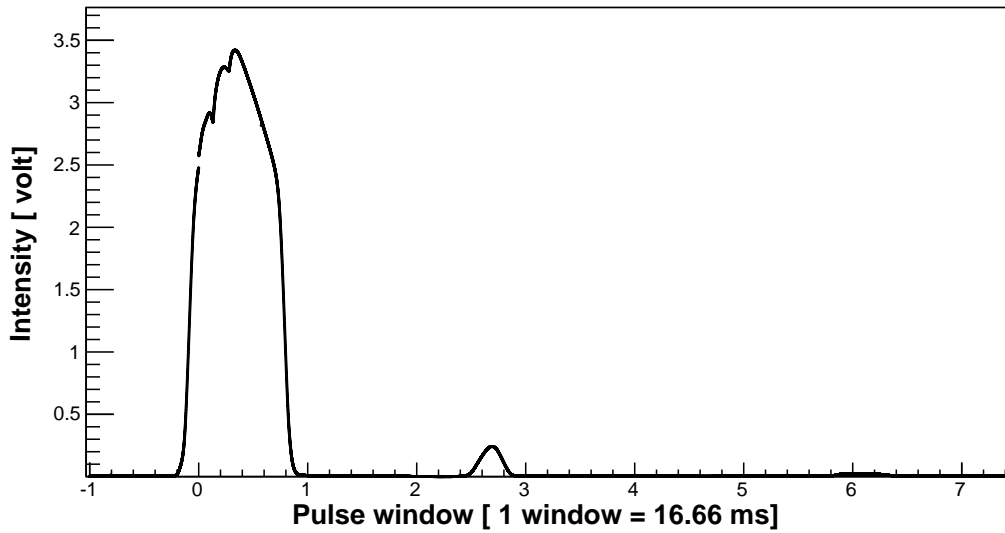


Figure 2.26: The image (surrogate/unconvoluted) pulse generated using the dropped pulse

In Fig. 2.27, we show the image pulse with  $y$ -axis set to log scale. Here we find every detail of the image pulse. To show the injection flash we start from window number -1, which is basically the pulse before the dropped pulse. The injection flash, main pulse and up to three wrap around signals are shown in the plot.

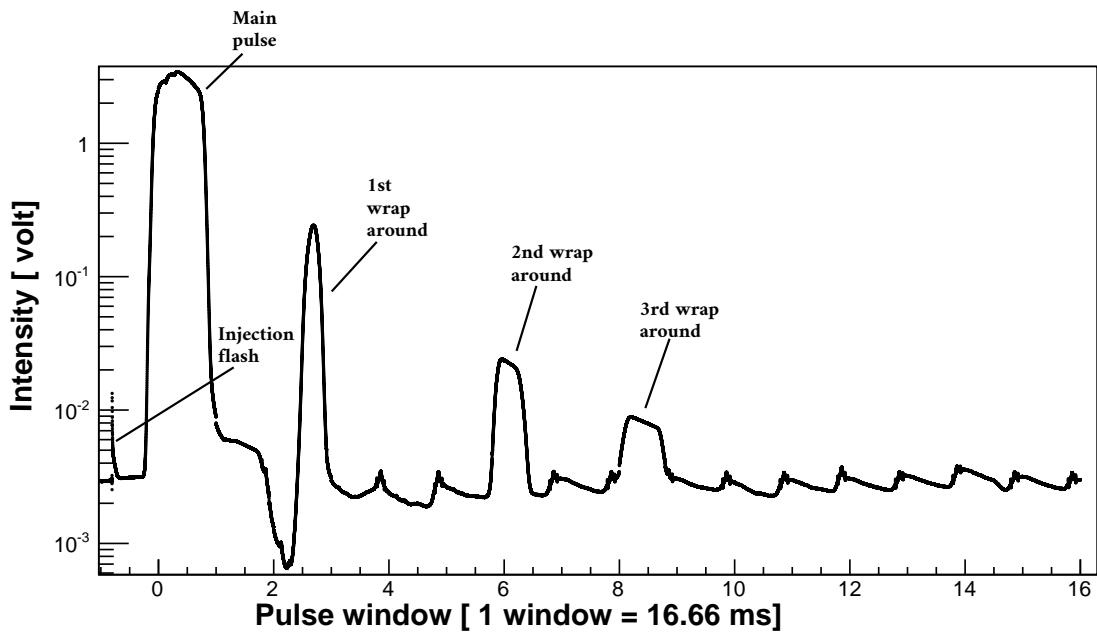


Figure 2.27: The wrap around in the image pulse

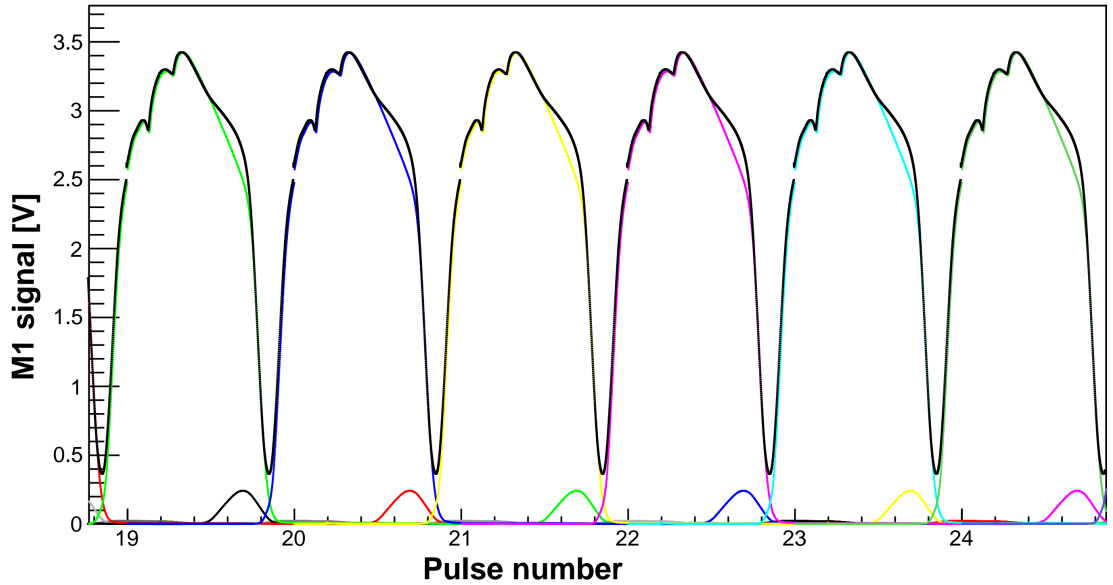


Figure 2.28: In various colors (other than black) are the image (surrogate) pulses. The black one is the resultant pulse.

The convoluted neutron spectrum consists of these image pulses. Fig. 2.28 and Fig. 2.29 shows the convoluted signals made out of the image pulses. The situation is better illustrated with  $y$ -axis on log scale as shown in Fig. 2.29. Here looking at any particular pulse, we can identify each component in the convolution. Any pulse has non-trivial contributions from — i) the main pulse ii) chopper closing leakage (overlap) from previous pulse iii) chopper opening leakage from next pulse iv) the injection flash from next pulse, very fast unmoderated neutrons and gammas immediately after the proton pulse hits the Hg target v) three wrap around bumps from earlier pulses. What we see from any ordinary M1 signal is the result of all of these components as shown in black in Fig. 2.29.

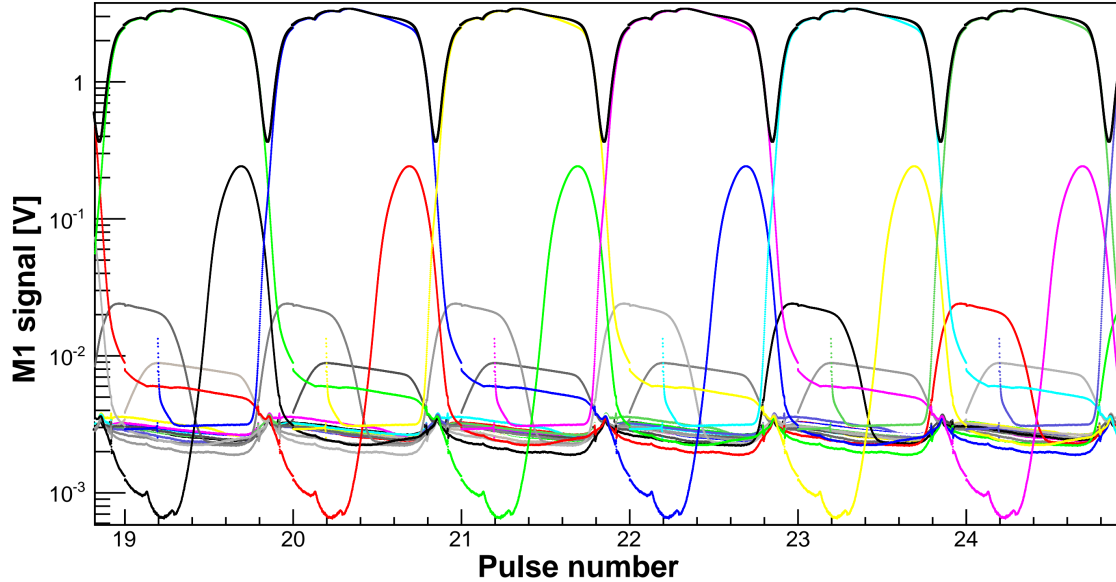


Figure 2.29: (In various colors other than black) The image (surrogate) pulses with contribution from wrap around and injection flash. (In black) The pulses when all the contributions are integrated.

### 2.4.3 Neutron beam spatial profile

We investigated the spacial distribution of the beam before entering the target and also far back from the target. We wanted to know how it would change from the upstream to the downstream position because of the small beam divergence. We did a spatial beam scan to know that. This beam scan was also necessary to know the beam centroid in order to align the collimator and the target precisely.

We used an  $xy$  robot (stepper motor driven Velmex linear stages) that held the beam monitor behind a 1 cm aperture, then moved it along the  $xy$  plane with small increments. For upstream we did a  $17 \times 19$  scan and for downstream we did a  $17 \times 22$  scan with varying step size. The  $xy$  robot was programmed to automate the scan and to give the user the ability to control it remotely.

Fig. 2.30 shows the spatial beam profile in the upstream position (i.e. before the beam enters the target). Fig. 2.31 shows the same thing but for the downstream position (i.e. far back from the target). We note that going from the upstream to downstream the beam spreads out. This is expected because of the small beam divergence once the beam comes out of the guide. The divergence is defined by the guide reflectivity parameter, in our case guide has  $m = 3$ , this defines the glancing angle of the neutron on guide surface. This means low energy neutrons have larger divergence.

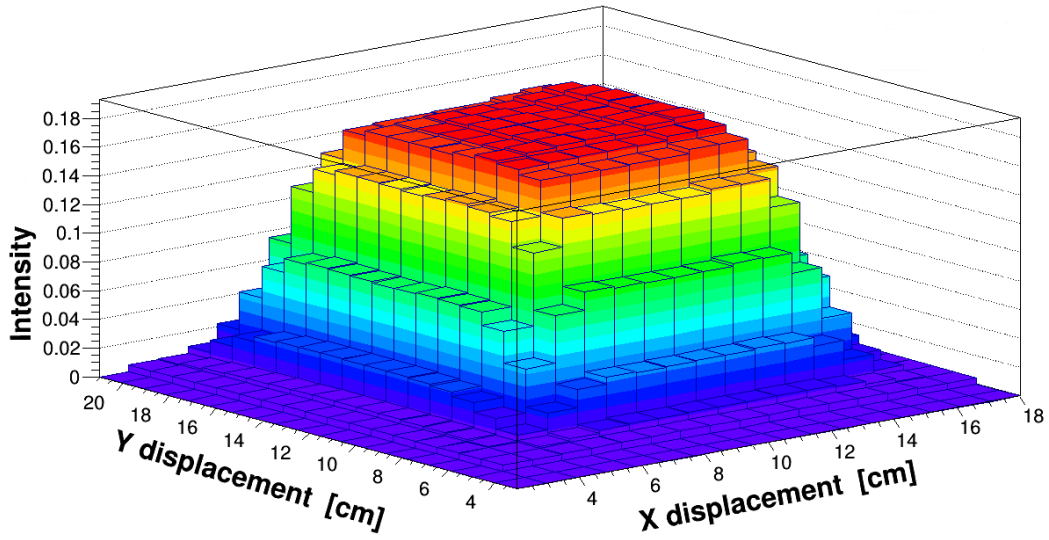


Figure 2.30: Upstream beam profile from the scan. The measured intensity is normalized by the M1 signal.

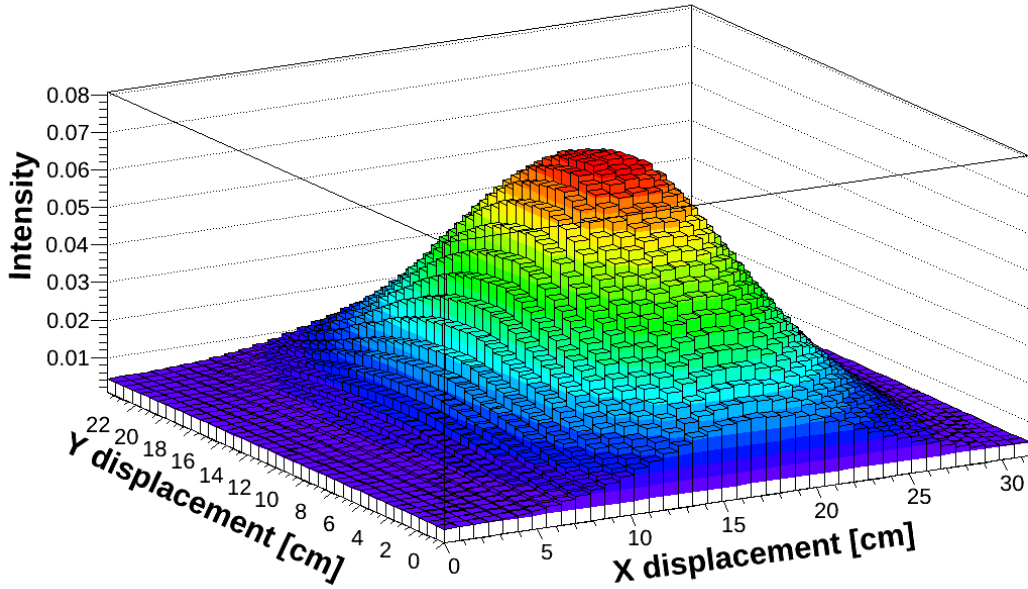


Figure 2.31: Downstream beam profile from the scan. The intensity is normalized by the integrated M1 signal.

From the data of these plots, we calculated the beam centroid both for the upstream

and downstream position using

$$\bar{x} = \frac{\sum_i x_i I_i}{\sum_i I_i}, \quad (2.7)$$

$$\bar{y} = \frac{\sum_i y_i I_i}{\sum_i I_i}, \quad (2.8)$$

where  $I_i$  is the average normalized beam intensity at position  $(x_i, y_i)$  on the  $xy$  plane. The calculated beam centroid is shown in Fig. 2.32. Then we used a laser beam to pass through both of these centroids and used the connecting straight line as a reference to align the target and collimator to the beam center.

#### 2.4.4 Beam collimation

The beam is collimated in the experiment to fit it to the full width of the chamber in a way to let the daughter products of the reaction range out inside the chamber. A collimator made with Cd and Li-6 is used in the experiment. Fig. 2.32 shows a CAD model of the collimator with all the dimensions and labels. In normal operating condition, we used a collimating opening of horizontal  $\times$  vertical = 10 cm  $\times$  8.2 cm in the UD mode and 8.2 cm  $\times$  10 cm for the LR mode.

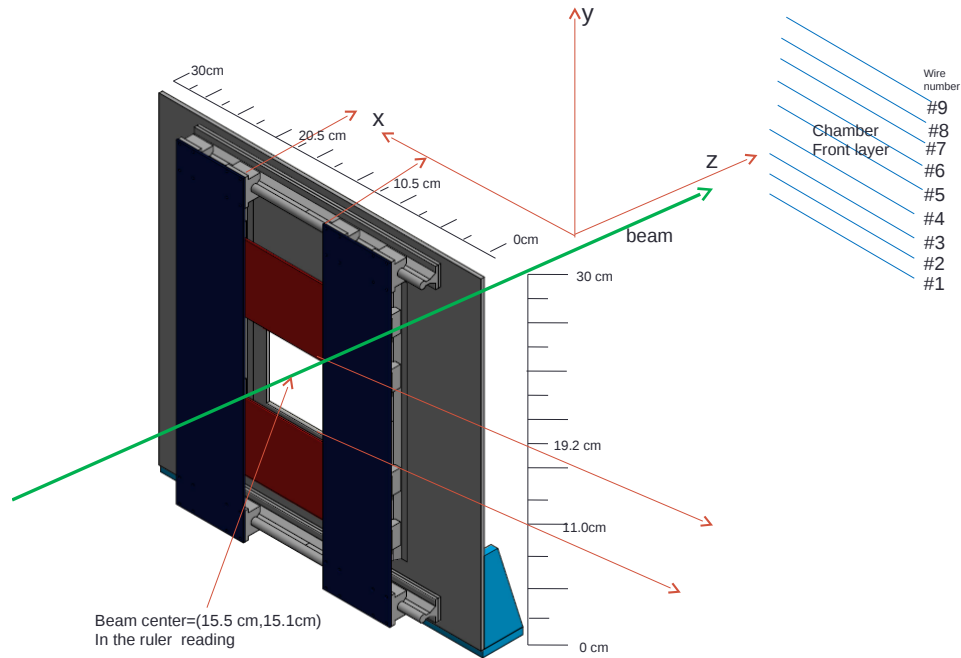


Figure 2.32: Beam collimator located in the front of the target chamber. The beam centroid shown was calculated using the two beam scan measurements and relative to the ruler attached to the collimator. The signal wire alignment shown is for the UD mode. The CAD model part of the diagram is courtesy of Chris Hayes [59].



The beam centroid label on the figure was calculated using the beam scan explained in the previous section. The coordinate system shown in the figure represents the conventions used in the experiment for the directions. The signal wire alignment shown here is for the UD mode. The wire labeling was established using the collimation scan and same labeling convention is used everywhere including for the data analysis. For the LR mode, the chamber is rotated beam left  $90^0$  counter clockwise looking downstream. In the LR mode, signal wire #9 is in the beam left side (towards the  $+x$  axis in this diagram). In UD mode #9 is on the top.

# Chapter 3

## Spin flipper & Detector

---

In this chapter we briefly discuss about the principles, functionalities and the roles of two of the most important components of the experiment – radio frequency spin flipper (RFSF) and the ion chamber. The ion chamber acts both as target and detector. The RFSF is the subject of the Ph.D. thesis of Chris Hayes [59] and the  $n\text{-}^3\text{He}$  ion chamber is the subject of the Ph.D. thesis of Mark McCrea [56]. The details outside this chapter can be found in their theses.

### 3.1 Radio frequency spin flipper (RFSF)

---



(a) Wire windings on the inner and outer shell.



(b) The spin flipper inside the aluminum housing

Figure 3.1: The spin flipper interior and housing [59]

The experiment uses a radio frequency spin flipper (RFSF) to flip the neutron spin. The spin flipper is a double cosine theta coil and has the working principle analogous

to that of NMR (explained in the next section). It allows for both longitudinal and transverse spin rotation. The spin flipper is composed of wire windings over two semi-circular outer shells and one cylindrical inner shell as shown in Fig. 3.1. These shells were 3D printed. The design of the spin flipper was aimed to minimize the interference of the RFSF field with the ion chamber or readout electronics. The double cosine theta coil was chosen over a cosine theta coil to achieve uniform magnetic field in the interior region but no magnetic field in the outside as shown in Fig. 3.2. An additional layer of shielding is imposed by placing the spin flipper inside a thick aluminum shell (as shown in Fig. 3.1 b) to ensure that the RF field does not leak outside.

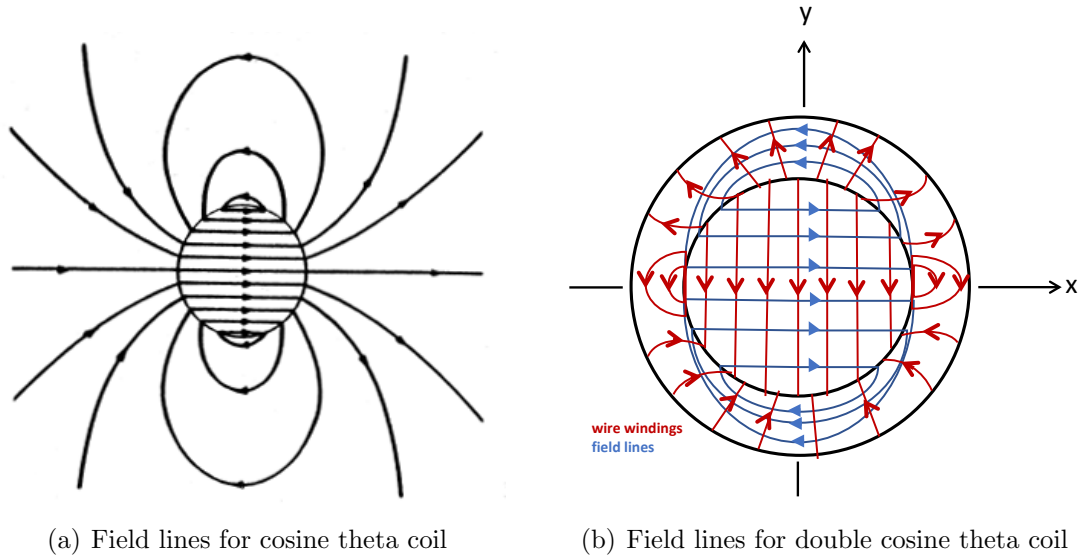


Figure 3.2: Field lines for cosine theta coil and double cosine theta coil. In the case of double cosine theta coil, the inner and outer shell and the associated windings are used to cancel out any residual field and finally giving uniform magnetic field inside the spin flipper but zero field outside.

### 3.1.1 RFSF working principle

Two standard techniques for rapid reversal of the neutron polarization are a) “adiabatic fast passage” (AFP) and b) resonant spin flipper (RSF). Both of them use radio-frequency field. But AFP requires a substantial magnetic field gradient which, upon spin reversal in the geometry of the experiment, will create a substantial change in the neutron beam transverse momentum; the resulting change in the incident neutron spatial distribution at the target can easily give a systematic effect at the sought level of experimental sensitivity [63], [64]. So in order to eliminate the magnetic field gradient deflection the experiment uses a resonant spin flipper, which is also based on the application of a RF field, in this case, in the presence of a homogeneous static magnetic field.

Now the spin flip principle can be discussed either using a semi-classical formulation (using rotating frame) or using a quantum mechanical formulation (Rabi formula) as presented in the original Rabi, Ramsey and Schwinger paper[65]. Here we consider the first formulation.

Consider a classical magnetic moment  $\vec{\mu}$  in a field  $\vec{B}_0 = B_0 \hat{k}$ . It will precess around  $\vec{B}_0$  at a frequency

$$\vec{\omega}_0 = -\gamma \vec{B}_0, \quad (3.1)$$

where  $\gamma$  is called gyromagnetic ratio. Now suppose we view this process in a frame that is rotating at a frequency  $\vec{\omega}$  parallel to  $\vec{B}_0$ . In this rotating frame, the precession frequency will be

$$\vec{\omega}_r = \vec{\omega}_0 - \vec{\omega} = -\gamma \vec{B}_0 - \vec{\omega} = -\gamma \left( \vec{B}_0 + \frac{\vec{\omega}}{\gamma} \right). \quad (3.2)$$

Thus the effective field in this rotating frame will be

$$\vec{B}_r = \vec{B}_0 + \frac{\vec{\omega}}{\gamma}. \quad (3.3)$$

This result is valid even if  $\vec{\omega}$  and  $\vec{B}_0$  are not parallel. We now consider the problem of our interest, where in a non-rotating frame the B-field is

$$\vec{B} = B \cos(\omega t) \hat{i} - B \sin(\omega t) \hat{j} + B_0 \hat{k}, \quad (3.4)$$

where  $B \ll B_0$

At  $t = 0$

$$\vec{\mu}(0) = \mu \hat{k}. \quad (3.5)$$

Now we would like to find out the evolution of  $\vec{\mu}(t)$ . Since  $\vec{B}$  depends on time, it proves advantageous to first consider the problem in a frame that rotates at the same frequency  $\vec{\omega} = -\omega \hat{k}$  as the small clockwise rotating field B. In this frame, the rotating component of  $\vec{B}$  gets frozen (say along the  $x$ -axis) and the constant component  $B_0 \hat{k}$  gets reduced according to Eq. 3.3 so that the effective time independent field is

$$\vec{B}_r = B \hat{i}_r + \left( B_0 - \frac{\omega}{\gamma} \right) \hat{k}, \quad (3.6)$$

where  $\hat{i}_r$  is the unit vector in the  $x$ -direction in the rotating frame and  $\hat{k} = \hat{k}_r$ . In this frame  $\vec{\mu}$  will precess around  $\vec{B}_r$  at a frequency

$$\vec{\omega}_r = -\gamma \vec{B}_r, \quad (3.7)$$

where

$$|\vec{\omega}_r| = \omega_r = \gamma \left[ B^2 + \left( B_0 - \frac{\omega}{\gamma} \right)^2 \right]^{\frac{1}{2}}. \quad (3.8)$$

To get the time evolution of  $\mu_z(t)$ , we consider the situation in the rotating frame illustrated in Fig. 3.3. In this case, the effective magnetic field is  $\vec{B}_r$ . The magnetic moment starts out along the  $z$  axis and precesses around  $\vec{B}_r$ . The  $z$ -component of the moment oscillates with amplitude  $\mu \sin^2 \alpha$ , where  $\alpha$  is the opening angle of the cone. At resonance,  $\vec{B}_r$  lies along the  $x$  axis and  $\vec{\mu}$  precesses in the plane normal to it. The amplitude of the  $\mu_z$  oscillation is then at its maximum value of  $\mu$ .

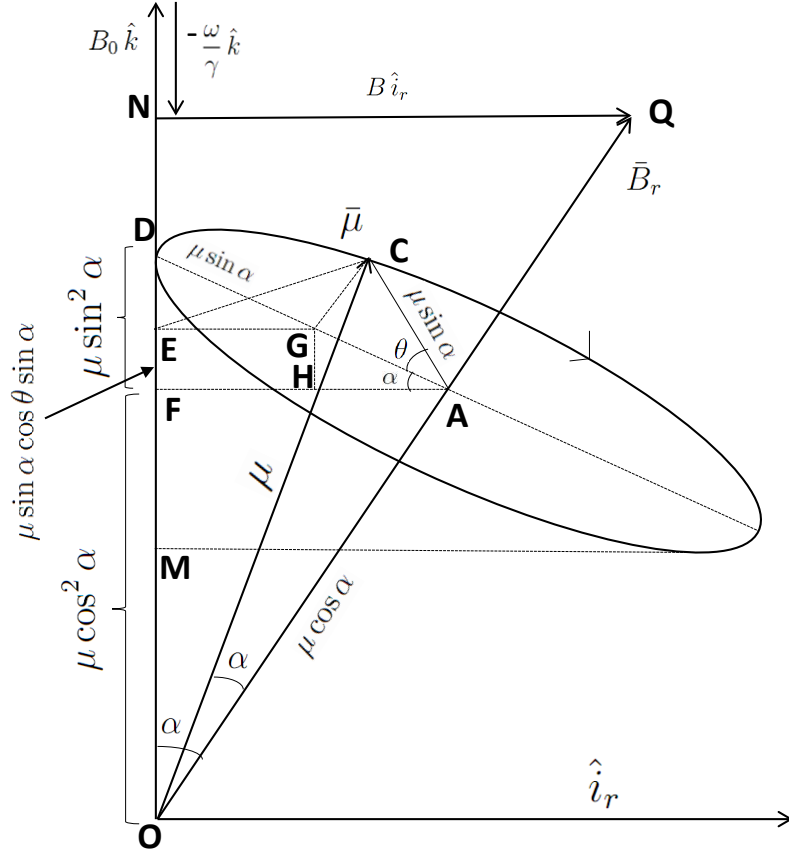


Figure 3.3: The situation in the rotating frame

From Fig. 3.3, we can write the time evolution for  $\mu_z$  as

$$\mu_z(t) = \mu \cos^2 \alpha + \mu \sin^2 \alpha \cos \omega_r t. \quad (3.9)$$

It is easy to show (see appendix B.1) from the Fig. 3.3 that, by expressing  $\cos^2 \alpha$  and  $\sin^2 \alpha$  in terms of  $\omega$ ,  $\omega_0$ ,  $\gamma$  and  $B$ , the time evolution can be written as,

$$\mu_z(t) = \mu_z(0) \left[ \frac{(\omega_0 - \omega)^2}{(\omega_0 - \omega)^2 + \gamma^2 B^2} + \frac{\gamma^2 B^2 \cos \omega_r t}{(\omega_0 - \omega)^2 + \gamma^2 B^2} \right]. \quad (3.10)$$

This formula for  $\mu_z(t)$  applies in the lab frame as well, since  $\mu_z$  is invariant under  $z$ -rotations. As  $\omega$  increases from 0, the  $z$ -component of  $\vec{B}_r$  steadily decreases;  $\alpha$ , the

opening angle of the cone, increases and the amplitude of oscillation,  $\mu \sin^2 \alpha$ , grows. At magnetic resonance,  $\omega = \omega_0$ ,  $\vec{B}_r = B \hat{i}_r$ ,  $\alpha = \pi/2$  and the cone becomes a circle in the  $y$ - $z$  plane, and  $\mu_z$  oscillates with the largest amplitude  $\mu$  at a frequency  $\gamma B$ . The behavior for  $\omega > \omega_0$  is obvious. Now if we apply the rotating field at resonance frequency, but for a time  $t = \tau$  such that

$$\omega t = \gamma B \tau = \frac{\pi}{2}. \quad (3.11)$$

then Eq. 3.10 gives  $\mu_z = 0$ . Such a pulse called  $90^\circ$  pulse, will swing the magnetic moment into the  $x - y$  plane (in either frame). There after  $\vec{\mu}$  will precess around  $B_0 \vec{k}$  at the frequency  $\omega_0$  in the lab frame.

Now, if we apply a  $180^\circ$  pulse, i.e. choose  $t = \tau$  such that

$$\omega t = \gamma B \tau = \pi, \quad (3.12)$$

$$\tau = \frac{\pi}{\gamma B}. \quad (3.13)$$

Then, from Eq. 3.10

$$\mu_z(t) = -\mu_z(0), \quad (3.14)$$

i.e. the pulse will reverse the sign of  $\vec{\mu}$  and leave it pointing down the  $z$ -axis where it will stay (in either frame).

### 3.1.2 $1/t$ ramp for the RF field amplitude

In the experimental set-up a RF field is confined to a limited space along the neutron beam, in the presence of a homogeneous guide field, with the neutron momentum direction along  $\hat{z}$ , the direction of the RF field. For fixed RF and guide field values the time/amplitude relation for the spin reversal can be satisfied for only a single velocity component of a continuous beam. However, for a spallation source,  $B$  can be varied as a function of time of flight, satisfying the spin reversal condition for all the neutrons in a pulse. If we assume an RF field confined to a length  $L_c$  along the beam and the spin flip coil located at  $L_0$  from the spallation source, the RF amplitude have to be varied with the time as

$$\tau = \frac{L_c}{v(t)}. \quad (3.15)$$

Invoking Eq. 3.13 we can write

$$\frac{\pi}{\gamma B} = \frac{L_c}{L_0/t}, \quad (3.16)$$

$$B(t) = \frac{\pi L_0}{\gamma L_c t}, \quad (3.17)$$

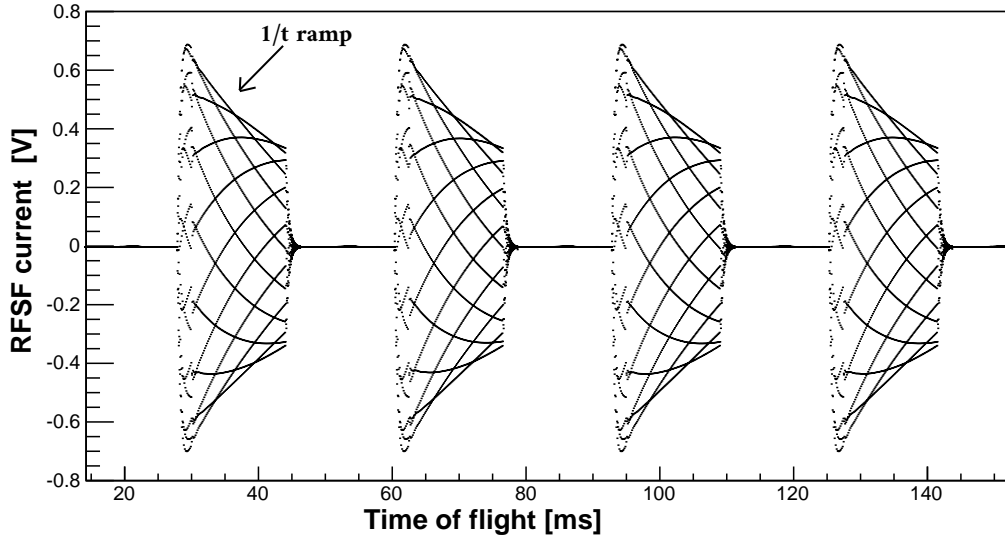


Figure 3.4: The RFSF current vs neutron time of flight

which shows that the RF amplitude needs to be tuned as  $1/t$ . Here,  $t$  is the neutron time of flight. Fig. 3.4 shows the RFSF current vs neutron time of flight plot, in this plot we see the  $1/t$  envelop used for the magnitude of the RF field.

Fig. 3.5 shows the spin flip ratio for different guide field values from a measurement to tune the vertical guide field at fixed  $\omega_0$ .

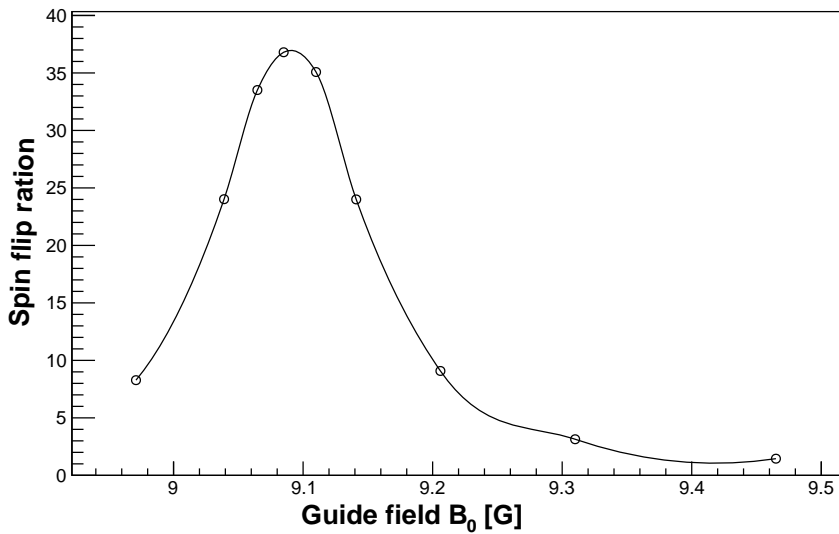


Figure 3.5: Spin flip ratio for different guide field values at fixed  $\omega_0$ .

### 3.1.3 $^3\text{He}$ transmission polarimetry

During the n- $^3\text{He}$  data taking process polarimetry was performed on a monthly basis to measure the consistency of the RFSF performance and keep a history of neutron polarization. The n- $^3\text{He}$  polarimetry utilized  $^3\text{He}$  cell as analyzer and filter to measure the beam polarization and the RFSF efficiency. The method relies on the fact that, the neutron absorption in  $^3\text{He}$  is strongly spin-dependent, i.e. spin-polarized  $^3\text{He}$  volume transmits neutrons with one spin component while absorbing the other. Unpolarized  $^3\text{He}$  volume shows no neutron spin dependence preference. The  $^3\text{He}$  cell used for the polarimetry is initially polarized using the technique of Spin Exchange Optical Pumping (SEOP), and the polarization of the cell is reversed using Adiabatic Fast Passage (AFP) [59]. Fig. 3.6 shows average neutron beam polarization from 8 polarimetry measurements. Fig. 3.7 shows average spin flipper efficiency from the polarimetry measurements.

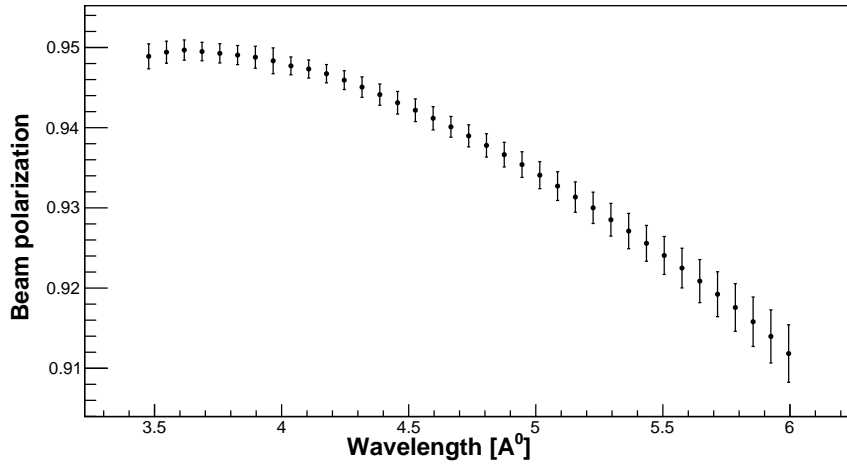


Figure 3.6: Average neutron beam polarization. The small slope is attributed to the super mirror polarizer. Note, the plot is zero suppressed. The data is taken from the appendix of Ref. [59].

Averaging over all wavelengths the average values for beam polarization and spin flipper efficiency were reported [59] to be

$$\langle P_n \rangle = 0.936 \pm 0.002 \quad \text{and} \quad \langle \epsilon_{sf} \rangle = 0.998 \pm 0.001. \quad (3.18)$$

These values in Eq. 3.18 are used to correct the polarization in the extracted physics asymmetry according to the relation[59]

$$A_p = \frac{A'_p}{\langle P_n \rangle \langle \epsilon_{sf} \rangle}, \quad (3.19)$$

where  $A'_p$  is the physics asymmetry without correction for effective polarization. It was found that the small dependence of beam polarization and spin flipper efficiency on neutron time of flight (or wavelength) do not affect our physics asymmetry significantly. So, only their average values are used in Eq. 3.19.



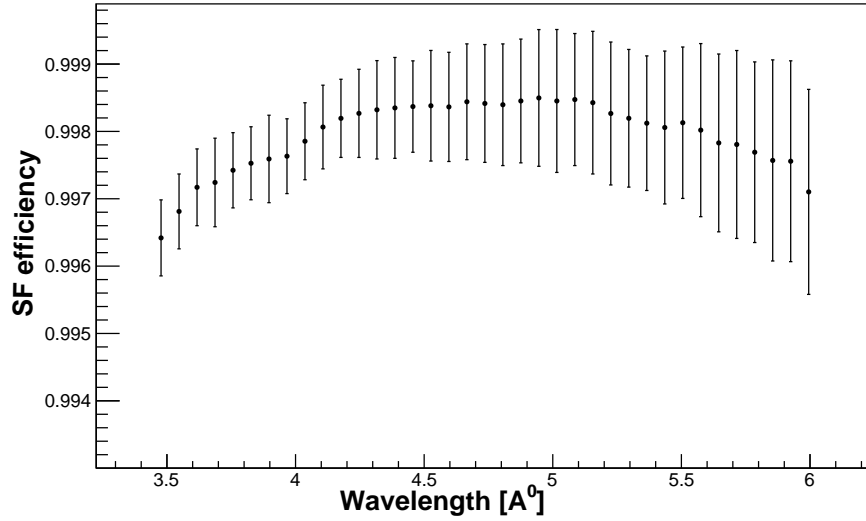


Figure 3.7: Average spin flipper efficiency from the polarimetry measurements. Data from table A.3 of Ref. [59]

## 3.2 Ion Chamber / Detector

---

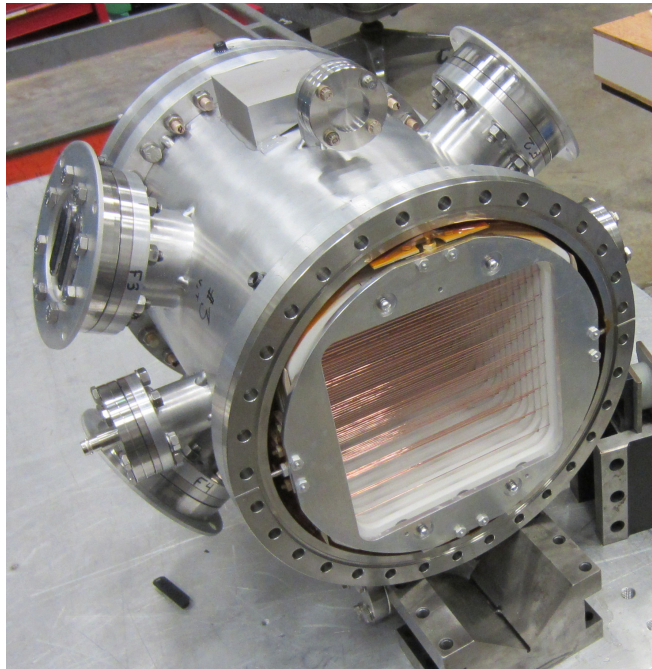


Figure 3.8: The  $n$ - $^3\text{He}$  ion chamber [56]. The ion chamber acts both as target and detector.

The detector for the  $n$ - $^3\text{He}$  experiment is a multi-wire proportional chamber [62],[56] filled with pure  $^3\text{He}$  gas at 0.47 atmosphere. As a multi-wire ionization chamber, it

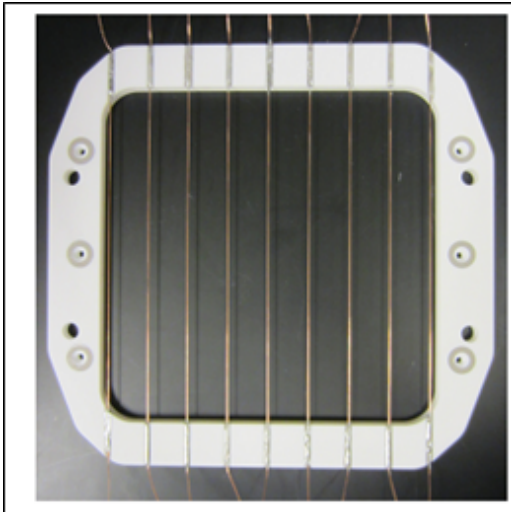
has multiple wires as the electrodes — high voltage (HV) wires to provide bias for the charges and signal wires for charge collection.

The use of pure fill  $^3\text{He}$  gas enables us to use the ion chamber as  $^3\text{He}$  target for the experiment and also ionization detector for measuring the ionization distribution.

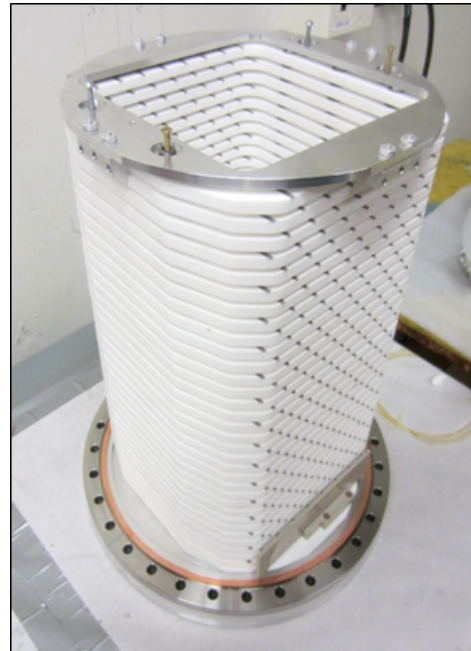
The use of gas mixture could improve the HV characteristics, but that would complicate extraction of neutron capture signals due to  $^3\text{He}$  from others. To minimize the signal variation from individual capture, we use wires as the electrodes instead of plates inside the chamber, so that most of the protons and tritons can range out inside the chamber. Also, the length of the chamber and pressure are determined in a way that the full neutron beam is absorbed within the chamber to maximize the statistics.

### 3.2.1 Target chamber interior structure

The ion chamber has 17 high voltage frames with 8 wires each and 16 signal frames with 9 wires each. So, in total we have 144 signal wires and each of the signal wires is used to extract the asymmetry. Fig. 3.9 (a) shows an isolated signal wire plane and Fig. 3.9 (b) shows all the high voltage and signal planes stacked on top of each other.



(a) One signal wire plane



(b) Planes stacked on top of each other

Figure 3.9: The signal and high voltage planes (layers) used inside the ion chamber

Fig. 3.10 shows a 2D side view for the orientation of high voltage wires and signal wires in the chamber. In red are 17 high voltage (HV) planes with 8 wires each

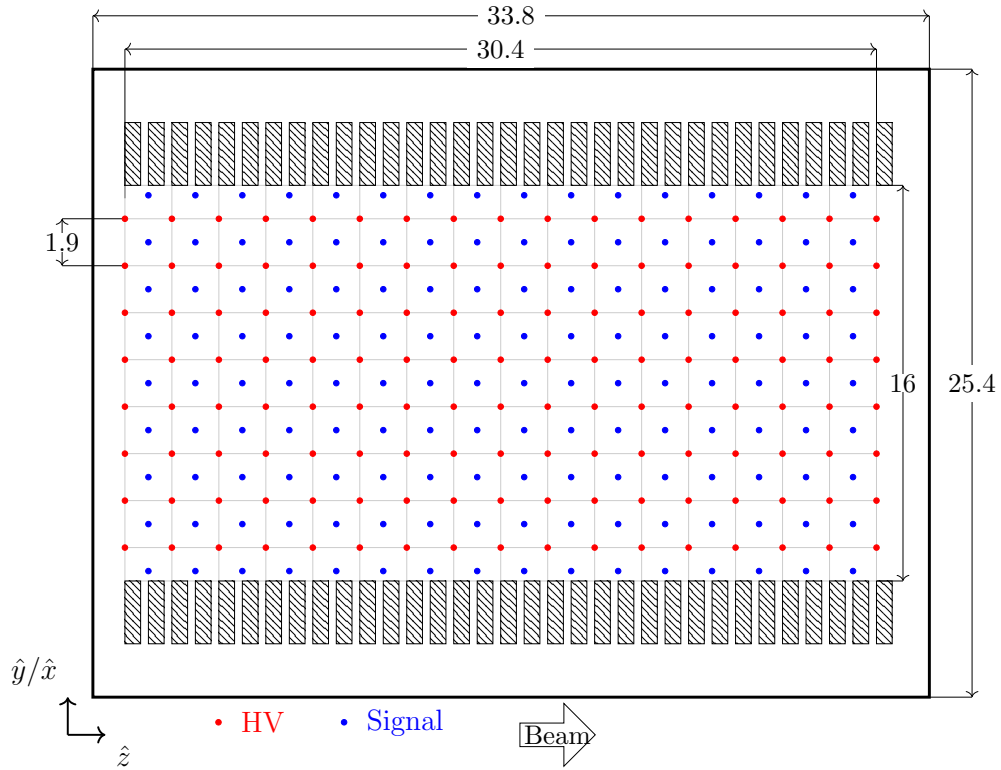


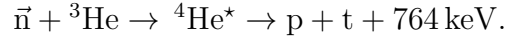
Figure 3.10: Signal and high voltage wires inside the ion chamber (2D side view). During the operation the wires were aligned parallel to either  $\hat{x}$  (horizontal) or  $\hat{y}$  (vertical) beam-line axis for PV and PC asymmetry measurements respectively. Dimensions are mentioned in cm. Diagram courtesy of M. McCrea [56].

and in blue are 16 signal wire planes with 9 wires each. The applied high voltage was chosen to be -353 V for normal data taking operation. Two adjacent wires are separated by 1.9 cm and the length of the chamber is 33.8 cm. As a result each signal wire is surrounded captured ions in an equipotential volume of dimension 16 cm  $\times$  1.9 cm  $\times$  1.9 cm. This volume is less for the top and bottom wires. Moreover, there is a 1.29 cm separation between first HV plane and the first window of the ion chamber. As mentioned in the experimental setup, the wires are horizontally aligned with respect to the beam axis for the parity violating asymmetry measurement. For the parity conserving asymmetry measurement, the ion chamber is rotated 90<sup>0</sup> counter clockwise (with respect to the beam axis), so that in this case the wires inside the chamber are vertical.

### 3.2.2 Signal from the ion chamber

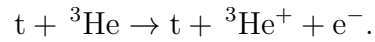
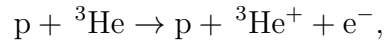
Once a thermal neutron reaches  ${}^3\text{He}$  inside the ion chamber, two interactions take place – i) Interaction of the neutron with nuclei ii) Interaction of charged reaction products with atomic electrons.

In the first case, the neutron is absorbed according to the reaction:



The energy is carried away as the kinetic energy of the daughter products and they move in the opposite directions to conserve momentum. Since triton is three times more massive than proton, an outgoing proton carries 573 keV and triton carries 191 keV of the total kinetic energy.

Next follows the electromagnetic interaction with atomic electrons when proton and triton travel through the  ${}^3\text{He}$  gas:



Here proton and triton lose energy due to this ionization process. As a result ion pairs are created. These charge pairs are then collected by the nearest electrodes as shown in Fig. 3.11 because of the equipotential wall created around the wire.

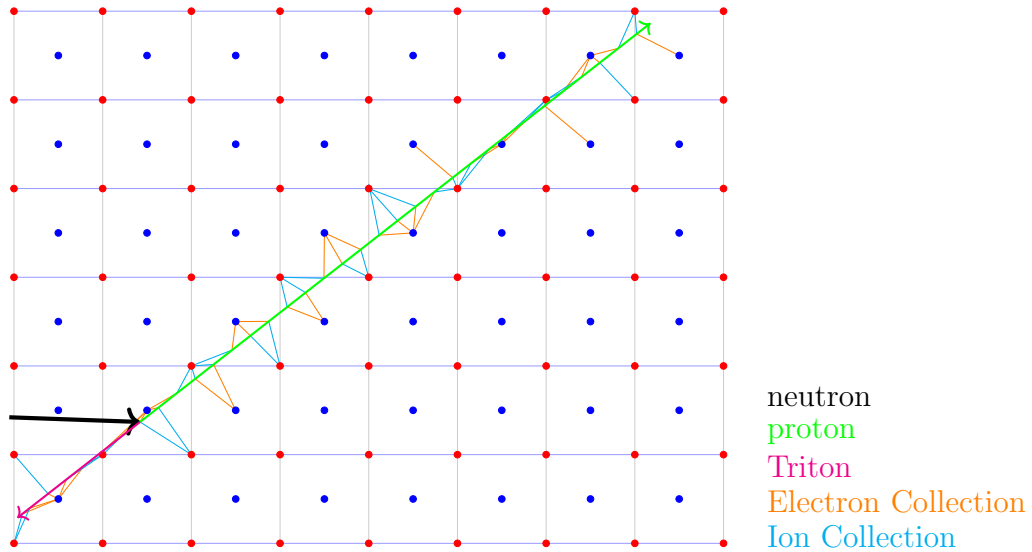


Figure 3.11: Creation and collection of ion pairs along the proton and triton tracks [56]

The energy loss by proton and triton during the ionization process can be used to estimate numbers of ion pairs created. For heavy charged particles ( $m_{\text{incident}} \gg m_e$ ), the rate of energy loss due to collisions with electrons, is given by the Bethe-Bloch formula [51],[52]

$$-\frac{dE}{dx} = \frac{4\pi n z^2 Z^2 e^4}{m_e v^2} \left[ \ln \frac{2m_e v^2}{I[1 - (v/c)^2]} - \left(\frac{v}{c}\right)^2 \right]. \quad (3.20)$$

Here,  $-dE$  is the energy lost in a distance  $dx$ ,  $n$  the number of electrons per  $\text{cm}^3$  in the stopping substance and  $Z$  its atomic number;  $m_e$  the electron mass;  $ze$  the charge and  $v$  the speed of the particle and  $I$  is the mean excitation potential of the atoms in the stopping substance.

Fig. 3.12, generated using the Geant4 simulation discussed in chapter 5, shows the rate of energy loss by the proton and triton as a function of distance from the vertex.

The rate of energy loss is also known as stopping power. Since the production of an ion pair requires a fixed amount of energy, the density of ionization is proportional to the stopping power.

The density of ions created

$$n_{\text{ion}} \propto -\frac{dE}{dx}. \quad (3.21)$$

Thus, Fig. 3.12 is also referred to as the ionization curve.

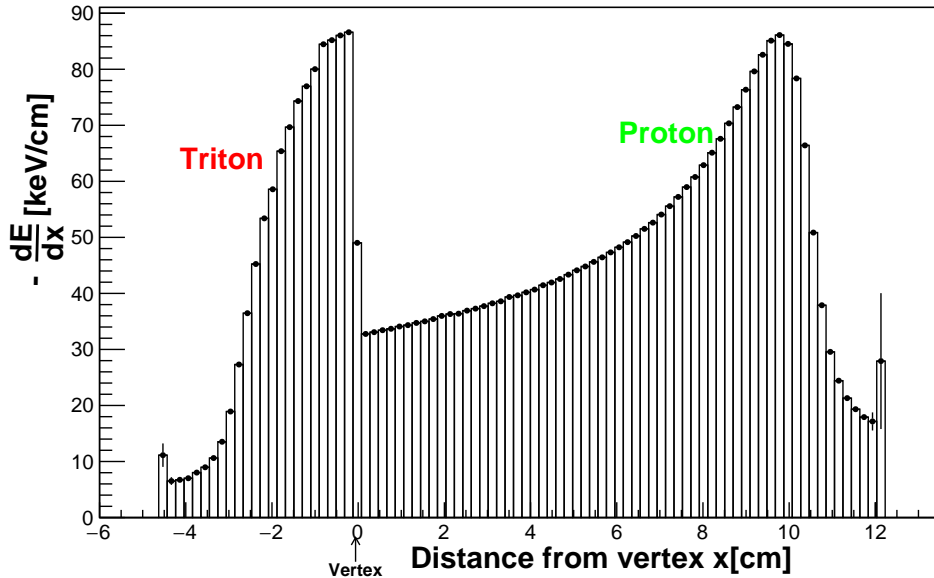


Figure 3.12: The ionization curve for proton and triton inside  $^3\text{He}$ . The stopping power ( $-\frac{dE}{dx}$ ) is proportional to the density of ions produced along the tracks.

The mean range of proton or triton can be calculated by integrating the reciprocal stopping power over the energy, i.e. the range

$$R = \int_0^{E_0} \left[ -\frac{dE}{dx} \right]^{-1} dE. \quad (3.22)$$

As we can see from Fig. 3.12, at 0.47 atmosphere the proton range is 12.1 cm and triton range is 4.3 cm. Details of the stopping power and range are discussed in chapter 5. For each capture event, the energy deposition happens in multiple wires making the wire signals correlated.

The ion chamber, as a detector, works in current mode instead of counting mode (pulse mode). This is because of the large neutron flux from the SNS and the large number of capture events occurring in a short period of time. In counting mode, for each capture event the signal and time are recorded. But this approach has the limitation that if a large number of captures happen in a short time, the individual events can not be separated. The pile-up of the events reduces the efficiency of the detector. But in current mode, a continuous output current is measured from each signal wire, which is proportional to the energy deposited around the signal wire

$$E \propto Q_s = \int i_s(t) dt. \quad (3.23)$$

In current mode, the measured signal consists charge from ionization and electronic noise. High event rates does not affect the detector efficiency in current mode. The design of readout electronics is different for counting mode versus current mode operation. In the next chapter, the details of readout electronics are discussed.

# Chapter 4

## Readout electronics

---

The signals from the ion chamber signal wires are converted to voltages using a current to voltage preamplifier. Then, the voltages are digitized using a 24-bit ADC to store the data. So, the  $n\text{-}^3\text{He}$  readout electronics consists of two major components: current to voltage preamplifier (preamp) and data acquisition system.

### 4.1 Preamplifier

---

The experiment uses a current to voltage preamplifier to convert current from the detector running in current mode to voltage. These preamps were designed at the Oak Ridge National Laboratory. Fig. 4.1 shows one of the four preamp boards used in the experiment. There are 36 channels per board. Fig. 4.2 shows the circuit diagram for the preamp.

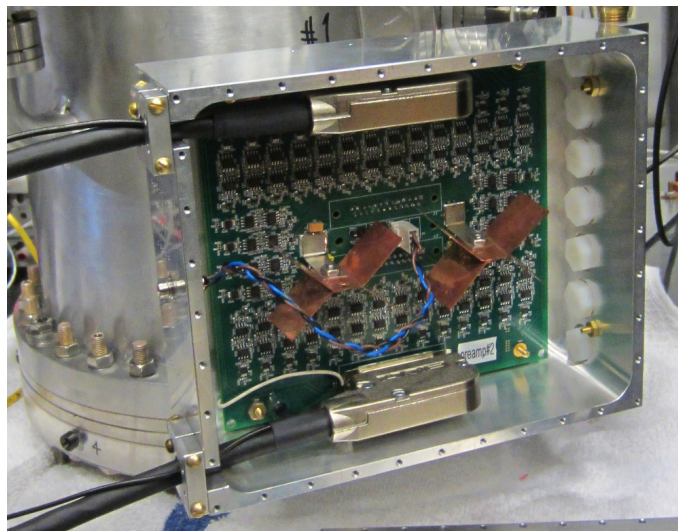


Figure 4.1: The preamplifier attached to the ion chamber

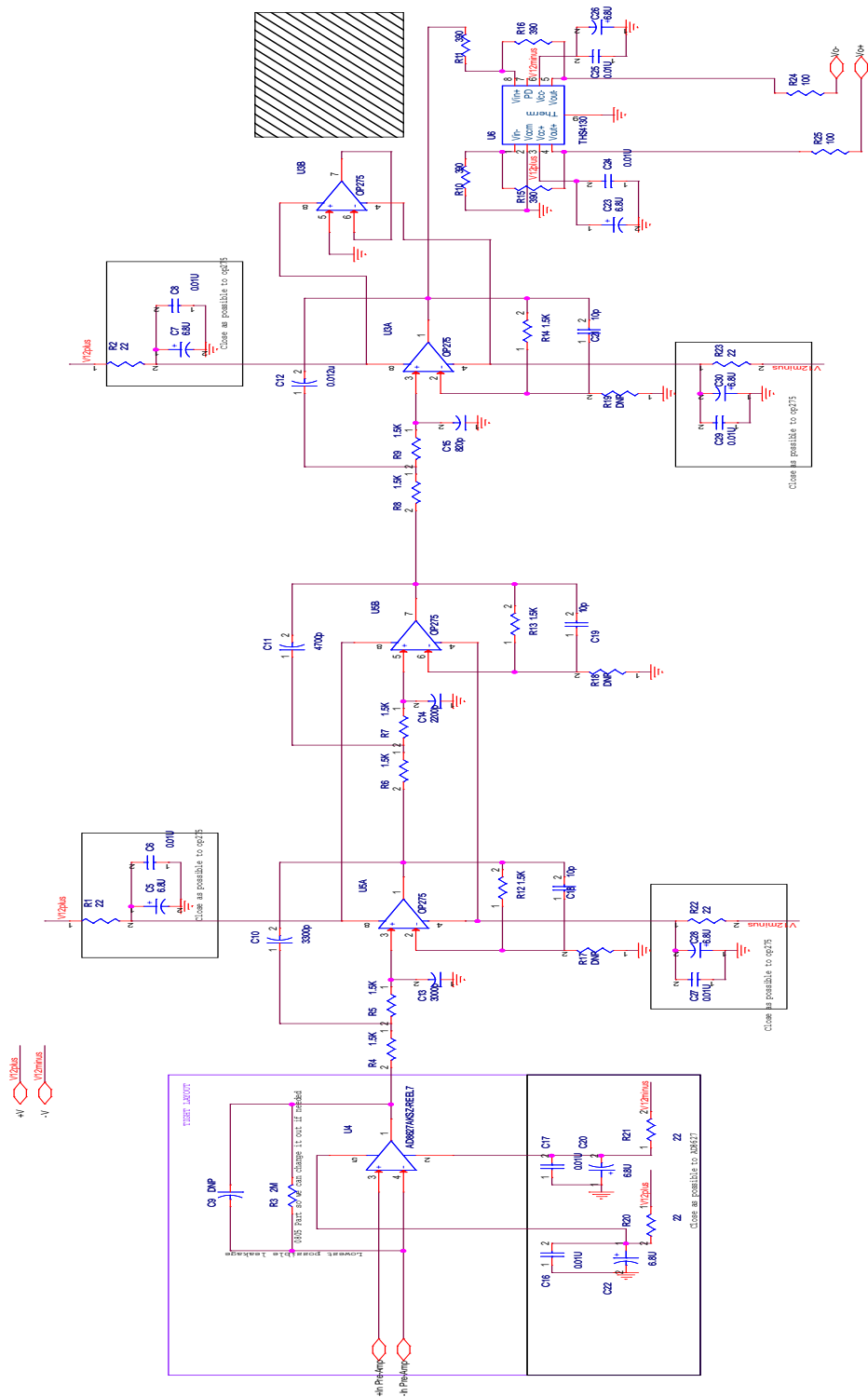


Figure 4.2: The preamp circuit diagram. There are total 4 boards with 36 channels per board.



## 4.2 Data acquisition system

---

It is evident that a suitable data acquisition system (DAQ) is vital in achieving the goal of our precision. A detailed list of expected requirements were worked out which would fit the nature of our data collection.

To achieve our goal, following are our expectations for the DAQ in general:

- The DAQs are expected to be capable of dealing with large amount of data at high sample rate but maintain very low ADC noise.
- We expect them to have high channel density with simultaneous input.
- We expect maximum sampling rate but the file size manageable.
- Triggering on the accelerator  $T_0$  with jitter  $< 50$  ns.
- The DAQ is expected to be capable to take data only in our region of interest.
- Time bin and the number of entries per run can be adjusted.
- It should be possible to synchronize all the ADC modules with  $T_0$
- We expect to have checksum algorithm to detect corrupt data .
- We expect to have built in event header.

Now for the systematics we have more challenging expectations. The 1st plane of the detector can be set to as high as 10 V (full scale). The back plane of the detector is as small as  $\sim 0.1\%$  of full scale. The size of the asymmetry is,  $A \sim 10^{-7}$ . Our expected uncertainty in the asymmetry is,  $\Delta A = 2 \times 10^{-8}$  (statistical). The expected maximum contribution from systematics is  $\Delta A_{\text{sys}} = 10\%$  of  $\Delta A$ . This gives the constraint  $\Delta A_{\text{sys}} < 10^{-9}$ . Thus the biggest challenge is limiting  $\Delta A_{\text{sys}}$  due to electronic pickup of the spin flipper in the experiment, which turns on and off at 30 Hz.

### 4.2.1 The DAQ modules

To fulfill all these expectations we use the DAQ (model ACQ1002R –  $2 \times$  ACQ435ELF-24) from D-tAcq solutions. We requested D-tAcq solutions to include some custom features to fit out requirements. The requested features were: Capability to operate in repeating gate mode, user trigger, programmable transient length, resynchronization of sample clock on the trigger, sum and decimation and an embedded event signature with sample count and checksum. In addition to our requested features it has the following standard features:

- The ACQ1002R motherboard contains Xilinx Z7020 (Zynq) hybrid FPGA with 2 ARM CPU cores and 2 FMC slots.
- The modules have delta-sigma ADCs (TI ADS1278 chip).

- They are 24 bit ADC per channel with true simultaneous analog input.
- The maximum sampling rate is 128 kSPS (hi res) or 50 kSPS (low res) and minimum is 8 kSPS per channel.
- They have 2x24 channels per module.
- The signal to noise ratio is 104 dB (high speed) or 108 dB(high resolution).
- They have 1GB DDR memory on board.
- They have external clock, trigger and an internal clock.
- They run embedded Linux.
- The firmware is in flash memory and can be updated easily.
- The DAQ can be accessed through ssh or a serial console port.
- It has several separate sites (TCP/IP) for capture and configuration.
- The data is transferred and saved to the control computer using a TCP/IP connection (e.g. using netcat).
- It supports EPICS CSS for controlling the DAQ.
- The Data and run time parameters can be viewed in real time using CSS.



(a) The ADC modules

(b) Single ADC card

Figure 4.3: The ADCs used for the n-<sup>3</sup>He experiments

Each DAQ module uses three Texas Instrument ADS1278 ADCs[55]. They allow simultaneous sampling of 8 channels. Traditionally, industrial delta-sigma ADCs offer good drift performance using digital filters with large passband droop. As a result they have limited signal bandwidth and are mostly suited for DC measurement. High-resolution ADCs in audio applications offer larger usable bandwidth, but the offset and drift specifications are significantly weaker than the respective industrial counterpart. The ADS1278 combines both features of these types of converters,

allowing high-precision measurement with excellent DC and AC specifications. To allow trade-offs between speed, resolution and power, it supports four operating modes (hi-speed, high-resolution, low-power, low-speed), which the user can select based on requirements.

The high-order, chopper-stabilized modulator achieves very low drift with low in-band noise. The on-board decimation filter suppresses modulator and signal out-of-band noise. These ADCs provide a usable signal bandwidth up to 90% of the Nyquist rate with less than 0.005dB of ripple.

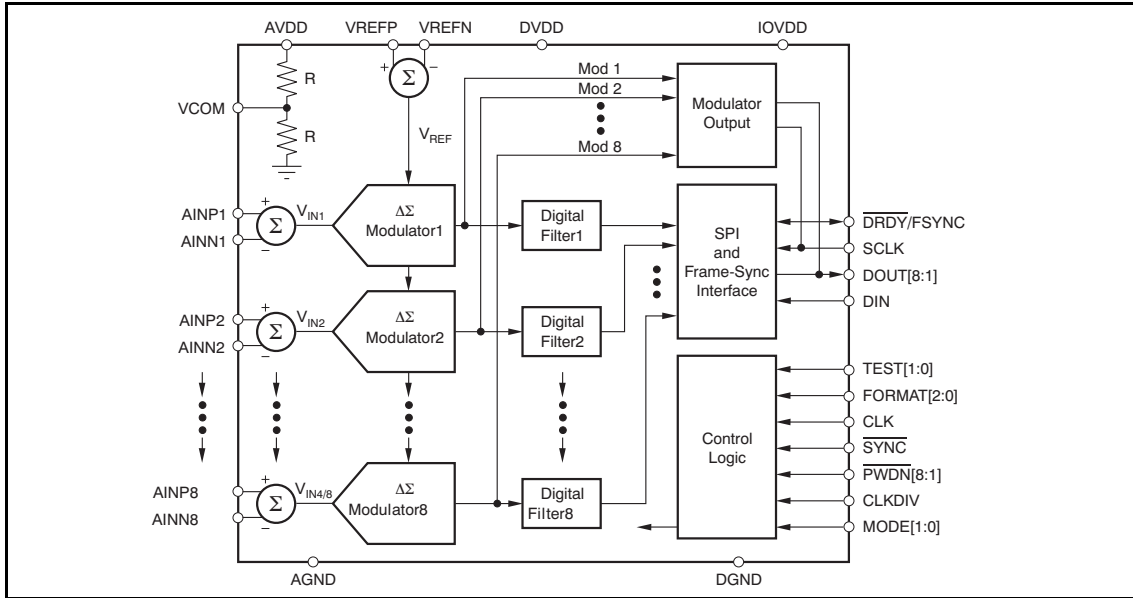


Figure 4.4: ADS1278 block diagram[55]. Each n-<sup>3</sup>He DAQ contains 6 of these IC's, 3 in each of two modules

In the experiment five such DAQ modules are used. Four of them (clean DAQs, named as DAQ21-24) are used for the detector signals and the fifth one (dirty DAQ, named as DAQ30) is used for the RFSF and M1 signal. Each module has 2×24 channels. For the clean DAQ, 18 of the 24 channels of each of the two DAQ modules are connected to the preamp signals and for dirty DAQ only 2 channels are used.

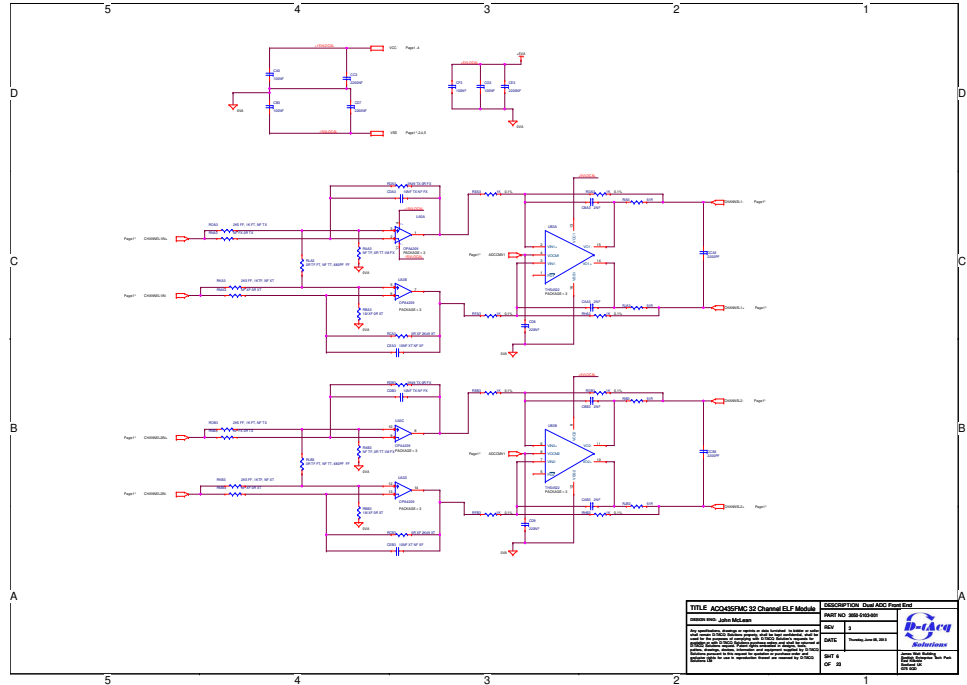


Figure 4.5: Analog input front-end circuit of the DAQ

## 4.2.2 ADC characteristics

Extensive tests and various measurements were performed to characterize the DAQ performance and to make sure it would fulfill our requirements. Bare ADC noise was measured to be  $27 \mu\text{V}$  at 50 kHz sample rate as shown in Fig. 4.6.

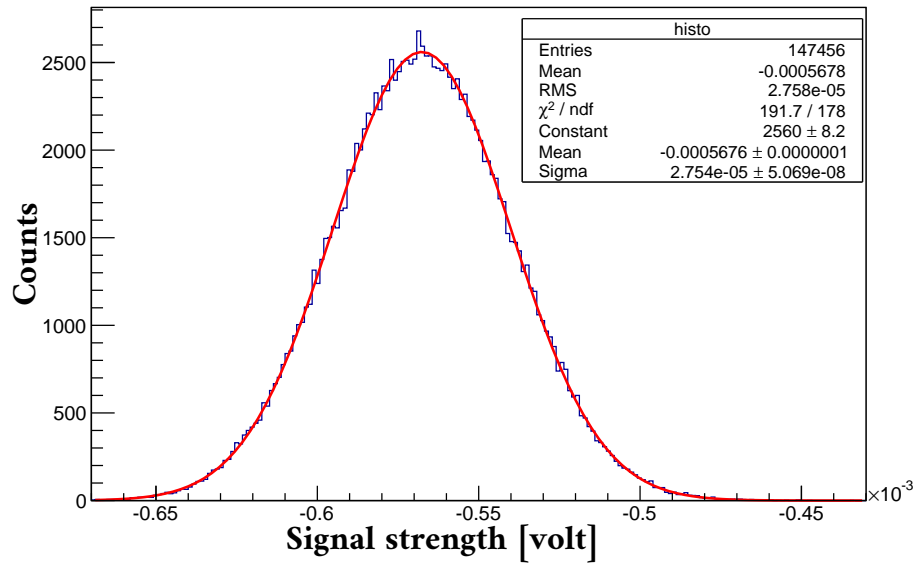


Figure 4.6: Distribution of the bare ADC signal. The DAQ was running at 50 kHz sample rate.

To decide which sample rate would be most appropriate for the experiment, we measured the bare ADC noise by running it at different sample rates. Performance of the ADC against different sample rates shows that the noise jumps after a cutoff (around 52 kHz) as shown in Fig. 4.7, because the ADC shifts from high-resolution mode to high-speed mode.

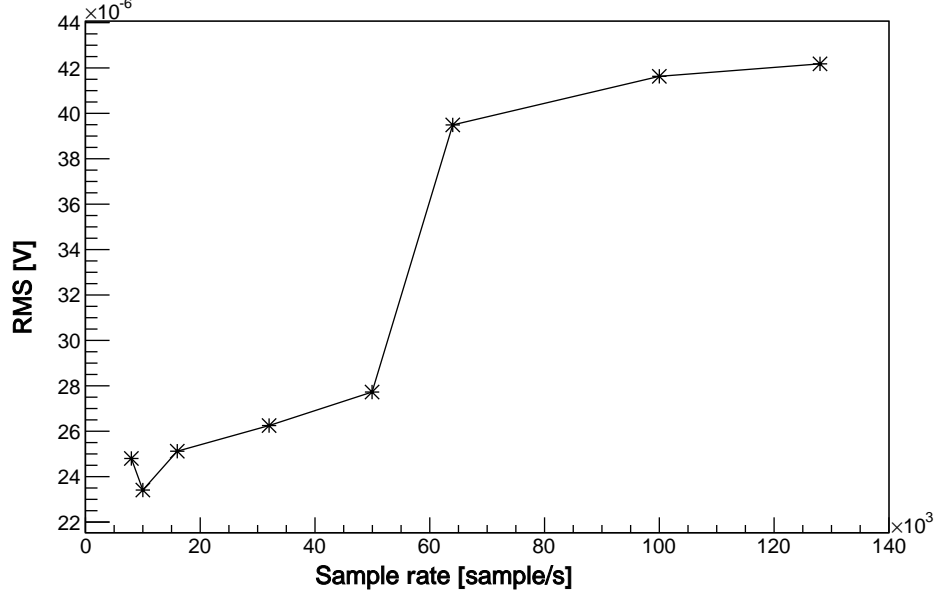


Figure 4.7: ADC noise at different sampling rate

In the experiment, averaging of 16 samples was performed on the detector signals. This way we kept all the information but reduced the file size to a manageable level. The DAQ does the averaging in real time while taking the data. We decided to run the experiment with 50 kHz sample rate and to average 16 samples per output sample for the detector signals. For the dirty DAQ, we decided to run at 100 kHz sample rate with no averaging, since the RFSF signal had at a very high frequency ( $\sim 30$  kHz) and for the M1 signal we wanted to keep the resolution as high as possible for each time bin.

To verify the randomness of the noise, we computed autocorrelations for the noise data values at varying time lag. Fig. 4.8 shows the autocorrelation plot up to 100 time bins. Here the data were taken with the DAQ running at a 10 kHz sample rate. In the plot the vertical axis is the autocorrelation coefficient  $R_h = C_h/C_0$ , where  $C_h$  is the autocovariance function

$$C_h = \frac{1}{N} \sum_{t=1}^{N-h} (Y_t - \bar{Y})(Y_{t+h} - \bar{Y}), \quad (4.1)$$

and  $C_0$  is the variance

$$C_0 = \frac{1}{N} \sum_{t=1}^N (Y_t - \bar{Y})^2, \quad (4.2)$$

and the horizontal axis is the time lag  $h$  ( $h = 1, 2, 3, \dots$ ). In this plot 1 lag =  $100\mu\text{s}$ . By definition  $R_h$  is between -1 and +1.

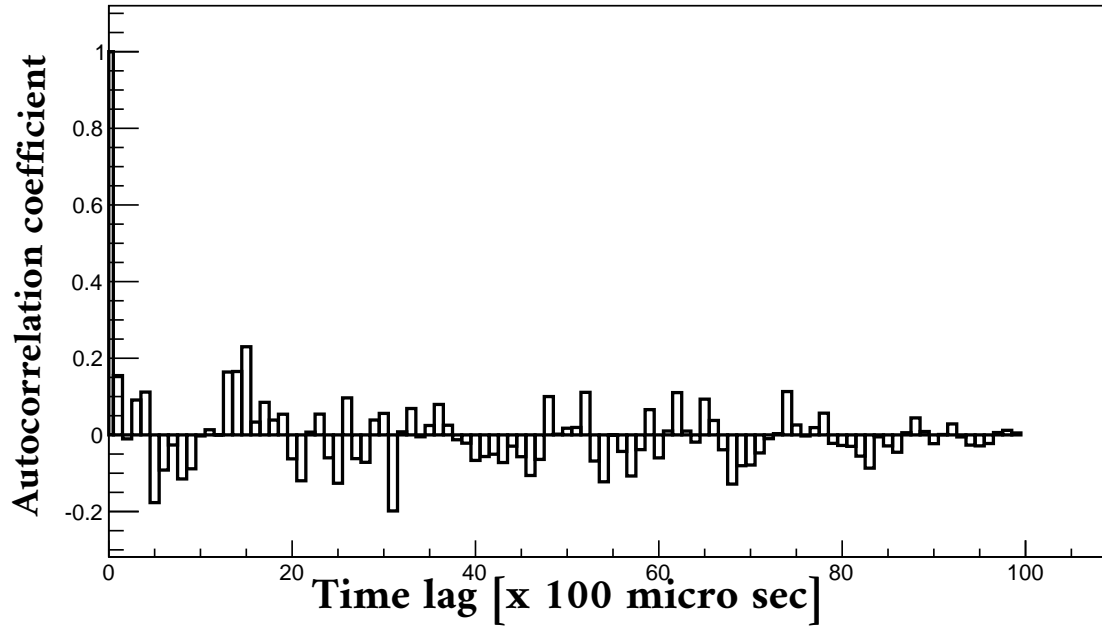


Figure 4.8: Autocorrelation plot for the ADC noise data. The DAQ was running at 10 kHz.

To validate the sampling at the maximum sampling rate, we took a signal having a rise time comparable to the maximum sample rate (128 kHz) and then took data for the rise time with the DAQ running at 128 kHz. Fig. 4.9 shows the rise time measurement.

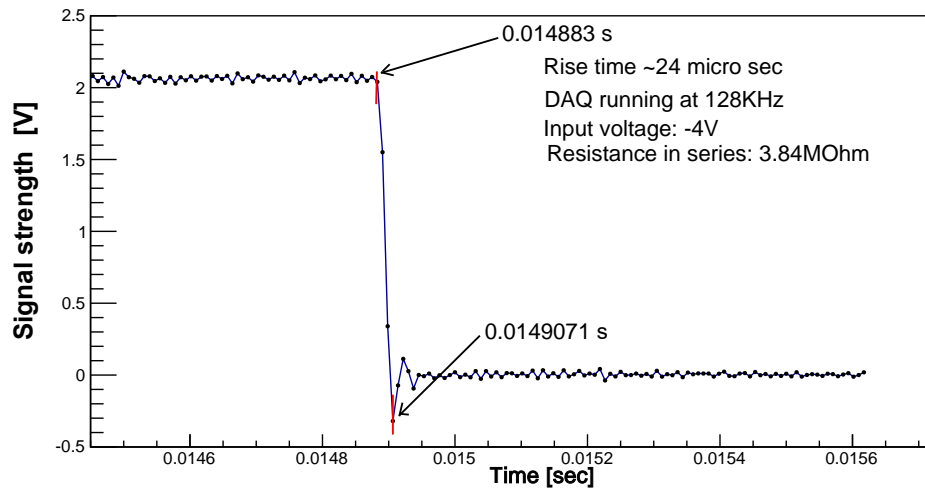


Figure 4.9: Rise time measurement with DAQ running at 128 kHz

The DAQ can average samples ( $n = 2, 4, 8, 16, \dots \dots 128$ ) during the data taking process. Fig. 4.10 shows a test to confirm this feature of the DAQ. In this test we recorded a pulse with rising and falling edges and the data is recorded at 50 kHz sampling rate in resynchronization mode (explained in the next section) first without any averaging and then averaging four samples. Since they were recorded in resynchronized mode, we expect the samples from both dataset to be consistent up to the jitter. In the plot we compare the signal from three datasets: non-averaging mode, averaging four samples and data obtained by interpolating (averaging) four samples from the first dataset.

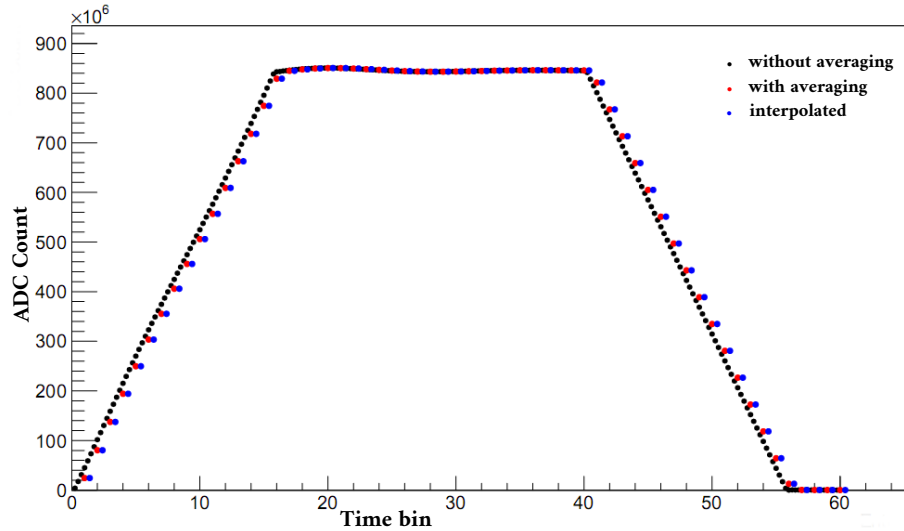


Figure 4.10: The test for the averaging feature of the DAQ. For blue points, a small offset of 0.4 time bin has been added to distinguish them from the red points. The maximum height of the signal is 4 V. (1 ADC count =  $4.6566 \times 10^{-9}$  V and 1 time bin =  $20 \mu\text{s}$ .)

### 4.2.3 Resynchronization and jitter

The ADC has a 30 MHz internal clock which is used as the reference for the sample clock (rate). Jitter in ADC ( Jitter in time  $\times$  slope) must be less than the counting statistics. Furthermore, systematic spin-dependent jitter would cause a false asymmetry. For this reason, the ADC was customized to resynchronize to the nearest clock cycle after each event to reduce jitter to less than 35 ns. The following test confirmed the desired jitter of the ADC:

A 60 Hz pulse with ramp of width  $320 \mu\text{s}$ , a leading edge of  $100 \mu\text{s}$ , and a trailing edge of  $100 \mu\text{s}$  was fed to the ADC in repeating gate mode with a trigger on the rising edge. Then each rising edge of the pulse (5 points in the middle of rising edge) was fitted to the linear equation  $y = ax + b$  using the least square method. This gives the  $x$ -intercept and the slope of the rising edge. For each fit, the  $x$ -value of the header

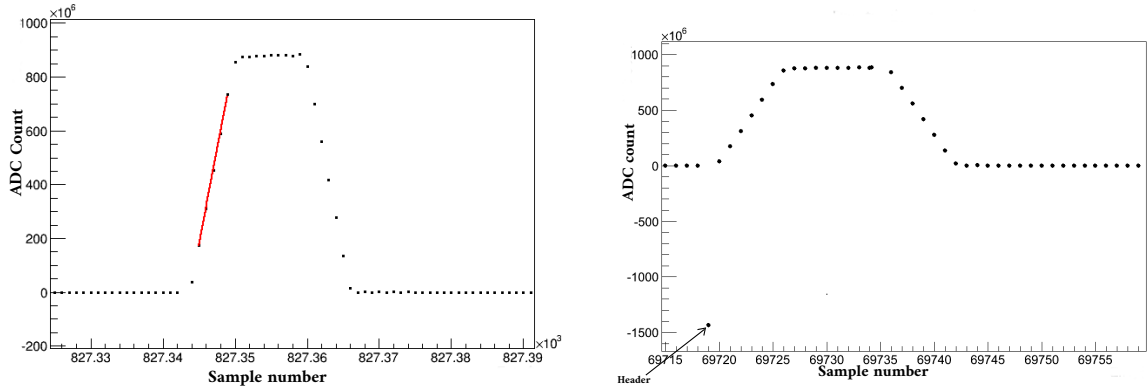


Figure 4.11: Test signal for testing resynchronization of the ADC

is subtracted from the  $x$ -intercept of the rising edge. This gave  $\Delta t = t_i - t_0$ , where  $t_i$  = the intercept from the fit,  $t_0$  = the  $x$ -value for header. This was done for all the pulses. Finally  $\Delta t$  vs the pulse number was plotted as in Fig. 4.12. Also a histogram for all the  $\Delta t$  was drawn. The histogram in Fig. 4.13 shows that the jitter is 36 ns. Thus the jitter was found to be as expected ( $1/30$  MHz), with a small deviation because of slow drifts, the convolution with the bit noise and the jitter in the signal generator.

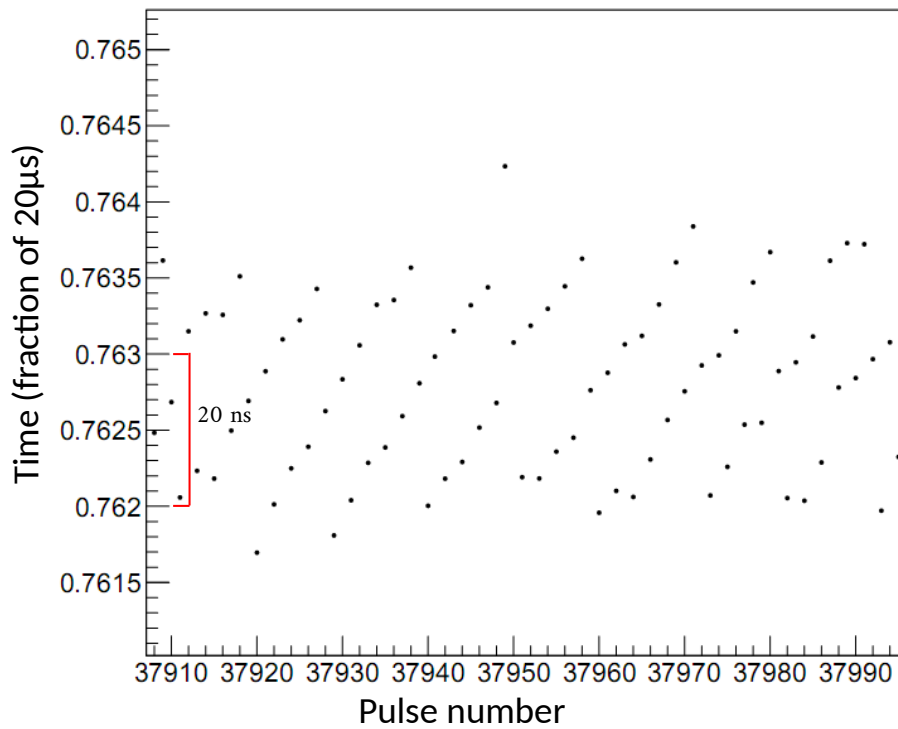


Figure 4.12: Jitter from the intercepts.



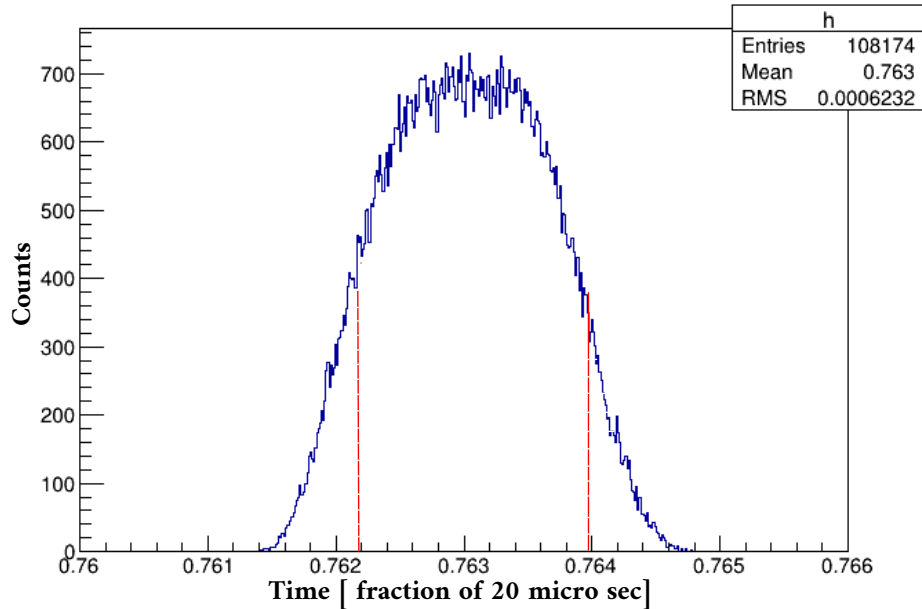


Figure 4.13: Jitter from the intercepts. Projection of Fig. 4.12 on  $y$ -axis. FWHM was found to be 36 ns.

#### 4.2.4 Event length, dead time and file size

The DAQ allows setting the number of samples to be recorded per trigger or  $T_0$  (one event). For the DAQs of the detector signals (called clean DAQs), the sample rate was set to 50 kHz. Thus, the maximum achievable number of samples is  $50 \text{ kHz} \times 16.667 \text{ ms} = 833$  samples per  $T_0$ . We decided to set the event length for clean DAQs to 830 to allow time for triggering. The DAQ (called dirty DAQ) of the RFSF and M1 signals, was set to take data at 100 kHz. The maximum achievable number of samples per event is  $100 \text{ kHz} \times 16.6666 \text{ ms} = 1667$ . We set the event length for dirty DAQ to 1660. The clean DAQs were set to average 16 samples, but no averaging was performed for dirty DAQ. Moreover the DAQs have fixed dead time (readout time) of 35 samples (with no averaging) at the end of any event. This amount of time was missed for every event.

Thus, the recorded number of samples per event was:

Clean DAQ:  $(830-35)/16 \sim 50$  (1 header + 49 samples)

Dirty DAQ:  $(1660-35) = 1625$  (1 header + 1624 samples)

The dead time in the DAQ is calculated to be:

Clean DAQ:  $(52.06 - 49) \times 320 \mu\text{s} = 0.98 \text{ ms}$

Dirty DAQ:  $(1667-1624) \times 10 \mu\text{s} = 0.430 \text{ ms}$

To allow for long enough duration for uninterrupted data taking, but still separated into runs, we recorded 25000  $T_0$  pulses (events) per run. With 25000  $T_0$ 's per run, the clean DAQ file size was  $25000 T_0 \times 50 \text{ samples} \times 4 \text{ bytes per sample} \times 48 \text{ Channels}$

=  $240 \times 10^6$  bytes. We process the recorded data file of the dirty DAQ to keep only the signal 2 channels and discard the remaining.

The dirty DAQ file size (before processing) was  $25000 T_0 \times 1625$  samples  $\times$  4 bytes per sample  $\times$  8 channels =  $1300 \times 10^6$  bytes. The dirty DAQ file size (after processing):  $25000 T_0 \times 1625$  samples  $\times$  4 bytes per sample  $\times$  2 channels =  $325 \times 10^6$  bytes.

### 4.2.5 The data file structure

For each clean DAQ unit, the 48 channels are divided into two sites – site 1 and site 2, with each site (module) having 24 channels. In the data stream, each sample is 4 bytes long. Out of these 32 bits (4 bytes), our data is 24 bits and remaining least significant 8 bits record the channel ID. All clean DAQ data streams have the data structure as shown in Fig. 4.14. In Fig. 4.14,  $n$  is the event length (number of samples per pulse) and  $N$  is the number of events (pulses) per run. For  $n$ - $^3\text{He}$ ,  $n = 50$  and  $N = 25000$  for the detector data. The first sample of any event is the event-header with information shown in (4.15). Here,  $0xaa55f154$  or  $0xaa55f15f$  are event makers (called event magic) to distinguish the event-header from signal. The checksums are to ensure data integrity and any event-header contains checksum from immediate previous event. For the dirty DAQ data file, the data structure reduces to the structure shown in Fig. 4.16 after processing (after throwing away unused channels), with the first sample of any event being checksum and sample number, respectively, as shown in Fig. 4.17.

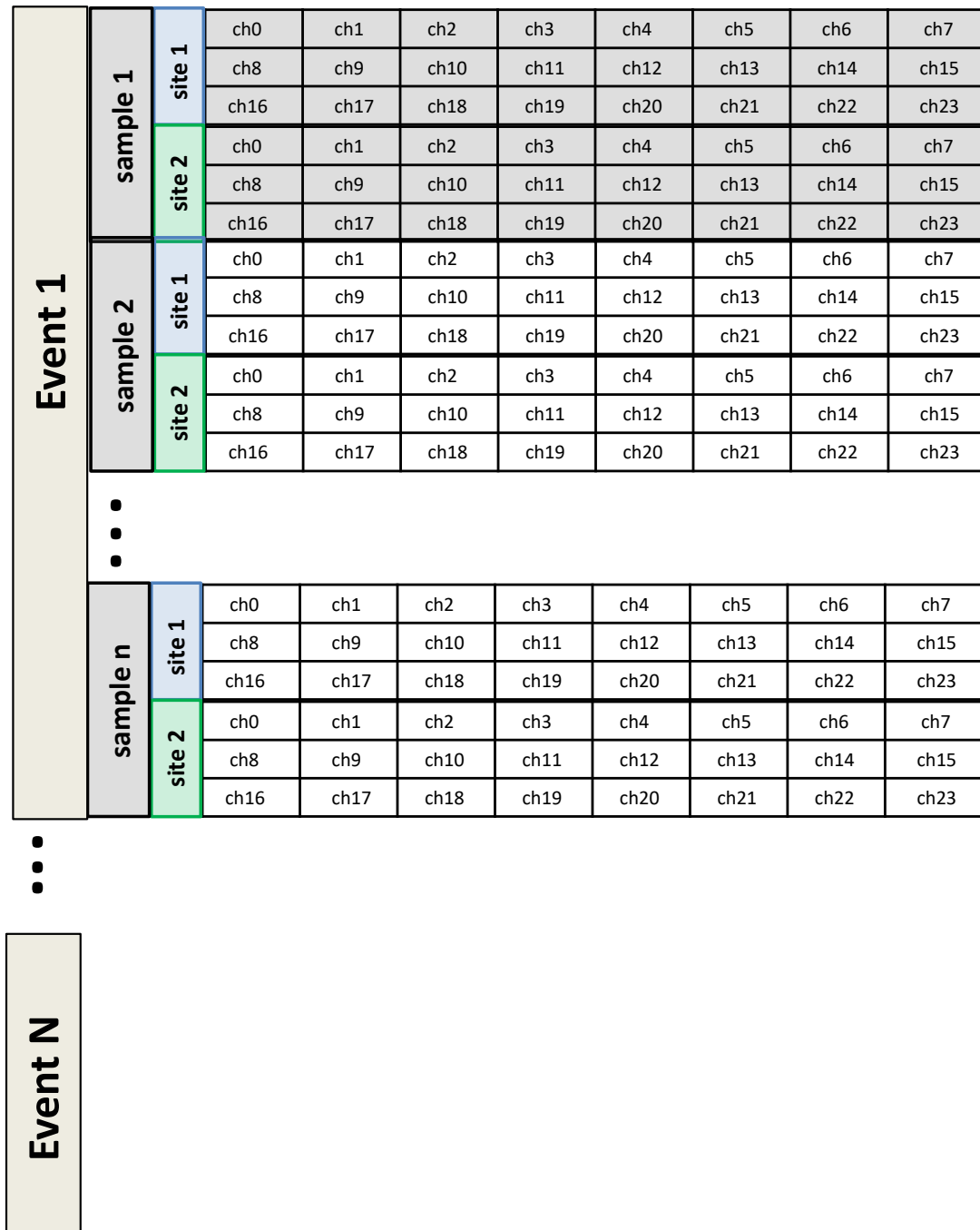


Figure 4.14: Deata file structure for the detector data

sample 1	site 1	0: 0xaa55f154	1: 0xaa55f154	2: 0xaa55f154	3: 0xaa55f154	4: Event number	5: Checksum 1	6: Sample number	7: Checksum 2
		8: 0xaa55f154	9: 0xaa55f154	10: 0xaa55f154	11: 0xaa55f154	12: Event number	13: Checksum 1	14: Sample number	15: Checksum 2
	16: 0xaa55f154	17: 0xaa55f154	18: 0xaa55f154	19: 0xaa55f154	20: Event number	21: Checksum 1	22: Sample number	23: Checksum 2	
	site 2	0: 0xaa55f15f	1: 0xaa55f15f	2: 0xaa55f15f	3: 0xaa55f15f	4: 0	5: Checksum 1	6: Sample number	7: Checksum 2
8: 0xaa55f15f		9: 0xaa55f15f	10: 0xaa55f15f	11: 0xaa55f15f	12: 0	13: Checksum 1	14: Sample number	15: Checksum 2	
16: 0xaa55f15f		17: 0xaa55f15f	18: 0xaa55f15f	19: 0xaa55f15f	20: 0	21: Checksum 1	22: Sample number	23: Checksum 2	

Figure 4.15: Content of the header for the detector data

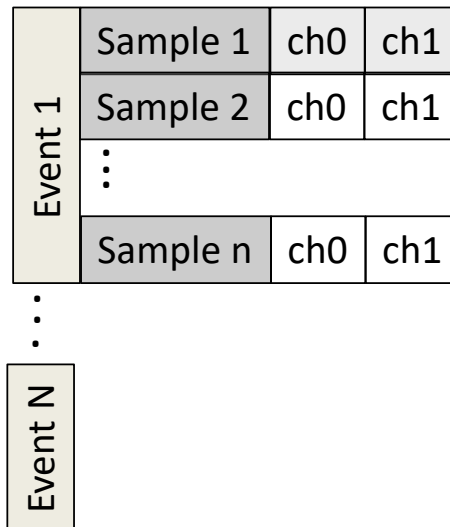


Figure 4.16: Data file structure (after processing) for the M1 and RFSF signals

Sample 1	0: Checksum	1: sample number
----------	-------------	------------------

Figure 4.17: Content of the header (M1 and RFSF data)

## 4.2.6 ADC count to volt conversion and time bin

The bit resolution and voltage input range of a DAQ device determine the smallest detectable change in the input signal. The smallest detectable change, called the resolution, can be calculated using the the formula –

$$\text{Resolution} = \frac{\text{ADC Range}}{2^{\text{bit resolution}}}. \quad (4.3)$$

The n-<sup>3</sup>He DAQ is a 24-bit ADC. But each sample is stored as a 32-bit wording. Out of these 32 bits, the least significant 8 bits record the channel ID and the remaining 24 bits contain the signal. The ADC has a range of +10 V to -10 V. Then

$$\text{Resolution} = \frac{20 \text{ V}}{2^{32}}. \quad (4.4)$$

Thus,  $4.656612873 \times 10^{-9}$  is used for the conversion factor from ADC value to voltage (if the least 8 bits are not already thrown away). But if the least significant 8 bits out of 32 bits are already thrown away, then

$$\text{Precision} = \frac{20 \text{ V}}{2^{24}}, \quad (4.5)$$

i.e.  $1.192092896 \times 10^{-6}$  is used as the ADC count to voltage conversion factor.

The time bin (tbin) depends on the sample rate at which the DAQ takes the data. Thus, for clean (detector) data each time bin corresponds to

$$1 \text{ tbin}_c = 16 \times \frac{1}{50 \text{ kHz}} = 320 \mu\text{s}. \quad (4.6)$$

For dirty data, it is

$$1 \text{ tbin}_d = \frac{1}{100 \text{ kHz}} = 10 \mu\text{s}. \quad (4.7)$$

## 4.3 Wire map and the network

---

Out of 48 clean ADC channels, only 36 ADC channels are connected to the preamps (ADC channels 0 to 17 and channels 24 to 41). Each clean DAQ is connected to four wire planes (layers). There are two bad channels: DAQ21 channels 5 and 6(both signals are combined on channel 6). Moreover, (in UD mode) DAQ22 channel 35 and DAQ24 channels 35, 39 have opposite polarity which are corrected by reversing the sign in the analysis. Fig. 4.18 shows the signal wire to ADC channel map [56].

Four clean DAQs and one dirty DAQ are connected to a gigabit ethernet switch, which is in turn connected to the control computer. The control computer communicates to the DAQs through the TCP/IP protocol to transfer the data and control the DAQs.

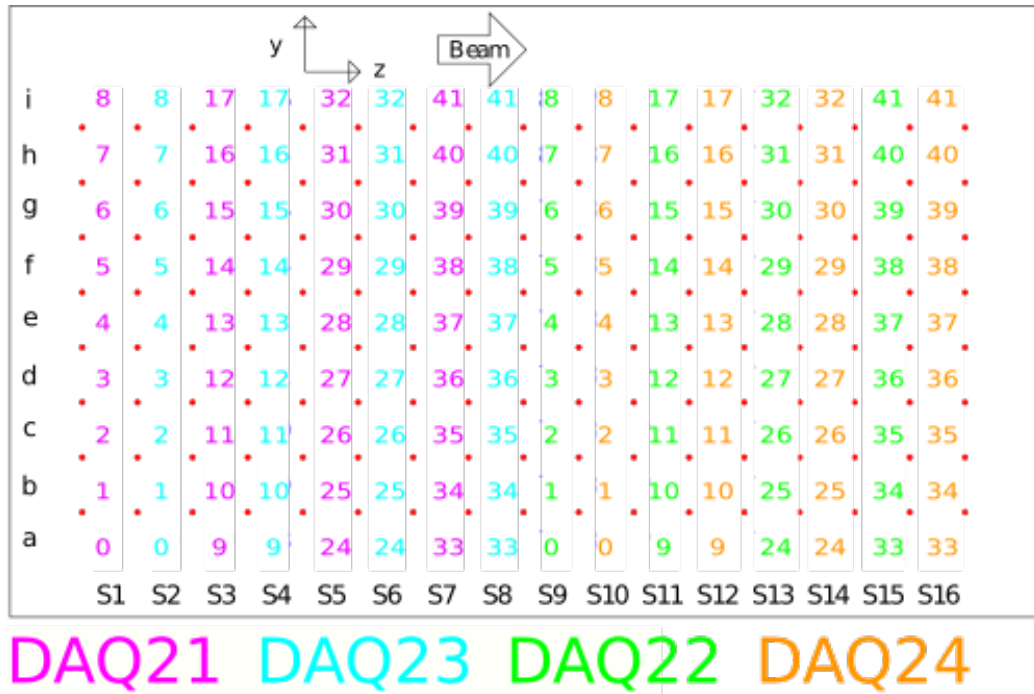


Figure 4.18: Signal wire to ADC channel map

The control computer is connected to a portable hard disk to store the data as backup. From the control computer, the data is instantly transferred to a remote workstation with RAID, which is accessible from off-site for offline analysis. Other data that go into the data stream are the magnetic field data and preamp temperature data. The control computer is equipped with a DAQ control GUI to manage run configuration, a data plotter GUI for instant online analysis for a data quality check, a magnetic field and temperature monitoring GUI, a watchdog program and other necessary software [57] for long-term data taking. Fig. 4.19 shows the network diagram connecting all the components.

All the components (five DAQs, RFSF and control computer) are synchronized with the accelerator  $T_0$  through the trigger logic. The accelerator provides a 60 Hz  $T_0$  signal indicating the release of a proton pulse. A constant delay of 13.5 ms is applied to this  $T_0$  to accommodate for the time taken by the neutrons to arrive at the detector position from the moderator. In the individual level, each DAQ module is synchronized to the same delayed  $T_0$  trigger. To synchronize with the control computer at the start of the run, trigger logic is used. The control computer can send command to the DAQ module over TCP/IP to provide either 0 mV or 500 mV digital output. Only DAQ30 is used to produce the digital output signal for synchronization with the control computer. This digital signal is amplified to a TTL signal levels. This TTL signal is then ANDed with the delayed  $T_0$ . Finally this ANDed trigger is input to each DAQ module and also to the signal generator connected to the RFSF. All the

trigger connections are optically isolated. Each DAQ is powered through an isolation transformer to avoid ground loops. The only path to the building ground is through the ion chamber.

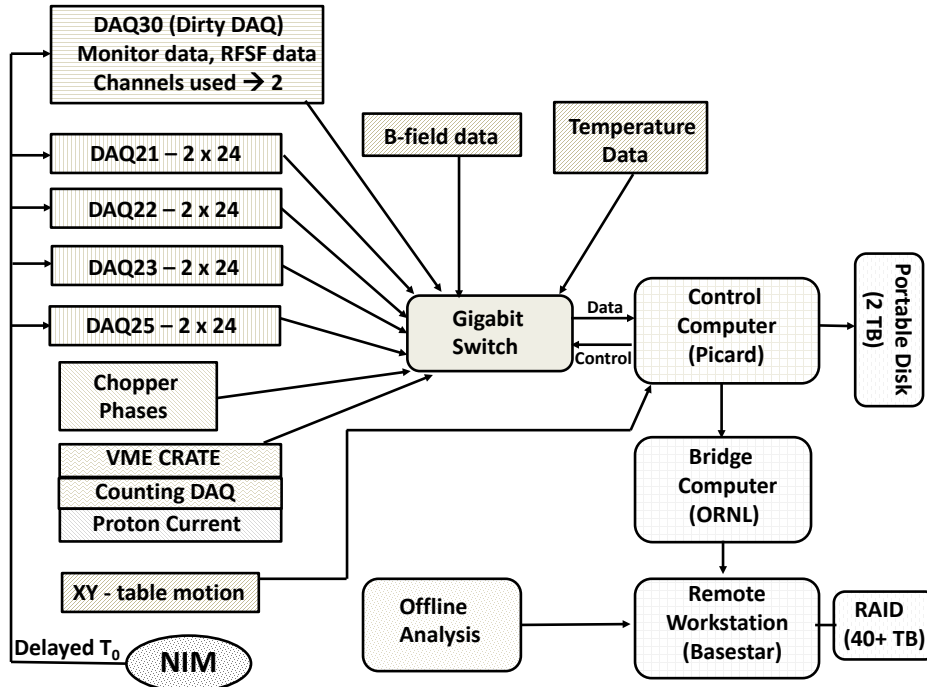


Figure 4.19: The network diagram of the n-<sup>3</sup>He experiment

## 4.4 Processed and compressed data file

To facilitate and speed up the analysis, two additional intermediate processed files were generated. In one case we integrated over all time bins within each pulse to make one file per run and in the other case we kept all the time bins but integrate each time bins over the all the runs. We call the former processed files 'summary files' and the later one a "data summary tape" or DST.

### Summary file:

For each run with sufficient beam (which is analyzable for either LR or UD asymmetry), a summary file was processed integrating over time bins (sum of signals) for each event. This is done both for the detector channels (clean DAQ channels) and dirty DAQ channels (M1 signal and RFSF current). An asymmetry for pair of adjacent pulses of each detector channel was also computed. All these values were saved in tree structure (TTree) in a root file. The tree has three branches : "*sumc*" (sum of signals from clean DAQ), "*sumd*" (sum of signals from dirty DAQ) and "*asym*" (calculated asymmetry), with the following structure:

*sumc[4][36]*: The first index is for the DAQ number (0→DAQ21, 1→DAQ22, 2→DAQ23, 3→DAQ24)

and second index is for each channel number (the channel index is made continuous here).

*sumd[2]*: *sumd[0]* is the M1 signal integrated over time bins and *sumd[1]* is the same thing for the RFSF current.

*asym[4][36]*: The first index is the DAQ number and second is the channel number. The first entry of the branch “*asym*” is a flag with the run number. The second entry is asymmetry between first event and second event of the run, the third entry is asymmetry between second and third event of the run and so on, as shown in Table (4.1).

Entry#	Content
0	Run number
1	Asymmetry between pulse# 0 & 1
2	Asymmetry between pulse# 1 & 2
3	Asymmetry between pulse# 2 & 3
4	Asymmetry between pulse# 3 & 4
...	
24991	Asymmetry between pulse# 24990 & 24991

Table 4.1: Content of the branch “*asym*” in the summary file

In the analysis, the first entry is always skipped, since it is a flag for run number, and only either odd entries or even entries are considered to avoid double counting. In calculating the above asymmetry, the signal of each channel for each event is normalized by the sum over all the detector signals to remove the beam fluctuation. We also subtract the background from each signal following the approach explained in section 6.1.3.

The asymmetry is constructed using:

$$A' = \frac{Y_{\text{on}} - Y_{\text{off}}}{Y_{\text{on}} + Y_{\text{off}}},$$

which differs by a negative sign from the desired spin asymmetry:

$$A = -A' = \frac{Y^\uparrow - Y^\downarrow}{Y^\uparrow + Y^\downarrow}.$$

The ROOT file for each run has 24991 entries, as some events at the beginning and end of the run are skipped.

### Data summary tape (DST):

In this global summary file we keep all the time bins but integrated over the signals in all runs. We divided the entire dataset into 600 pulse sequences with only one dropped



pulse in any sequence, which is at the beginning of the sequence. Any sequence that had irregular dropped pulses was skipped. We integrated over the same time bins of all pulses for each 600 pulse sequence over the entire dataset separately for two groups: in one group all the sequences have the RFSF turned “on” during the dropped pulse and in the other group the RFSF was turned “off” during the dropped pulse. We did this processing for all the detector signals, the M1 signals and corresponding time bin asymmetries. All this processed information was saved in a tree data structure (**TTree**) in a ROOT file with different branches. Each branch has a multidimensional array with indices for the RFSF state during the dropped pulse, the number of pulses after the dropped pulse, the ADC channel and the time bin number.

## 4.5 The n-<sup>3</sup>He analysis tools

---

The n-<sup>3</sup>He analysis tool (library) [58] was implemented on top of ROOT [50] – an object oriented data analysis framework based on C++. The library was integrated as a shared library adding additional classes tailored for the n-<sup>3</sup>He data analysis to the ROOT functionality. These additional features along with ROOT constitute a robust data analysis tools and capable of extracting any imaginable information from the n-<sup>3</sup>He data. To provide the users (of the analysis tool) the freedom to add their own functionality based on their analysis requirement, the library was divided into two parts. The first part (**libn3He**) is the core n-<sup>3</sup>He library that provides various interface for accessing the raw n-<sup>3</sup>He data using the ROOT. This part is common to all users and generally is not modified by individual users. The second part is the analysis library (**libAnalysis**) where the user can add his own analysis functionality using the data access functionality provided by **libn3He** and other ROOT’s core features. Table (4.2) shows some of the major functionality of the n-<sup>3</sup>He analysis library.

Class/Function	Functionality
TBranchBinary	Creating TBranch object out of binary data
TTreeRaw	Creating TTree object for the given run number
TTreeAsymmetry	Making processed file with asymmetries calculated
n3HeChain	Creating TChain object for specified run range
Help	Print all the available options
List	List all the available functionalities with data members
RunStatus	Show run status for specified run number or range
GFactor	Get geometry factor for specified layer and wire number
Wire2adc	Wire to ADC map conversion
PlotIntensity	Yield distribution in ion chamber
TreeMaker	Creating processed summary file
MakeDST	Creating data summary tape
Analyzer	Standard asymmetry analyzer
AnalyzeChain	Asymmetry analysis using TChain
BeamPowerDist	Plot beam power distribution
FxAnalyzer	Asymmetry analysis from raw data with flexibility
CalInstAsym	Calculate instrumental asymmetry
Correlation	Correlation calculation for single run
n3HeAnalyzer	Asymmetry analysis with A and B separation
BatchAnalyzer	Analyze batch data
FitAlongBatches	Physics asymmetry from fit along batches
FitAlongWires	Physics asymmetry from fit along wires
GetBatchInfo	Get batch data information
GetLevelInfo	Get level data information
... ..	... Many more functionalities

Table 4.2: Some of the major functionalities in the n-<sup>3</sup>He analysis tools integrated in the ROOT.

## 4.6 Instrumental asymmetry

---

A test was performed to check the instrumental asymmetry in the combined setup of the preamp, DAQ and RFSF. We tested the test setup as shown in Fig. 4.20 with the worst possible scenario, where the RFSF was running close to the preamp with the window open. A fake  $T_0$  signal of 60 Hz was fed to a clock divider to make a 30 Hz signal. This 30 Hz signal was used to control (to turn on and off) the signal generator that produced the 30 kHz signal for the RFSF. Another part of the 60 Hz fake  $T_0$  was gated and fed to the preamplifier through an optical isolator. This signal in the preamplifier was used as a reference for spin flipper state. The first pulse of the 60 Hz signal was synchronized to known RFSF state. Data was recorded in this configuration. Using the reference signal in the preamplifier for the RFSF state, the asymmetry was constructed for signals on other preamp channels.

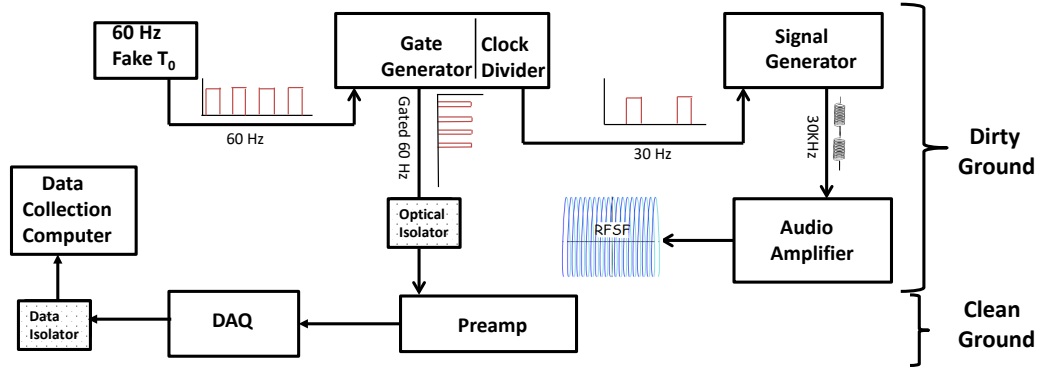


Figure 4.20: Setup for the instrumental asymmetry measurement

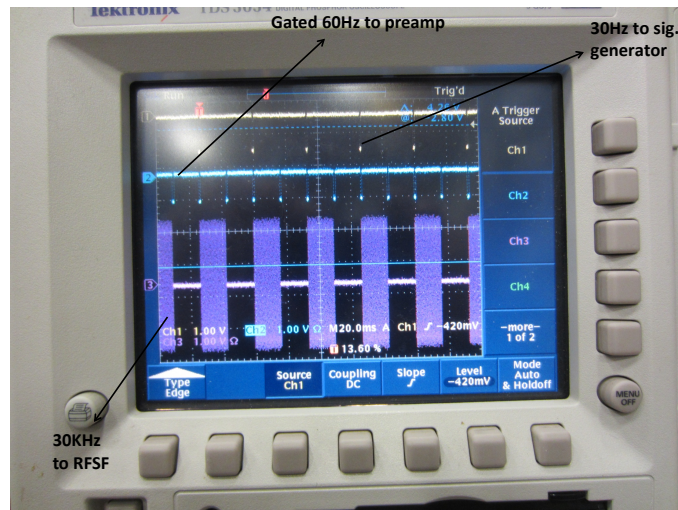


Figure 4.21: Signal used for the instrumental asymmetry measurement

In this case, for each pair of pulses, the asymmetry was defined as  $A = (V_{on} - V_{off})/20$ , where  $V_{on}$  or  $V_{off}$  is the average voltage between two peaks (excluding the peaks) and 20 V is the normalization coming from the full scale of the ADC.

Fig. 4.22 shows the distribution of instrumental asymmetry from one of the preamp channels. As shown in Fig. 4.23, analysis of 5 hours of data taken at 25 kHz sampling rate showed that we get instrumental asymmetry of the order of  $\sim 10^{-10}$ .

$$A_{ins} = (2.64 \pm 1.64) \times 10^{-10}.$$

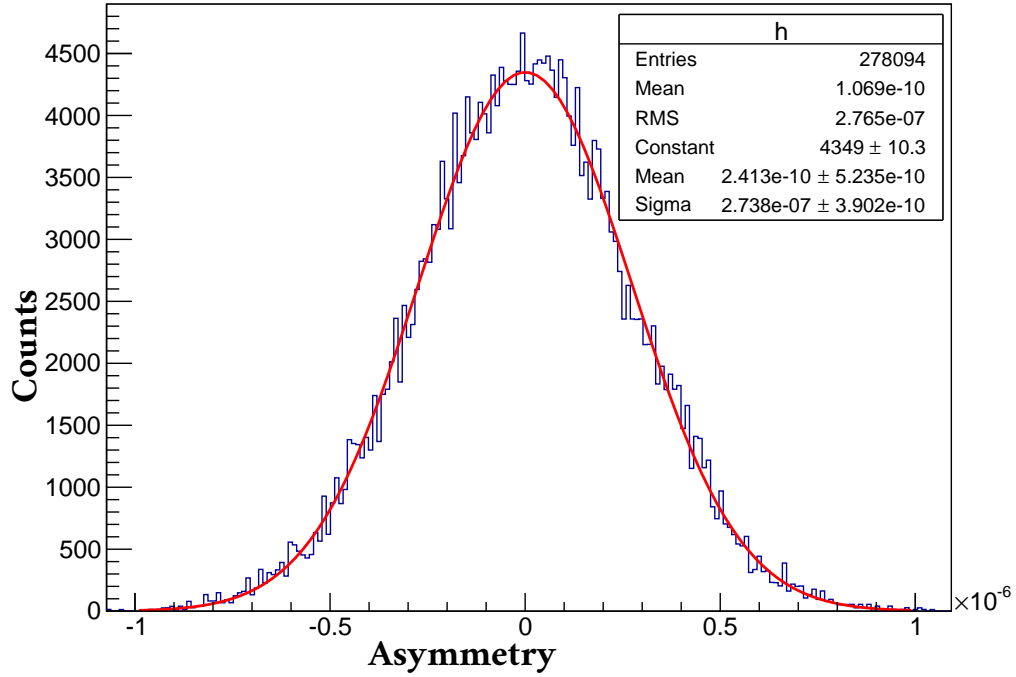


Figure 4.22: Instrumental asymmetry from one of the channels

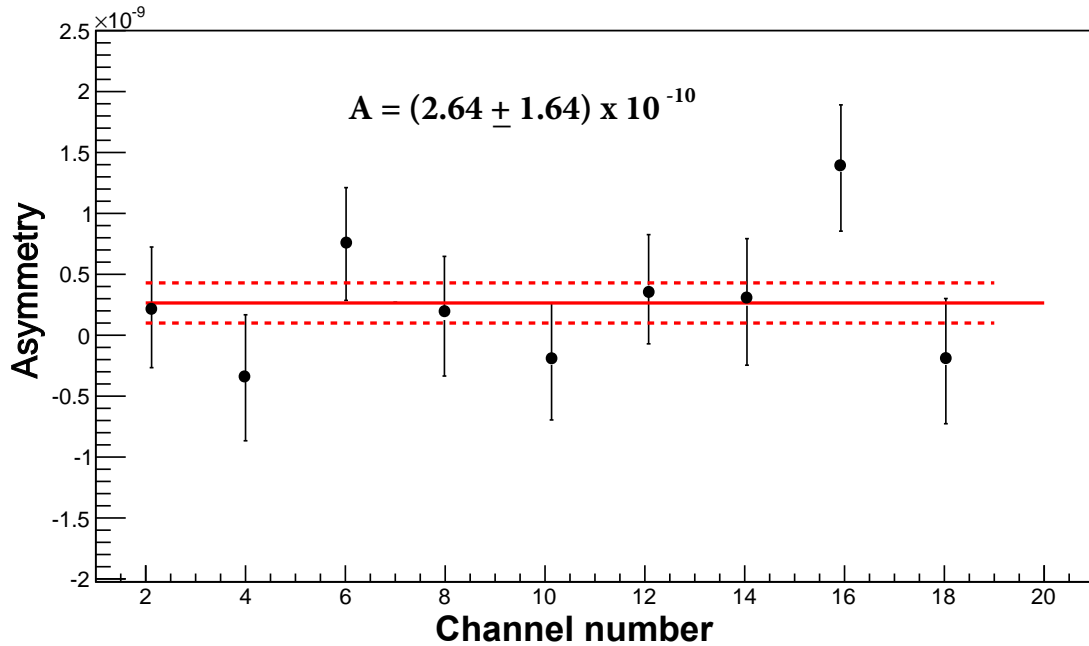


Figure 4.23: Instrumental asymmetry from different channels. The channel numbers have been reorganized in this plot.

# Chapter 5

## Simulation

---

In the experiment an ion chamber of fixed volume is used. Because of the geometry of the ion chamber (detector) and the beam, not all of the signal wires are equally sensitive to the desired physics asymmetry. This gives rise to the geometry factor for each individual signal wire, that is used to extract correct physics asymmetry from measured raw wire asymmetry. These geometry factors can not be measured experimentally and must be calculated from the simulation. Moreover, there are other motivations for doing a robust Monte Carlo simulation of the experiment, for example, optimizing the pressure of  $^3\text{He}$  in the ion chamber, determining the ionization response in each wire plane, determining the statistical error and correlations of the signals in each wire plane.

### 5.1 Geometry factors

---

For a collection of events where neutrons hitting  $^3\text{He}$  target produce protons and tritons, following Eq. 1.13 we can relate the yield in the  $i$ -th wire to the energy deposition as:

$$Y_i^h = \langle E_i(1 + hPA_p \cos \theta) \rangle, \quad (5.1)$$

where  $h$  is the neutron helicity,  $E_i$  is the energy deposition around the  $i$ -th wire by all tracks,  $\theta$  is the angle between proton momentum and neutron spin,  $P$  is the polarization and  $A_p$  is the physics asymmetry.

Now considering both helicity states we construct our measured asymmetry for the  $i$ -th wire as

$$A_m^i = \frac{Y_i^+ - Y_i^-}{Y_i^+ + Y_i^-}. \quad (5.2)$$

Invoking Eq. 5.1 this can be written as

$$A_m^i = PA_p \frac{\langle E_i \cos \theta \rangle}{\langle E_i \rangle}. \quad (5.3)$$

The factor sitting with the physics asymmetry  $A_p$  on the right hand side of the above equation is called the geometry factor. Thus, the geometry factor for the  $i$ -th wire is

$$G_i = \frac{\langle E_i \cos \theta \rangle}{\langle E_i \rangle}. \quad (5.4)$$

With this definition of the geometry factor, the physics asymmetry can be extracted from the measured asymmetry by normalizing it by the geometry factors, i.e.

$$A_p = \frac{1}{P} \frac{A_m^i}{G_i}. \quad (5.5)$$

The expectation value of  $E_i$  in Eq. 5.4 is evaluated as the sum over energy deposition  $Q_i^k$  by individual tracks of a pulse

$$\langle E_i \rangle = \sum_{k=1}^N Q_i^k. \quad (5.6)$$

So, for a collection of events the geometry factor for the  $i$ -th wire is then

$$G_i = \frac{\sum_{k=1}^N Q_i^k \cos \theta_i^k}{\sum_{k=1}^N Q_i^k}. \quad (5.7)$$

At this point two features of the experiment are taken into account:

First, the high voltage wires around the signal wire create equipotential field lines. As a result all the charges created within any particular cell (parallelepiped volume around a signal wire bounded by high voltage wires) will be collected by that particular signal wire.

Second, while we are interested in the correlation between the neutron spin and proton momentum direction, we can think of energy deposition (ionization) from the triton track as a dilution to our asymmetry. We collect energy deposition in a cell from both the proton and triton tracks.

$$G_i = \frac{\sum_{k=1}^N (Q_i^p + Q_i^t)_k \cos \theta_k}{\sum_{k=1}^N (Q_i^p + Q_i^t)_k}, \quad (5.8)$$

where  $Q_i^p$  and  $Q_i^t$  are the energies deposited in the  $i$ -th cell by proton and triton respective for any particular event and  $\theta_k$  is the angle of the proton track.

Then from a simulation point of view, in order to evaluate Eq. 5.8 we need to tabulate the energy deposited in each cell from the combination of proton and triton tracks, and the corresponding angle between proton momentum and neutron spin for any particular capture event.

We can easily infer the distribution of geometry factors across the ion chamber from the form on the right hand side of Eq. 5.8. It is illustrated in the sketch in Fig. 5.1. Since  $\theta$  is the angle between  $y$ -axis (direction of neutron spin for spin up neutrons) and the proton momentum direction, the numerator in Eq. 5.8 is positive for top rows, and negative for bottom rows.

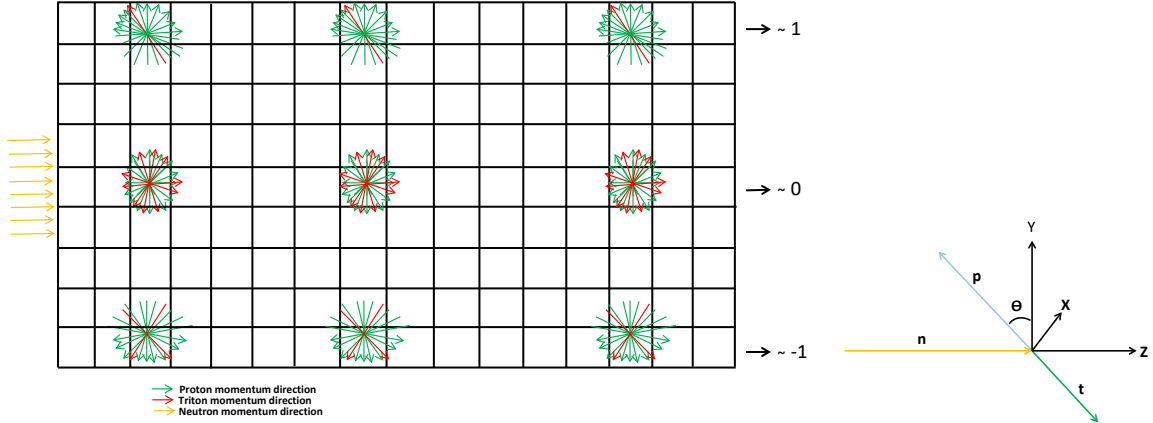


Figure 5.1: Intuitive distribution of geometric factors inside the chamber. The neutron spin direction is along the vertical axis.

This gives rise to positive geometry factors in the upper half and negative geometry factors in the lower half of the ion chamber. Because of finite collimation of the beam, in the top most rows and the bottom most rows the proton tracks are unidirectional as shown in the Fig. 5.1. Triton tracks are mostly absent from the top and bottom rows since triton will not reach the ends because of its short range. On the other hand, in the central rows the tracks are bi-directional. For central rows, we have both the proton and triton tracks coming from both above and below the cell. Thus the geometry factor is mostly washed away in the central row ( $\sim 0$ ), it is maximally positive ( $\sim 1$ ) for the top row and maximally negative ( $\sim -1$ ) for the bottom row.

## 5.2 Simulation toolkit

The Geant4 (GEometry ANd Tracking) simulation toolkit [49] (version 10.3) was used to do a robust simulation of the experiment. Geant4 is a toolkit, written in C++, for simulating the passage of particles through matter using the Monte Carlo approach. It includes a complete range of Monte Carlo functionality including tracking, geometry, physics models and hits. The physics processes offered cover a comprehensive range, including electromagnetic, hadronic and optical processes, a large set of long-lived particles, materials and elements over a wide energy range. The software provides all the tools needed for a complete Monte Carlo simulation of the experimental set-up, including modeling of geometry, detector response, event management and user interface. In Geant4 there is a wide range of physical models capable of describing interactions of particles with matter. There are several alternative models, which can be chosen by the user for many physical processes. The toolkit is developed and maintained by an international collaboration. The toolkit has become the leading simulation method for high energy physics, nuclear physics, astrophysics, space science and medical physics.

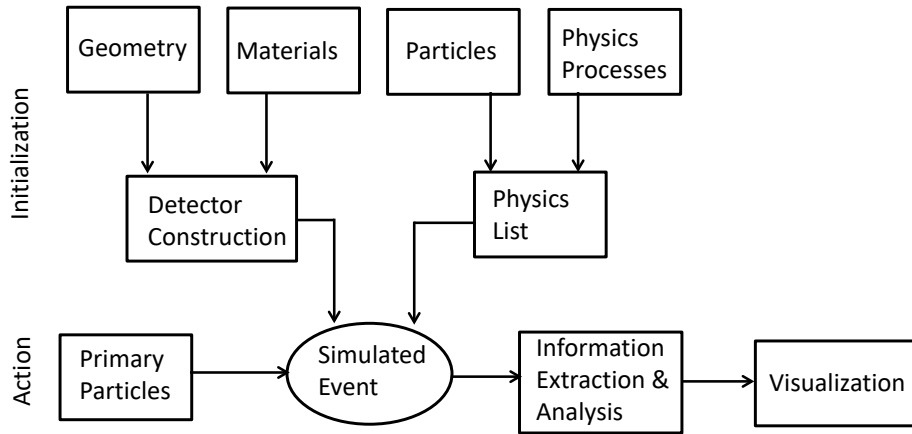


Figure 5.2: A basic simulation process flow in the Geant4

The basic simulation approach in Geant4 requires specifying the user defined geometry and materials. A set of physical models, describing interactions of particles, is included by the users to specify the physical processes in the simulation. Once those two are set, user can specify how the primary particles are generated to mimic the physical source. The Geant4 kernel transports the primaries and steps them through the geometry. The track step lengths are limited by the process with the shortest mean free path. If applicable, secondaries are generated along the track and/or at the end of the track. For stopped particles, the final state and any final products are calculated based on the processes and models that were registered for the particles. The user can interact with the kernel to get all the desired information associated with the tracks and particles. Along the track, the energy deposition and change in momentum can be extracted. The user also has access to the final state energy, momentum, positions etc.

### 5.3 Geometry and materials

For simplicity, only the inner active part of the ion chamber is modeled in the geometry. Other components taken into account in the geometry are the exit of the beam guide and the collimator. To construct the inner active portion of the ion chamber, a three dimensional box of dimension  $30.4 \text{ cm} \times 16 \text{ cm} \times 16 \text{ cm}$  is used. We refer to Fig. 3.10 for the dimensions and geometry of the ion chamber. To construct the active charge collection volume around any signal wire a parallelepiped volume of dimension  $16 \text{ cm} \times 1.9 \text{ cm} \times 1.9 \text{ cm}$  is considered. This volume represents one signal wire with the surrounding charge collection area. Nine of such volumes, stacked on top of each other (along Y axis), represent a signal layer of the ion chamber. Such a signal layer is then repeated 16 times along the Z axis to model the 16 signal layers



inside the chamber. The parallelepiped volumes corresponding to the end signal wires have slightly smaller vertical width than others.

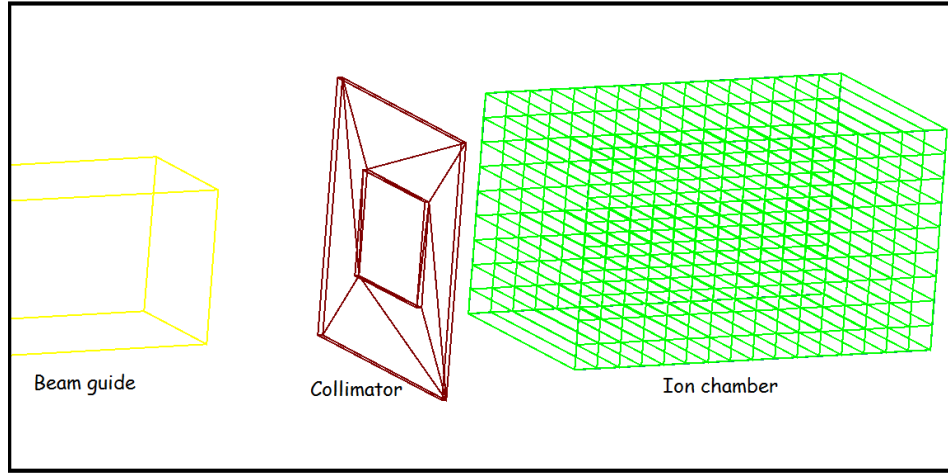


Figure 5.3: A simplified geometry of the setup

The volume was filled with 100%  $^3\text{He}$  gas. To construct the  $^3\text{He}$  material inside the chamber, an isotope was constructed with atomic number  $Z = 2$ , atomic weight  $a = 3.0160293201$  g/mole and mass number  $A = 3$ . The density of  $^3\text{He}$  inside the chamber was calculated in the following way: In the experiment the target chamber is filled with 100%  $^3\text{He}$  with a pressure of 0.47 atm at room temperature. Assuming that  $^3\text{He}$  is an ideal gas, the ideal gas relation  $PV = nRT$  can be used to calculate the density of  $^3\text{He}$ .

$$\rho = \frac{m}{V} = \frac{PM}{RT}, \quad (5.9)$$

where

$m$  = mass of  $^3\text{He}$  gas in the ion chamber,

$M$  = atomic mass of  $^3\text{He} = 3.0160293201$  gm/mole,

$P$  = pressure of the ion chamber = 0.47 atm,

$T$  = filling temperature = 298 K,

$R$  = molar gas constant =  $82.057338(47)$   $\text{cm}^3 \text{ atm K}^{-1} \text{ mol}^{-1}$ .

Using these values, we get density of  $^3\text{He}$ ,  $\rho = 5.796952 \times 10^{-5}$  g/cm $^3$ .

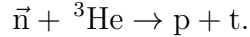
Each of the parallelepiped volume, filled with  $^3\text{He}$  is registered in the Geant4 kernel as a sensitive volume, which allows access to the energy deposited. The other component of the geometry, the collimator, was made of Lithium-6 and has an opening of  $10 \text{ cm} \times 8.2 \text{ cm}$  in the default setting. The beam exit has a dimension of  $10 \text{ cm} \times 12 \text{ cm}$ . The distance between the beam exit and the center of the chamber is 165 cm and the collimator is 2.5 cm away from the first window of the chamber.

## 5.4 Physics list

---

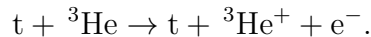
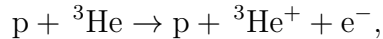
Out of many possible physics processes, three processes are relevant for our experiment:

- The neutron absorption reaction:



This is an inelastic hadronic process. Implementation of this hadronic process requires registering it in the Geant4 kernel, choosing a suitable model, and incorporating the appropriate cross section data set. The relevant Geant4 class used for this process is `G4NeutronInelasticProcess`. The High Precision (HP) model was used, with the relevant Geant4 class `G4ParticleHPInelastic`. The corresponding data comes from the class `G4ParticleHPInelasticData`, which incorporates the ENDF/B-VII (repackaged in `G4NDL`) cross-section and final state data.

- The energy loss of the proton and triton through ionization of the  ${}^3\text{He}$  atoms. This happens through the interaction with atomic electrons when the proton and triton travel inside the ion chamber:



This is an electromagnetic process and the relevant class is `G4hIonisation`. This class is responsible for ionization of any charged particle.

- The transportation process that applies to all the primaries (neutrons) and secondaries (protons and tritons) is activated using the class `G4Transportation`. This process transports particles through the detector geometry.

For completeness, other processes registered are as follows:

Neutron: Elastic, capture, thermal neutron scattering, radioactive decay, fission.

Proton: Elastic, bremsstrahlung

Triton: Elastic, hadronic inelastic, radioactive decay.

Gamma, electron, positron and alpha: Standard electromagnetic processes.

Instead of using a custom physics list, the same identical result was achieved while using the Geant4 reference physics list `QGSP_BERT_HP`. It has all the required setup with the collection of models – Quark Gluon String (QGS) model, Precomputed (P) model used for de-excitation, Bertini-style cascade (BERT) and High Precision (HP) neutron model. The list `QGSP_BERT_HP` is widely used and recommended for low energy nuclear physics simulation.

**Effect of temperature:**

The density of helium defines the energy-range relationship of the outgoing particles. In calculating the density of  $^3\text{He}$  in the simulation in Eq. 5.9, we used  $T = 298$  K. For fixed volume, the density does not depend on the temperature. It is possible to set the temperature in the constructor of the Geant4 material definition, which is optional. If this temperature is set above 0 K, the High Precision (HP) model takes into account  $^3\text{He}$  thermal motion and associated boosts which lead to the wrong angular distribution of outgoing momentum in our case. This optional temperature was set to 0 K in our simulation to calculate the geometry factors.

## 5.5 Primary particles: Neutron beam profile

---

Once the detector geometry and physics processes are set, the final step of the implementation process is to generate the correct primary events, which in this case is the correct neutron beam profile. Construction of the neutron beam profile is done in the following two steps:

- Neutron energy distribution: The beam monitor-1 (M1) signal was used to generate the neutron energy profile at the detector position.
- Neutron spatial profile: The beam scan data was used to get the neutron's position distribution in the xy plane at the front edge of the detector.

### 5.5.1 Neutron energy distribution

We are interested in neutron flux as a function of energy at the detector position, while the monitor-1 (M1) signal is a voltage proportional to the beam intensity at the beam exit position. Getting the correct energy distribution at the detector position from the M1 signal involves several steps.

The first thing to consider is, the M1 signal that we see is a convolved signal of current pulse and wraparound from previous pulses. But the ion chamber receives the unconvolved spectrum i.e. the reaction cross-section depends on the energy of the individual neutron. So, instead of the ordinary convolved signal, we use the unconvolved (image) M1 signal (chopped). We make the unconvolved M1 signal following the algorithm explained in the section 2.4.2 and use that as the reference signal instead of the regular M1 signal.

The next step is to propagate the M1 signal at the detector position. The pulse will shift as it travels from the M1 position to the detector position. We start with the M1 signal as a function of the time of flight (TOF). Now the time of flight window at the M1 position is (AC.1):

$$\begin{aligned} \text{TOF}_{min} &= 13.94 \times 10^{-3} \text{ sec,} \\ \text{TOF}_{max} &= 30.17 \times 10^{-3} \text{ sec,} \end{aligned}$$

spanned over 1624 equally spaced M1 TOF bins.

This TOF was tuned using  $T_0$  delay so that we have full pulse at the detector position. Another way to propagate the M1 signal at the detector position is to utilize the Bragg peak. The shift in Bragg peak from first layer of the ion chamber to the last layer is known from the detector signal. This information with the measured M1 to detector distance can be used to propagate the M1 signal at the detector position.

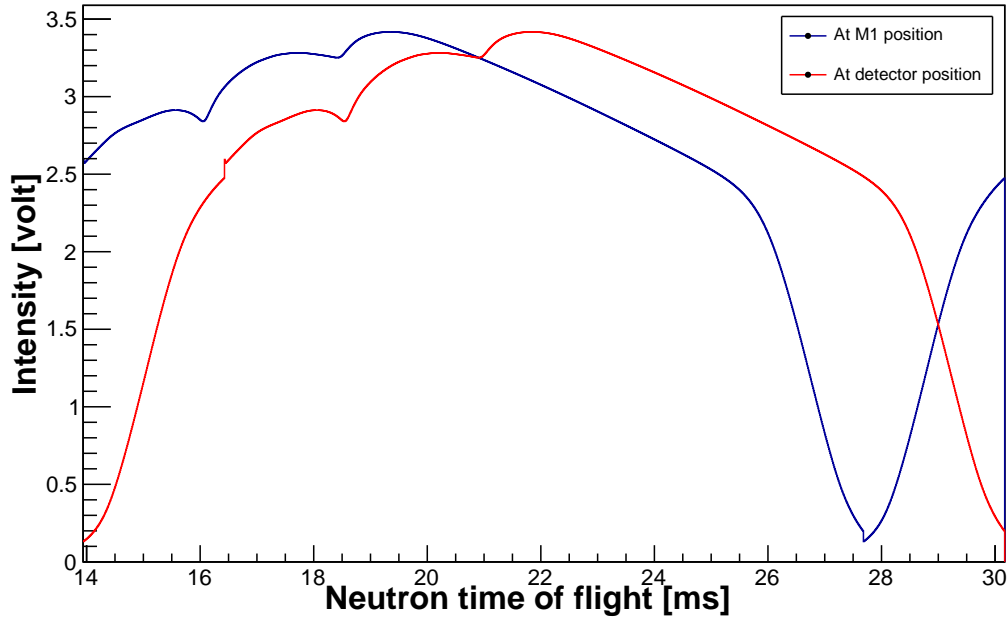


Figure 5.4: Propagating the unconvoluted M1 signal at the detector position

The M1 signal is represented as a function of wave length using de Broglie's equation

$$\lambda = \frac{h}{p} = \frac{h}{m_n v} = \frac{h}{m_n \frac{d}{t}} = \frac{ht}{m_n d}, \quad (5.10)$$

where  $t$  is the time of flight,  $d = 18$  m is the distance traveled and  $m_n$  is the neutron mass. Using the corresponding values, we get the wavelength window (AC.1)

$$\lambda_n^{min} = 3.064 \text{ \AA},$$

$$\lambda_n^{max} = 6.63 \text{ \AA}.$$

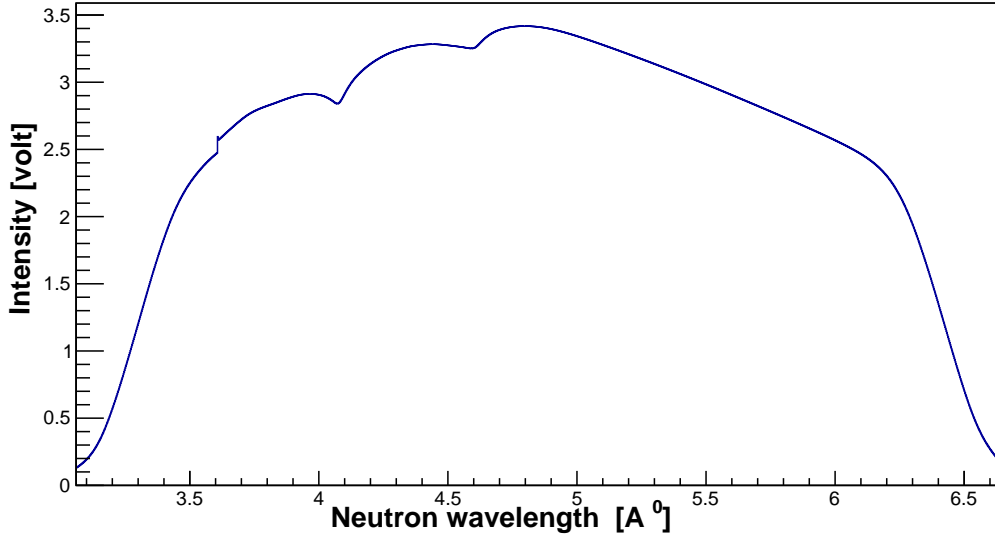


Figure 5.5: Unconvoluted M1 signal at the detector position as a function of the wavelength

Next, we consider the wavelength or energy dependence of the cross section. The M1 monitor contains helium gas and the yield we see comes from neutron capture in the helium gas. This yield depends on the number of neutrons captured or specifically on capture cross section. But we are interested in the original neutron flux. Now, for thermal neutrons (in the  $1/v$  region), the absorption cross-section increases as the velocity (kinetic energy) of the neutron decreases, i.e.

$$\sigma_a \sim \frac{1}{v} \sim TOF \sim \frac{1}{\sqrt{E}}. \quad (5.11)$$

The yield in M1 depends on both the neutron flux and the capture cross section,

$$Y \sim \sigma_a \times \Phi_n,$$

where  $\Phi_n$  is the neutron flux which we are interested in and  $Y$  is the yield in M1.

So the correct weight for the neutron flux at the detector position is achieved by attenuating the M1 signal by a factor proportional to the TOF:

$$\Phi_n \sim \frac{Y}{\sigma_n} \sim \frac{Y}{TOF}.$$

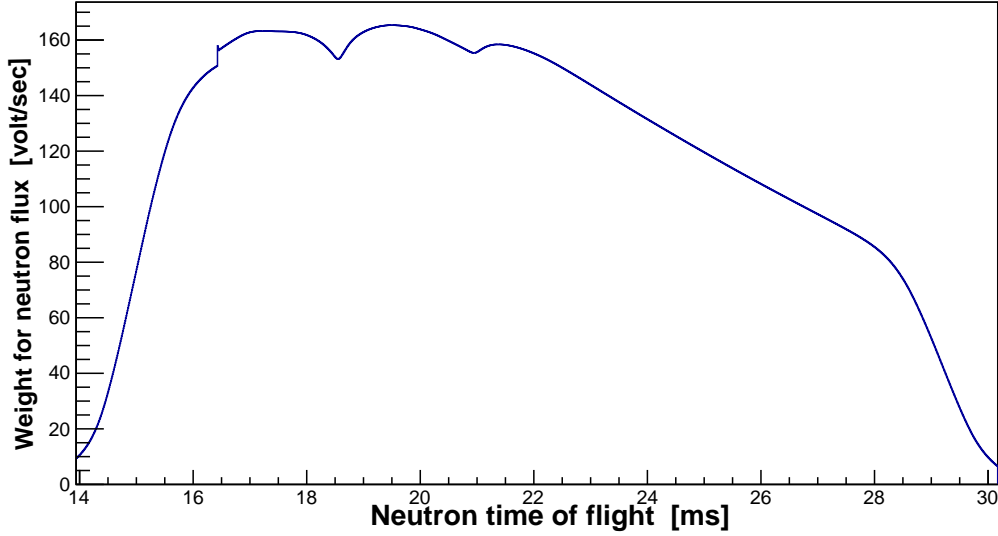


Figure 5.6: Corrected unconvoluted M1 signal at the detector position

For the simulation, we need neutron flux as a function of energy. To go to the energy domain from time of flight domain, we use the relations,

Neutron velocity,  $v = \frac{d}{t}$  And neutron energy,  $E_n = \frac{1}{2}m_n v^2$ .

Plugging in the corresponding values we get (AC.1)

$$E_n^{max} = 8.716 \text{ meV},$$

$$E_n^{min} = 1.861 \text{ meV}.$$

This range spans over 1624 bins for our desired window. The distribution (in Fig. 5.7) is now peaked near lower energies and falls quickly at higher energies. This happens for non-linear dependence of energy on the time of flight. This distribution is used to generate primary neutrons of different energies in the simulation.

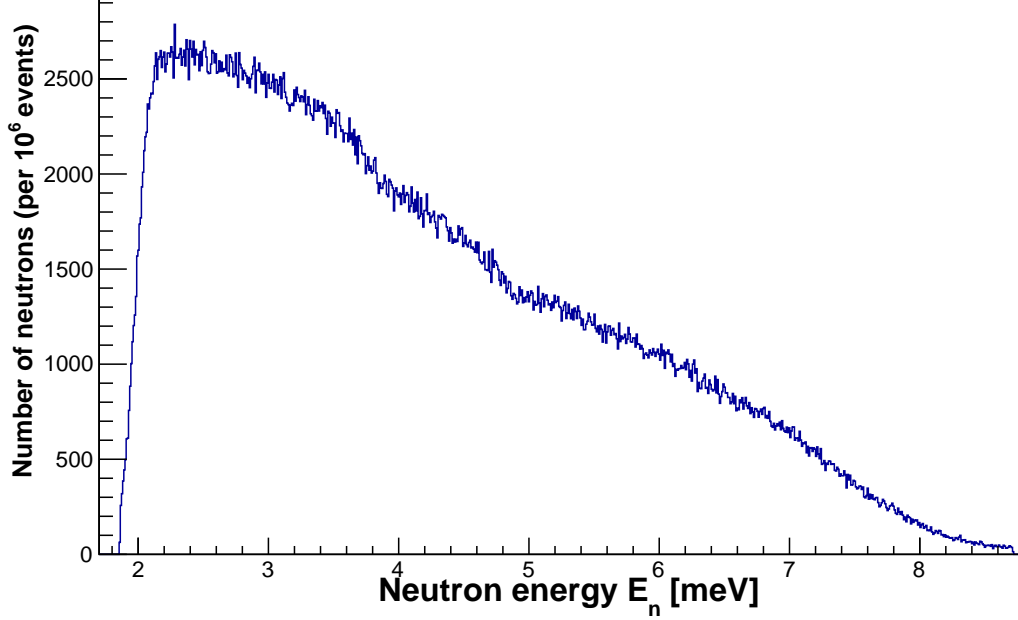


Figure 5.7: Generated neutron energy distribution

### 5.5.2 Neutron spatial profile

The beam divergence spreads out in the  $xy$  plane as it propagates along the  $z$ -axis. We know the spatial beam profile from the beam scan in the upstream and downstream positions explained in section 2.4.3. Fig. 2.30 shows the neutron spatial beam profile at upstream position. The upstream beam scan data was used as input to generate the position of the neutron on the  $xy$  plane at the front of the detector. Neutrons with spatial coordinates which fall outside of the collimator opening are blocked by the collimator, and only neutrons having  $(x, y)$  coordinate within the opening will pass through to the ion chamber. Once the neutrons outside the opening are removed, the spatial distribution is shown in Fig. 5.8. To facilitate generation of the neutron's energy with the distribution of Fig. 5.7, and spatial  $(x, y)$  coordinates with the distribution of Fig. 2.30, the data analysis framework ROOT [50] was integrated into Geant4. The distributions (5.7) and (2.30) were used as input for TH1D and TH2D classes to generate numbers that follow those distributions. Once the geometry, physics list and primary particles all were set, a test run (with 200 primaries for example) produced the simulated events with tracks shown in Fig. 5.9.

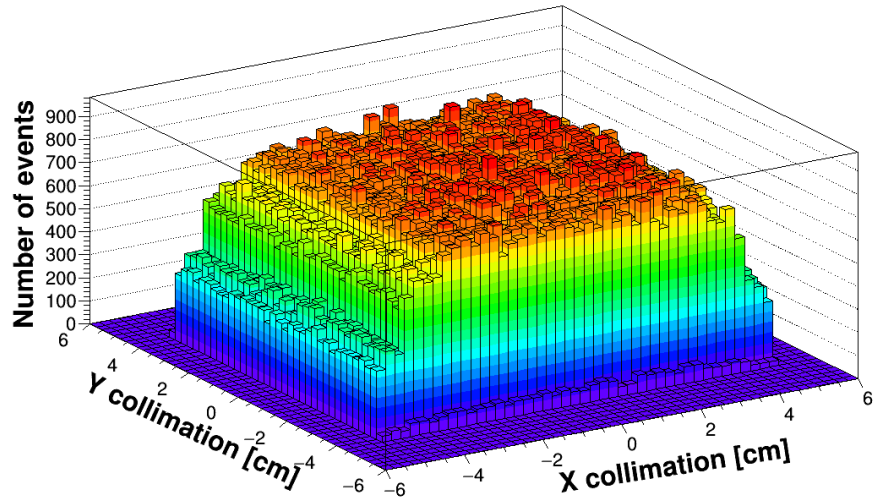


Figure 5.8: Neutron position distribution on the  $xy$  plane from simulation after collimation (default collimation). Total  $10^6$  primary events are considered.

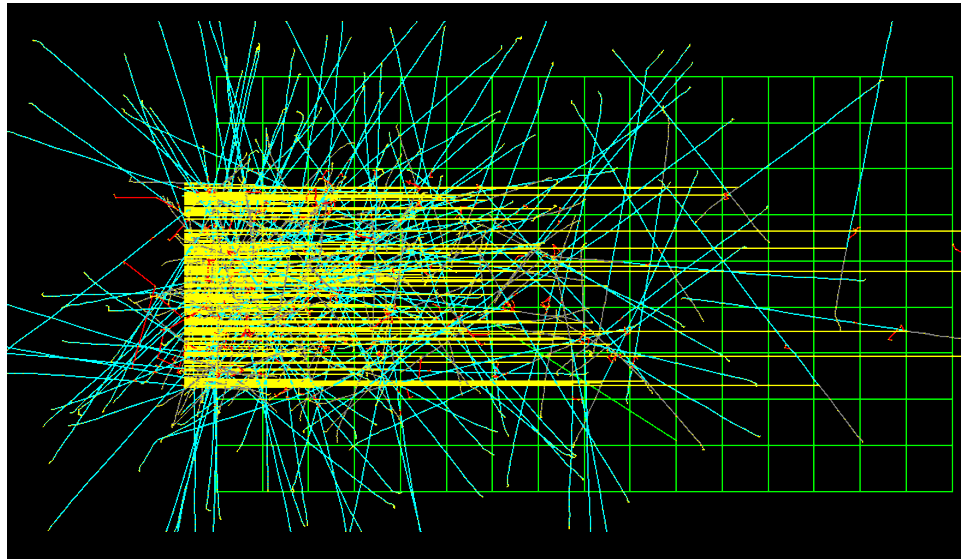


Figure 5.9: Example of simulated capture events (2D view) inside the chamber. Yellow tracks are neutrons, blue tracks are protons and gray tracks are tritons. Also visible, few red tracks which are electrons, and green tracks which are gammas.



## 5.6 Validation of the simulation

---

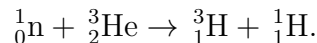
The simulation was validated using the following benchmarks:

1. Conservation of energy.
2. Cross section comparison.
3. Energy dependence of the cross section.
4. Comparison of the stopping power with PSTAR and SRIM.
4. Energy range relationship comparison with PSTAR and SRIM.
6. The angular distribution of the outgoing particle momenta.
7. Comparison of yields with the data.
8. Comparison with the collimation scan data.

In the following subsections each of the validation attempts is discussed.

### 5.6.1 The conservation of energy

The neutron is absorbed in the helium filled ion chamber according to the reaction



The theoretical Q-value for this reaction is already known from the resulting mass change.

The masses of the reactants are

$${}^1_0\text{n} = 1.008665 \text{ amu},$$

$${}^3_2\text{He} = 3.01603 \text{ amu},$$

$${}^3_1\text{H} = 3.01605,$$

$${}^1_1\text{H} = 1.007825 \text{ amu}.$$

Binding energy of  $e^- = 0.14 \text{ eV}$  ( $1.5 \times 10^{-8} \text{ amu}$ ).

So the resulting mass change is

$$\Delta m = 1.008665 + 3.01603 - 3.01605 - 1.007825 - 2 \times 1.5 \times 10^{-8} = 0.0008199 \text{ amu}.$$

Thus, the Q-value =  $0.0008199 \times 931.5 \text{ MeV} = 763.74 \text{ keV}$ .

$$E_p = 573 \text{ keV},$$

$$E_t = 191 \text{ keV}.$$

So in the simulation we would expect proton and triton to come out always with this initial energy. Fig. 5.10 shows that this is precisely the case in the simulation.

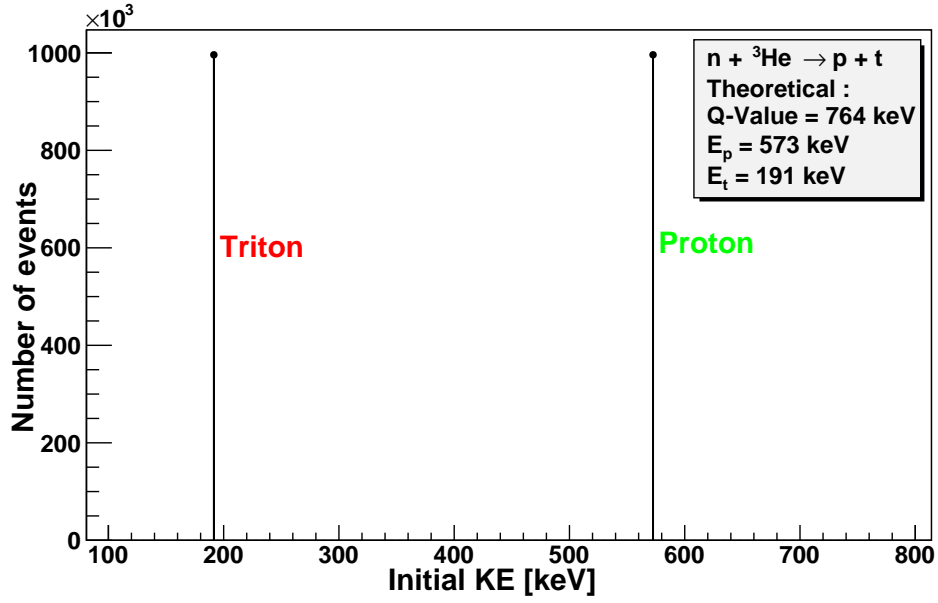


Figure 5.10: Initial kinetic energy of proton and triton in the simulation. Total  $10^6$  events are considered.

### 5.6.2 Cross section comparison

Next, we verified the reaction depth or capture cross section. In the simulation we kept track of the number of captures as a function of the distance inside the chamber. To extract the cross section value from this information, we note that the number of surviving neutrons at position  $x$  inside the chamber is related to the capture cross section as –

$$I'(x) = I_0 e^{-N\sigma x}, \quad (5.12)$$

where

$N$  = Density of the nuclei in the volume (nuclei/cm<sup>3</sup>),

$\sigma$  = The capture cross section (barn =  $10^{-28}$  m<sup>2</sup>),

$I_0$  = Initial beam intensity (cm<sup>-2</sup>s<sup>-1</sup>),

$I'(x)$  = Beam intensity at distance  $x$ , The prime is to indicate surviving neutrons.

The number of neutrons captured per unit length is [53],

$$I(x) = I_0 e^{-N\sigma x} N\sigma. \quad (5.13)$$

Linearizing the equation we write

$$\ln I(x) = -N\sigma x + \ln(I_0 N\sigma). \quad (5.14)$$

Using Eq. 5.9,  $N = 12.3092559 \times 10^{18}$  nuclei cm<sup>-3</sup>. In a linear fit for  $\ln I(x)$  the slope and constant from that fit correspond to  $-N\sigma_n$  and  $\ln(I_0 N\sigma)$  respectively, so

that

$$\sigma = \frac{-Slope}{N}.$$

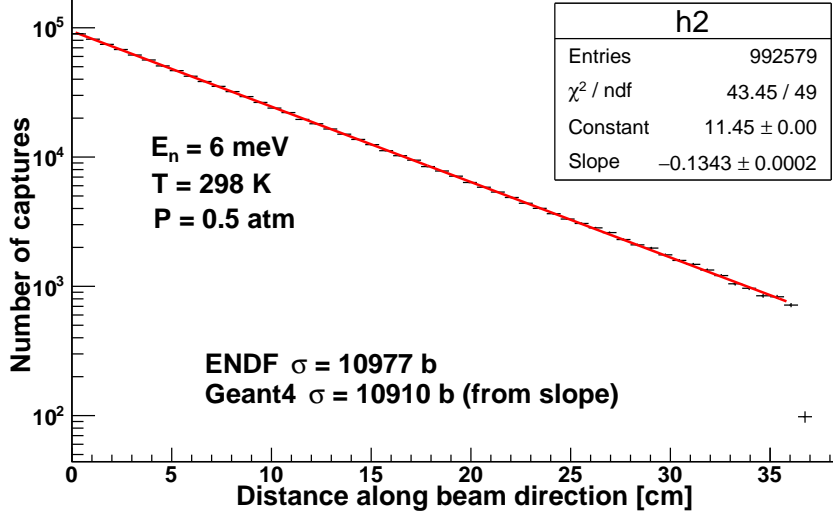


Figure 5.11: Capture cross section from the simulation with pencil beam. Target is at room temperature. The cross section from the simulation is compared with ENDF cross section value.

For example, from the simulation for 6 meV neutrons and  $10^6$  number of incident primary neutrons in Fig. 5.11 we get slope =  $-0.1343 \text{ cm}^{-1}$  and constant = 11.45. This gives

$$\sigma_{\text{Sim}} = \frac{0.1343 \text{ cm}^{-1}}{12.3092559 \times 10^{18} \text{ cm}^{-3}},$$

$$\sigma_{\text{Sim}} = 10.910 \times 10^3 \text{ barn},$$

which can be compared with available cross section data from different nuclear physics databases for the same neutron energy. Here, we compared with the data from ENDF database, found on JANIS web, for 6 meV incident neutrons

$$\sigma_{\text{ENDF}} = 10.977 \times 10^3 \text{ barn}.$$

Also,  $\ln(I_0 N \sigma) = 11.81$  (calculated) can be compared with the constant from the fit, which is 11.45.

### 5.6.3 Energy dependence of the cross section

The simulation used thermal neutrons of energies 1.861 meV to 8.716 meV. The reaction cross section depends on neutron energy. Here in Fig. 5.12, we check if the cross section falls off as  $\frac{1}{\sqrt{E}}$ .

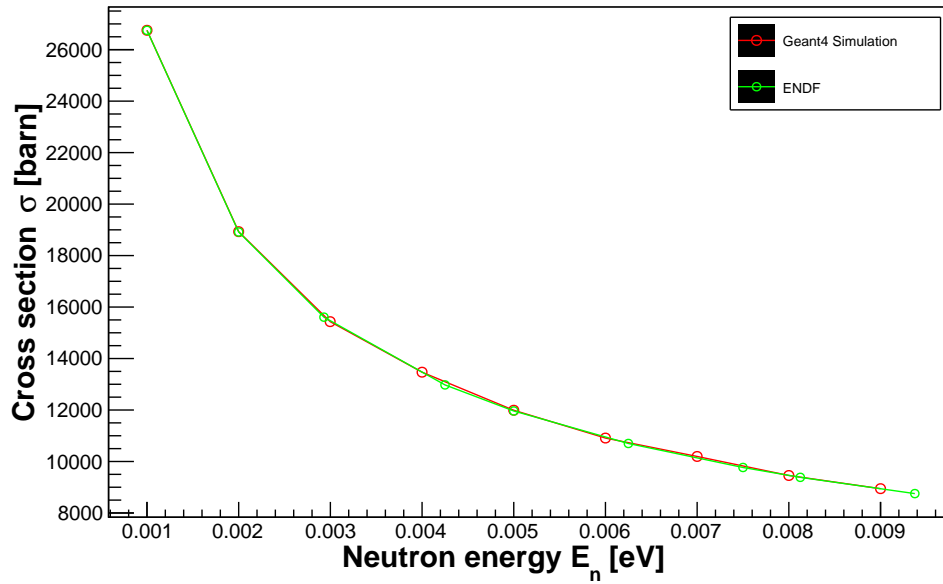


Figure 5.12: ENDF vs Geant4 cross section comparison for different thermal energies

In the  $\frac{1}{v}$  region the slope of  $\log\sigma$  vs  $\log E_n$  has a value of -0.5, as verified in Fig. 5.13.

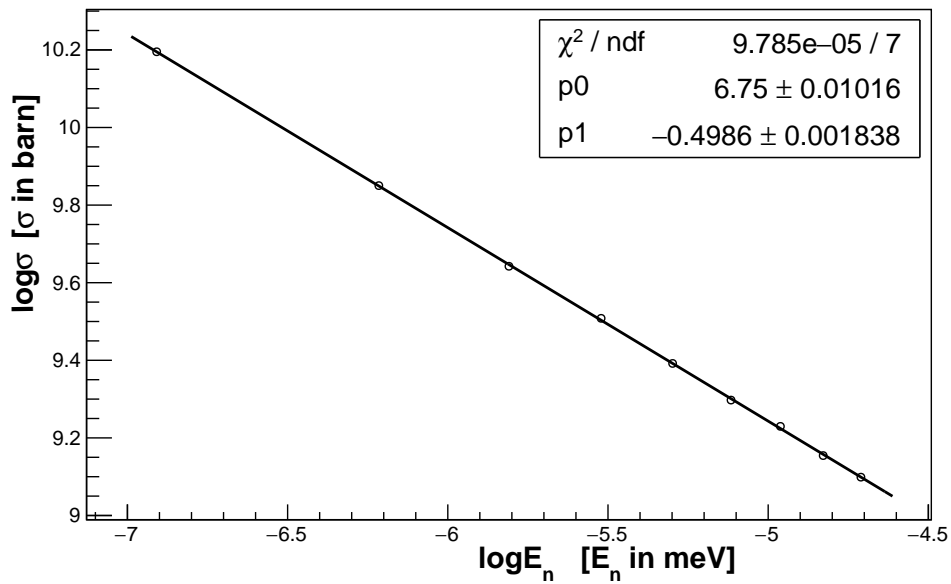


Figure 5.13:  $\frac{1}{\sqrt{E}}$  dependence of cross section from the simulation

### 5.6.4 The stopping power and ionization curve

One of the most important parameters for the simulation or experiment is the stopping power or the energy loss per unit length of the proton and triton as they travel through the ion chamber. Since the production of an ion pair requires a fixed amount of energy, the density of ionization is proportional to the stopping power.

Our next validation compared the energy loss per unit length with available data. Here we compared with the PSTAR data from the NIST database and with the data from the simulation program SRIM (SRIM.org).

At first we consider the PSTAR data. There are couple of points to be considered here. First of all, we have data for the material  $^4\text{He}$ , not for  $^3\text{He}$ . Next, PSTAR gives data for the proton as the incident particle, not the triton. To resolve the first issue we go back to Bethe-Bloch formula. For heavy charged particles ( $m_{\text{incident}} \gg m_e$ ), the rate of energy loss due to collisions with electrons is given by the Bethe-Bloch formula [51],[52] Eq. 3.20. It depends on the number density of stopping material which, for gaseous a material, depends on the pressure and temperature; the mass of the nuclei of the material is irrelevant for electronic processes. Thus we use  $^4\text{He}$  data for  $^3\text{He}$  ( $Z = 2$  for both). However, since  $-\frac{dE}{dx}$  or the range ( $R$ ) are usually mentioned in units of MeV cm<sup>2</sup>/g (for  $-\frac{dE}{dx}$ ) and g/cm<sup>3</sup> (for  $R$ ), we need to multiply or divide by the appropriate mass density to get them in units of MeV/cm and cm respectively.

For the triton, it is possible to interpolate  $-\frac{dE}{dx}$  and  $R$  in the medium  $^4\text{He}$  from the PSTAR data for the proton. To do that, we again refer to Bethe-Bloch formula in Eq. 3.20 and note that the energy loss per unit length depends on the speed (or energy) of the projectile particle. So a proton and triton with the same velocity will give the same  $-\frac{dE}{dx}$ .

Since a triton is three times heavier than a proton, i.e.  $m_t = 3m_p$ , if the triton and proton have same velocity, triton will be three times more energetic, i.e  $\text{KE}_t = 3\text{KE}_p$ . So

$$\left[ \frac{dE_p}{dx} \right]_{E=E_0} = \left[ \frac{dE_t}{dx} \right]_{E=3E_0}. \quad (5.15)$$

Next, to get the range of the triton we note that, the range is related to  $-\frac{dE}{dx}$  as follows:

For the proton range,

$$R_p = \int_0^{E_p} \left[ -\frac{dE_p}{dx} \right]^{-1} dE_p, \quad (5.16)$$

and for the triton range,

$$R_t = \int_0^{E_t} \left[ -\frac{dE_t}{dx} \right]^{-1} dE_t,$$

$$R_t(E_t) = \int_0^{E_t} \frac{dE_t}{-\frac{dE_t}{dx}(E_t)},$$

$$R_t(E_t) = \int_0^{E_t} \frac{dE_t}{-\frac{dE_p}{dx}\left(\frac{E_t}{3}\right)},$$

where we have used the relation in Eq. 5.15.

$$R_t(E_t) = 3 \int_0^{E_t} \frac{\frac{dE_t}{3}}{-\frac{dE_p}{dx}\left(\frac{E_t}{3}\right)}.$$

Now, we make a change of variable,  $u = \frac{E_t}{3}$ , so that,  $du = \frac{dE_t}{3}$  when  $E_t = 0$ ,  $u=0$ , and when  $E_t = E_t$ ,  $u = \frac{E_t}{3} = u$ , so that

$$R_t(E_t) = 3 \int_0^u \frac{du}{-\frac{dE_p}{dx}(u)} = 3R_p(u),$$

$$R_t(E_t) = 3R_p\left(\frac{E_t}{3}\right),$$

or

$$R_t(E) = 3R_p\left(\frac{E}{3}\right). \quad (5.17)$$

So the conclusion is, to get  $-\frac{dE_t}{dx}$  at energy E for a triton, we need to pick the value of  $-\frac{dE_p}{dx}$  at  $\frac{E}{3}$  from the table for a proton. And to get  $R_t$  at energy E from proton data, we need to pick the value of  $R_p$  at  $\frac{E}{3}$  and multiply it by 3.

For data from the SRIM program, it follows its own simulation/transformation to produce data for protons and tritons in  $^3\text{He}$ . Thus a comparison with SRIM also provides a means to validate our scaling relations in Eq. 5.15 and 5.17. Fig. 5.14 compares energy loss per unit length of proton in  $^3\text{He}$  as predicted by our simulation with that from the PSTAR data and SRIM.

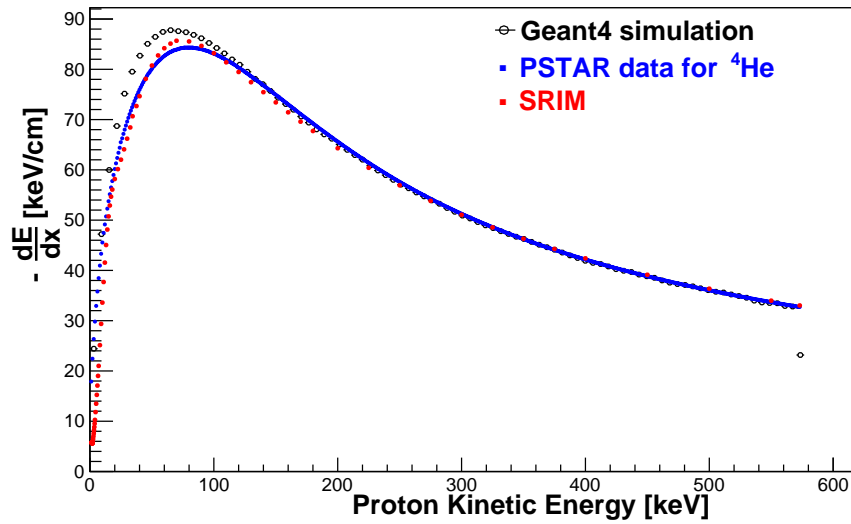


Figure 5.14: Proton stopping power as a function of the kinetic energy from the Geant4 simulation, PSTAR data and SRIM. The target is at room temperature (298K) and 0.47 atm pressure.

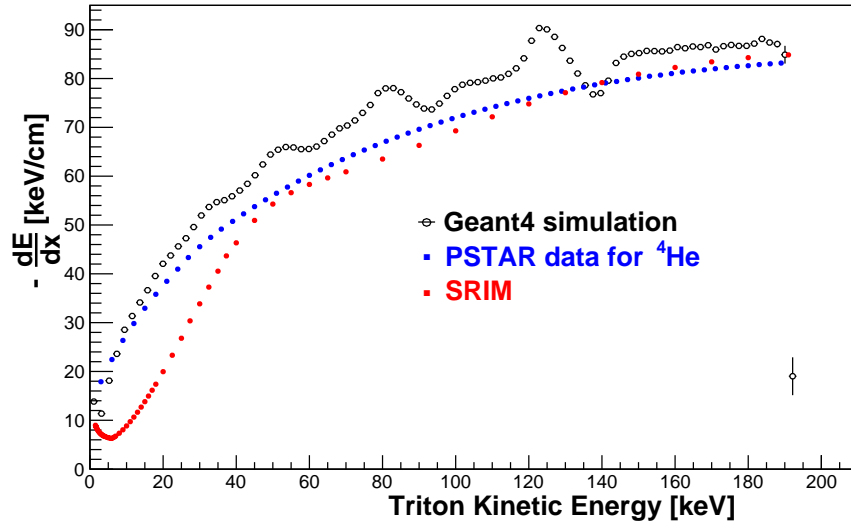


Figure 5.15: Triton stopping power as a function of the kinetic energy from the simulation, PSTAR data and SRIM. The target is at room temperature (298K) and 0.47 atm pressure.

Fig. 5.15 compares energy loss per unit length of triton in  $^3\text{He}$  as predicted by our simulation with that from the PSTAR data and SRIM. Fig. 5.16 shows  $-\frac{dE_t}{dx}$  as a function of distance from the vertex. In all cases the triton data for PSTAR was evaluated from proton using the scaling relation in Eqs. 5.15 and 5.17.

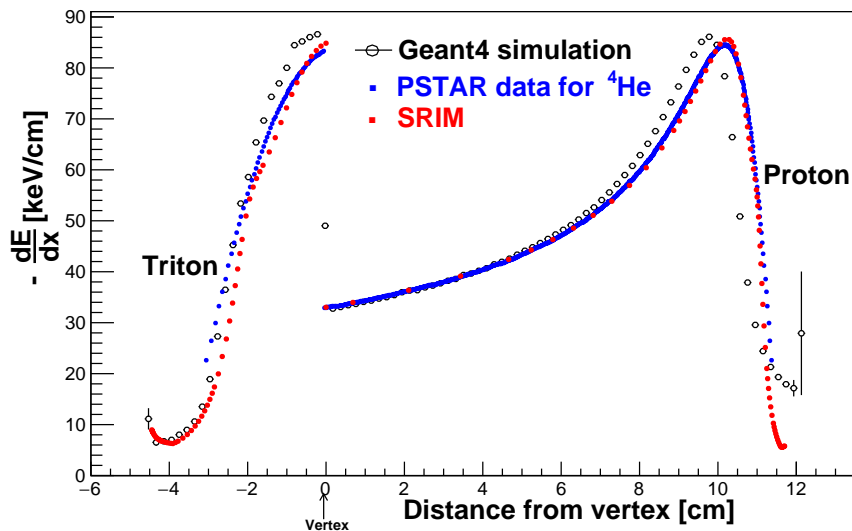


Figure 5.16: The ionization curve from the simulation, PSTAR data and SRIM. The target is at room temperature (298K) and 0.47 atm pressure.



### 5.6.5 The energy range relationship

Most of the transport calculations and Monte Carlo simulations for the calculation of range are based on the Continuous Slowing Down Approximation (CSDA). In this approximation, it is assumed that the particle loses its energy in a continuous way and at a rate equal to the stopping power. Thus, the CSDA range is calculated using Eq. 5.17. The CSDA range is the path length traveled by the particle. Since the particle's path is usually not straight due to scattering, the CSDA range is always higher than projected range, which is the distance between the point where the particle enters the stopping medium and the point where the particle is absorbed (or comes to rest), projected onto the original direction of travel. SRIM uses the PRAL (Projected Range ALgorithm) equations for calculating the projected range.

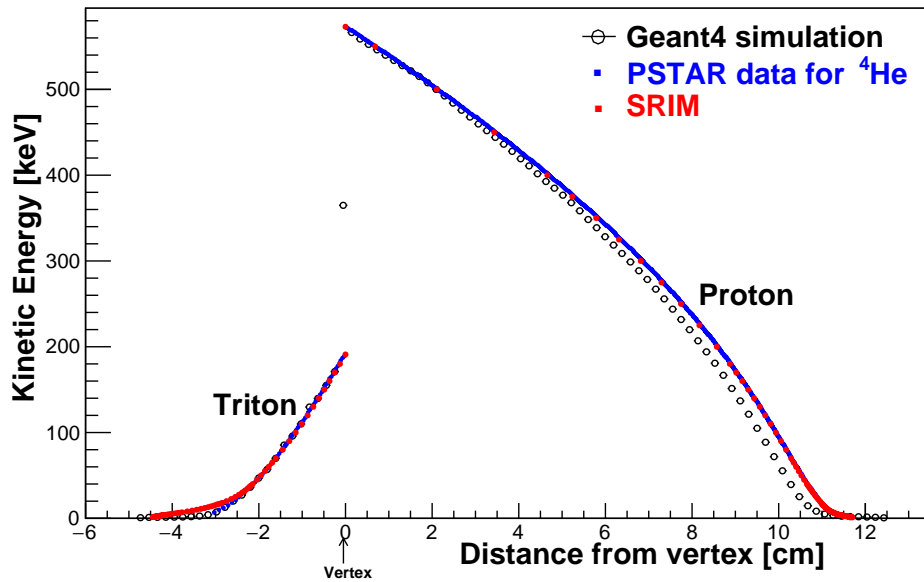


Figure 5.17: Comparison of proton and triton energy vs distance in  $^3\text{He}$  after the reaction from the simulation with the PSTAR data and SRIM.

In our energy regime both the CSDA and projected ranges in the PSTAR tables are very close. Here we used the CSDA range from the PSTAR data and the range for the triton was evaluated from the proton data using the scaling relation in Eq. 5.17. Here, we note that while both the PSTAR and SRIM data are provided as actual range, but we plot in Fig. 5.16 and 5.17 as the residual range with respect to the vertex to emulate our reaction inside the ion chamber.

## 5.6.6 The angular distribution of tracks

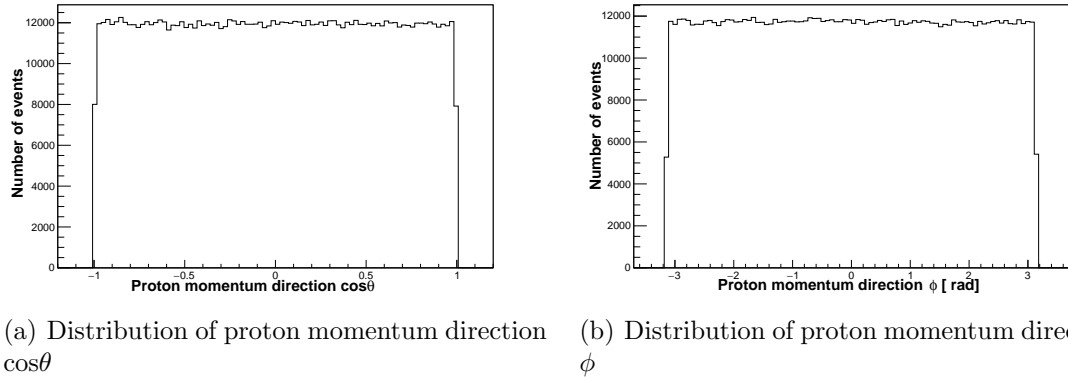


Figure 5.18: Proton momentum angular distribution from the simulation. Total primary events considered  $10^6$ .

Next, we verify the angular distribution of outgoing proton and triton momenta. Fig. 5.18 shows distribution of polar angle  $\theta$  and azimuthal angle  $\phi$  of the outgoing proton's momentum. Fig. 5.19 shows the same thing for the triton momentum. In both cases the  $\cos\theta$  and  $\phi$  distributions are isotropic.

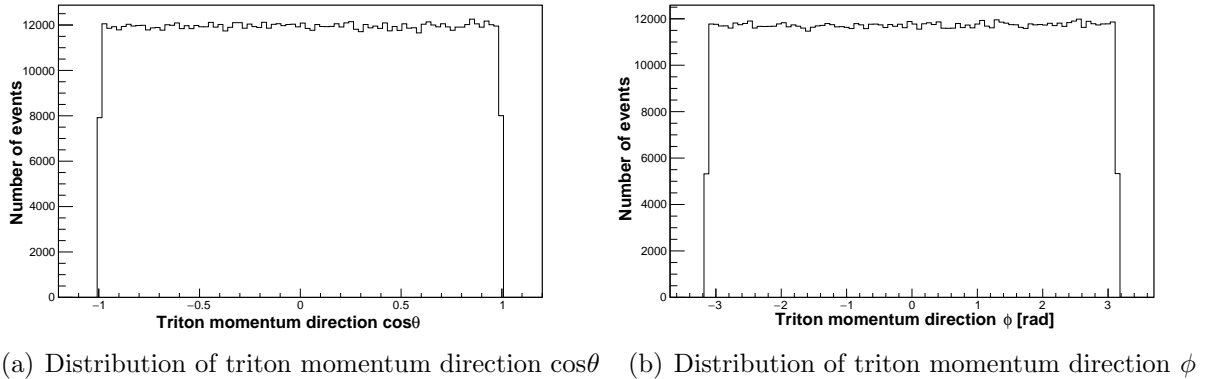
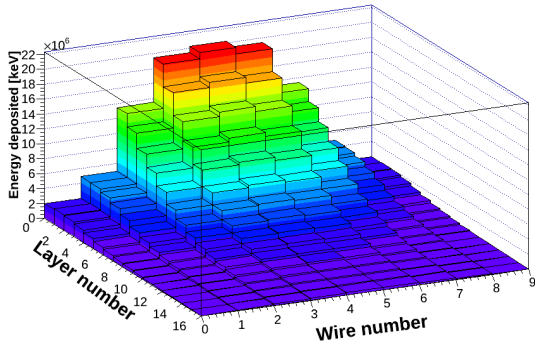


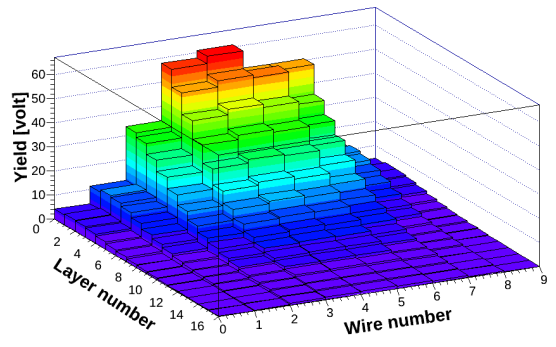
Figure 5.19: Triton momentum angular distribution from the simulation for  $10^6$  primary events.

## 5.6.7 Comparison of yield

We compare the yield from the simulation with that of the  $n$ - $^3\text{He}$  data. Fig. 5.20(a) is the simulated yield distribution inside the chamber with the default  $n$ - $^3\text{He}$  collimation setting, compared with the yield distribution from a typical  $n$ - $^3\text{He}$  run as shown on Fig. 5.20 (b) with the same collimation. In Fig. 5.20, since the yield from the



(a) Yield distribution from the simulation



(b) Yield distribution form typical  $n\text{-}^3\text{He}$  data

Figure 5.20: Yield distribution in the ion chamber from the simulation and typical  $n\text{-}^3\text{He}$  run data.

simulation and the  $n\text{-}^3\text{He}$  data are in different units, we compare the distribution in normalized yields in Fig. 5.21. The wires numbered 6 and 7 in the first layer are bad.

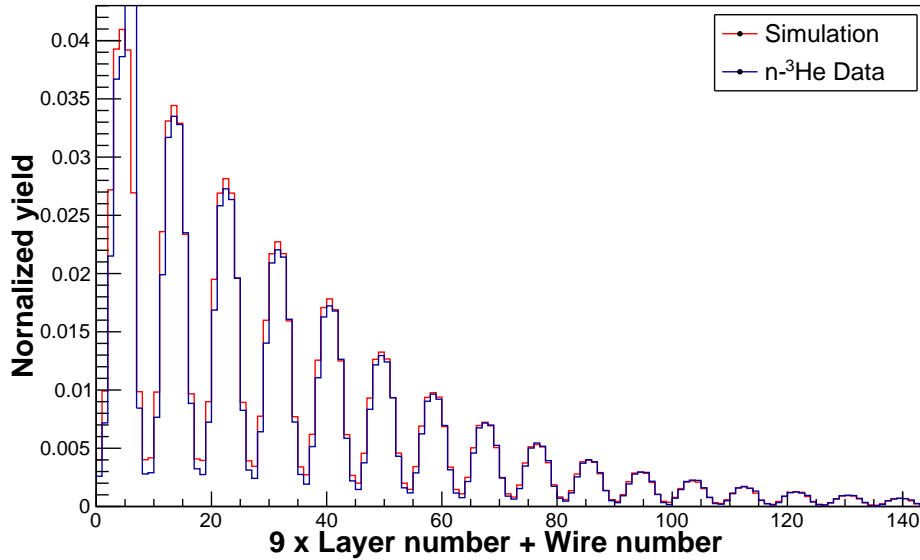
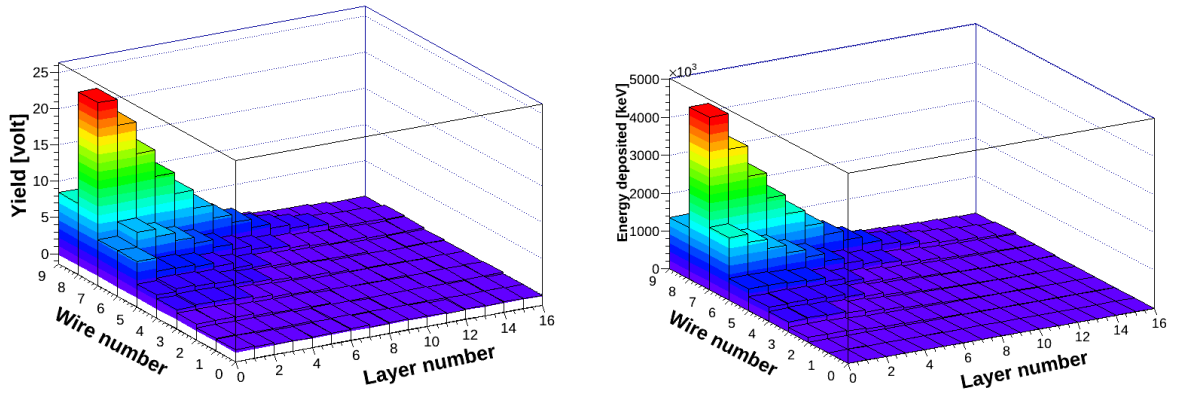


Figure 5.21: Yield distribution in the ion chamber from the simulation and typical  $n\text{-}^3\text{He}$  data.

### 5.6.8 Comparison with beam scan data

Here, we compare the yield in the chamber from the collimation scan data with that from the simulation with same collimation setting. In the summer of 2015, we took collimation scan data (run numbers 37987 - 38022) which includes both vertical and horizontal scans.



(a) Yield distribution from the data for the collimation scan: run# 37990

(b) Yield distribution from the simulation for collimation scan: run# 37990

Figure 5.22: Yield distribution in the ion chamber from the simulation and the data for the collimation scan: run# 37990

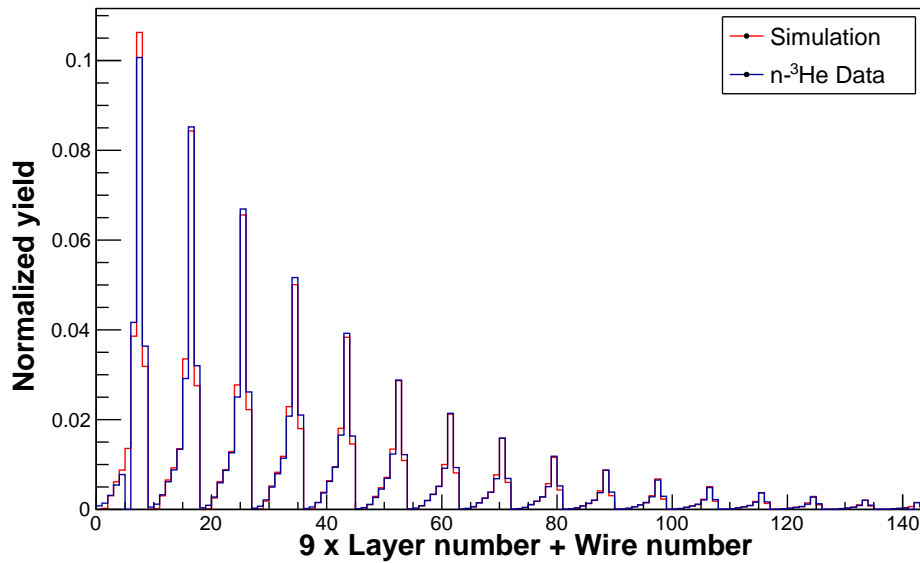
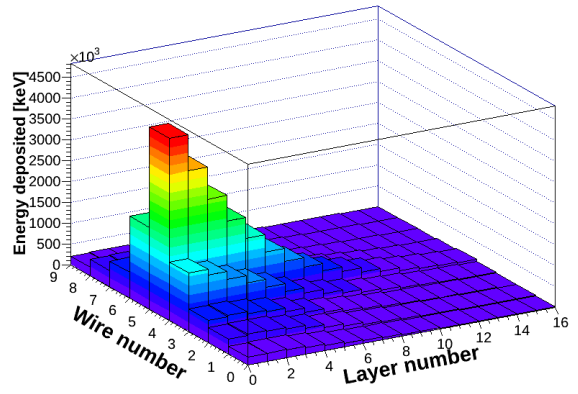
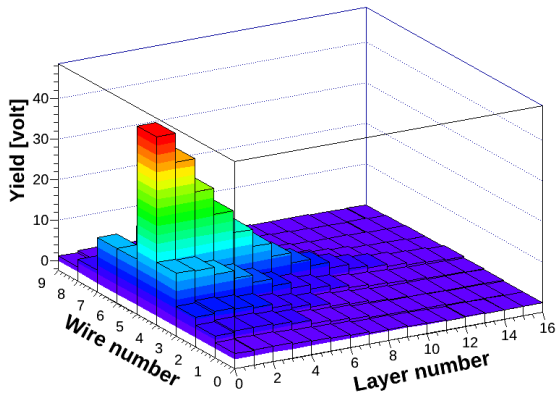


Figure 5.23: Yield distribution in the ion chamber from the simulation and the data for the collimation scan: run# 37990



(a) Yield distribution from the data for the collima-  
tion scan: run# 38000

(b) Yield distribution from the simulation for the  
collimation scan: run# 38000

Figure 5.24: Yield distribution in the ion chamber from the simulation and the data for the collimation scan: run# 38000

For the vertical scan, the x-collimation position was fixed with a width of 10 cm, and the y-collimation width was 2 cm with position varying from top to bottom wire. Fig. 5.22 and 5.23 compare a scan that covers one of the top wires. Figs. 5.24 and (5.25) compare scan data in which y-collimator illuminates one of the middle wires (wire 5).

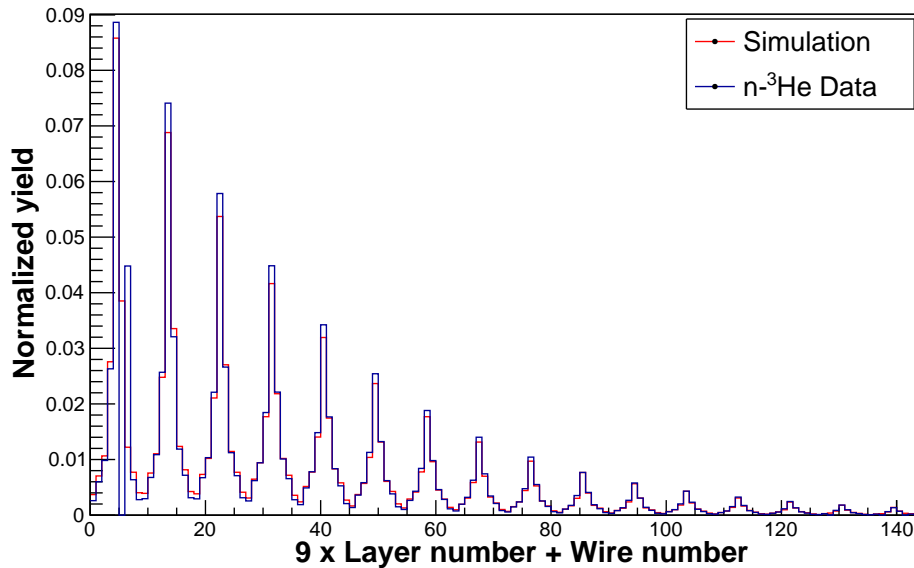
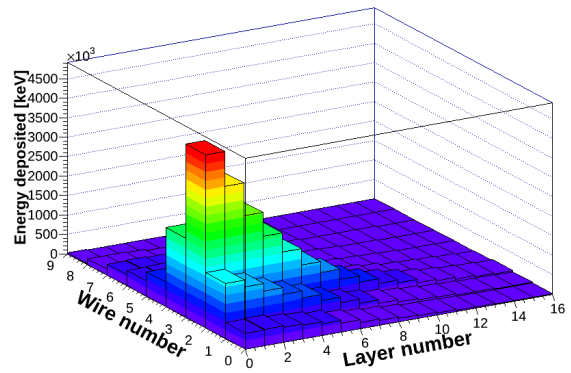
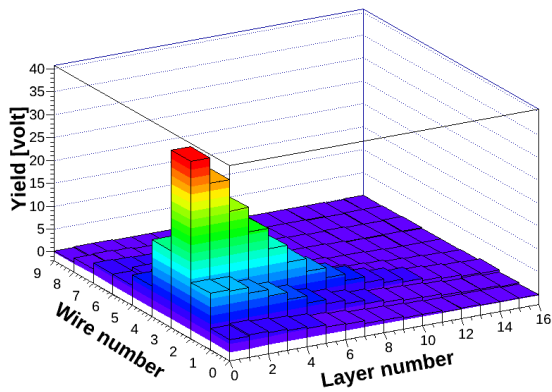


Figure 5.25: Yield distribution in the ion chamber from the simulation and the data for the collimation scan: run# 38000



(a) Yield distribution from the data for the collimation scan: run# 38006

(b) Yield distribution from the simulation for the collimation scan: run# 38006

Figure 5.26: Yield distribution in the ion chamber from the simulation and the data for the collimation scan: run# 38006

Figs. 5.26 and 5.27 compare scan data (run number 38006) in which the y-collimator illuminates one of the bottom wires.

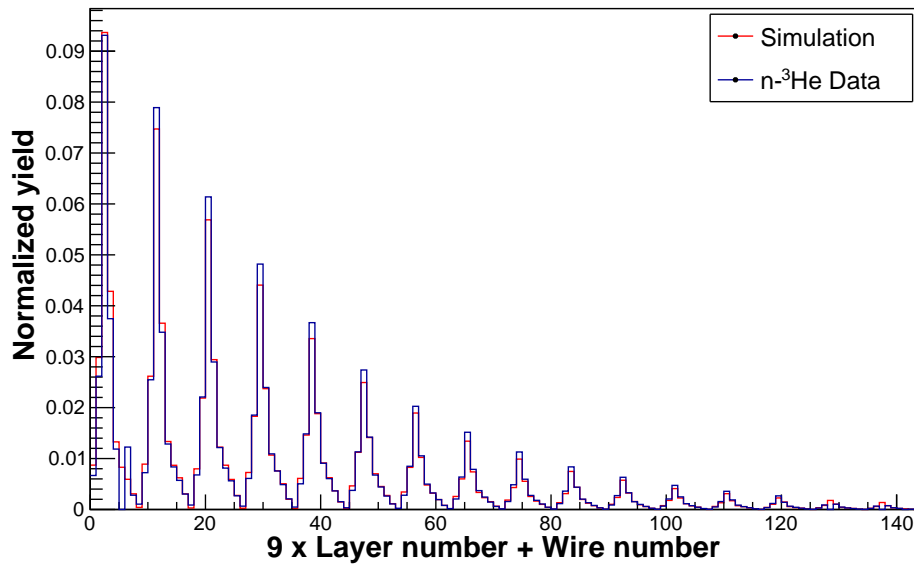


Figure 5.27: Yield distribution in the ion chamber from the simulation and the data for the collimation scan: run# 38006

## 5.7 Outcome from the simulation

Once we are satisfied with all the validation tests, we calculate the geometry factors from the simulation using Eq. 5.7. Fig. 5.28 shows the distribution of the geometry factors for all 144 wires. The uncertainties in various measured parameters, used as input in the simulation contribute to the uncertainty in our estimation of the geometry factors. Fig. 5.29 shows the the worst possible deviation of the geometry factors from our best calculated values. Systematic effects associated with the geometry factor calculation are discussed in section 6.5.

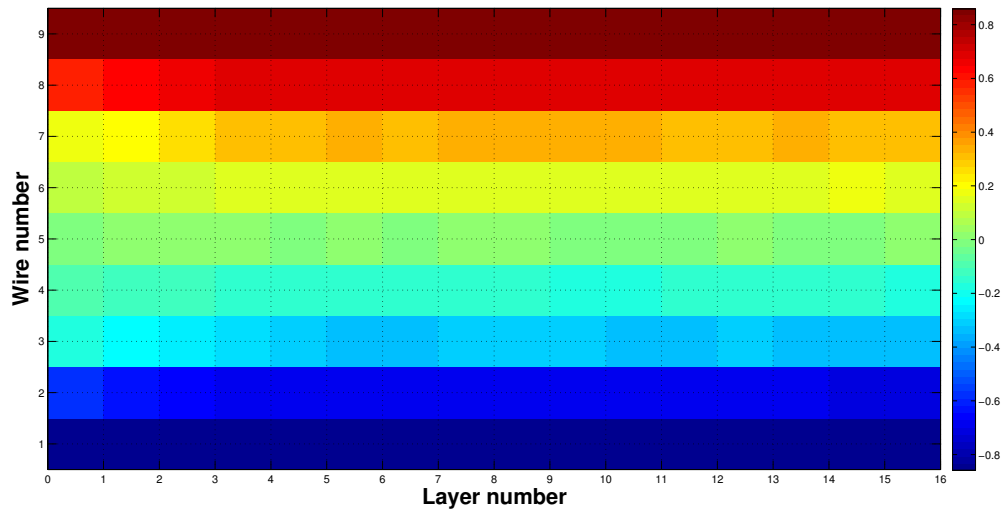


Figure 5.28: The distribution of the geometry factors for all the signal wires

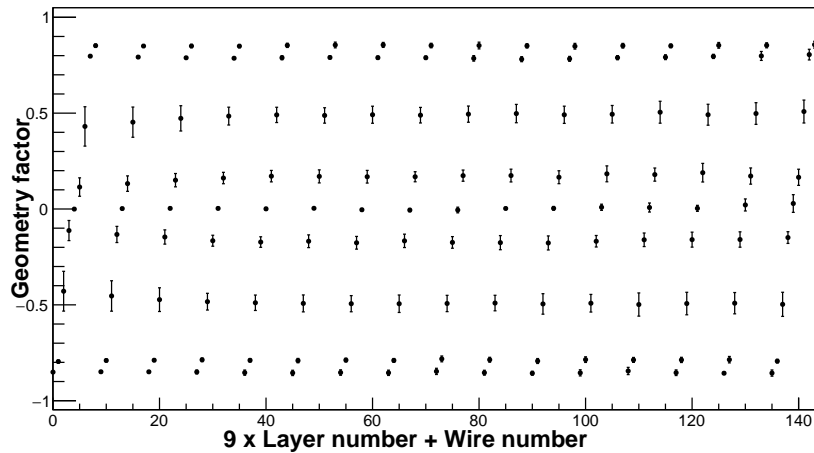


Figure 5.29: The geometry factors with errors

# Chapter 6

## Data analysis

---

In more than one year of data taking, we acquired around 46000 runs, each run having a duration of about seven minutes. Here, we present the analysis of the entire n-<sup>3</sup>He dataset, both the LR and UD measurement. We first present different possible avenues to analyze the data and argue why we chose a particular one over the others. We also discuss the basis of our data selection. We first analyze the LR data and then analyze the UD data. One important aspect of our signals is that they are correlated. We discuss the approach to correct for correlation as they appear. The data analysis presented here exclusively uses the data summary files explained in section 4.4.

### 6.1 Data analysis method

---

#### 6.1.1 Asymmetry definition

Following Eq. 1.13, we write our measured observable, the yield in k-th signal wire, as

$$Y_k = I_0 \epsilon_k (1 + PG_k^{pc} A_{pc} + PG_k^{pv} A_{pv}) + b_k, \quad (6.1)$$

where,  $I_0$  is the initial SNS beam intensity,  $\epsilon_k$  is the wire efficiency,  $G_k$  is the geometry factor,  $A_{pc}$  is the parity conserving physics asymmetry,  $A_{pv}$  is the parity violating physics asymmetry, and  $b_k$  is the pedestal or its associated electronic noise.

Since the alignment of the detector makes the yield sensitive either to the parity conserving or parity violating physics asymmetry, we represent the physics asymmetry as  $A_p$  to indicate either the PC or PV physics asymmetry.

$$Y_k = I_0 \epsilon_k (1 + PG_k A_p) + b_k \quad (6.2)$$

In the experiment we consider two step spin sequences ( $\uparrow\downarrow$ ).

$$Y_k^\uparrow = I_0^\uparrow \epsilon_k (1 + P^\uparrow G_k A_p) + b_k^\uparrow, \quad (6.3)$$



$$Y_k^\downarrow = I_0^\downarrow \epsilon_k (1 + P^\downarrow G_k A_p) + b_k^\downarrow. \quad (6.4)$$

As the spin flipper efficiency is high and stable, we can take,  $P^\uparrow \approx -P^\downarrow = P$ , then

$$Y_k^\uparrow = I_0^\uparrow \epsilon_k (1 + P G_k A_p) + b_k^\uparrow, \quad (6.5)$$

$$Y_k^\downarrow = I_0^\downarrow \epsilon_k (1 - P G_k A_p) + b_k^\downarrow. \quad (6.6)$$

There are several avenues that can be followed to extract the physics asymmetry  $A_p$  using these observables. Each approach has some advantages over the other.

1) Spin asymmetry: The most obvious one is to consider the spin asymmetry

$$A_k^s = \frac{Y_k^\uparrow - Y_k^\downarrow}{Y_k^\uparrow + Y_k^\downarrow}, \quad (6.7)$$

where the superscript  $s$  indicates spin asymmetry. Using Eq. 6.5 and Eq. 6.6 this can be written as

$$A_k^s = \frac{(I_0^\uparrow + I_0^\downarrow) P G_k A_p + (I_0^\uparrow - I_0^\downarrow)}{(I_0^\uparrow + I_0^\downarrow) + P G_k (I_0^\uparrow - I_0^\downarrow) + (b_k^\uparrow + b_k^\downarrow)/\epsilon_k} + \frac{b_k^\uparrow - b_k^\downarrow}{Y_k^\uparrow + Y_k^\downarrow}. \quad (6.8)$$

Now, since  $(I_0^\uparrow + I_0^\downarrow) \gg P G_k (I_0^\uparrow - I_0^\downarrow) + (b_k^\uparrow + b_k^\downarrow)/\epsilon_k$ , Eq. 6.8 can be simplified further as

$$A_k^s = P G_k A_p + \frac{(I_0^\uparrow - I_0^\downarrow)}{(I_0^\uparrow + I_0^\downarrow)} + \frac{b_k^\uparrow - b_k^\downarrow}{Y_k^\uparrow + Y_k^\downarrow}. \quad (6.9)$$

In Eq. 6.9, we can easily identify the first term as the contribution from the physics asymmetry, the second term as the beam asymmetry and the third term as the instrumental asymmetry.

In the experiment,  $b_k^\uparrow \approx b_k^\downarrow = b_k$  i.e. the instrumental asymmetry is significantly smaller than the physics asymmetry contribution. This statement is also verified by measuring the instrumental asymmetry with no beam data. In that case

$$A_k^s = P G_k A_p + \frac{(I_0^\uparrow - I_0^\downarrow)}{(I_0^\uparrow + I_0^\downarrow)}. \quad (6.10)$$

Eq. 6.10 shows that this approach works best with very stable beam power. However, as shown in section (6.1.4), we have significant beam fluctuations. This demands some approach that will cancel the beam fluctuations.

2) Asymmetry with normalized yields: To cancel the beam asymmetry we normalize the yield by the beam intensity. From Eq. 6.5 and Eq. 6.6, we construct the modified yields as

$$\mathcal{Y}_k^\uparrow = \frac{Y_k^\uparrow - b_k}{I^\uparrow}, \quad (6.11)$$

$$\mathcal{Y}_k^\downarrow = \frac{Y_k^\downarrow - b_k}{I^\downarrow}, \quad (6.12)$$

where  $I^\uparrow$  or  $I^\downarrow$  is an estimate for (proportional to) the total beam intensity. Here, we assume  $b_k^\uparrow \approx b_k^\downarrow = b_k$  as before. In the experiment the M1 monitor uses only a fraction of the beam to measure the beam intensity. So, instead of the M1 signal we use a sum over all the detector signals as a measure of the beam intensity, i.e.

$$I^\uparrow = \sum_k (Y_k^\uparrow - b_k), \quad (6.13)$$

$$I^\downarrow = \sum_k (Y_k^\downarrow - b_k). \quad (6.14)$$

Now we can easily relate  $I^\uparrow$  and  $I^\downarrow$  to  $I_0^\uparrow$  and  $I_0^\downarrow$  respectively, as

$$\begin{aligned} I^\uparrow &= \sum_k (Y_k^\uparrow - b_k) \\ &= I_0^\uparrow \sum_k \epsilon_k (1 + PG_k A_p) \\ &= I_0^\uparrow \left[ \sum_{k=1}^{144} \epsilon_k + \sum_{i=1}^{64} (\epsilon_i PG_i A_p + \epsilon_{i^*} PG_{i^*} A_p) + \sum_{j=1}^{16} \epsilon_j PG_j A_p \right], \end{aligned}$$

where  $k$  is the single wire index,  $i$  is the pair of wire index with  $i^*$  being the conjugate wire and  $j$  is the index for the central wires.

Now, we utilize the symmetry of the detector and invoke the fact that  $G_i \approx -G_{i^*}$ ,  $\epsilon_i \approx \epsilon_{i^*}$  and  $G_j \approx 0$ . This gives

$$I^\uparrow \approx I_0^\uparrow \sum_k \epsilon_k = KI_0^\uparrow.$$

Similarly,

$$I^\downarrow \approx I_0^\downarrow \sum_k \epsilon_k = KI_0^\downarrow,$$

where,  $K$  is a constant,

$$K = \sum_k \epsilon_k .$$

We construct the asymmetry from these modified yields as

$$A_k^n = \frac{\mathcal{Y}_k^\uparrow - \mathcal{Y}_k^\downarrow}{\mathcal{Y}_k^\uparrow + \mathcal{Y}_k^\downarrow}, \quad (6.15)$$

where the superscript  $n$  indicates asymmetry constructed from yields which are normalized by sum over all detectors' signal.

Now,

$$\begin{aligned}
A_k^n &= \frac{\frac{Y_k^\uparrow - b_k}{I^\uparrow} - \frac{Y_k^\downarrow - b_k}{I^\downarrow}}{\frac{Y_k^\uparrow - b_k}{I^\uparrow} + \frac{Y_k^\downarrow - b_k}{I^\downarrow}} \\
&= \frac{\frac{Y_k^\uparrow - b_k}{KI_0^\uparrow} - \frac{Y_k^\downarrow - b_k}{KI_0^\downarrow}}{\frac{Y_k^\uparrow - b_k}{KI_0^\uparrow} + \frac{Y_k^\downarrow - b_k}{KI_0^\downarrow}} \\
&= \frac{\frac{Y_k^\uparrow - b_k}{I_0^\uparrow} - \frac{Y_k^\downarrow - b_k}{I_0^\downarrow}}{\frac{Y_k^\uparrow - b_k}{I_0^\uparrow} + \frac{Y_k^\downarrow - b_k}{I_0^\downarrow}}.
\end{aligned}$$

Using Eq. 6.11 and Eq. 6.12 this reduces to

$$A_k^n = \frac{\epsilon_k(1 + PG_k A_p) - \epsilon_k(1 - PG_k A_p)}{\epsilon_k(1 + PG_k A_p) + \epsilon_k(1 - PG_k A_p)}. \quad (6.16)$$

$$A_k^n = PG_k A_p \quad (6.17)$$

The measured asymmetry  $A_k^n$  in Eq. 6.17 is now immune to the beam fluctuation and can easily be used to extract the physics asymmetry  $A_p$ . This is the approach we use here.

3) Pair asymmetry: Another approach to suppress the beam fluctuation is to utilize the symmetry of the detector to construct pair asymmetries. Here we consider the ratio of yields from conjugate wires, i.e. wire pairs on opposite sides of the central wire. This approach also requires the yield to be pedestal subtracted before we construct the ratios.

$$R_{kk^*}^\uparrow = \frac{y_k^\uparrow}{y_{k^*}^\uparrow} \text{ and } R_{kk^*}^\downarrow = \frac{y_k^\downarrow}{y_{k^*}^\downarrow}, \quad (6.18)$$

where

$$y_k^\uparrow = Y_k^\uparrow - b_k \text{ and } y_k^\downarrow = Y_k^\downarrow - b_k.$$

We construct the asymmetry as

$$\begin{aligned}
A_{kk^*}^r &= \frac{R_{kk^*}^\uparrow - R_{kk^*}^\downarrow}{R_{kk^*}^\uparrow + R_{kk^*}^\downarrow} \\
&= \frac{\frac{\epsilon_k(1+PG_k A_p)}{\epsilon_{k^*}(1+PG_{k^*} A_p)} - \frac{\epsilon_k(1-PG_k A_p)}{\epsilon_{k^*}(1-PG_{k^*} A_p)}}{\frac{\epsilon_k(1+PG_k A_p)}{\epsilon_{k^*}(1+PG_{k^*} A_p)} + \frac{\epsilon_k(1-PG_k A_p)}{\epsilon_{k^*}(1-PG_{k^*} A_p)}}.
\end{aligned} \quad (6.19)$$

Now, utilizing the symmetry of the detector, we use the fact that,  $G_k \approx -G_{k^*}$  to get

$$\begin{aligned}
A_{kk^*}^r &= \frac{\frac{(1+PG_k A_p)}{(1-PG_k A_p)} - \frac{(1-PG_k A_p)}{(1+PG_k A_p)}}{\frac{(1+PG_k A_p)}{(1-PG_k A_p)} + \frac{(1-PG_k A_p)}{(1+PG_k A_p)}} \\
&= \frac{4PG_k A_p}{2 + 2(PG_k A_p)^2} \\
&\approx 2PG_k A_p,
\end{aligned} \tag{6.20}$$

where in the last step we have used  $(PG_k A_p)^2 \ll 1$ .

4) Another way to get the same result of Eq. 6.20 is to construct the difference of the conjugate wire asymmetries

$$A_k - A_{k^*} = \frac{y_k^\uparrow - y_k^\downarrow}{y_k^\uparrow + y_k^\downarrow} - \frac{y_{k^*}^\uparrow - y_{k^*}^\downarrow}{y_{k^*}^\uparrow + y_{k^*}^\downarrow}, \tag{6.21}$$

where  $y_k^{\uparrow\downarrow}$  or  $y_{k^*}^{\uparrow\downarrow}$  are the pedestal subtracted yields.

$$\begin{aligned}
A_k - A_{k^*} &= \frac{I_0^\uparrow \epsilon_k (1 + PG_k A_p) - I_0^\downarrow \epsilon_k (1 - PG_k A_p)}{I_0^\uparrow \epsilon_k (1 + PG_k A_p) + I_0^\downarrow \epsilon_k (1 - PG_k A_p)} - \frac{I_0^\uparrow \epsilon_{k^*} (1 + PG_{k^*} A_p) - I_0^\downarrow \epsilon_{k^*} (1 - PG_{k^*} A_p)}{I_0^\uparrow \epsilon_{k^*} (1 + PG_{k^*} A_p) + I_0^\downarrow \epsilon_{k^*} (1 - PG_{k^*} A_p)} \\
&= \frac{I_0^\uparrow (1 + PG_k A_p) - I_0^\downarrow (1 - PG_k A_p)}{I_0^\uparrow (1 + PG_k A_p) + I_0^\downarrow (1 - PG_k A_p)} - \frac{I_0^\uparrow (1 - PG_k A_p) - I_0^\downarrow (1 + PG_k A_p)}{I_0^\uparrow (1 - PG_k A_p) + I_0^\downarrow (1 + PG_k A_p)} \\
&= \frac{(I_0^\uparrow + I_0^\downarrow) PG_k A_p + (I_0^\uparrow - I_0^\downarrow)}{(I_0^\uparrow + I_0^\downarrow) + PG_k A_p (I_0^\uparrow - I_0^\downarrow)} - \frac{(I_0^\uparrow - I_0^\downarrow) - PG_k A_p (I_0^\uparrow + I_0^\downarrow)}{(I_0^\uparrow + I_0^\downarrow) + PG_k A_p (I_0^\uparrow - I_0^\downarrow)},
\end{aligned} \tag{6.22}$$

where in the second step we have used  $G_k \approx -G_{k^*}$ .

Again, using  $(I_0^\uparrow + I_0^\downarrow) \gg PG_k A_p (I_0^\uparrow - I_0^\downarrow)$  in the denominator, we have

$$A_k - A_{k^*} \approx PG_k A_p + \frac{I_0^\uparrow - I_0^\downarrow}{I_0^\uparrow + I_0^\downarrow} - \frac{I_0^\uparrow - I_0^\downarrow}{I_0^\uparrow + I_0^\downarrow} + PG_k A_p. \tag{6.23}$$

Thus

$$\Delta A_{kk^*} = A_k - A_{k^*} \approx 2PG_k A_p. \tag{6.24}$$

It is also evident from Eq. 6.23 that if we take the sum of the conjugate wire asymmetries, we get an estimate for the beam asymmetry

$$\sum A_{kk^*} = A_k + A_{k^*} \approx 2 \frac{I_0^\uparrow - I_0^\downarrow}{I_0^\uparrow - I_0^\downarrow}. \tag{6.25}$$

In the remainder of this chapter we analyze the asymmetry constructed from the yield which is pedestal subtracted and normalized by sum over all detectors (the

second approach). The equations of interest are 6.11,6.12, 6.13, 6.14, 6.15 and 6.17. In Eq. 6.17, the polarization  $P$  is close to 1 and we omit the polarization until the end of the analysis. We also replace the superscript  $n$  by  $r$  on the left hand side of Eq. 6.17 hereafter and refer to this quantity as the measured or raw asymmetry. In the analysis, the time of flight integrated yield over the optimal TOF window, shown in Fig. 6.1, is taken as the wire yield ( $Y^{\uparrow\downarrow}$ ) for that pulse.

## 6.1.2 Data selection

As we saw in Fig. 2.28 and Fig. 2.29, each pulse has a small contamination from the previous pulse and next pulse. Also, the choppers are opening and closing in this region. So we exclude the first 5 time bins and last 4 time bins of any pulse as shown in Fig(6.1). Thus, time bins 5 - 44 are the TOF window used in the analysis.

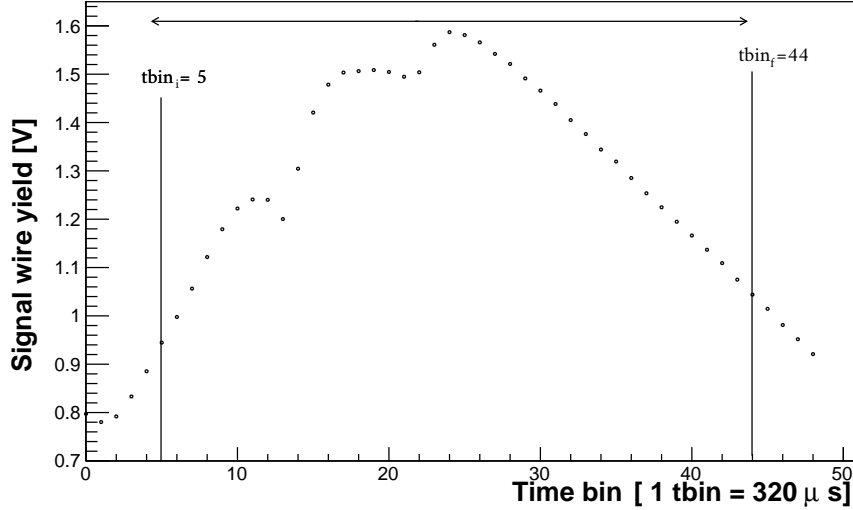


Figure 6.1: The TOF window used for the anymmetry extraction. The plot shows signal from layer 1 wire 5.

Next, while the dropped pulses are useful for doing detailed beam characterization and extracting the pedestal, from the analysis perspective, we need to exclude those pulses. As shown in section (2.4.2), a dropped pulse omits the injection flash in the previous pulse and missing wrap around in the next few pulses. We not only exclude the dropped pulse, but one pulse before it and 19 pulses after the dropped pulse (21 pulses in total, as shown in Fig. 6.2) from the analysis.

Additionally, we require considering 600-pulse sequences with no irregular dropped pulse in between; the rationale for this data selection is explained in section (6.1.5).

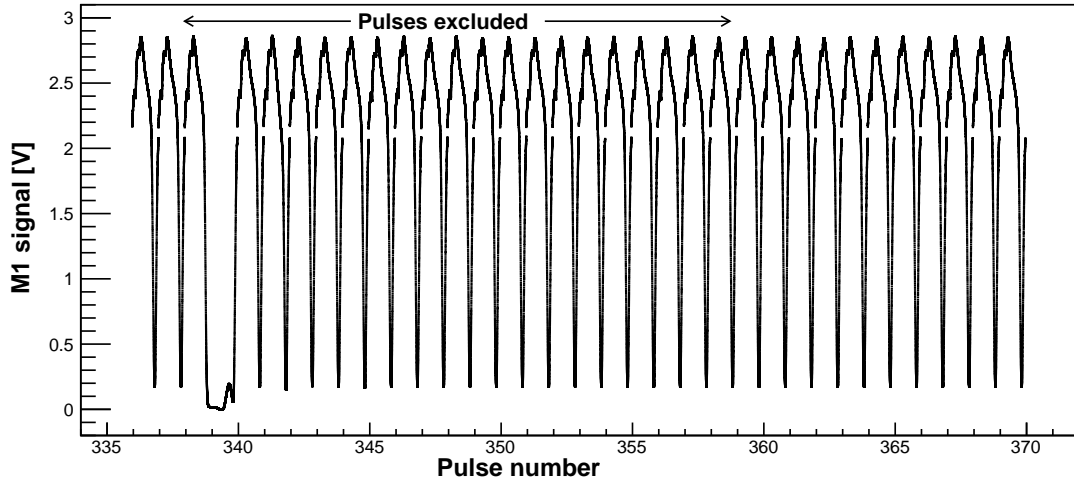


Figure 6.2: The pulses excluded from the analysis

### 6.1.3 Background subtraction

Each ADC channel has a time independent DC offset (pedestal). But, because of piled-up wrap-around, there is also a significant time dependent contribution to the signal. This is evident if we look at the signal for the dropped pulse. The signal for the dropped pulse is non-zero for any time bin because of this contribution. This background signal is small compared to an actual signal for the front wires, but it dominates for the wires from the back layers where the beam is weak. This background also depends on the accelerator beam power.

To remove this background we use the dropped pulse. From the dropped pulse signal, the time bin with lowest signal is used to get the constant offset. Time bins 37 and 670 from the dropped pulses are used to determine the offset for the detector and M1 signals, respectively. This constant offset is subtracted from the signals corresponding to all the time bins of the regular pulses. The constant offset is calculated for each channel and is updated in every 600-pulse sequence from the most recent regularly dropped pulse.

### 6.1.4 Beam fluctuations

Fig. 6.8 (for the LR data) and Fig. 6.26 (for the UD data) show the beam power fluctuations from run to run. There are also beam power fluctuations within each run. In most cases this fluctuation is due to dropped pulses or comparatively low beam power pulses. The top plot in Fig. 6.4 shows the distribution of the M1 asymmetry for all the pulses including dropped pulses. In this distribution the largest asymmetries, near +1 and -1, come from the dropped pulses. In Fig. 6.4, the asymmetries far from zero are because of the pulses with low beam power. The bottom plot shows the distribu-

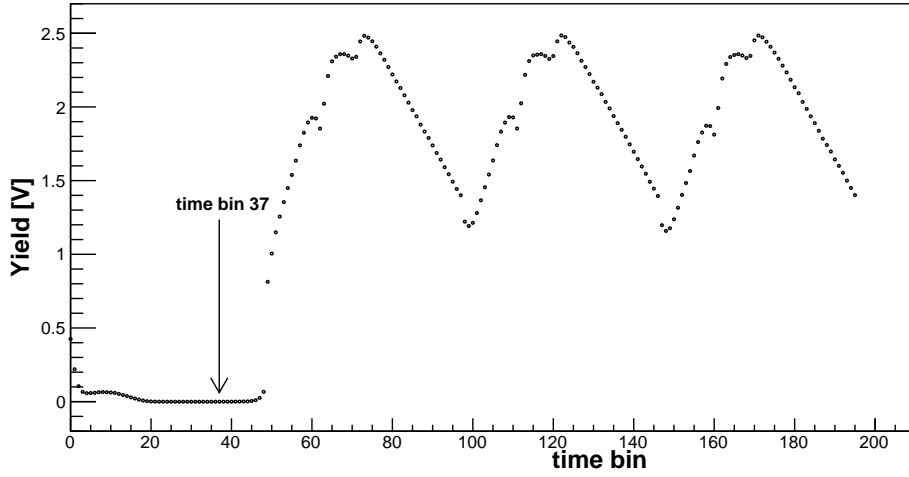


Figure 6.3: Pedestal measured from the dropped pulse: The signal corresponding to time bin 37 (for detector signals) of the regularly dropped pulse is used as the offset for signals corresponding to all other time bins.

tion once we exclude the dropped pulses and neighbors as shown in Fig. 6.2. Fig. 6.5 shows the M1 asymmetry for the LR data set (first five batches) after applying the data selection. For this slightly smaller dataset, the beam power was comparatively stable.

We also look at the beam fluctuation over a long time period. In Fig. 6.6, we plot  $(I_i - I_{ave})/I_{ave}$  versus distance from the dropped pulse. Here,  $I_i$  is the time bin integrated M1 signal for the  $i$ -th pulse starting from the dropped pulse. We used data summary tape (DST), explained in section 4.4, to generate this plot. This plot shows how the beam intensity varies within a sequence with respect to the average pulse intensity over a long period of time. So, we do not expect this variation to affect our asymmetry. To remove pulse to pulse beam fluctuations (as in Fig. 6.4 , 6.5), we follow the asymmetry definition mentioned in Eq. 6.15, i.e. asymmetry in terms of modified yield which is pedestal subtracted and normalized by a sum over all detectors' signal. To account for run to run beam fluctuations (as in Fig. 6.8 and Fig. 6.26) we divide the entire data set into batches based on beam stability. Then the asymmetries, extracted from each of those batches, are combined to get an overall average asymmetry.

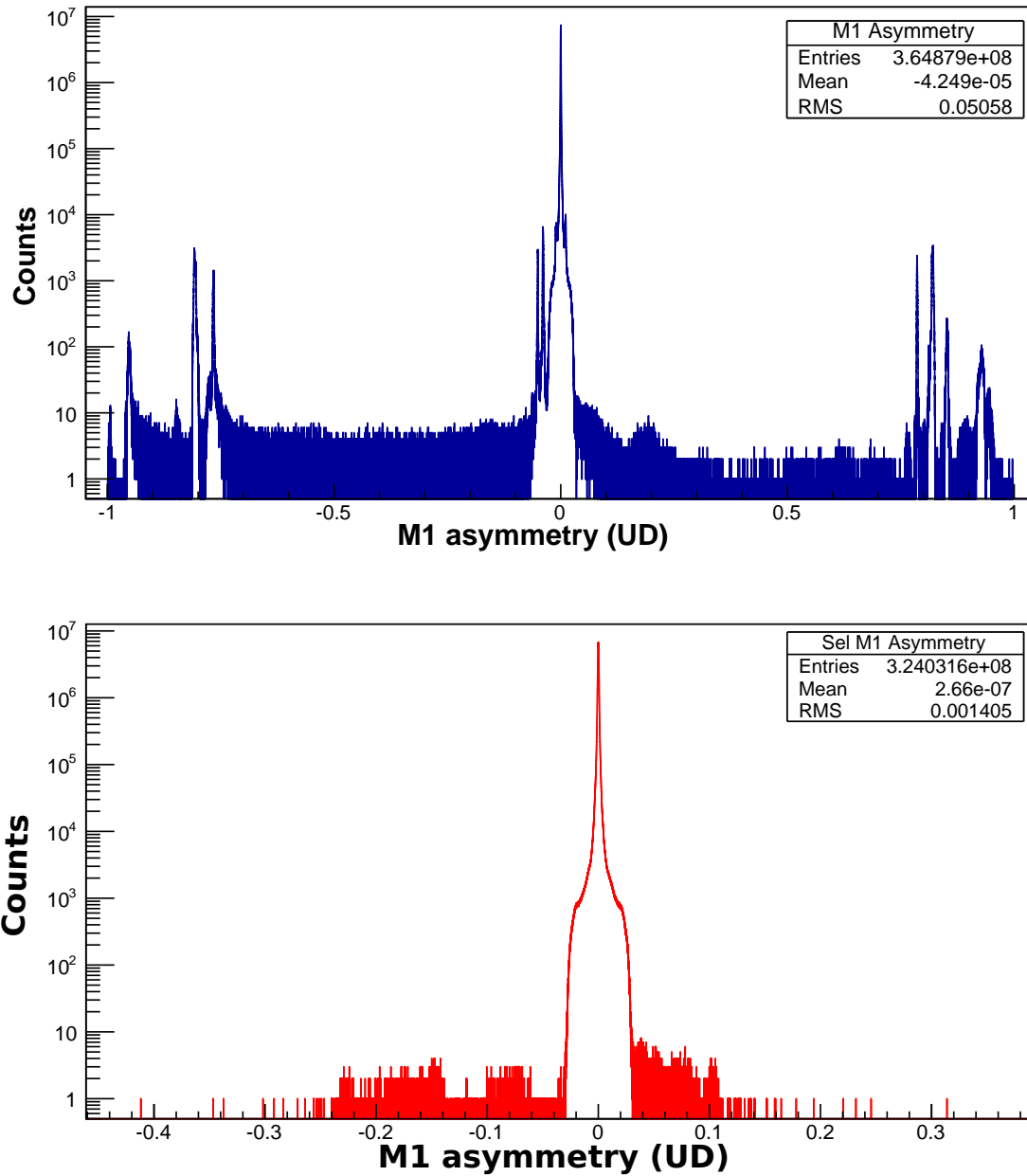


Figure 6.4: The M1 asymmetry from the UD data. The top graph includes all the pulses. The bottom graph excludes dropped pulses and neighbors.



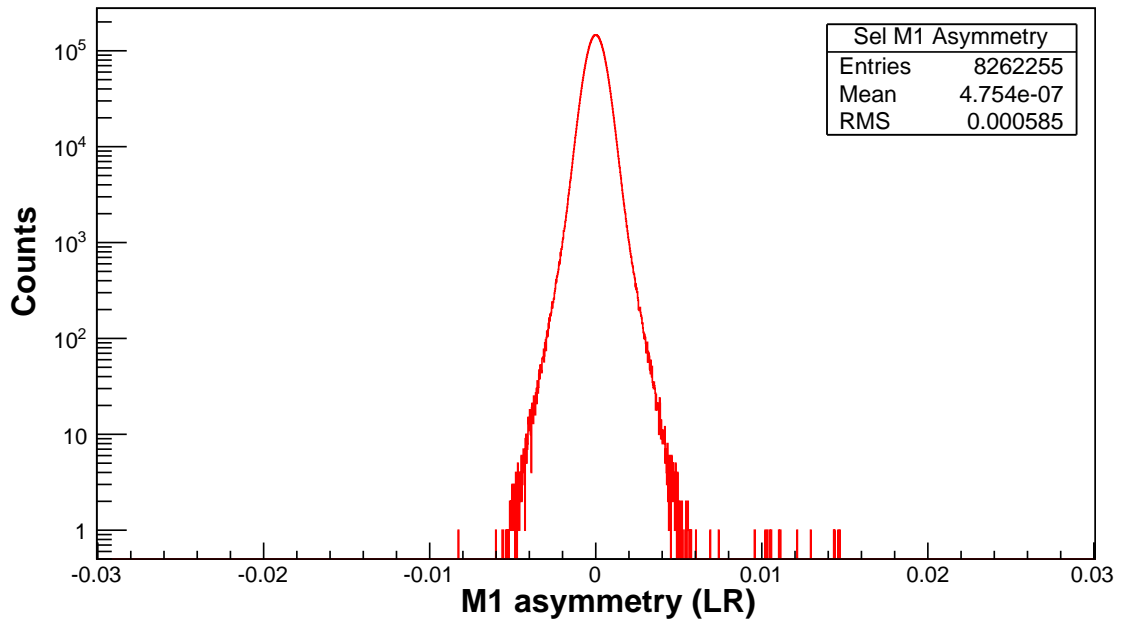


Figure 6.5: The M1 asymmetry from the LR data (first five batches) after excluding dropped pulses and neighbors.

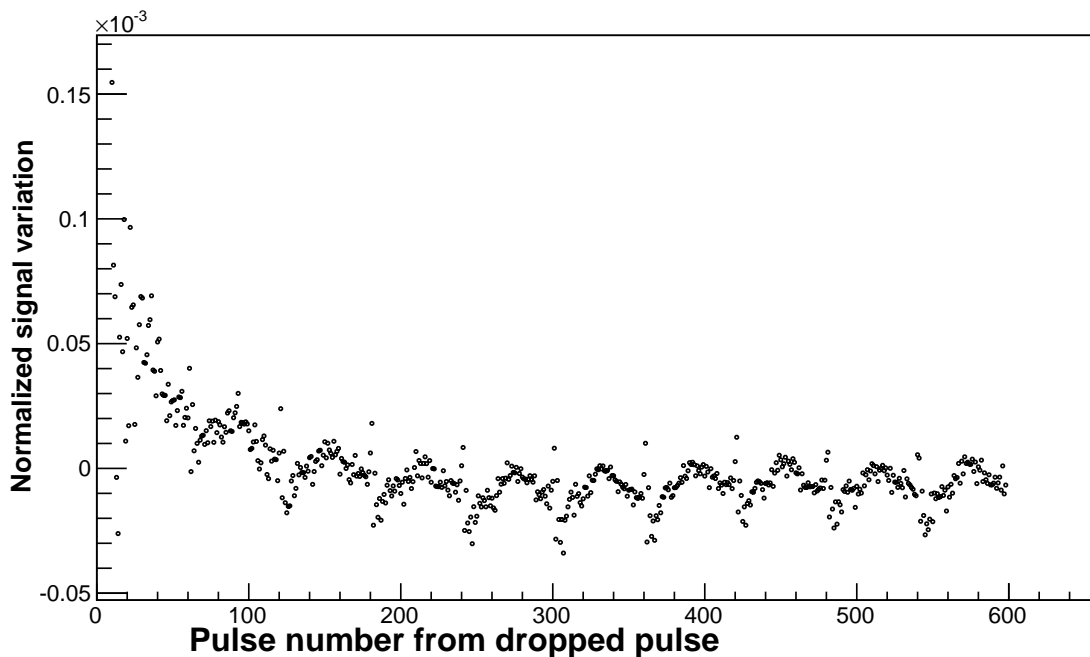


Figure 6.6: Normalized M1 signal variation as a function of distance from the dropped pulse. Along the  $y$ -axis is  $(I_i - I_{ave})/I_{ave}$ , where  $i$  is the pulse number from dropped. The first 10 pulses with high variation are not shown in this plot.

### 6.1.5 False asymmetry

We noticed slow drift in the beam. This can be shown using the image pulse explained in section 2.4.2. Fig. 6.7 shows an image (surrogate) pulse with both axes on a log scale. The  $x$ -axis contains 600 pulses. We see, starting from the main pulse peak, the beam intensity is drifting slowly as we near the end of the sequence. This slow drift can easily give rise to false asymmetry in our analysis as shown in Fig. 6.10. To cancel this drift, we consider the pulses starting from one regular dropped pulse until the next regular dropped pulse. This constitutes a sequence of 600 pulses with the dropped pulse as the first pulse. We skip any sequence with an irregular dropped pulse. Now, the dropped pulse of any sequence can have two states — the RFSF is turned on or turned off. Based on the RFSF state during the dropped pulse, we group the sequence as  $\mathcal{A}$  (RFSF off) or  $\mathcal{B}$  (RFSF on). The false asymmetry contribution, because of the slow drift, in Eq. 6.15 will have opposite sign in group  $\mathcal{A}$  compared to group  $\mathcal{B}$ . So when we combine asymmetries from both groups, they will cancel out. This is the analysis strategy we follow — we analyze in sequences (each sequence having 600 pulses) and group them as  $\mathcal{A}$  and  $\mathcal{B}$ , and finally average them to cancel false asymmetry.

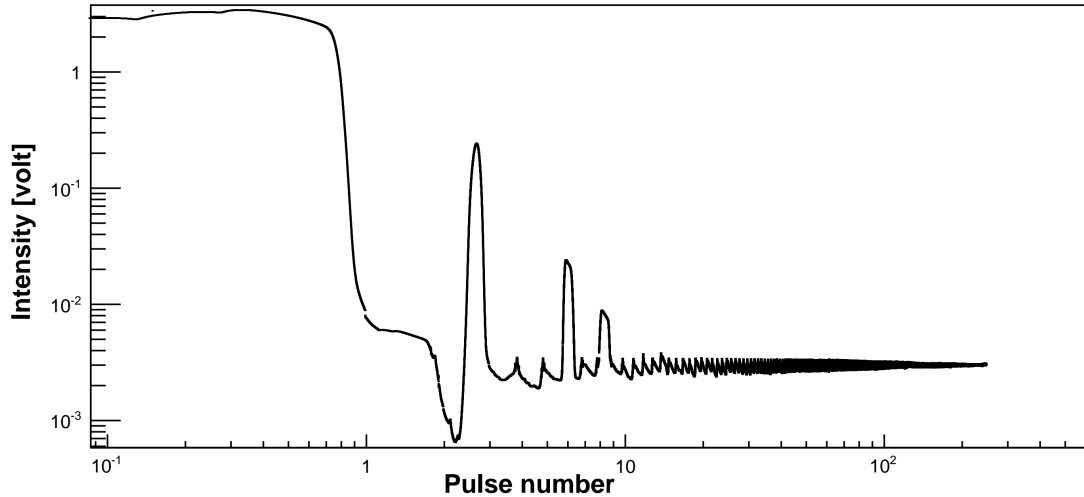


Figure 6.7: Slow drift from image pulse

## 6.2 Parity conserving (LR) asymmetry

We first present the analysis of the LR (parity conserving) data set. LR data were collected in two phases: once at the beginning of the experiment and again at the end of the experiment. In between those, UD data were collected for the most part of the experiment. Fig. 6.8 shows the average proton beam power for the LR dataset from the first phase (first five batches). The proton beam power was mostly stable. We note that the plot in Fig. 6.8 is zero-suppressed. The plot also marks the region of the five batches. Table 6.1 enumerates each LR batch and corresponding run range. For the LR asymmetry, the total number of runs analyzed was  $718 + 329$ .

Batch no.	Run range
Batch-1	14785 - 14880
Batch-2	14881 - 15235
Batch-3	15236 - 15520
Batch-4	15521 - 15785
Batch-5	15786 - 15860
Batch-6	57403 - 57600
Batch-7	57601 - 57796

Table 6.1: The batch numbers and corresponding run ranges of the LR data set

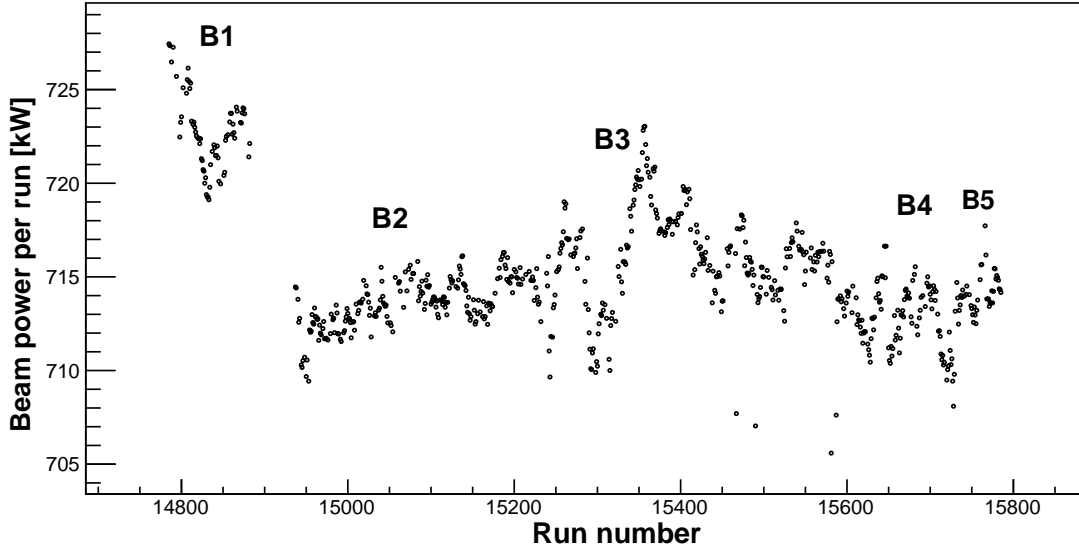


Figure 6.8: Different batch groups and beam power for the LR runs. Pulses around the dropped pulse are excluded from the beam power calculation. Note, the plot is zero suppressed.

Within each batch and each group ( $\mathcal{A}$  or  $\mathcal{B}$ ), the measured or raw asymmetry is calculated according to Eq. 6.15. Fig 6.9 shows the distribution of the LR raw asymmetry for layer 1, wire 1. If the beam power is stable, which is the case for Fig(6.9), the distribution is purely Gaussian.

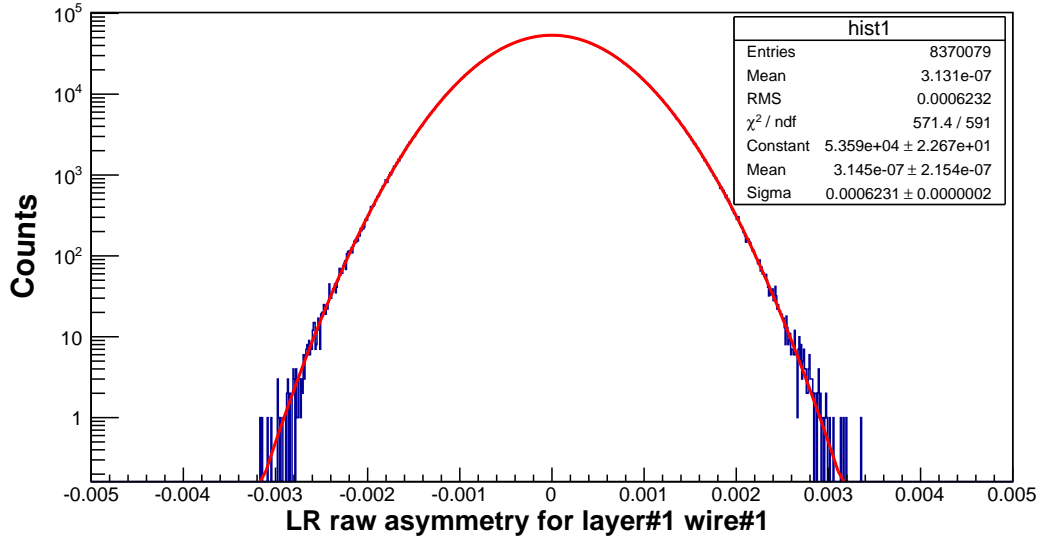


Figure 6.9: The LR raw asymmetry from the layer number 1, wire 1

To illustrate that the raw asymmetries from group  $\mathcal{A}$  and  $\mathcal{B}$  have false asymmetry contributions with opposite sign, we plot the raw asymmetries from both groups on the same graph in Fig. 6.10. This plot represents raw asymmetries from all the LR data (all data as a single batch) separated in two groups.

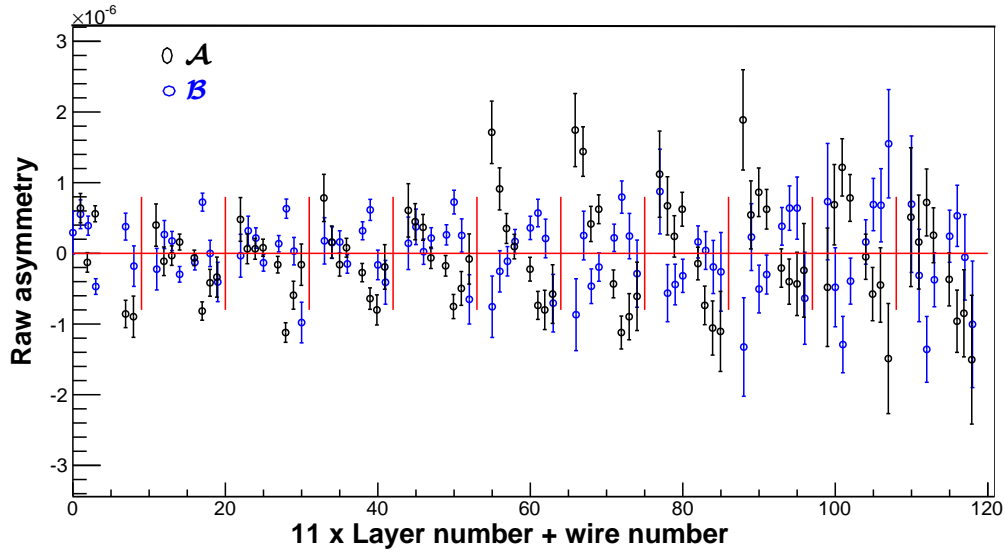


Figure 6.10: Raw asymmetry from the entire LR data set: Group  $\mathcal{A}$  and Group  $\mathcal{B}$ . The vertical red lines separate each layer of the ion chamber.

The resultant asymmetries, that we get by taking the average of asymmetries from group  $\mathcal{A}$  and  $\mathcal{B}$ , are plotted in Fig. 6.11. We see that within each layer the raw asymmetry is maximum for the end wires and antisymmetric about the middle wire of each layer. This trend follows the geometry factors of each wire. This clearly indicates a non-zero parity conserving asymmetry.

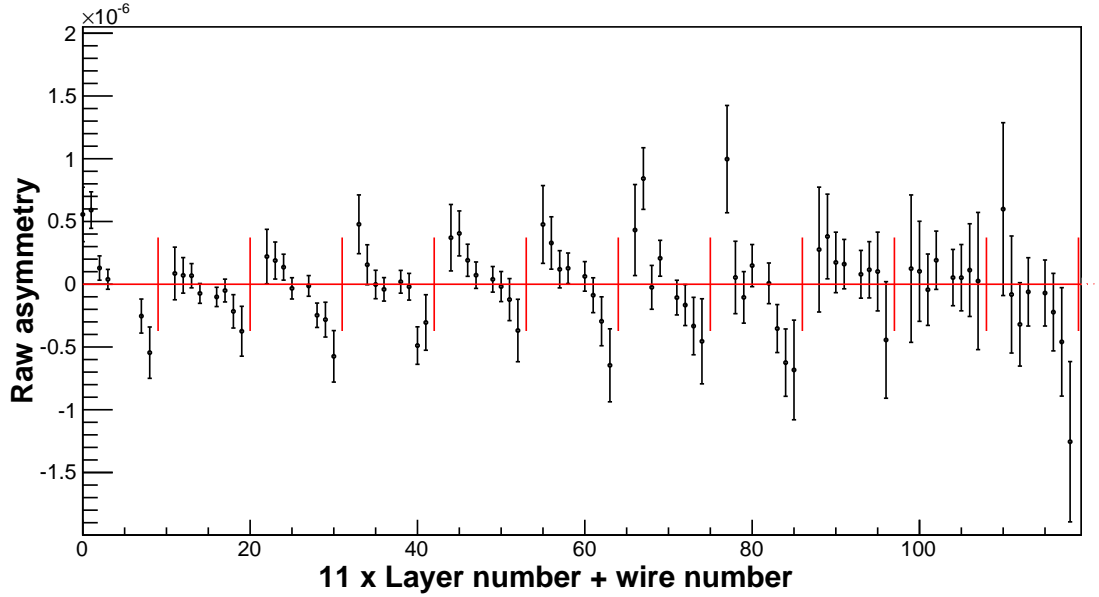


Figure 6.11: Raw asymmetry from the entire LR data set: Group  $\mathcal{A}$  + Group  $\mathcal{B}$ . The vertical red lines separate the layers of the ion chamber.

We analyze each of the LR batches separately and combine asymmetries from group  $\mathcal{A}$  and group  $\mathcal{B}$  using simple averaging within each batch.

To get the physics asymmetry from the combined raw asymmetry, we normalize each raw asymmetry by the corresponding geometry factors calculated in section 5.7. Fig. 6.12 shows the physics asymmetry for all wires from the LR batch-2 group  $\mathcal{A}$  data. Fig. 6.13 shows the physics asymmetry for all the wires from the LR batch-2 group  $\mathcal{B}$  data.

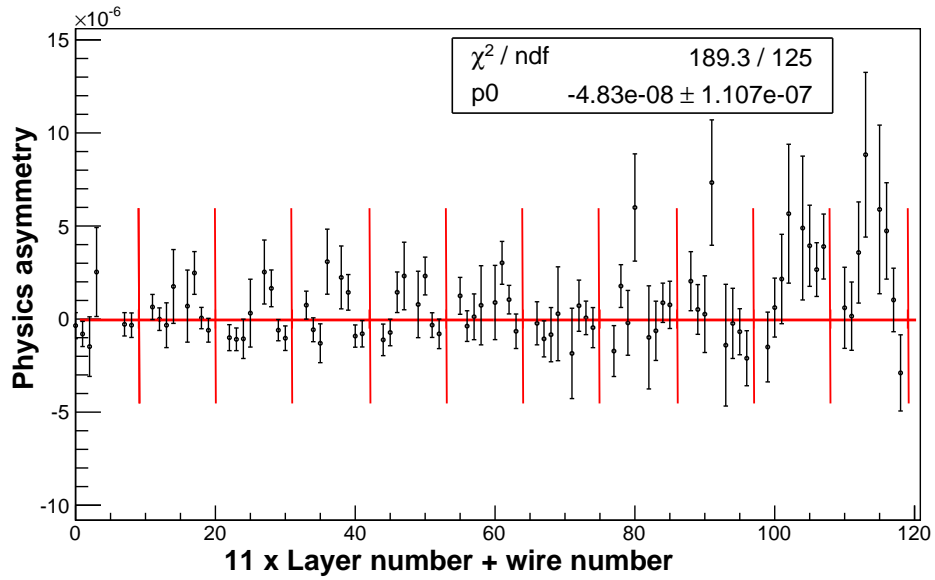


Figure 6.12: The LR physics asymmetry (uncorrected) from batch  $2\mathcal{A}$ . The vertical red lines separate the layers of the ion chamber. The fit values in the box are without correction for correlation.

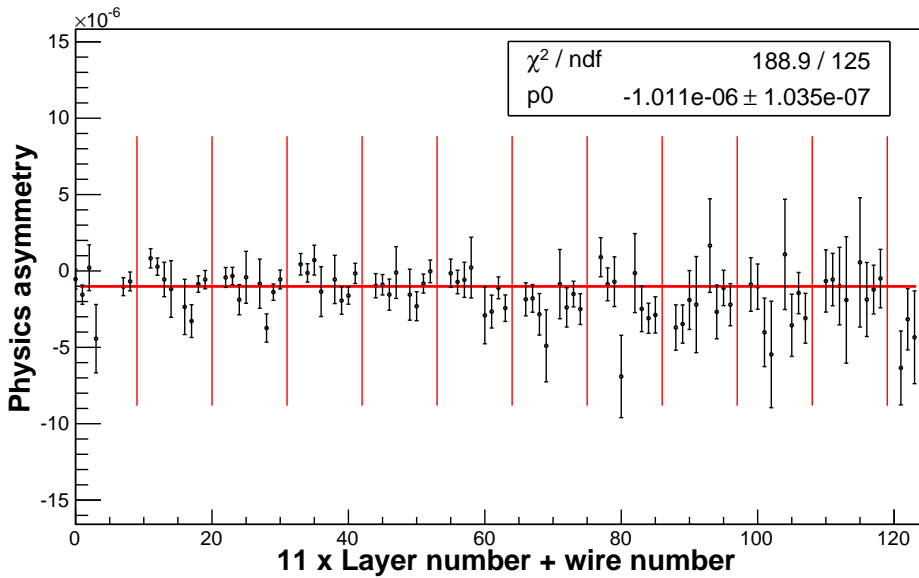


Figure 6.13: The LR physics asymmetry (uncorrected) from batch  $2\mathcal{B}$ . The vertical red lines separate the layers of the ion chamber. The fit values in the box are without correction for correlation.

To combine the physics asymmetries from the two groups, we use

$$\bar{A}_{\mathcal{A}+\mathcal{B}}^i = \frac{\bar{A}_{\mathcal{A}}^i + \bar{A}_{\mathcal{B}}^i}{2}, \quad (6.26)$$

$$\Delta\bar{A}_{\mathcal{A}+\mathcal{B}}^i = \frac{\sqrt{(\Delta\bar{A}_{\mathcal{A}}^i)^2 + (\Delta\bar{A}_{\mathcal{B}}^i)^2}}{2}, \quad (6.27)$$

where  $\bar{A}_{\mathcal{A},\mathcal{B}}^i$  is the average physics asymmetry from the  $i$ -th wire in group  $\mathcal{A}$  or  $\mathcal{B}$ .  $\bar{A}_{\mathcal{A}+\mathcal{B}}^i$  and  $\Delta\bar{A}_{\mathcal{A}+\mathcal{B}}^i$  are the average physics asymmetry and its error of the  $i$ -th wire after combining groups  $\mathcal{A}$  and  $\mathcal{B}$ . The combined physics asymmetries of groups  $2\mathcal{A}$  and  $2\mathcal{B}$  are plotted in Fig(6.14). The physics asymmetry, presented here, is without the correction for polarization.

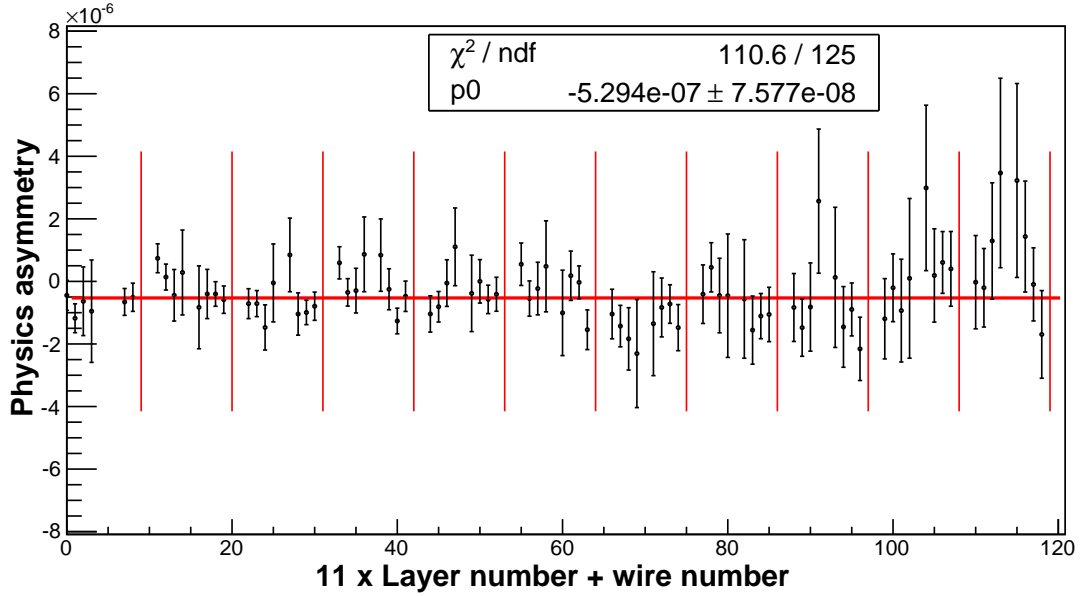


Figure 6.14: The LR physics asymmetry (uncorrected) from batch  $2\mathcal{A} + 2\mathcal{B}$ . The vertical lines separate the layers of the ion chamber. The fit values in the box are without correction for correlation.

Since each signal wire is expected to give a similar physics asymmetry, we fit to a constant here to get the average of all the signal wires. The fit values shown in the boxes are without correction for correlations. So, the fit values for  $p_0$  represents an uncorrected physics asymmetry. In the next section we discuss how to correct for the correlation.

### 6.3 Correction for correlation

As we mentioned in section(3.2.2), the energy deposition in multiple wires from a single event makes the wires correlated. This is also evident from Fig. 6.15, where we plotted the raw asymmetries from two adjacent wires along the two axes. The slanted major axis of the ellipse is an indication of the correlation.

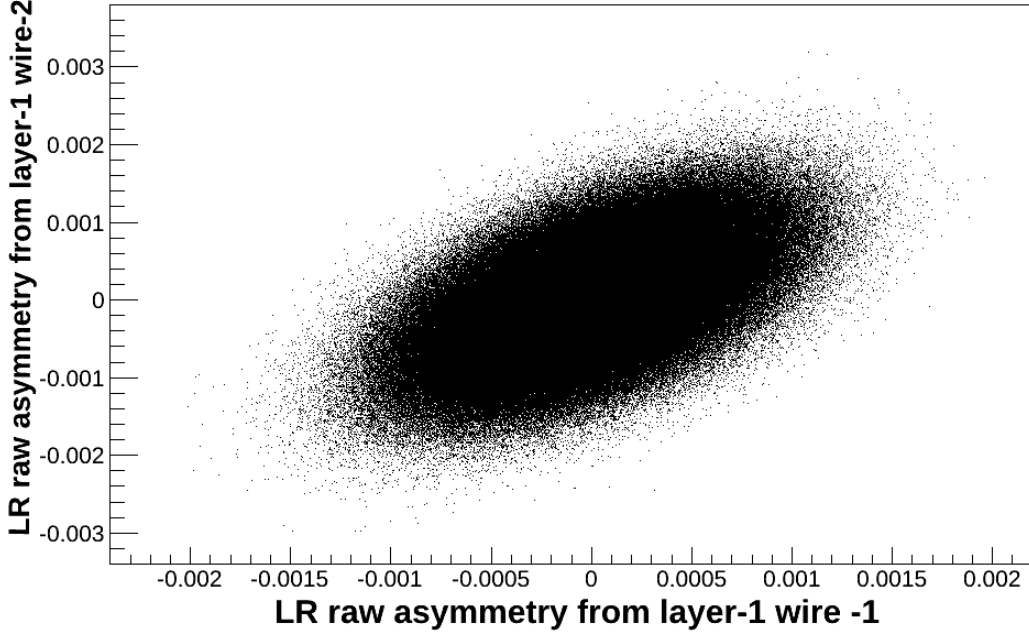


Figure 6.15: The raw asymmetry correlation between wires. Here the correlation is presented between layer-1, wire-1 and layer-1, wire-2 raw asymmetries from 68 LR runs.

We calculate the covariance for raw asymmetry using

$$\text{Cov}(A_i^r, A_j^r) = \frac{1}{N} \sum_{k=1}^N (A_k^r{}^i - \bar{A}^r{}^i)(A_k^r{}^j - \bar{A}^r{}^j), \quad (6.28)$$

where  $i$  and  $j$  are the wire number indices. Here, the raw asymmetry  $A_i^r$  is calculated according to Eq. 6.15. The covariance of the physics asymmetries is

$$\text{Cov}(A_i^p, A_j^p) = \frac{\text{Cov}(A_i^r, A_j^r)}{G_i G_j}, \quad (6.29)$$

where superscript  $r$  indicates raw asymmetry and  $p$  indicates physics asymmetry. Indices  $i$  and  $j$  are again for the wire numbers.  $G$  indicates the geometry factor.



We are actually interested in the covariance of mean, which is normalized by the number of entries (pulse pairs),

$$\text{Cov}(\bar{A}_i^p, \bar{A}_j^p) = \frac{1}{N} \frac{\text{Cov}(A_i^r, A_j^r)}{G_i G_j}. \quad (6.30)$$

If  $i = j$ , then Eq. 6.28 reduces to

$$\sigma_i^2 = \frac{1}{N} \sum_{k=1}^N (A_k^{r\ i} - \bar{A}^{r\ i})^2, \quad (6.31)$$

which are the variances and the diagonal terms of the covariance matrix. For uncorrelated observables, the off-diagonal terms are all zero and only diagonal terms enter into the weight. In the case of correlated observables, non-zero off-diagonal terms will remain.

The measure of covariance is often expressed as the correlation coefficient, which is just the normalized covariance, defined as

$$\rho = \frac{\text{Cov}(A_i^p, A_j^p)}{\sigma_i \sigma_j}, \quad (6.32)$$

where  $\sigma_i$  and  $\sigma_j$  are the standard deviations (square root of variance) corresponding to the physics asymmetries. The correlation coefficient varies between -1 (anti-correlated) and +1 (correlated), where the sign indicates the sense of correlation. If the variables are perfectly correlated linearly, then  $|\rho| = 1$ ; if the variables are independent then  $\rho = 0$ . Fig. 6.16 shows the correlation coefficient between the physics asymmetries of different wires. Here we used data from the LR batch 2. Along the  $x$  and  $y$  axes are the wire numbers, and the color represents the value of the correlation coefficient. We note that, the plot is symmetric as expected from Eq. 6.32. The red diagonal line represents each wire's self-correlation. On both sides of the red line, we see two bands representing non-zero correlation. The first band, sticking to the red line, represents the correlation between the wires of the same layer in the left-right direction (in the LR mode) or in the up-down direction (in the UD mode). The other band, a little bit away from the red line, represents the correlation between the wires of the adjacent layers. This band is away from red line because of the way the wire numbers are made serialized on the axes. Each gap in this band is for an end wire in a layer which has no neighboring wire on one side.

We follow two independent approaches to take into account the correlation in our weighted average or fit. These two approaches are discussed in the following two subsections.

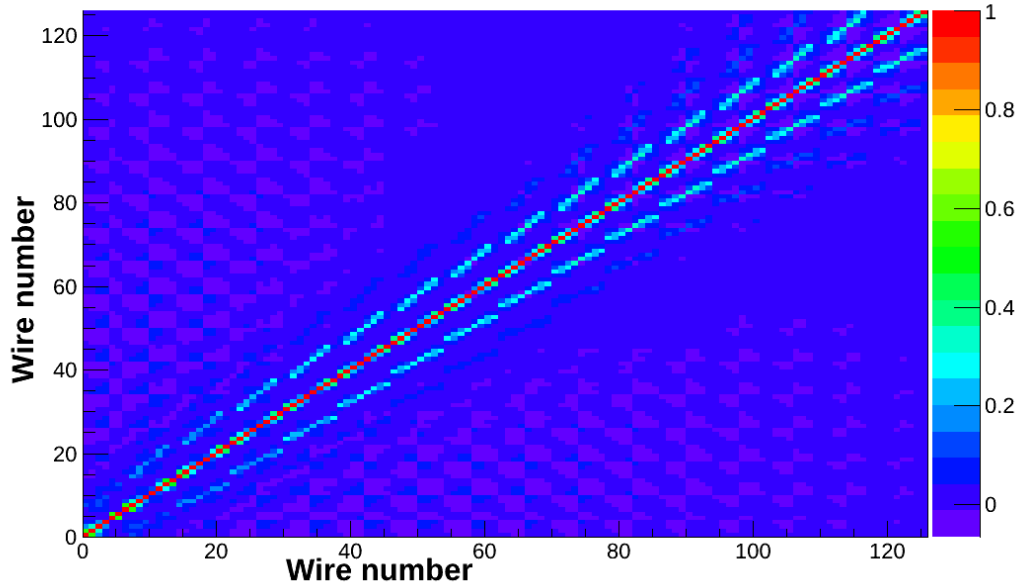


Figure 6.16: The physics asymmetry correlation between wires from the LR batch-2 data. The color represent the correlation coefficient  $\rho$  defined in Eq. 6.32. The labels “wire number” along the axes here actually represent  $8 \times \text{Layer number} + \text{wire number}$ . The middle wire in each layer is omitted.

### 6.3.1 Correlation correction by direct inversion of the covariance matrix

In this approach we note that, since the off diagonal term of the covariance matrix is not zero because of correlation between wires, we need to consider the full covariance matrix in defining the weight used to average individual wire asymmetry. We can no longer just use the diagonal elements (variances), as used for the case when there is no correlation. So, we generalize our typical weighting method on the left with the full covariance matrix on the right as shown below:

$$\text{Weight: } w_i = \frac{1}{(\delta \bar{A}_i^p)^2} = \frac{1}{\sigma_{\bar{A}_i^p}^2} \Rightarrow w_i = \sum_j \text{Cov}(\bar{A}_i^p, \bar{A}_j^p)^{-1}, \quad (6.33)$$

$$\text{Weighted average: } \bar{A}^p = \frac{\sum_i w_i \bar{A}_i^p}{\sum_i w_i} \Rightarrow \bar{A}^p = \frac{\sum_{ij} \text{Cov}(\bar{A}_i^p, \bar{A}_j^p)^{-1} \bar{A}_i^p}{\sum_{ij} \text{Cov}(\bar{A}_i^p, \bar{A}_j^p)^{-1}}, \quad (6.34)$$

$$\text{Error: } \Delta \bar{A}^p = \frac{1}{\sqrt{\sum_i w_i}} \Rightarrow \Delta \bar{A}^p = \frac{1}{\sqrt{\sum_{ij} \text{Cov}(\bar{A}_i^p, \bar{A}_j^p)^{-1}}}, \quad (6.35)$$

$$\chi^2 : \quad \chi^2 = \sum_i \frac{(\bar{A}_i^p - \bar{A}^p)^2}{\sigma_{\bar{A}_i^p}^2} \Rightarrow \chi^2 = \sum_{ij} (\bar{A}_i^p - \bar{A}^p) \text{Cov}(\bar{A}_i^p, \bar{A}_j^p)^{-1} (\bar{A}_j^p - \bar{A}^p). \quad (6.36)$$

$\bar{A}_i^p$  is the mean physics asymmetry of the  $i$ -th wire and  $\bar{A}^p$  is the weighted average physics asymmetry of all the wires. Since we divide the data set in two groups  $\mathcal{A}$  and  $\mathcal{B}$ , and then combine them, the covariance of the combined result is calculated using

$$\text{Cov}(\bar{A}_i^p, \bar{A}_j^p)_{\mathcal{A}+\mathcal{B}} = \frac{1}{4} \left[ \frac{1}{N_{\mathcal{A}}} \text{Cov}(A_i^p, A_j^p)_{\mathcal{A}} + \frac{1}{N_{\mathcal{B}}} \text{Cov}(A_i^p, A_j^p)_{\mathcal{B}} \right]. \quad (6.37)$$

Eq. 6.37 easily follows from Eqs. 6.27 and 6.30.

We can use Eqs. 6.33 to 6.36 with the covariance in Eq. 6.37 to get the correlation-corrected average physics asymmetry and its error from the wire asymmetries.

### 6.3.2 Correlation correction by diagonalizing the covariance matrix

The basic idea in this approach is to transform the wire asymmetries and the corresponding uncertainties to an orthogonal basis where the covariance matrix is diagonal. With the diagonal covariance matrix, the asymmetries in the new basis or reference frame are independent (not correlated anymore) [66],[67]. Noting that the covariance matrix  $C \equiv \text{Cov}(\bar{A}_i^p, \bar{A}_j^p)_{\mathcal{A}+\mathcal{B}}$  is symmetric, we can always find an orthogonal transformation matrix  $S$  that diagonalizes it:

$$S^T C S = D, \quad \text{where } S^T S = I. \quad (6.38)$$

Here  $D$  is a diagonal matrix with diagonal elements

$$D = \text{Diag}(\sigma_1^2, \sigma_2^2, \sigma_3^2, \sigma_4^2, \dots, \sigma_n^2). \quad (6.39)$$

The transformation matrix  $S$  converts back and forth between the correlated and uncorrelated basis (reference frame). The matrix  $S$  can be built up from the eigenvectors of  $C$  as its columns, so that  $D$  is the diagonal matrix of eigenvalues. Before we transform everything into the new basis, we rewrite our fit procedure in the matrix representation. In the correlated frame we fit the physics asymmetry from all 144 signal wires to a constant, i.e. we fit to

$$\bar{A}_i = b, \quad (6.40)$$

where  $\bar{A}_i$  is the average physics asymmetry for the  $i$ -th signal wire and  $b$  is the weighted average, physics asymmetry from the fit over all the wires. In matrix representation the above fit can be represented as

$$\bar{A} = Xb, \quad (6.41)$$

where  $\bar{A}$  is a column matrix with 144 physics asymmetries as the entries and  $X$  is the design matrix. In the diagonal case,  $X$  is a column vector filled with all 1's. Clearly,  $b$  is a scalar and invariant, irrespective of our choice of the basis. By forming deviation from the expectation in Eq. 6.41 and forming the chi square, which we minimize, we can easily derive the following results [66], [67]:

$$\text{Weight:} \quad W = C^{-1}, \quad (6.42)$$

$$\text{Fit value (weighted average):} \quad b = (X^T W X)^{-1} X^T W \bar{A}, \quad (6.43)$$

$$\text{Error:} \quad (\Delta b)^2 = (X^T W X)^{-1}, \quad (6.44)$$

$$\text{Chi square:} \quad \chi^2 = (\bar{A} - Xb)^T W (\bar{A} - Xb). \quad (6.45)$$

In other words, Eq. 6.42 to Eq. 6.45 are nothing but equations 6.33 to 6.36 rewritten in the matrix representation. The above relations work both for correlated and uncorrelated data.

We note that, for uncorrelated data, the above expressions reduce to our well-known expressions:

$$w_i = \frac{1}{\sigma_i^2}, \quad (6.46)$$

$$b = \frac{\sum_i y_i \frac{1}{\sigma_i^2}}{\sum_i \frac{1}{\sigma_i^2}}, \quad (6.47)$$

$$\Delta b = \frac{1}{\sqrt{\sum_i \frac{1}{\sigma_i^2}}}, \quad (6.48)$$

$$\chi^2 = \sum_i \frac{(y_i - b)^2}{\sigma_i^2}. \quad (6.49)$$

Now we transform both our data and the fit according to Eq. 6.38 so that in this new orthogonal basis the covariance matrix is diagonal:

$$\bar{A}' = S^T \bar{A}, \quad (6.50)$$

$$X' = S^T X, \quad (6.51)$$

Our fit relation is

$$\bar{A}' = X'b. \quad (6.52)$$

We note that from Eq. 6.51, the entries of  $X'$  are no longer filled with 1's. In the new basis the expressions Eqs. 6.42 to 6.45 become

$$\text{Weight:} \quad W' = D^{-1}, \quad (6.53)$$

$$\text{Fit value (weighted average):} \quad b = (X'^T W' X')^{-1} X'^T W' \bar{A}', \quad (6.54)$$

$$\text{Error:} \quad (\Delta b)^2 = (X'^T W' X')^{-1}, \quad (6.55)$$

$$\text{Chi square:} \quad \chi^2 = (\bar{A}' - X'b)^T W' (\bar{A}' - X'b). \quad (6.56)$$

In the new basis, the  $\bar{A}' \rightarrow X'$  map is not flat any more. But the covariance matrix  $D$  is now diagonal, which means the individual mode is uncorrelated. The weight of each mode is just the inverse of the corresponding diagonal element (eigenvalue).

$$W' = D^{-1} = \text{Diag}\left(\frac{1}{\sigma_1^2}, \frac{1}{\sigma_2^2}, \frac{1}{\sigma_3^2}, \frac{1}{\sigma_4^2}, \dots, \frac{1}{\sigma_n^2}\right). \quad (6.57)$$

We can easily check that  $b$ ,  $(\Delta b)^2$  and  $\chi^2$  are invariant, irrespective of our choice of basis (primed or unprimed frame) as expected.

$$\begin{aligned} (\Delta b)^2 &= (X'^T W' X')^{-1} = [(S^T X)^T D^{-1} S^T X]^{-1} \\ &= [X^T S (S^T C S)^{-1} S^T X]^{-1} \\ &= [X^T S (S^{-1} C^{-1} S) S^T X]^{-1} \\ &= [X^T (S S^{-1}) C^{-1} (S S^T) X]^{-1} \\ &= (X^T W X)^{-1}, \end{aligned} \quad (6.58)$$

where we have used the orthogonality of the  $S$  matrix, i.e.  $S^T = S^{-1}$ ,  $S S^T = S S^{-1} = I$ , and the properties  $(AB)^T = B^T A^T$ ,  $(ABC)^{-1} = C^{-1} B^{-1} A^{-1}$ .

$$\begin{aligned} b &= (X'^T W' X')^{-1} X'^T W' \bar{A}' = (X^T W X)^{-1} (S^T X)^T D^{-1} S^T \bar{A} \\ &= (X^T W X)^{-1} X^T S (S^T C S)^{-1} S^T \bar{A} \\ &= (X^T W X)^{-1} X^T S (S^{-1} C^{-1} S) S^T \bar{A} \\ &= (X^T W X)^{-1} X^T C^{-1} \bar{A} \\ &= (X^T W X)^{-1} X^T W \bar{A}. \end{aligned} \quad (6.59)$$

$$\begin{aligned}
\chi^2 &= (\bar{A}' - X'b)^T W' (\bar{A}' - X'b) = (S^T \bar{A} - S^T Xb)^T (S^T C S)^{-1} (S^T \bar{A} - S^T Xb) \\
&= (\bar{A} - Xb)^T S (S^{-1} C^{-1} S) S^T (\bar{A} - Xb) \quad (6.60) \\
&= (\bar{A} - Xb)^T W (\bar{A} - Xb).
\end{aligned}$$

In the new basis, we still extract the same weighted average, its error and the chi square value for the fit, but the variables are now uncorrelated. Another advantage of this approach over the previous approach, presented in section 6.3.1, is that we can now plot the modes and fit with independent error bars giving an visual representation of the goodness of the fit.

From Eq. 6.52, we see that if we plot  $\bar{A}'$  vs the mode number, then the fit is scaled by  $X'$  for each mode instead of flat. Another way is to plot  $\bar{A}' X'^{-1}$  against the mode number, which is a flat fit. In both cases, the fit parameter gives us the weighted average, i.e. the average physics asymmetry from all wires, along with its error and chi square as an indication for the goodness of the fit.

Out of 144 signal wires, the 16 central wires have small geometry factors. These wires have very large error bars, since the physics signal is almost washed away. So they have a non-significant contribution to the overall average physics asymmetry. Moreover, we have two bad wires, which give rise to a singularity while inverting the covariance matrix. We exclude these 18 signal wires and work with the remaining 126 signal wires to get the correlation-corrected average physics asymmetry. We employed both approaches of the correlation correction and obtained the exact same result. Here, we present the result using the second approach, since it allows for a visual representation of the data.

### 6.3.3 Data reduction

To get the correlation-corrected average physics asymmetry from all the 126 signal wires, we combine all the wires in two different ways as a cross check. In one case, for each batch we calculate the correlation-corrected physics asymmetry by combining all the wires. Then we combine all the batches to get an overall average physics asymmetry from all batches. This data reduction approach is indicated on the right of Fig. 6.17. In the other approach, for a particular wire, we fit along all the batches to get an average value for that wire. We do this separately for every wire to get 126 wire average values from the fits. Then, we apply correlation correction on these 126 wire averages to get the overall physics asymmetry from all the batches. This approach is indicated on the bottom of Fig. 6.17. In both approaches, we get the same overall physics asymmetry.

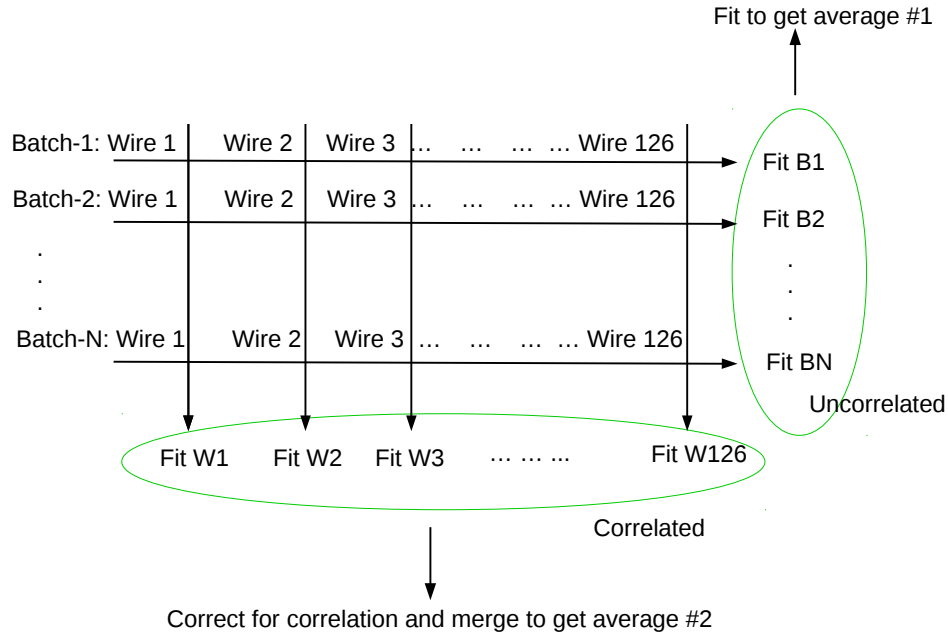


Figure 6.17: Two approaches of the data reduction process.

### 6.3.4 Correlation corrected LR asymmetry

In this section we apply the correction for the wire correlations to Fig. 6.14 using the approach explained in section 6.3.2. Fig. 6.18 (top) shows the transformation matrix  $S$ , which is formed from the eigenvectors of the covariance matrix as its columns. In the bottom plot of the same figure, we show the contribution of each wire to the eigenvector that corresponds to the most significant mode. Fig. 6.19 (top) shows the eigenvalues and (bottom) how the units in the matrix  $X$  change in the new basis. Both of them combined are used to determine the error bar in Fig. 6.20. In both cases, the modes have been sorted in ascending order of the error bar in Fig. 6.20 i.e. the most significant modes are plotted first. In Fig. 6.20 we have the LR physics asymmetry in the new basis scaled by  $X'$ . The fit of this plot, shown in the statistics box, gives us the correlation-corrected physics asymmetry (for the LR batch-2 data). Thus Fig. 6.20 is the correlation-corrected version of uncorrected plot in Fig. 6.14. We also compare  $\chi^2/ndf$  and the change in the uncertainty from each of the plots. Another approach of fitting to get the same result, with the  $A'_{LR}$  vs mode number plot, is presented in Appendix D.1. The other approach, explained in section (6.3.1), yields exactly the same answer.

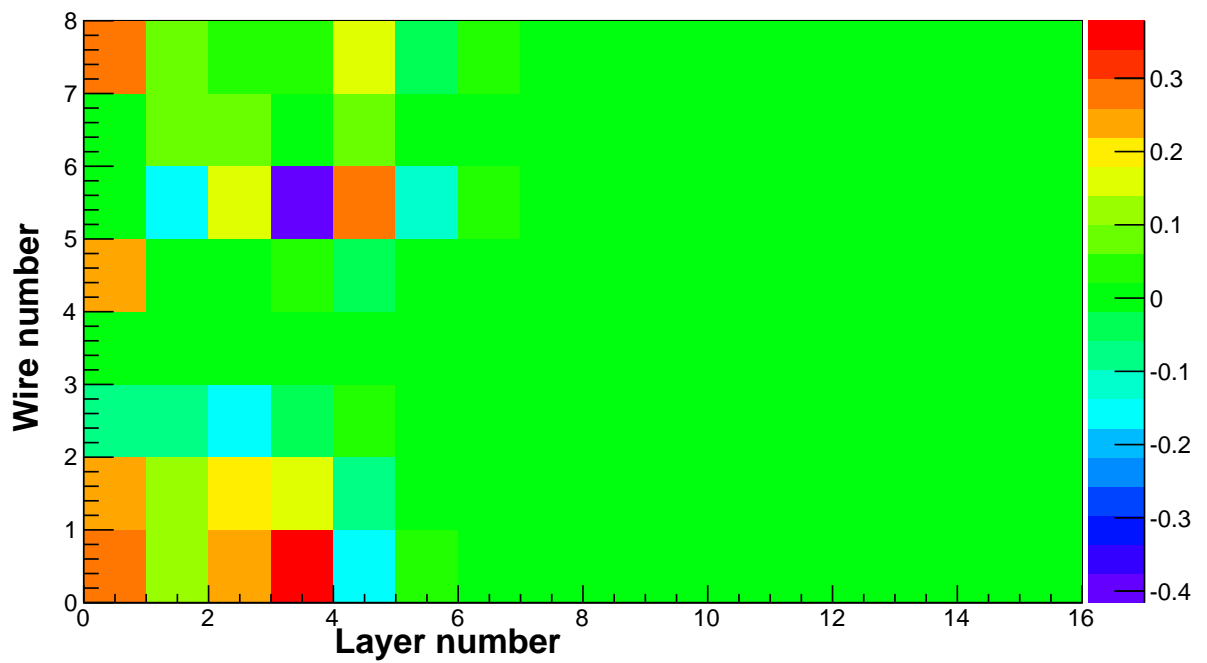
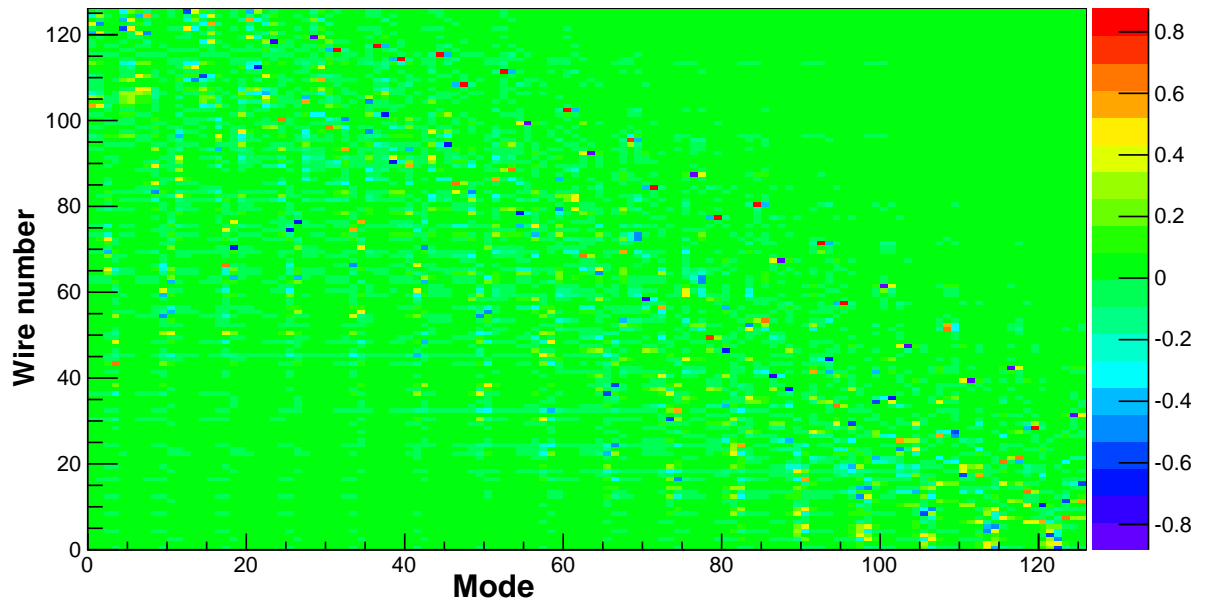


Figure 6.18: The top plot shows the transformation matrix  $S$  for the LR batch 2 data. The bottom plot shows the eigenvector corresponding to the most significant mode (mode 0) for the LR batch 2 data.



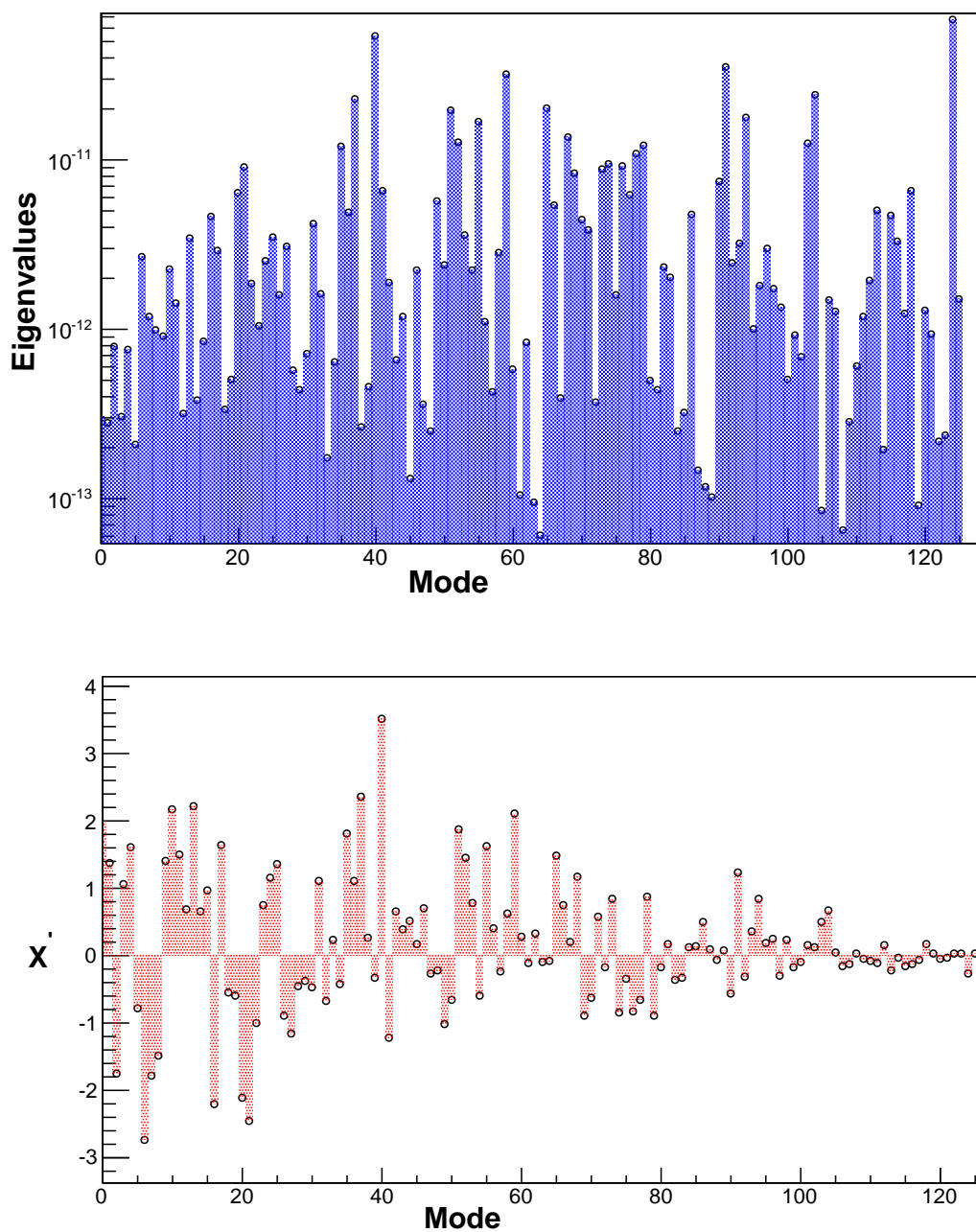


Figure 6.19: The top plot shows the eigenvalues for the LR batch 2 data. The bottom plot shows the entries of the matrix  $X'$ . Both of them combined determine the error bar in Fig. 6.20. In both cases, the modes have been sorted in ascending order of the error bar in Fig. 6.20 i.e. most contributing modes first.

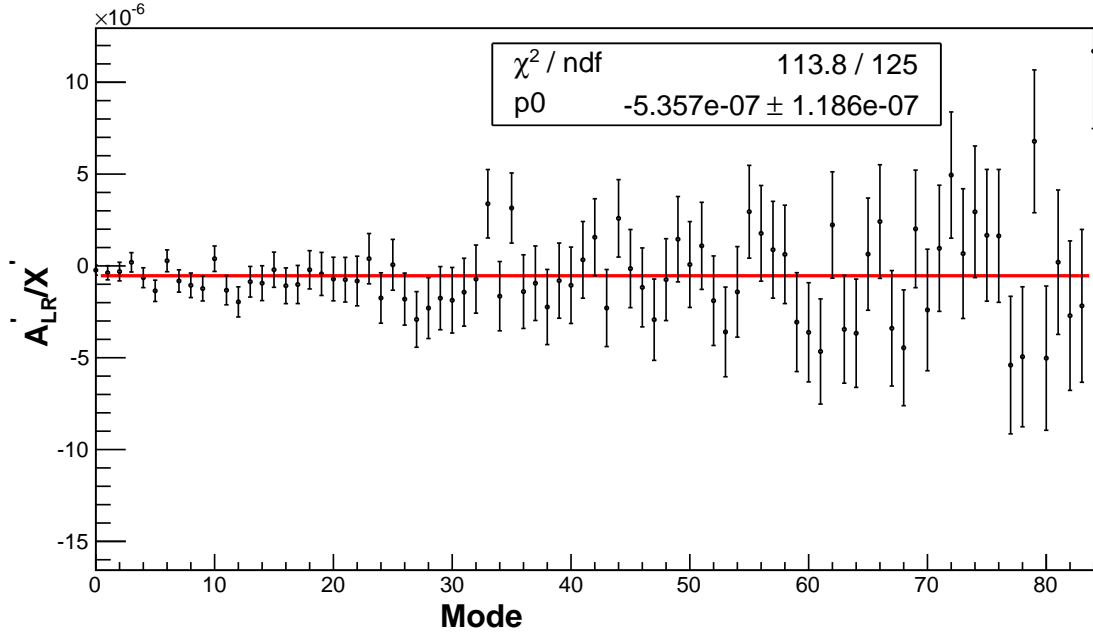


Figure 6.20: Fit for the correlation correction for the LR batch 2 data. The modes have been sorted in ascending order of the error bar, i.e. most contributing modes first. Only the most significant modes are shown here.

We apply the same recipe to all the LR batches. Table 6.2 shows the result from all the LR batches. The left most column labels the batch number with the number of runs analyzed in that batch in parenthesis.

Batch#	Physics asymmetry		Physics asymmetry $\mathcal{A} + \mathcal{B}$ (Uncorrected)		Physics asymmetry (Correlation corrected)	
	Group: $\mathcal{A}$	Group : $\mathcal{B}$	$A_{LR} \pm \Delta A_{LR}$	$\chi^2/ndf$	$A_{LR} \pm \Delta A_{LR}$	$\chi^2/ndf$
1 (64)	$-0.56 \pm 1.78$	$-7.89 \pm 2.09$	$-4.23 \pm 1.37$	113.58/125	$-3.81 \pm 2.15$	113.96/125
2 (208)	$-0.48 \pm 1.1$	$-10.11 \pm 1.03$	$-5.29 \pm 0.76$	110.64/125	$-5.35 \pm 1.19$	113.77/125
3 (197)	$0.91 \pm 1.07$	$-10.60 \pm 1.12$	$-4.85 \pm 0.78$	141.08/125	$-5.09 \pm 1.22$	150.37/125
4 (195)	$3.93 \pm 1.09$	$-8.63 \pm 1.12$	$-2.35 \pm 0.78$	132.35/125	$-2.72 \pm 1.22$	130.19/125
5 (57)	$4.81 \pm 2.08$	$-9.92 \pm 2.27$	$-2.55 \pm 1.54$	131.04/125	$-3.69 \pm 2.42$	147.85/125
6 (166)	$-1.46 \pm 1.30$	$-4.28 \pm 1.26$	$-2.87 \pm 0.90$	109.46/125	$-3.44 \pm 1.39$	117.17/125
7 (163)	$-13.00 \pm 1.10$	$4.61 \pm 1.05$	$-4.20 \pm 0.76$	115.51/125	$-3.97 \pm 1.17$	106.85/125

Table 6.2: LR asymmetries from all the batches. Asymmetries and their errors are in units of  $10^{-7}$ .

The next two columns show uncorrected physics asymmetries from group  $\mathcal{A}$  and group  $\mathcal{B}$ . The next two columns list uncorrected physics asymmetries after combining the two groups and the corresponding  $\chi^2/\text{NDF}$ . The last two columns are the correlation-corrected physics asymmetries with corresponding  $\chi^2/\text{NDF}$ .

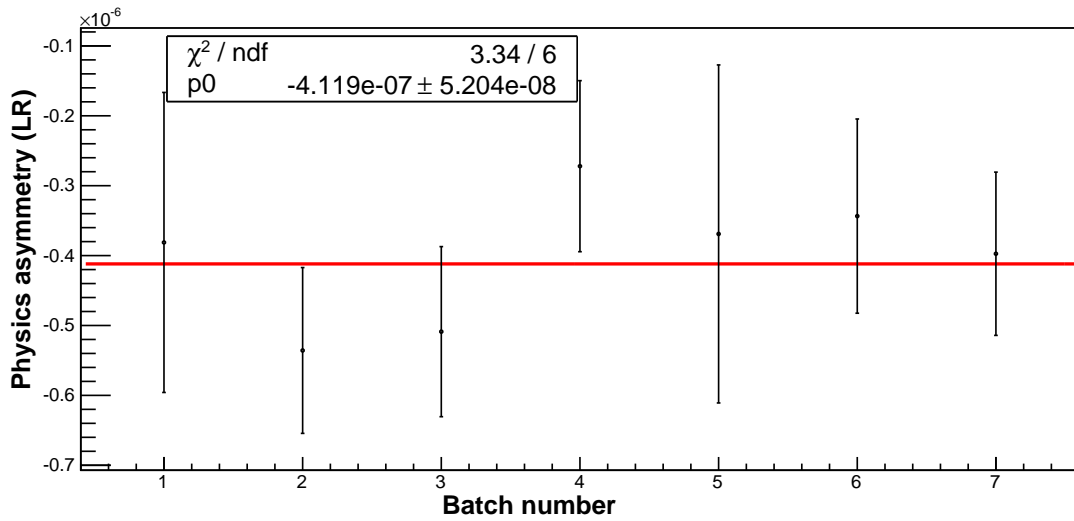


Figure 6.21: LR physics asymmetries (corrected) from all the batches

Fig. 6.21 shows the corrected LR physics asymmetries from all the batches. The fit value in the box represents the overall corrected LR physics asymmetry from all the LR runs, following the approach illustrated on the left in Fig. 6.17.

As a cross check of statistical consistency in time, we now follow the second data reduction approach illustrated in the bottom of Fig. 6.17.

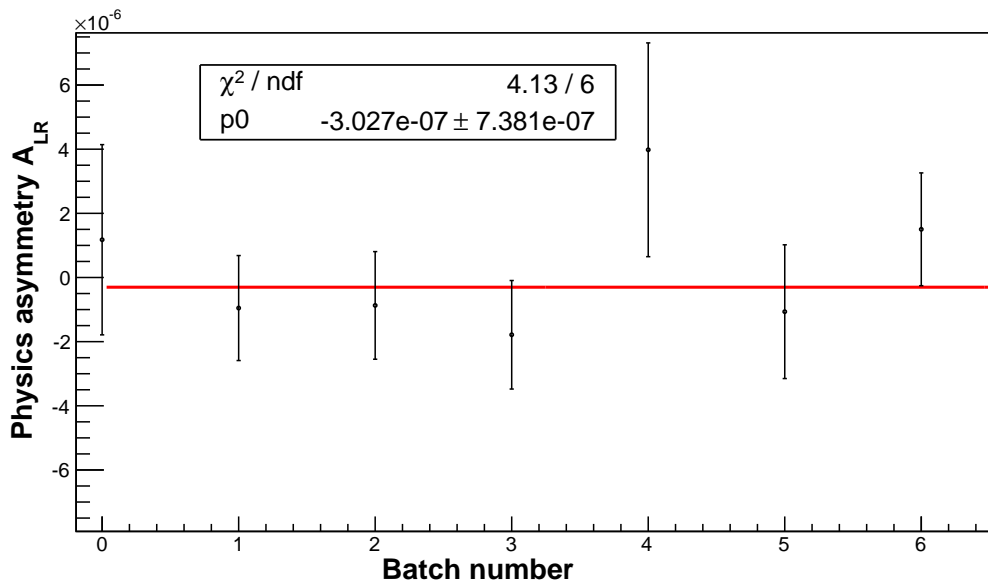


Figure 6.22: LR physics asymmetries (uncorrected) from different batches for layer-1, wire-4. Note, the batch number counting starts from zero here.

In this approach, we get the average wire physics asymmetry (uncorrected) by fitting the asymmetries for that wire from different batches. Fig. 6.22 shows such a fit

for layer-1, wire-4. We do a similar fit for all the other wires. Fig. 6.23 shows the distribution of wire physics asymmetries (uncorrected) that we get following the fit.

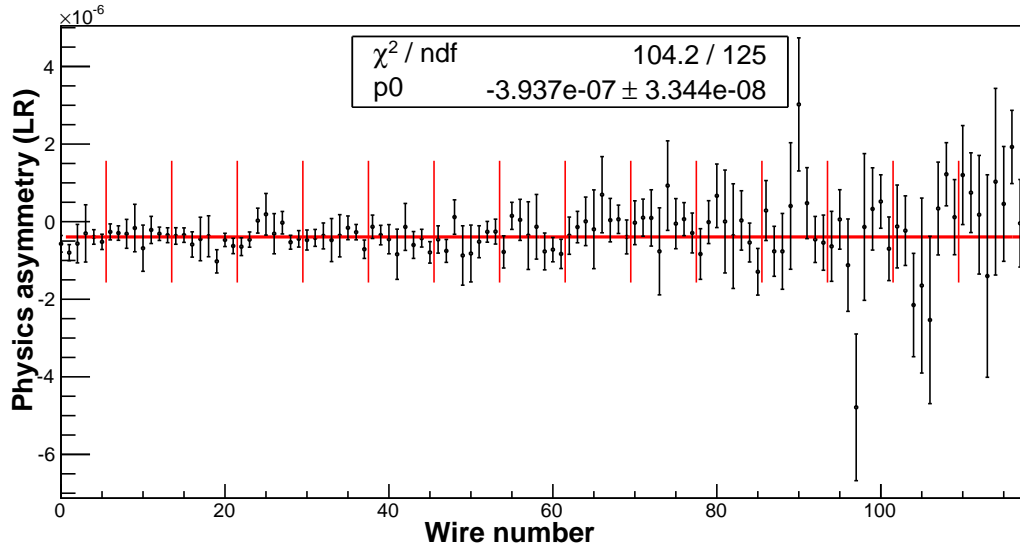


Figure 6.23: Physics asymmetry (uncorrected) for each wire obtained by fitting over all the batches.

We have 126 values for  $\chi^2$ , one from each fit to calculate the average physics asymmetry in a wire. Fig. 6.24 shows the distribution of  $\chi^2$ .

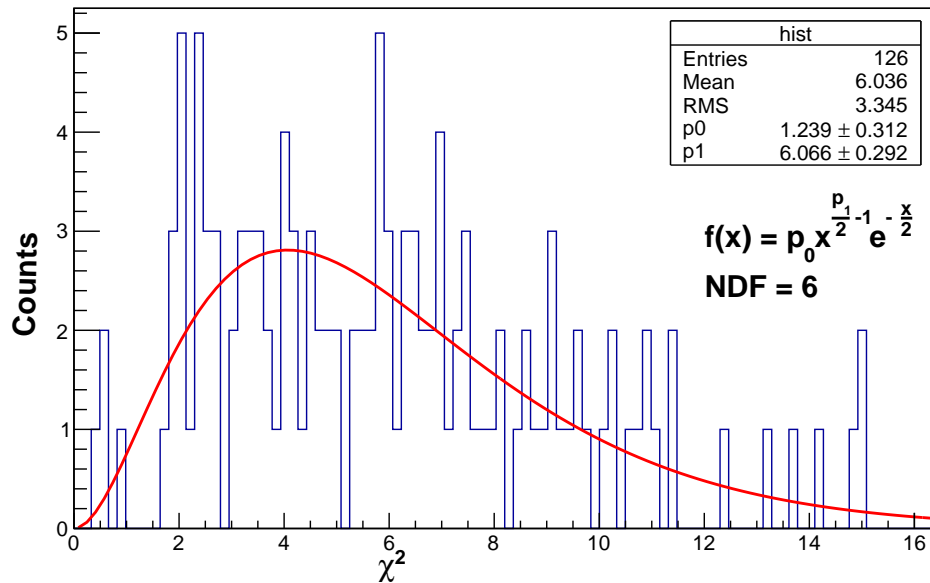


Figure 6.24: Chi square distribution for the fits. The log likelihood method is used for the fit. The function  $f(x)$  represents the  $\chi^2$  distribution.

We fit the distribution in Fig. 6.24 to the chi square distribution function. The values inside the box represent the fit values. Since there are 7 batches of LR data and one fit parameter, the number of degrees of freedom (NDF) is 6.

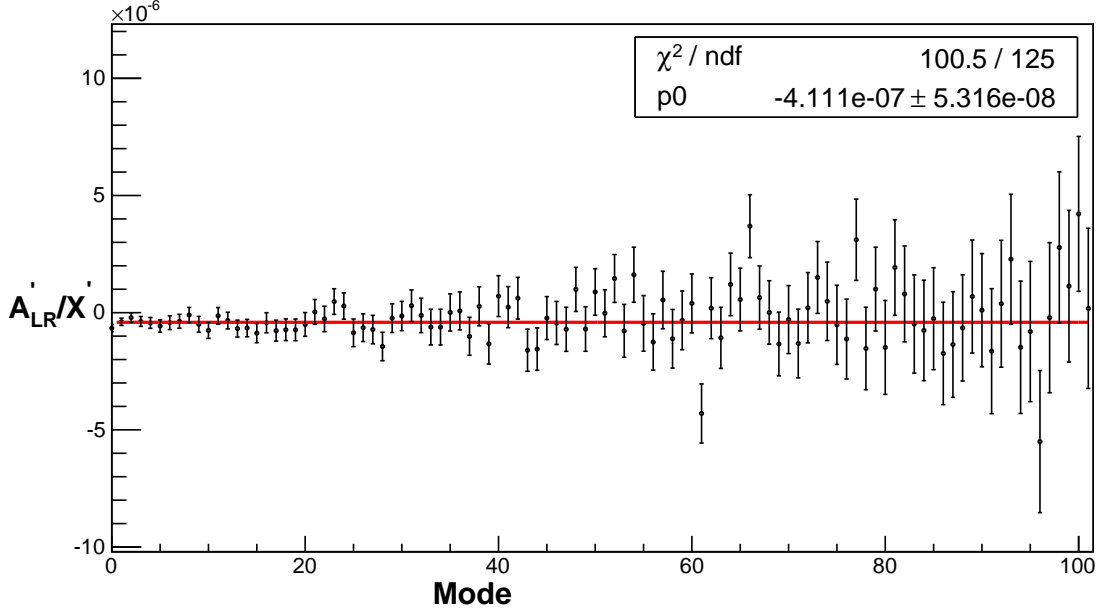


Figure 6.25: Fit for the correlation-corrected physics asymmetry. Here we used the average wire asymmetry, which is obtained by fitting over all the batches. The modes have been sorted in ascending order of the error, i.e. most significant modes first. Only most significant modes are shown here.

The LR physics asymmetry presented in Fig. 6.23 is without correction for correlation. To correct for correlation, we again follow the produces explained in section(6.3.2). The fit values shown in Fig. 6.25 give the correlation-corrected LR physics asymmetry. The fit values from Fig. 6.21 are in agreement with the fit values from Fig. 6.25. This confirms that both the data reduction approaches shown in Fig. 6.17 are equivalent. However, the first shows consistency of different wires, and the second of different batches.

Another validation for the analysis method is achieved by comparing the correlation from the data analysis with that from the simulation. By comparing the error from uncorrected fit and corrected fit, for example from Fig. 6.24 and Fig. 6.25, or from Table 6.2, we see an increase in error of  $\sim 57\%$ , which is pretty close to the prediction by the simulation of 59%.

The LR physics asymmetry is

$$A_{LR} = (-4.12 \pm 0.52) \times 10^{-7}, \quad (6.61)$$

without correction for polarization. After correcting for polarization using Eq. 3.18 and Eq. 3.19, the final LR physics asymmetry can be quoted as

$$A_{LR} = (-4.41 \pm 0.56) \times 10^{-7}. \quad (6.62)$$

## 6.4 Parity violating (UD) asymmetry

---

We now present the analysis of the parity violating (UD) data. The data analysis recipe is exactly same as the parity conserving (LR) data. The UD run numbers used in the analysis are in the range 18000 – 57000. We also divide this range into batches, mostly based on the beam power stability. Table 6.3 shows the batch number and the corresponding run range.

Batch no.	Run range
Batch 1	18000 - 22000
Batch 2	22001 - 26500
Batch 3	26501 - 29100
Batch 4	29101 - 30050
Batch 5	30051 - 31250
Batch 6	31251 - 31930
Batch 7	31931 - 33800
Batch 8	33801 - 35100
Batch 9	35101 - 35660
Batch 10	35661 - 36380
Batch 11	36381 - 38100
Batch 12	38101 - 40000
Batch 13	40001 - 43700
Batch 14	43701 - 45200
Batch 15	45201 - 47200
Batch 16	47201 - 49200
Batch 17	49201 - 51200
Batch 18	51201 - 53800
Batch 19	53801 - 54800
Batch 20	54801 - 56340
Batch 21	56341 - 57000

Table 6.3: All the batches and corresponding run ranges for the UD dataset.

Fig. 6.26 shows the average proton beam power distribution for all the UD runs. The batch numbers are also labeled on the plot. Labels for some intermediate batch numbers are omitted as they are very small and adjacent to each other.

We calculate the raw asymmetry using Eq. 6.15. Fig. 6.27 shows the distribution of raw asymmetry for one signal wire from some of the batch 1 runs. Generally, the distribution has more outliers if there are beam fluctuations. Within each batch we calculate the asymmetry in group  $\mathcal{A}$  and group  $\mathcal{B}$  based on the criteria explained above. Then we combine them to get the average asymmetry. We get the physics asymmetry from the raw asymmetry by normalizing by the same geometry factors used for the LR asymmetry.

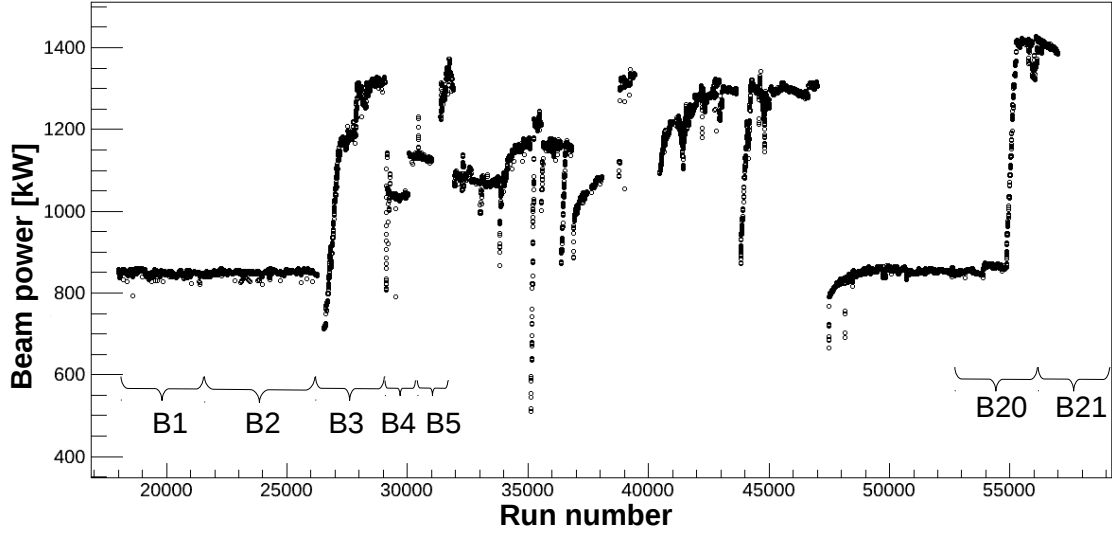


Figure 6.26: Average proton beam power distribution for the UD dataset. Dropped pulses have been excluded while calculating the beam power. Labels for the intermediate batch numbers from B6 to B19 are not shown in this plot.

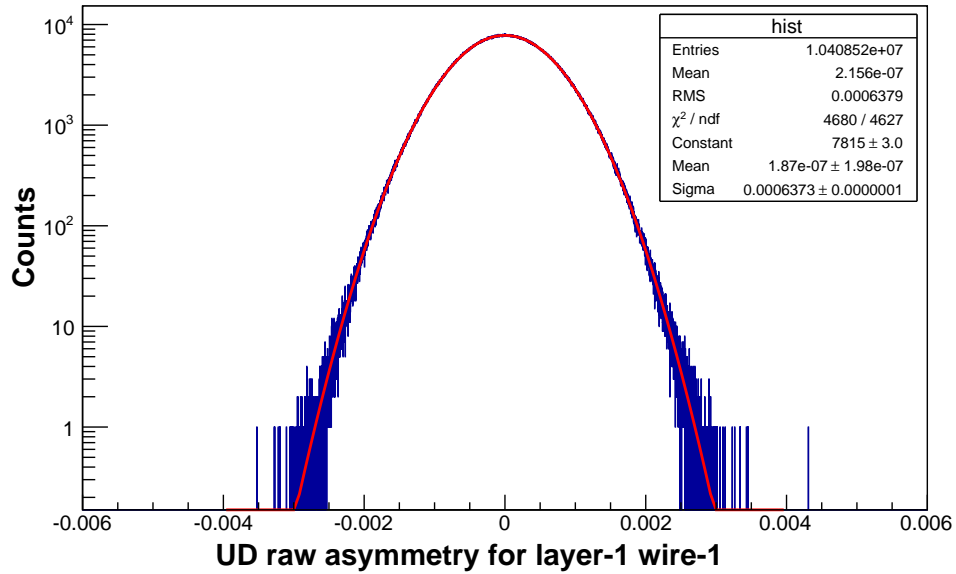


Figure 6.27: Distribution of the UD raw asymmetry from layer-1, wire-1, from  $\sim 900$  runs of batch 1.

Fig. 6.28 shows the distribution of UD physics asymmetries (uncorrected) from all the signal wires for the UD batch 2 data. The fit value in the box represents the average uncorrected UD physics asymmetry from all the wires for batch 2 data.

The correlation coefficient plot for the UD physics asymmetry is presented in Ap-

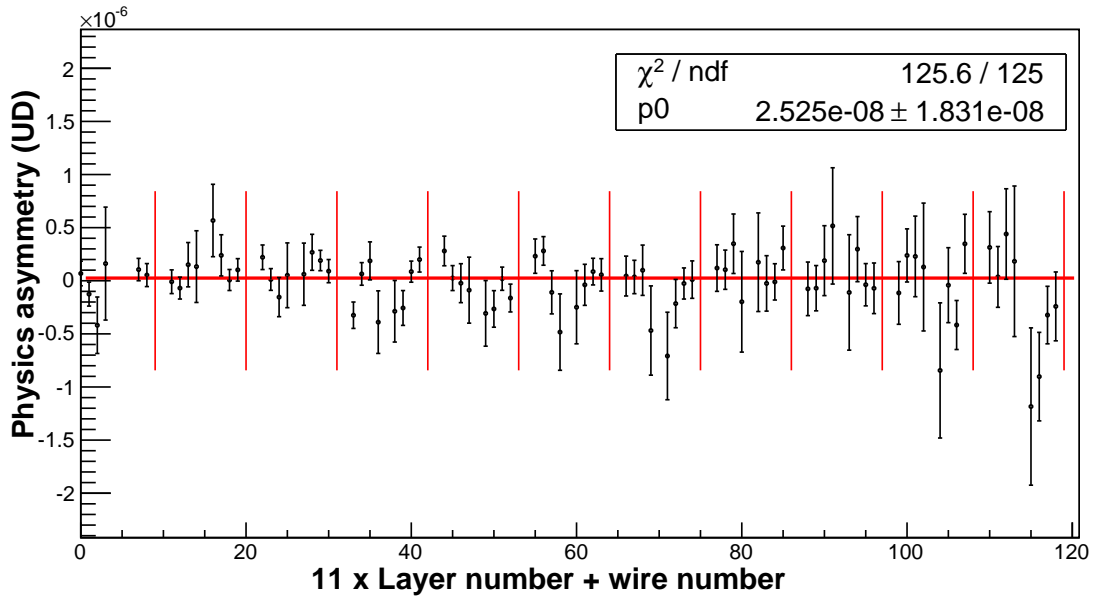


Figure 6.28: The UD physics asymmetry (uncorrected) for batch-2 after combining group  $\mathcal{A}$  and  $\mathcal{B}$ . The fit value in the box represents the uncorrected UD physics asymmetry for batch-2. The vertical red lines separate the layers of the ion chamber.

pendix D.6 and is similar to that of LR shown in Fig. 6.16.

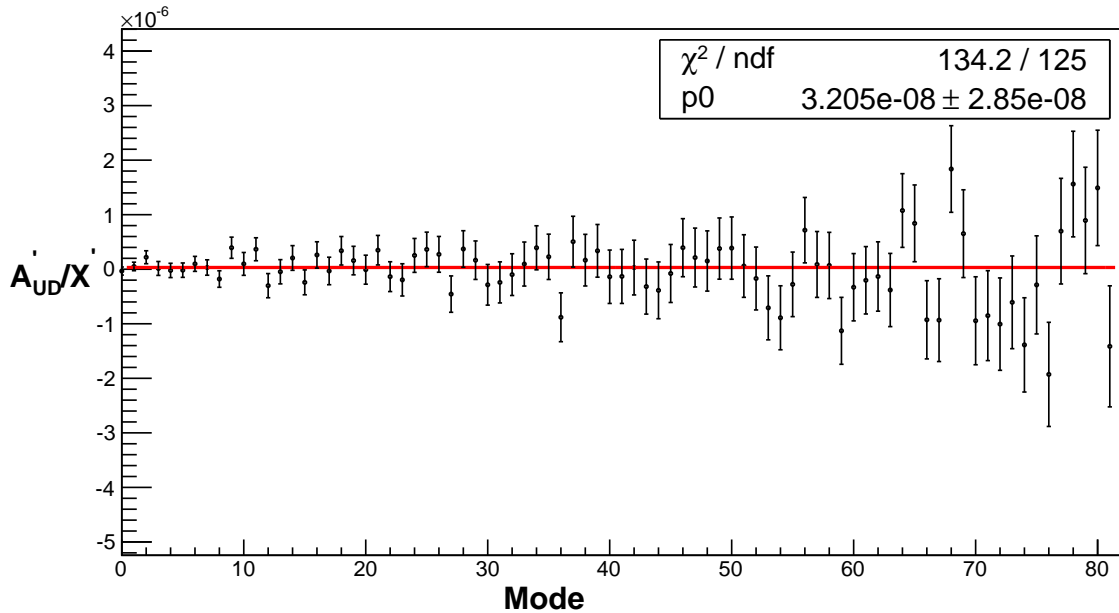


Figure 6.29: The UD physics asymmetry (corrected) for batch 2. The modes have been sorted by ascending error, i.e. most significant modes first. Only most significant modes are shown here.



Fig. 6.29 shows the correlation-corrected UD physics asymmetry using diagonalization of the covariance matrix explained in section (6.3.2). The fit value in the box represents the corrected physics asymmetry from batch 2. We analyzed all the other batches in the same way. Table (6.4) lists the asymmetries from all the UD batches. In the left most column, the number in parenthesis indicates the number of runs analyzed in that batch. We again note that the increase in error from uncorrelated

Batch no.	Physics asymmetry		Physics asymmetry $\mathcal{A} + \mathcal{B}$ (Uncorrected)		Physics asymmetry (Correlation Corrected)	
	Group: $\mathcal{A}$	Group : $\mathcal{B}$	$A_{UD} \pm \Delta A_{UD}$	$\chi^2/ndf$	$A_{UD} \pm \Delta A_{UD}$	$\chi^2/ndf$
1 (3242)	-13.16 $\pm$ 2.75	6.25 $\pm$ 2.73	-3.45 $\pm$ 1.94	142.25/125	-4.61 $\pm$ 3.04	142.07/125
2 (3679)	-6.57 $\pm$ 2.60	11.61 $\pm$ 2.58	2.52 $\pm$ 1.83	125.56/125	3.20 $\pm$ 2.85	134.22/125
3 (1954)	-1.69 $\pm$ 3.09	-7.09 $\pm$ 3.09	-4.39 $\pm$ 2.18	146.96/125	-5.13 $\pm$ 3.40	136.34/125
4 (782)	8.11 $\pm$ 5.08	1.77 $\pm$ 5.20	4.95 $\pm$ 3.64	142.68/125	5.81 $\pm$ 5.69	133.15/125
5 (729)	14.64 $\pm$ 5.07	-4.66 $\pm$ 5.13	4.99 $\pm$ 3.61	146.91/125	2.91 $\pm$ 5.62	158.73/125
6 (397)	15.53 $\pm$ 6.33	-18.76 $\pm$ 6.77	-1.62 $\pm$ 4.63	105.16/125	-2.82 $\pm$ 7.17	110.00/125
7 (1483)	14.58 $\pm$ 3.66	-13.72 $\pm$ 3.69	0.43 $\pm$ 2.60	142.05/125	-0.96 $\pm$ 4.06	145.58/125
8 (1072)	9.78 $\pm$ 4.30	-8.57 $\pm$ 4.18	0.60 $\pm$ 3.00	152.35/125	1.36 $\pm$ 4.68	125.17/125
9 (467)	-16.97 $\pm$ 6.61	14.69 $\pm$ 6.71	-1.13 $\pm$ 4.71	134.70/125	0.73 $\pm$ 7.37	142.04/125
10 (609)	-10.24 $\pm$ 5.37	7.54 $\pm$ 5.74	-1.35 $\pm$ 3.93	153.14/125	0.25 $\pm$ 6.13	154.30/125
11 (1270)	10.17 $\pm$ 3.97	-2.06 $\pm$ 4.12	4.06 $\pm$ 2.86	201.82/125	3.37 $\pm$ 4.48	182.78/125
12 (503)	-12.46 $\pm$ 6.18	-9.33 $\pm$ 5.66	-10.90 $\pm$ 4.19	158.10/125	-8.32 $\pm$ 6.50	152.74/125
13 (2464)	1.15 $\pm$ 2.82	2.56 $\pm$ 2.77	1.85 $\pm$ 1.98	171.64/125	2.02 $\pm$ 3.07	148.87/125
14 (1045)	0.26 $\pm$ 4.68	-5.80 $\pm$ 4.56	-2.77 $\pm$ 3.26	103.27/125	-1.23 $\pm$ 5.08	102.23/125
15 (1553)	-0.06 $\pm$ 3.33	9.80 $\pm$ 3.46	4.87 $\pm$ 2.40	188.27/125	5.86 $\pm$ 3.73	185.47/125
16 (1498)	11.96 $\pm$ 4.16	3.32 $\pm$ 4.42	7.64 $\pm$ 3.04	106.6/125	5.78 $\pm$ 4.77	110.42/125
17 (1559)	4.57 $\pm$ 4.14	6.39 $\pm$ 4.00	5.48 $\pm$ 2.88	133.80/125	8.20 $\pm$ 4.52	148.30/125
18 (2280)	-4.37 $\pm$ 3.81	-4.46 $\pm$ 3.70	-4.41 $\pm$ 2.65	161.43/125	-4.31 $\pm$ 4.11	163.19/125
19 (891)	-34.02 $\pm$ 6.01	44.32 $\pm$ 6.05	5.15 $\pm$ 4.26	146.76/125	4.58 $\pm$ 6.59	128.37/125
20 (1111)	18.33 $\pm$ 3.78	-23.47 $\pm$ 4.06	-2.57 $\pm$ 2.77	131.20/125	-0.42 $\pm$ 4.31	144.69/125
21 (614)	14.52 $\pm$ 5.33	5.21 $\pm$ 4.85	9.86 $\pm$ 3.60	161.43/125	9.87 $\pm$ 5.60	114.66/125

Table 6.4: UD asymmetries from all the batches. Asymmetries and their errors are presented in units of  $10^{-8}$ .

to correlated physics asymmetry is  $\sim 57\%$ , in agreement with the prediction from the simulation. Fig. 6.30 shows the corrected UD physics asymmetry from all the batches and the weighted average of them. So, the fit value in the statistics box is the corrected UD physics asymmetry considering all the UD batches.

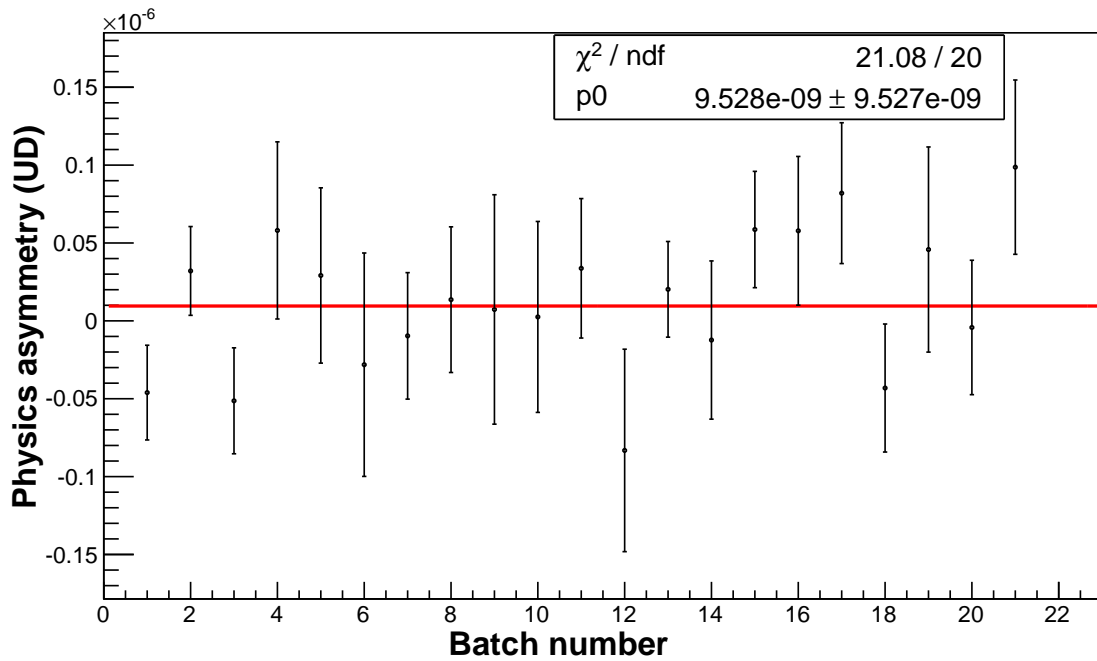


Figure 6.30: UD physics asymmetries (corrected) from all the batches

As a cross check we also follow the second data reduction approach explained in Fig. 6.17. Here, for each signal wire, we fit over all the batches to get an average uncorrected physics asymmetry of that wire. Fig. 6.31 shows such a fit for layer 1, wire 1 over all the UD batches. We have 126 such fit values with errors and corresponding  $\chi^2$  values. This gives 126  $\chi^2$  values from all the fits. Fig. 6.32 shows the distribution of  $\chi^2$ . We also fit the distribution to a chi square distribution function  $f(x)$  as shown on the plot. The box statistics in the plot shows the fit values. The number of degrees of freedom (NDF) is 20, since we have 21 batches for the UD data and one fit parameter.

The wire asymmetries, obtained from the fit over all the batches, were not corrected for correlations. As before, we go to a new basis where those asymmetries are uncorrelated and calculate the fit value in this new basis. Fig. 6.33 shows the fit outcome. The modes are sorted, and the most dominant modes have been shown in the plot. The fit value in the box represents the corrected UD physics asymmetry from all the UD batches.

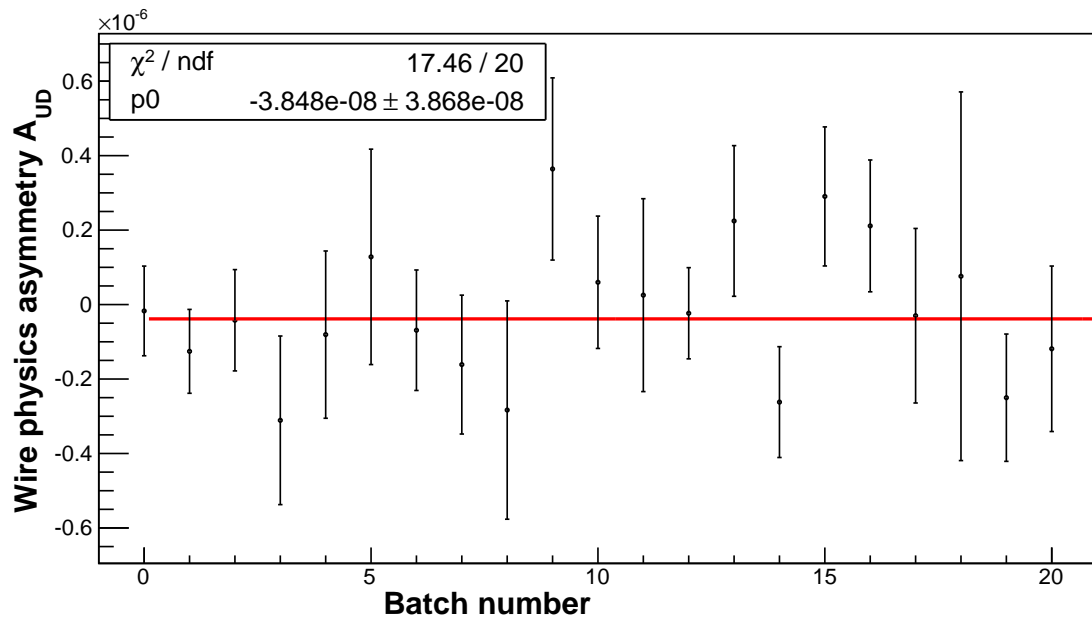


Figure 6.31: Physics asymmetry for wire 1 from all the batches. The fit value represents the wire average.

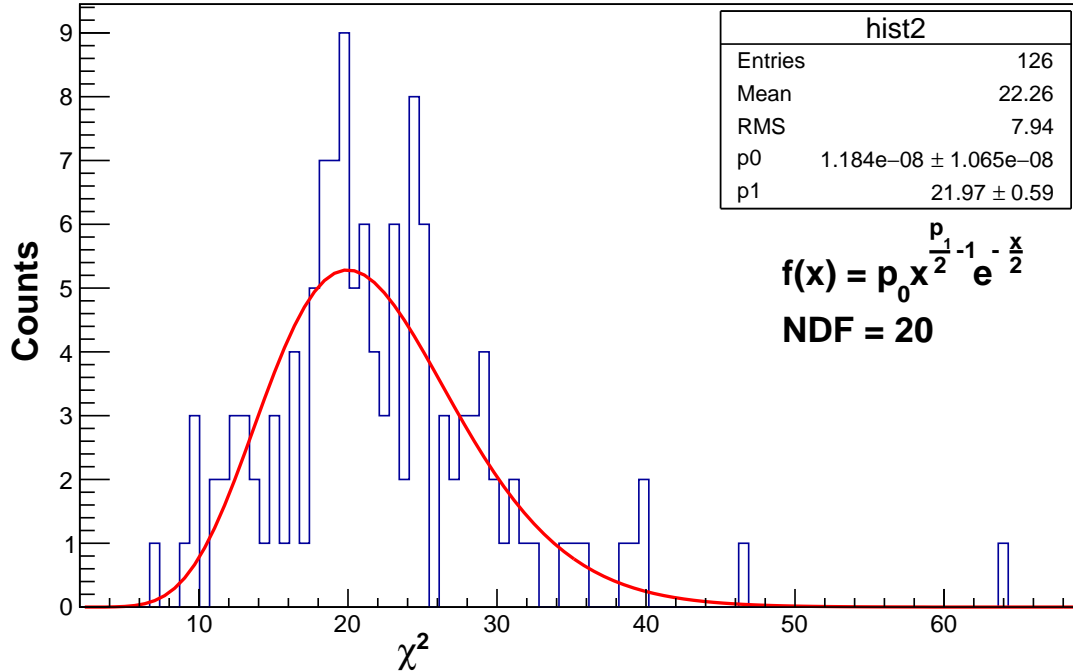


Figure 6.32: Chi square distribution from the fits. The log likelihood method was used for the fit. The function  $f(x)$  is the  $\chi^2$  distribution.

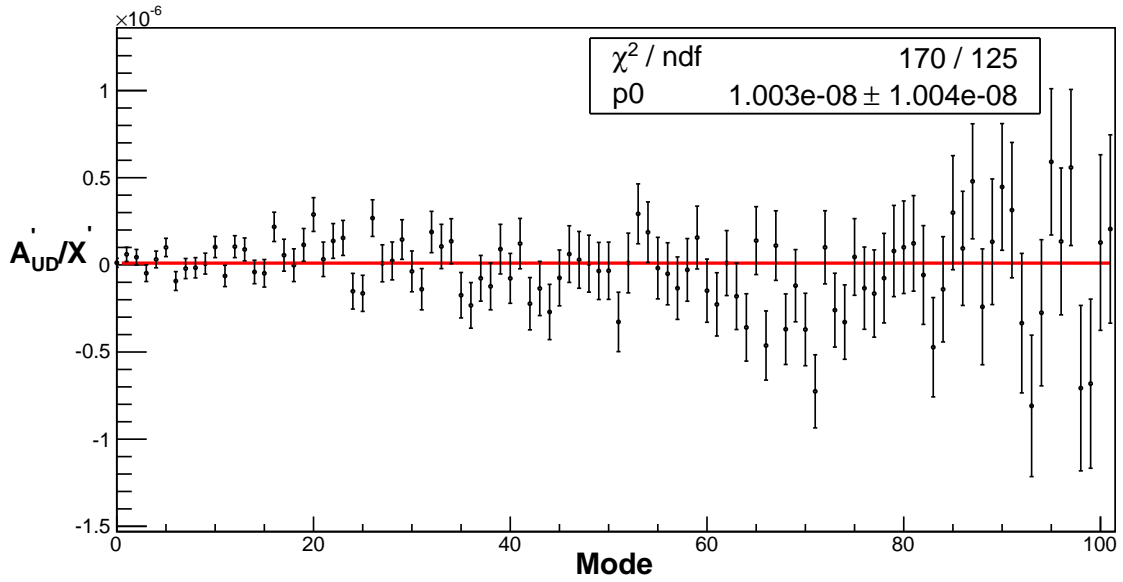


Figure 6.33: The UD physics asymmetry (corrected) using wire asymmetries obtained by fitting over all the batches. The modes have been sorted in ascending order of error, i.e. most significant modes first. Only most significant modes are shown here.

The corrected UD physics asymmetry, found in the later approach (in Fig 6.33) agrees with that to the earlier approach (in Fig. 6.30). We use the fit value of Fig. 6.30 as the final corrected UD physics asymmetry considering all the batches:

$$A_{\text{UD}} = (0.9528 \pm 0.9527) \times 10^{-8}, \quad (6.63)$$

not including the correction for polarization. After correcting for polarization using Eq. 3.18 and Eq. 3.19, our final UD physics asymmetry can be quoted as

$$A_{\text{UD}} = (1.02 \pm 1.02) \times 10^{-8}. \quad (6.64)$$

## 6.5 Systematic effects

---

We discuss possible sources of systematics that might affect our physics asymmetry. We consider the effect of the M1 asymmetry, the detector asymmetry, the instrumental asymmetry and systematics associated with the geometry factor calculations.

We get the size of the M1 asymmetry from the lower plot of Fig. 6.4 (for the UD data) and from Fig. 6.5 (for the LR data set). Here the M1 asymmetry is calculated using Eq. 6.65.

$$\text{M1 asymmetry: } A_b = \frac{M_1^\uparrow - M_1^\downarrow}{M_1^\uparrow + M_1^\downarrow} = 2.66 \times 10^{-7} \text{ (UD) and } 4.75 \times 10^{-7} \text{ (LR)}. \quad (6.65)$$

The M1 asymmetry is taken as the beam asymmetry. The detector asymmetry is constructed between two conjugate wires for the same pulse.

$$\text{Detector asymmetry: } A_d^i = \frac{Y_i - Y_{i^*}}{Y_i + Y_{i^*}} \quad (6.66)$$

where  $i$  and  $i^*$  are conjugate wire indices. Fig. 6.34 shows the distribution of detector asymmetries for all the conjugate pair of detectors.

The weight average detector asymmetry is calculated using

$$A_d = \frac{\sum_i w_i A_d^i}{\sum_i w_i}, \quad (6.67)$$

$$w_i = \delta^{-2} A_{phy}^i, \quad (6.68)$$

where  $\delta^{-2} A_{phy}^i$  is the square of the error of the wire physics asymmetry considering all runs in a single batch. This gives  $A_d = 0.0723$ . Thus we get

$$A_b A_d = 1.9 \times 10^{-8} \text{ (UD) and } 3.43 \times 10^{-8} \text{ (LR)}. \quad (6.69)$$

We use the data taken without any beam to estimate the size of the instrumental asymmetry. To calculate the instrumental asymmetry, we first note that the measured asymmetry has a contribution from the actual signal plus a contribution from the pedestal or instrumental noise as shown in equation Eq. 6.70. Thus we treat the contribution from the instrumental noise exactly in the same way we treat the physics signal.

$$A_i = \frac{Y_i^\uparrow - Y_i^\downarrow}{Y_i^\uparrow + Y_i^\downarrow} = \frac{(S_i^\uparrow + b_i^\uparrow) - (S_i^\downarrow + b_i^\downarrow)}{(S_i^\uparrow + b_i^\uparrow) + (S_i^\downarrow + b_i^\downarrow)} \approx \frac{S_i^\uparrow - S_i^\downarrow}{S_i^\uparrow + S_i^\downarrow} + \frac{b_i^\uparrow - b_i^\downarrow}{S_i^\uparrow + S_i^\downarrow} \quad (6.70)$$

where  $b_i^{\uparrow\downarrow}$  is the contribution from pedestal and  $S_i$  is the contribution from the actual signal.

$$A_{\text{inst}}^i = \frac{1}{G_i} \frac{b_i^\uparrow - b_i^\downarrow}{2S_i} \quad (6.71)$$

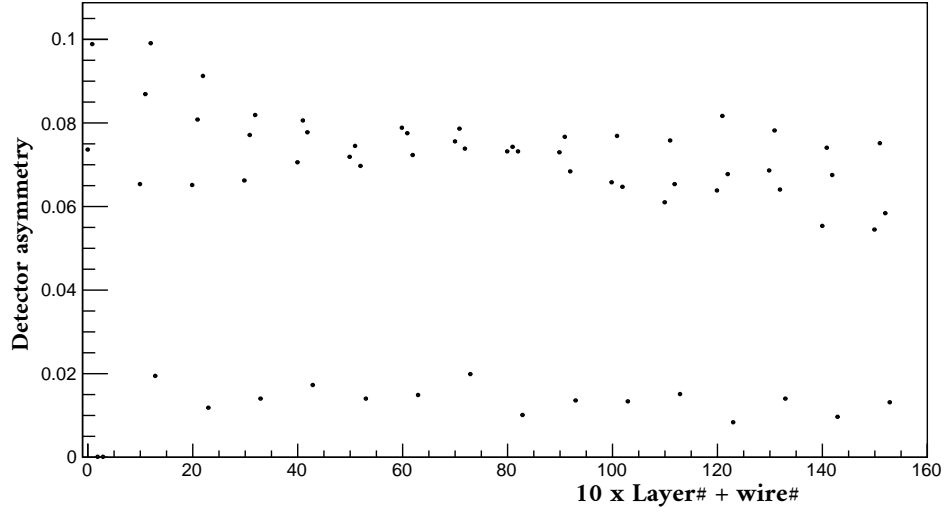


Figure 6.34: Detector asymmetry, is calculated from the signals of two conjugate wires for the same pulse.

$$A_{\text{inst}} = \frac{\sum_i w_i A_{\text{inst}}^i}{\sum_i w_i} \quad (6.72)$$

$$(\delta A_{\text{inst}})^2 = \frac{\sum_i w_i^2 (\delta A_{\text{inst}}^i)^2}{(\sum_i w_i)^2} \quad (6.73)$$

where

$$w_i = \delta^{-2} A_{\text{phy}}^i. \quad (6.74)$$

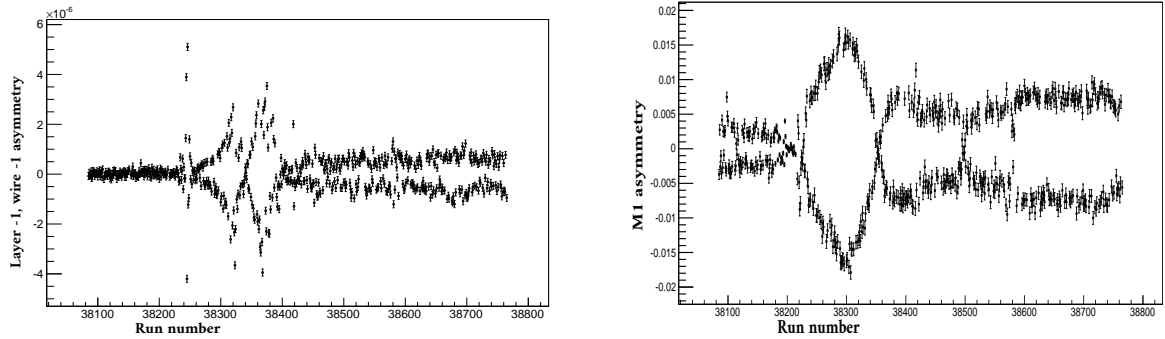
The instrumental asymmetry is normalized by the geometry factor. In Eq. 6.71 we approximated  $S_i^\uparrow \approx S_i^\downarrow = S_i$  and we use the average wire signal calculated considering all the runs as  $S_i$ . The instrumental asymmetries from all the wires are combined using the weight, which is calculated from the size of the error of the physics asymmetry corresponding to that wire. The no-beam data includes: a) runs taken during the summer when accelerator was down for longer period, b) maintenance day (every Tuesday) runs and c) accidental no beam runs taken during normal operation. From separate analysis of different groups of no-beam runs we find

$$\text{Summer runs (677 runs): } A_{\text{inst}} = (13.12 \pm 1.15) \times 10^{-9}, \quad (6.75)$$

$$\text{Tuesday runs (620 runs): } A_{\text{inst}} = (6.918 \pm 1.15) \times 10^{-9}, \quad (6.76)$$

$$\text{All runs (4383 runs): } A_{\text{inst}} = (3.14 \pm 0.60) \times 10^{-9}. \quad (6.77)$$

Fig. 6.35 shows the wire asymmetry and M1 asymmetry for no-beam data as a function of run number from the summer. This shows a phase changing pattern in the instrumental noise. Fig. 6.36 shows the correlation between the M1 asymmetry and the wire asymmetry with no-beam data.



(a) Layer-1, wire-1 asymmetry with no beam

(b) M1 asymmetry with no beam

Figure 6.35: The wire asymmetry and M1 asymmetry (with no-beam data) as a function of the run number. The summer runs have been used here. For the M1 asymmetry we used unit normalization.

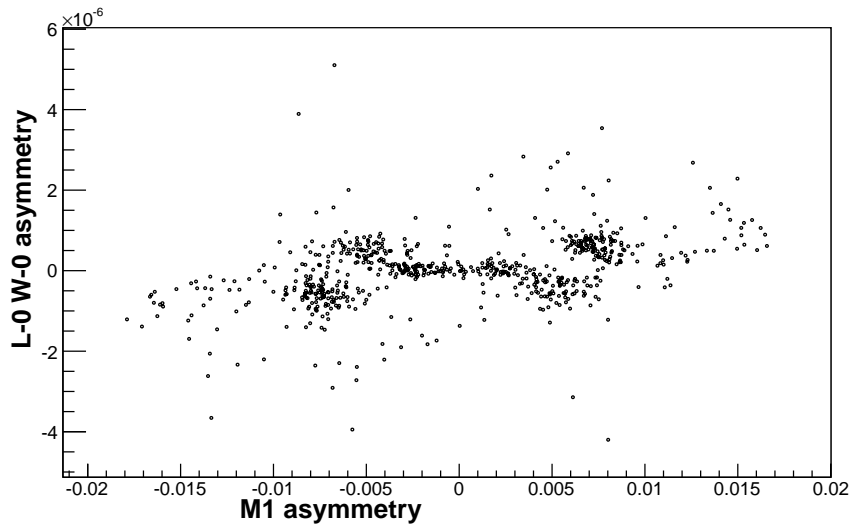


Figure 6.36: The correlation between the wire asymmetry and M1 asymmetry. Runs with no beam have been used here. For the M1 asymmetry we used unit normalization.

We see similar phase changing fluctuation in the M1 asymmetry with beam as shown in Fig. 6.37. Fig. 6.37 explains the shape of the distribution for M1 asymmetry shown in Fig. 6.4. Fig. 6.38 and Fig. 6.39 show that the calculated wire asymmetry (with

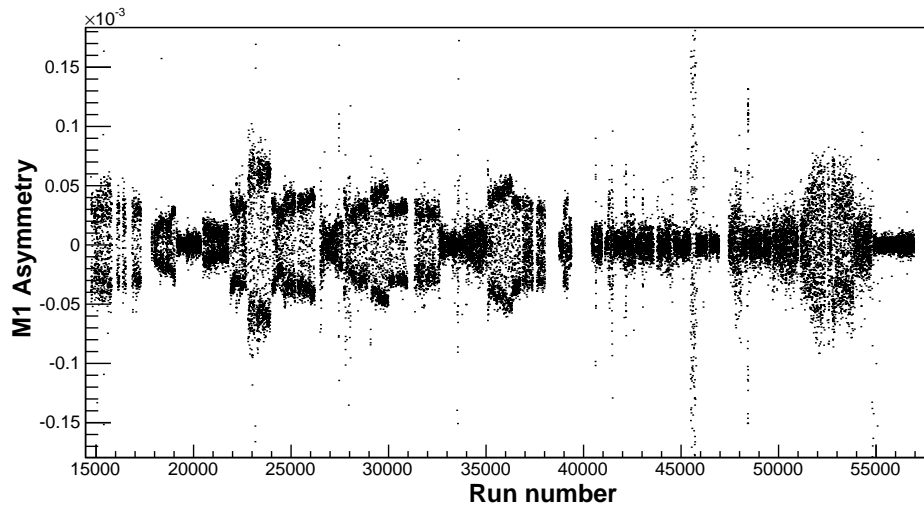


Figure 6.37: M1 asymmetry as a function of the run number (all LR and UD runs).

beam) is immune to the common mode fluctuation. Our analysis algorithm, explained in section 6.1.1, takes care of the common mode.

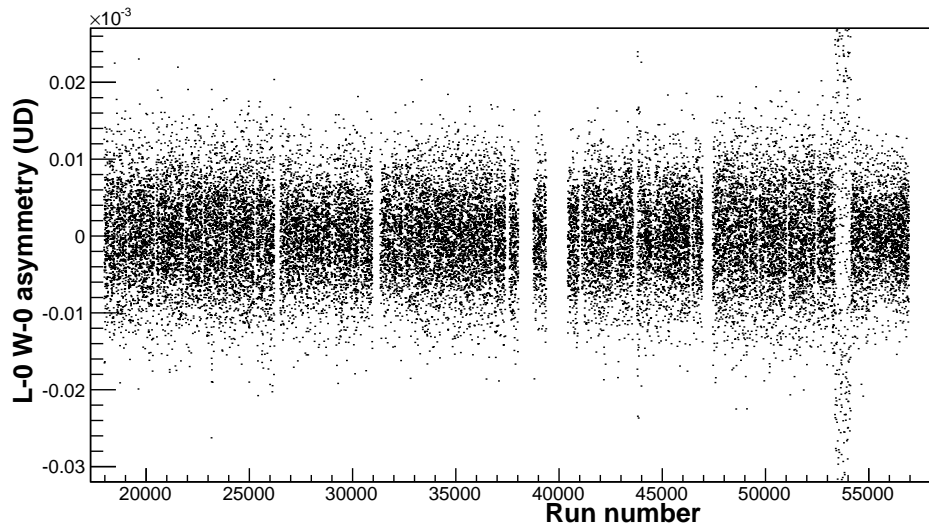


Figure 6.38: UD raw asymmetry from layer-1, wire-1 as a function of the run number.



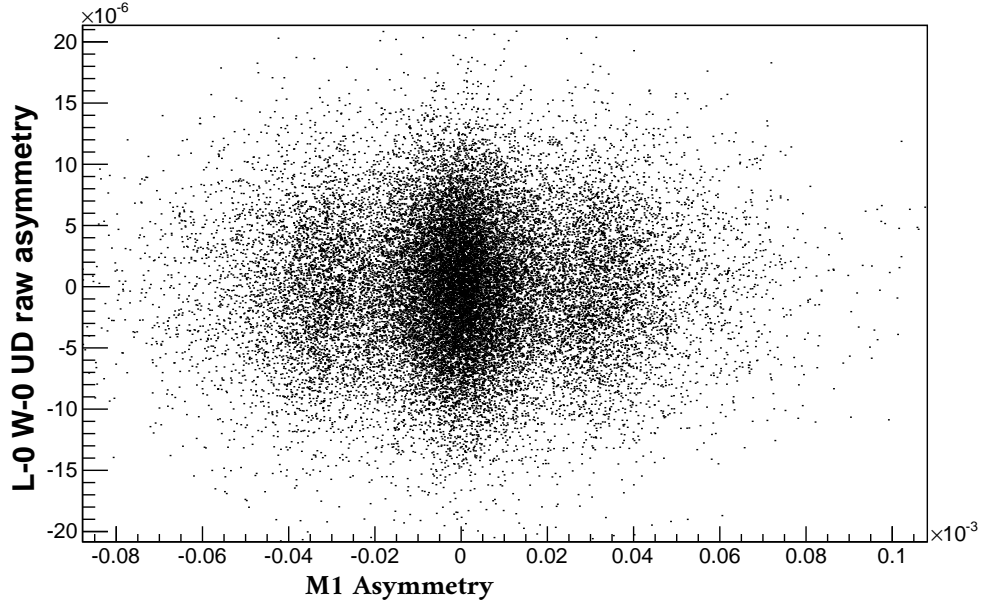


Figure 6.39: Correlation between UD raw asymmetry from layer-1, wire-1 and M1 asymmetry.

To calculate the systematics associated with the geometry factor calculation, we tuned the parameters: a) pressure, b) collimator width and c) beam centroid position used in the simulation. The tuning process provides the optimized parameter that gives lowest chi square between simulated yield and yield from the data. The geometry factors calculated with the optimized parameter were used to calculate the deviation in physics asymmetry. For pressure, we get the pressure optimization plot as shown in Fig. 6.40. From the plot

$$P = 0.47 \text{ atm} \quad P_0 = 0.491 \text{ atm}, \quad (6.78)$$

where  $P_0$  is the optimal pressure for the simulation and  $P$  is the pressure measured in the experiment which has been used to calculate the geometry factors.

$$A_{\text{UD}}(P) = 1.02 \times 10^{-8} \quad A_{\text{UD}}(P_0) = 1.0057 \times 10^{-8}. \quad (6.79)$$

This gives

$$\delta A_{\text{UD}}(P) = 1.43 \times 10^{-10}. \quad (6.80)$$

$$A_{\text{LR}}(P) = -4.41 \times 10^{-7} \quad A_{\text{LR}}(P_0) = -4.343 \times 10^{-7}. \quad (6.81)$$

This gives

$$\delta A_{\text{LR}}(P) = -6.7 \times 10^{-9}. \quad (6.82)$$

Optimization of collimator width  $y$  (half width) produces a plot as shown in Fig. 6.41 (a). From the plot we find that

$$y = 4.1 \text{ cm} \quad y_0 = 3.85 \text{ cm}. \quad (6.83)$$

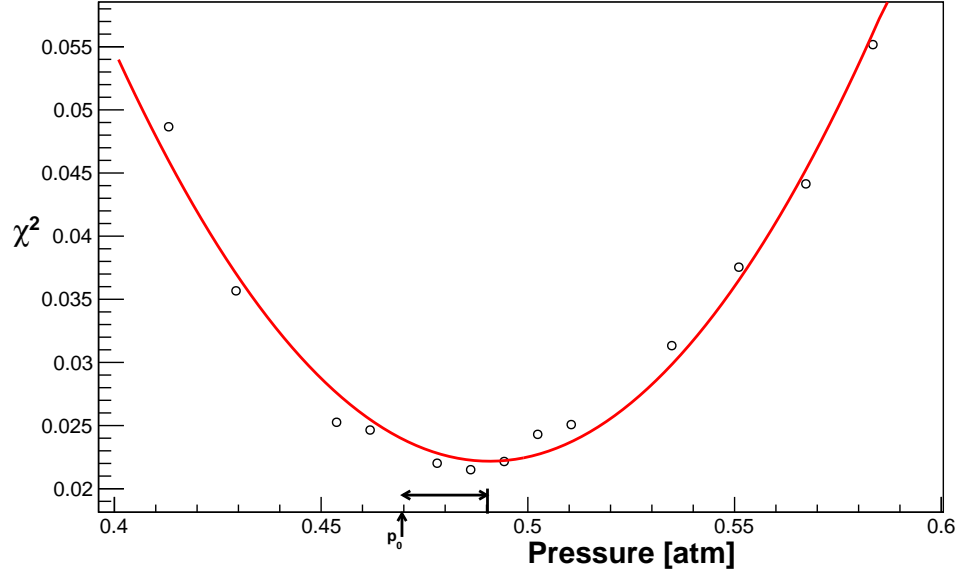
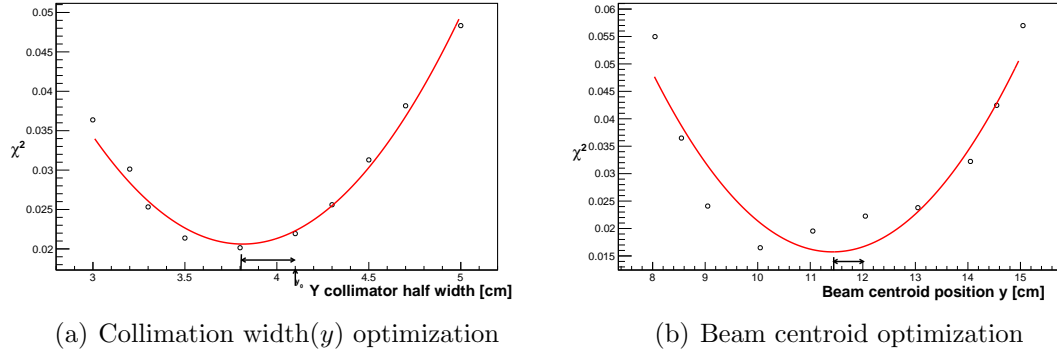


Figure 6.40: Pressure optimization in the simulation



(a) Collimation width( $y$ ) optimization

(b) Beam centroid optimization

Figure 6.41: Optimization of collimation width and beam centroid

And the corresponding geometry factors give

$$A_{UD}(y) = 1.02 \times 10^{-8} \quad A_{UD}(y_0) = 1.00711 \times 10^{-8}. \quad (6.84)$$

This gives

$$\delta A_{UD}(y) = 1.2 \times 10^{-10}. \quad (6.85)$$

For LR we find

$$A_{LR}(y) = -4.41 \times 10^{-7} \quad A_{LR}(y_0) = -4.1257 \times 10^{-7}. \quad (6.86)$$

This gives

$$\delta A_{LR}(y) = -0.28 \times 10^{-7}. \quad (6.87)$$

Similarly for the optimization of beam centroid position ( $y$ ), we get the plot shown in Fig. 6.41 (b). From this plot we get

$$y^{\text{bc}} = 12.04 \text{ cm} \quad y_0^{\text{bc}} = 11.5 \text{ cm}. \quad (6.88)$$

For UD data this gives

$$A_{\text{UD}}(y^{\text{bc}}) = 1.02 \times 10^{-8} \quad A_{\text{UD}}(y_0^{\text{bc}}) = 1.00027 \times 10^{-8}, \quad (6.89)$$

$$\delta A_{\text{UD}}(y^{\text{bc}}) = 2 \times 10^{-10}. \quad (6.90)$$

For LD data

$$A_{\text{LR}}(y^{\text{bc}}) = -4.41 \times 10^{-7} \quad A_{\text{LR}}(y_0^{\text{bc}}) = -4.2937 \times 10^{-7}, \quad (6.91)$$

$$\delta A_{\text{LR}}(y^{\text{bc}}) = -0.11 \times 10^{-7}. \quad (6.92)$$

To get the total systematic asymmetry, we add all these deviations of asymmetry in quadrature. This gives

$$\Delta A_{\text{UD}}^{\text{sys}} = 2.74 \times 10^{-10}, \quad (6.93)$$

$$\Delta A_{\text{LR}}^{\text{sys}} = 3.08 \times 10^{-8}. \quad (6.94)$$

Lastly, we briefly summarize the systematic effects from the physics background. These effects were carefully considered and calculated in the full proposal of the experiment[68, 69].

The possible physics-induced background asymmetries can be identified by their Cartesian invariants. The measurement is performed by reversing the neutron spin direction in a fixed geometry and then measuring the change in yield. Any invariant that excludes spin does not contribute to the detector asymmetry. Because  $\sigma_i \sigma_j = \delta_{ij} + i\epsilon_{ijk} \sigma_k$ , it is sufficient to consider Cartesian invariants that are linear in  $\vec{\sigma}_n$ , the spin of the neutron. We are then left with the remaining independent vectors, which are the momentum of the neutron ( $\vec{k}_n$ ) and the momentum of the proton ( $\vec{k}_p$ ). From conservation of momentum, the momentum of the proton and the momentum of the triton are opposite to each other ( $\vec{k}_T = -\vec{k}_p$ ). Table (6.5) gives a list of the most significant systematic effects for the experiment.

From table 6.5, where the PV asymmetry ( $\vec{\sigma}_n \cdot \vec{k}_p$ ) and most significant background asymmetries are shown, we see that all background contributions are well below the statistical sensitivity. The most significant background is a parity allowed  $(\vec{k}_n \times \vec{\sigma}_n) \cdot \vec{k}_p$  asymmetry. We measured the size of the parity allowed asymmetry to be  $-4.41 \times 10^{-7}$ . We kept the average beam axis  $\vec{k}_n$ , the magnetic field direction  $\vec{\sigma}_n$  and the detector wire planes  $\vec{k}_p$  all aligned within 10 mrad to suppress this background asymmetry below  $10^{-9}$ . The commissioning was confirmed to be well within the tolerance. The

Invariant	Parity	Size	Comments
$\vec{\sigma}_n \cdot \vec{k}_p$	Odd	$3 \times 10^{-7}$	Nuclear capture asymmetry
$(\vec{k}_n \times \vec{\sigma}_n) \cdot \vec{k}_p$	Even	$2 \times 10^{-10}$	Nuclear capture asymmetry
	Even	$6 \times 10^{-12}$	Mott-Schwinger scattering
$\vec{\sigma}_n \cdot \vec{B}$	Even	$1 \times 10^{-10}$	Stern-Gerlach steering
	Even	$2 \times 10^{-11}$	Boltzmann polarization of ${}^3\text{He}$
	Even	$4 \times 10^{-13}$	Neutron induced polarization of ${}^3\text{He}$
$\vec{\sigma}_n \cdot \vec{k}_n$	Odd	$1 \times 10^{-11}$	Neutron beta decay

Table 6.5: List of the systematic effects [68, 69].

other invariant,  $\vec{\sigma} \cdot \vec{B}$ , produces a spin-dependent velocity which can couple with the velocity-dependent cross-section to produce a false asymmetry. This effect was eliminated by requiring magnetic field uniformity at the level of 0.3 mG (1%) between the spin flipper and the detector. Finally the spin-dependent  $\beta$ -decay PV background is suppressed due to the small probability of decay inside the chamber, and the fact that almost all of the energy is carried by the minimum-ionizing beta particle.

# Chapter 7

## Results & discussion

---

In summarizing our result, we measured the parity conserving LR physics asymmetry to be

$$A_{\text{LR}} = (-4.41 \pm 0.56) \times 10^{-7}, \quad (7.1)$$

and found the parity violating UD physics asymmetry to be

$$A_{\text{UD}} = (1.0 \pm 1.0) \times 10^{-8}. \quad (7.2)$$

The sizes of the errors in both measurements are consistent with the predicted errors according to counting statistics in Eq. 2.1. This is the smallest absolute error in any nuclear asymmetry measurement. We did not find non-zero PV signal in our experiment, similar to the many other few-body experiments which measured a result consistent with zero. The only non-zero PV measurement in the NN system comes from the  $\vec{p}p$  system. Fig. 7.1 shows how the result from this experiment contributes in constraining the DDH coupling constants with other experiments.

Another representation is to include our result in Fig. 1.5, which shows constraints by the previously existing data. The analysis is an approximate since, n-<sup>3</sup>He is sensitive to a different linear combination of couplings. From Eq. 1.11, the n-<sup>3</sup>He result can be related to the observable as

$$(0.1 \pm 0.1) / -0.185 = h_{\pi}^1 - 0.12h_{\rho}^1 - 0.27h_{\omega}^1 + 0.21h_{\rho}^0 + 0.12h_{\omega}^0, \quad (7.3)$$

where we have neglected  $h_{\rho}^2$  term as it has negligible contribution according to Eq. 1.11. Eq. 7.3 can be rearranged as

$$-0.21 \times (h_{\rho}^0 + 0.6h_{\omega}^0) = h_{\pi}^1 - 0.12h_{\rho}^1 - 0.27h_{\omega}^1 + (0.54 \pm 0.54). \quad (7.4)$$

If we take

$$y = -(h_{\rho}^0 + 0.6h_{\omega}^0) \sim -(h_{\rho}^0 + 0.7h_{\omega}^0), \quad (7.5)$$

and

$$x = h_{\pi}^1 - 0.12h_{\rho}^1 - 0.27h_{\omega}^1 \sim h_{\pi}^1 - 0.12h_{\rho}^1 - 0.18h_{\omega}^1, \quad (7.6)$$

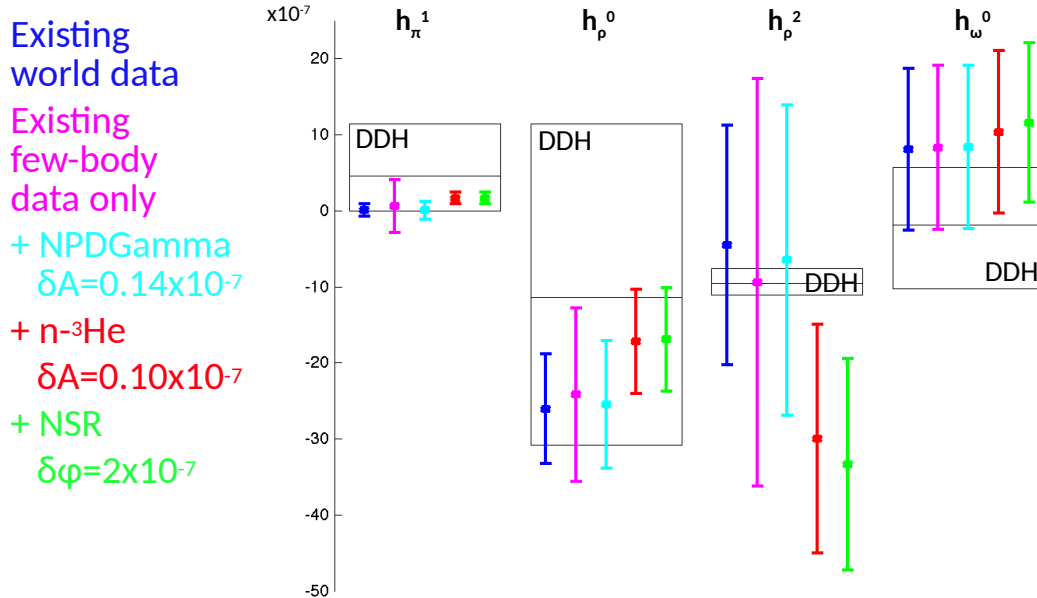


Figure 7.1: Contribution of the  $n$ - $^3\text{He}$  experiment in constraining the coupling constants. The spread of the rectangular box indicates the DDH ranges. Figure courtesy of Chris Crawford.

we can rewrite Eq. 7.4 as

$$y = 4.8x + (2.6 \pm 2.6). \quad (7.7)$$

If  $x = 0$ ,  $y_{\max} = 5.2$ ,  $y_{\min} = 0.0$

If  $y = 35$ ,  $x_{\max} = 7.3$ ,  $x_{\min} = 6.2$

This gives the green band on Fig. 7.2.

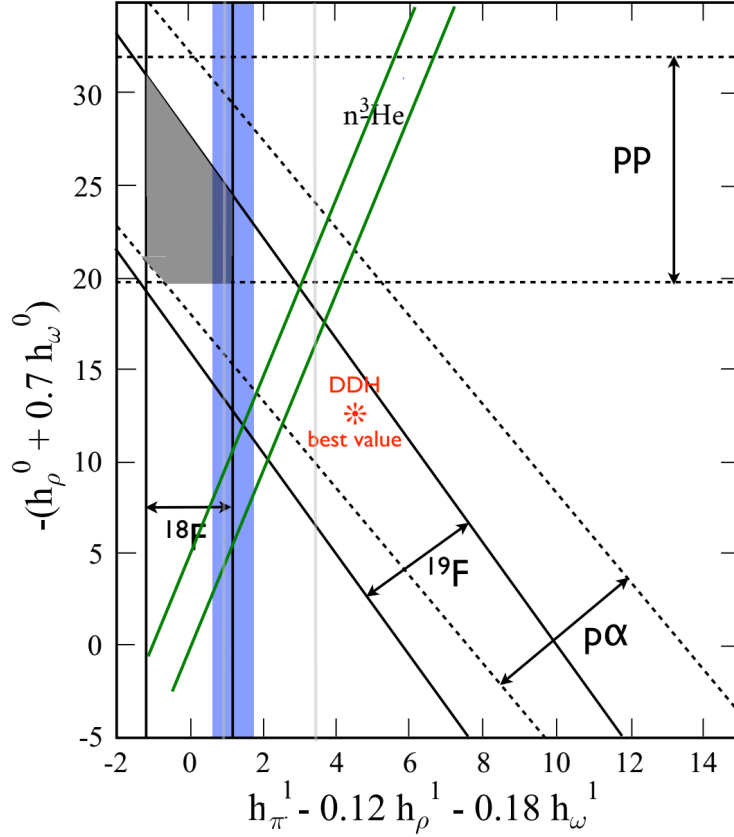


Figure 7.2: The  $n$ - ${}^3\text{He}$  result on the DDH plot

From a third perspective, we note that there are five low energy weak couplings irrespective of the descriptions (LECs, DDH or Girlanda coefficients) as shown in Table 7.1. In a recent paper [70], Susan Gardner *et al.* analyzed the experimental implications of HWI experiments in terms of LECs in the large- $N_c$  expansion inspired by the work of [71],[72], where  $N_c$  is the number of colors in QCD. In the analysis, 5D space of LECs  $\Lambda$  (along 5 orthogonal axes) are considered to two new principle axes, along 2D  $I = 0$  plane and  $I = 2$  direction

$$\begin{aligned} \Lambda_0^+ &\equiv \frac{3}{4}\Lambda_0^{3S_1-1P_1} + \frac{1}{4}\Lambda_0^{1S_0-3P_0} \sim N_c, \\ \Lambda_2^{1S_0-3P_0} &\sim N_c, \end{aligned} \quad (7.8)$$

and the other three axes are suppressed in the  $1/N_c$  counting

$$\begin{aligned} \Lambda_0^- &\equiv \frac{1}{4}\Lambda_0^{3S_1-1P_1} - \frac{3}{4}\Lambda_0^{1S_0-3P_0} \sim 1/N_c, \\ \Lambda_1^{1S_0-3P_0} &\sim \sin^2 \theta_w, \\ \Lambda_1^{3S_1-3P_1} &\sim \sin^2 \theta_w. \end{aligned} \quad (7.9)$$

These three directions contribute in relative order  $\sim 1/N_c^2$ . The weak mixing angle imposes additional suppression for  $\Delta I = 1$ ,  $\sin^2 \theta_w/N_c \sim 12$ . Table 7.1 also provides

the large- $N_c$  expansion for LECs  $\Lambda$ , DDH and Girlanda coefficients. The two important things to note here are - a)  $\mathcal{G}_1 \sim \tilde{\mathcal{G}}_1 \sim N_c$  and  $\mathcal{G}_1 + 2\tilde{\mathcal{G}}_1 \sim 1/N_c$ , and b)  $\Lambda_0^+$  and  $\Lambda_2^{1S_0-3P_0}$  are the only dominant ones which are orthogonal to each other. The NPDGamma experiment will test the smallness of  $\Lambda_2^{1S_0-3P_0}$ .

Coefficient	DDH	Girlanda	Large $N_c$
$\Lambda_0^+ \equiv \frac{3}{4}\Lambda_0^{3S_1-1P_1} + \frac{1}{4}\Lambda_0^{1S_0-3P_0}$	$-g_\rho h_\rho^0(\frac{1}{2} + \frac{5}{2}\chi_\rho) - g_\omega h_\omega^0(\frac{1}{2} - \frac{1}{2}\chi_\omega)$	$2\mathcal{G}_1 + \tilde{\mathcal{G}}_1$	$\sim N_c$
$\Lambda_0^- \equiv \frac{1}{4}\Lambda_0^{3S_1-1P_1} - \frac{3}{4}\Lambda_0^{1S_0-3P_0}$	$g_\omega h_\omega^0(\frac{3}{2} + \chi_\omega) + \frac{3}{2}g_\rho h_\rho^0$	$-\mathcal{G}_1 - 2\tilde{\mathcal{G}}_1$	$\sim 1/N_c$
$\Lambda_1^{1S_0-3P_0}$	$-g_\rho h_\rho^1(2 + \chi_\rho) - g_\omega h_\omega^1(2 + \chi_\omega)$	$\mathcal{G}_2$	$\sim \sin^2 \theta_w$
$\Lambda_1^{3S_1-3P_1}$	$\frac{1}{\sqrt{2}}g_{\pi NN}h_\pi^1(\frac{m_\rho}{m_\pi})^2 + g_\rho(h_\rho^1 - h_\rho^1) - g_\omega h_\omega^1$	$2\mathcal{G}_6$	$\sim \sin^2 \theta_w$
$\Lambda_2^{1S_0-3P_0}$	$-g_\rho h_\rho^2(2 + \chi_\rho)$	$-2\sqrt{6}\mathcal{G}_5$	$\sim N_c$

Table 7.1: The relationship between LECs  $\Lambda$ , DDH and Girlanda coefficients [70]. The right most column shows the large  $N_c$  expansion.

In the leading order approximation, the experimental constraints on large- $N_c$  LECs are

$$\begin{aligned}
\frac{2}{5}\Lambda_0^+ + \frac{1}{\sqrt{6}}\Lambda_2^{1S_0-3P_0} &= 419 \pm 43 & A_L(\vec{p}p), \\
1.3\Lambda_0^+ &= 930 \pm 253 & A_L(\vec{p}\alpha), \\
0.92\Lambda_0^+ &= 661 \pm 169 & A_\gamma(^{19}\text{F}), \\
\Lambda_0^+ + 0.48\Lambda_2^{1S_0-3P_0} &= 1063 \pm 518 & A_L(\vec{p}p)|_{221\text{MeV}}.
\end{aligned} \tag{7.10}$$

For the n- $^3\text{He}$ , based on the calculation by Viviani et al. [30]

$$\frac{364}{10^{-8}}A_p = -\Lambda_0^+ + 0.227\Lambda_2^{1S_0-3P_0}, \tag{7.11}$$

where the leading order approximation has been applied. Thus all the other experiments give contribution to  $\Lambda_0^+$  and  $\Lambda_2^{1S_0-3P_0}$  with the same sign (have negative slopes). An important feature of the n- $^3\text{He}$  experiment is that it gives contribution with the opposite sign (has positive slope). It helps to isolate the orthogonal combination of  $\Lambda_0^+$  and  $\Lambda_2^{1S_0-3P_0}$ . Because the n- $^3\text{He}$  is predominantly sensitive to  $h_\pi^1$ , it does not have the same sensitivity as pp scattering, but it is still in the opposite direction. Using the n- $^3\text{He}$  result, Eq. 7.11 becomes

$$-\Lambda_0^+ + 0.227\Lambda_2^{1S_0-3P_0} = (364 \pm 364). \tag{7.12}$$

Fig. 7.3 shows the constraints on the leading order large- $N_c$  solutions by the n- $^3\text{He}$  experiment with other experiments (using Eqs. 7.10 and 7.12). The blue band gives the constraint from  $A_L(\vec{p}p)$  at 15 MeV and 45 MeV energies, the red band for  $A_L(\vec{p}p)$  at 221 MeV, the orange band for  $A_L(\vec{p}\alpha)$ , the green band for  $A_\gamma(^{19}\text{F})$  and the brown band comes from the result ( $A_p$ ) of the n- $^3\text{He}$  experiment. We did not show the lattice QCD result since it has not happened. We see that the band added by the n- $^3\text{He}$  experiment is one  $\sigma$  away from the overlap of the bands by other experiments.



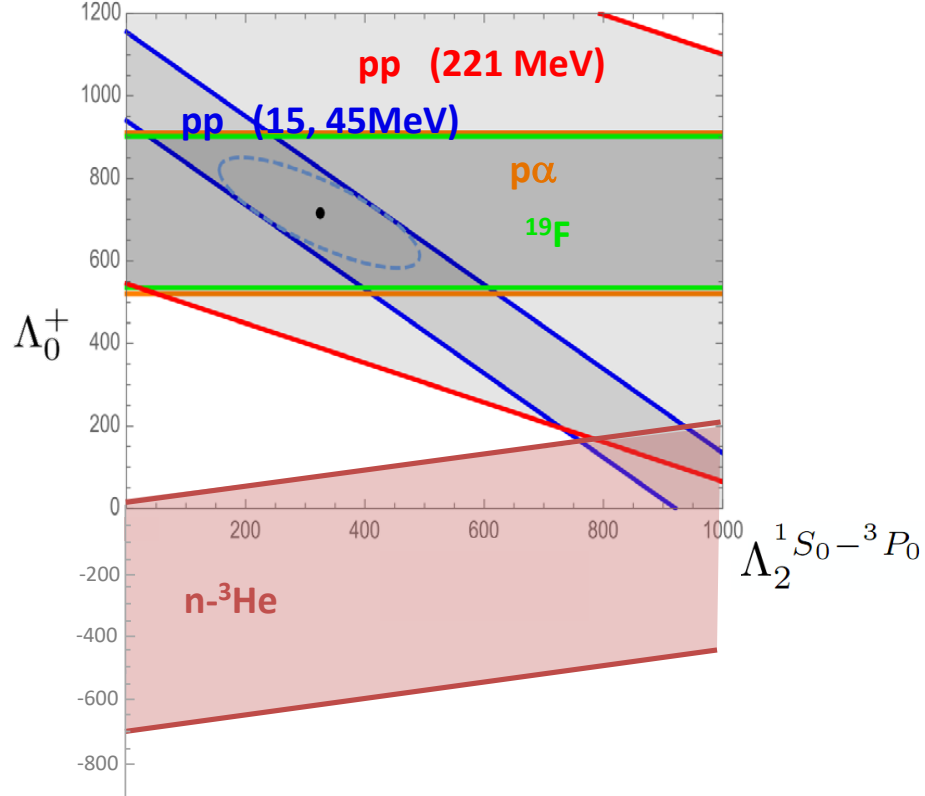


Figure 7.3: Constraints on the leading order large- $N_c$  solutions by different experiments. The LECs are presented in units of  $10^{-7}$ .

Thus Figs. 7.1, 7.2 and 7.3 represent the physics implications of the result from the  $n$ - ${}^3\text{He}$  experiment from three different perspectives. The  $n$ - ${}^3\text{He}$  result, with an expected result from the NPDGamma experiment [73] with higher precision, has the potential to enable us to identify a common area of overlap between the results from all few body experiments in Fig. 7.2 which might not be far from the predicted DDH best value. Taking into account all the implications, the result of the  $n$ - ${}^3\text{He}$  experiment makes a very important contribution to our understanding of the hadronic parity non-conservation.

# Appendices

# Appendix A

## List of n-<sup>3</sup>He parameters

---

### In normal operation:

Chopper 1 Phase: 14.045 CW

Chopper 2 Phase: 0.245 CCW

T<sub>0</sub> Delay :13.5 ms

DAQ dead time: 0.96 ms (detector data) and 0.430 ms (M1 and SFRF data)

Distance between moderator and detector front face: 18 m (approx)

Vertical B-field(Guide field) value:  $-9.14 \pm 0.02$  Gauss.

Number of time bin per event for the detector data: 49

Number of time bin per event for the M1 data: 1624

Width of each detector data time bin: 320  $\mu$  sec.

Width of each M1 data time bin: 10  $\mu$  sec

Each run length: 25000 T<sub>0</sub> (events) (in raw file)

Pressure in the chamber: 0.47 atm (approx)

Opening for Collimator:

*x*-axis: 10 cm

*y*-axis: 8.2 cm

In LR mode the *x* and *y* axis widths are interchanged.

Number of detector wires per layer: 9

Number of detector layers: 16

HV applied to the ion chamber: -353 V.

Run number range: 14785 - 61000

# Appendix B

## Spin flipper

---

### B.1 Time evolution of $\mu_z$

---

To get the time evolution of  $\mu_z(t)$ , we consider the situation in the rotating frame illustrated in Fig. 3.3. In this case, the effective magnetic field is  $\bar{B}_r$ . The magnetic moment starts out along the  $z$  axis and precesses around  $\bar{B}_r$ . The  $z$ -component of the moment oscillates with amplitude  $\mu \sin^2 \alpha$ , where  $\alpha$  is the opening angle of the cone. At resonance,  $\bar{B}_r$  lies along the  $x$  axis and  $\bar{\mu}$  precesses in the plane normal to it. The amplitude of the  $\mu_z$  oscillation is then at its maximum value of  $\mu$ .

In Fig. 3.3, D is the initial position of  $\bar{\mu}$  i.e.  $\bar{\mu}(0)$ . C is the position of  $\bar{\mu}$  at time  $t$ .  $\angle DAC = \theta = \omega_r t$  is the angular displacement in time  $t$ .

In Fig. 3.3,  $CA \perp OA$ ,  $CG \perp AG$ ,  $GH \perp AF$ ,  $GE \perp DF$ ,  $CE \perp OD$ .

From Fig. 3.3,  $\angle AOD = \angle COD = \angle GAH = \alpha$

Here,  $\mu_z(t)$  oscillates about the point F along  $z$ -axis.

$$\begin{aligned} DF = FM &= \text{amplitude of oscillation} \\ &= (\mu \sin \alpha) \sin \alpha = \mu \sin^2 \alpha \end{aligned}$$

Projection of  $\bar{\mu}$  on  $\bar{B}_r$ ,  $OA = \mu \cos \alpha$ .

Projection of OA on  $z$ -axis,  $OF = OA \cos \alpha = \mu \cos^2 \alpha$ .

$AC = \mu \sin \alpha$ , and  $AG = AC \cos \theta = \mu \sin \alpha \cos \theta$

Oscillating part of  $\mu$ , along  $z$ -axis,  $EF = GH = AG \sin \alpha = \mu \sin \alpha \cos \theta \sin \alpha$

$EF = GH = \mu \sin^2 \alpha \cos \omega_r t$

At time  $t$  ( at point C), the component of  $\bar{\mu}(t)$  along  $z$  -axis

$$\mu_z(t) = OF + EF,$$

$$\mu_z(t) = \mu \cos^2 \alpha + \mu \sin^2 \alpha \cos \omega_r t, \quad (\text{B.1})$$

$$\mu_z(0) = \mu \cos^2 \alpha + \mu \sin^2 \alpha = \mu.$$

From Eq. B.1

$$\mu_z(t) = \mu_z(0)(\cos^2 \alpha + \sin^2 \alpha \cos \omega_r t). \quad (\text{B.2})$$

Now, we express  $\cos^2 \alpha$  and  $\sin^2 \alpha$  in terms of  $\omega$ ,  $\omega_0$  and  $B$ .

From Fig(3.3),  $ON = (B_0 - \frac{\omega}{\gamma})$ ,  $NQ = B$  and  $OQ = B_r = \sqrt{B^2 + (B_0 - \frac{\omega}{\gamma})^2}$ .

From Fig(B.1)  $\bar{B}^2 = B^2 + B_0^2$ , which gives,  $\omega_0 = \gamma B_0$ .

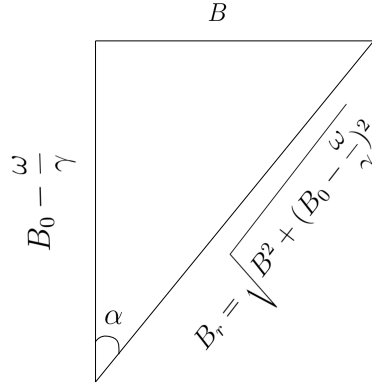


Figure B.1: Field components in rotating frame

Now,

$$\begin{aligned} \cos^2 \alpha &= \frac{(B_0 - \frac{\omega}{\gamma})^2}{B^2 + (B_0 - \frac{\omega}{\gamma})^2} \\ &= \frac{\gamma^2 (B_0 - \frac{\omega}{\gamma})^2}{\gamma^2 B^2 + \gamma^2 B_0^2 - 2B_0 \omega \gamma + \omega^2}, \end{aligned}$$

$$\cos^2 \alpha = \frac{(\omega - \omega_0)^2}{\gamma^2 B^2 + (\omega - \omega_0)^2}, \quad (\text{B.3})$$

$$\sin^2 \alpha = 1 - \cos^2 \alpha = \frac{\gamma^2 B^2}{\gamma^2 B^2 + (\omega - \omega_0)^2}. \quad (\text{B.4})$$

Using Eq. B.3 and Eq. B.4 in Eq. B.2 we get

$$\mu_z(t) = \mu_z(0) \left[ \frac{(\omega_0 - \omega)^2}{(\omega_0 - \omega)^2 + \gamma^2 B^2} + \frac{\gamma^2 B^2 \cos \omega_r t}{(\omega_0 - \omega)^2 + \gamma^2 B^2} \right]. \quad (\text{B.5})$$

# Appendix C

## Simulation

---

### C.1 M1 signal window

---

#### 1. Getting the TOF window for the M1 signal:

Converting the TOF on  $x$ -axis to neutron energy on the same axis.

$T_0$  delay = 13.5 ms

M1 data time bin = 10  $\mu$  sec.

Dirty DAQ dead time = 0.430 milli sec

So, total time of flight,  $t = (13.5 + 0.430 + i \times 0.010) \times 10^{-3}$  sec =  $(13.93 + i \times 0.010) \times 10^{-3}$  sec,

where  $i$  is the time bin in the M1 spectrum.

For any particular window

TOF<sub>min</sub> =  $13.94 \times 10^{-3}$  sec,

TOF<sub>max</sub> =  $30.17 \times 10^{-3}$  sec.

#### 2. Getting neutron energy window for the M1 signal:

Distance between the moderator and the detector front end  $d = 18.0$  m.

Mass of neutron  $m_n = 1.6750 \times 10^{-27}$  Kg.

So neutron velocity,  $v = \frac{d}{t}$ .

Neutron energy,

$$\begin{aligned} E_n &= \frac{1}{2} m_n v^2 \\ &= \frac{1}{2} \times 1.6750 \times 10^{-27} \text{kg} \times \left[ \frac{18.0 \text{ m}}{(13.93 + 0.01 \times i) \times 10^{-3} \text{sec}} \right]^2 \\ &= \frac{2.7135 \times 10^{-19} \text{Joule}}{(13.93 + 0.01 \times i)^2} \\ &= \frac{2.7135 \times 10^{-19} \times 6.242 \times 10^{21} \text{ meV}}{(13.93 + 0.01 \times i)^2} \end{aligned}$$

$$\frac{1693.767 \text{ meV}}{(13.93 + 0.01 \times i)^2},$$

where  $i = 1, 2, 3 \dots \dots 1624$  (The time bin number for the M1 signal).

Thus  $E_n^{max} = 8.716 \text{ meV}$ ,

and  $E_n^{min} = 1.861 \text{ meV}$ .

### 3. Getting wave length window for M1 signal

Wave length is related to the velocity as

$$\begin{aligned} \lambda &= \frac{h}{p} = \frac{h}{m_n v} = \frac{h}{m_n \frac{d}{t}} = \frac{ht}{m_n d} \\ &= \frac{6.6261 \times 10^{-34} \times (13.93 + 0.01 \times i) \times 10^{-3}}{1.6750 \times 10^{-27} \times 18.0} \text{ m} \\ &= \frac{6.6261 \times 10^{-27} \times (13.93 + 0.01 \times i)}{1.6750 \times 10^{-27} \times 18.0} \text{ \AA}^0 \\ &= 0.2198 \times (13.93 + 0.01 \times i) \text{ \AA}, \end{aligned}$$

where  $i = 1, 2, 3, 4 \dots \dots 1624$  ( M1 signal time bin number).

Thus

$$\lambda_n^{min} = 3.064 \text{ \AA},$$

$$\lambda_n^{max} = 6.63 \text{ \AA}.$$



# Appendix D

## Data analysis

---

### D.1 Parity conserving asymmetry

---

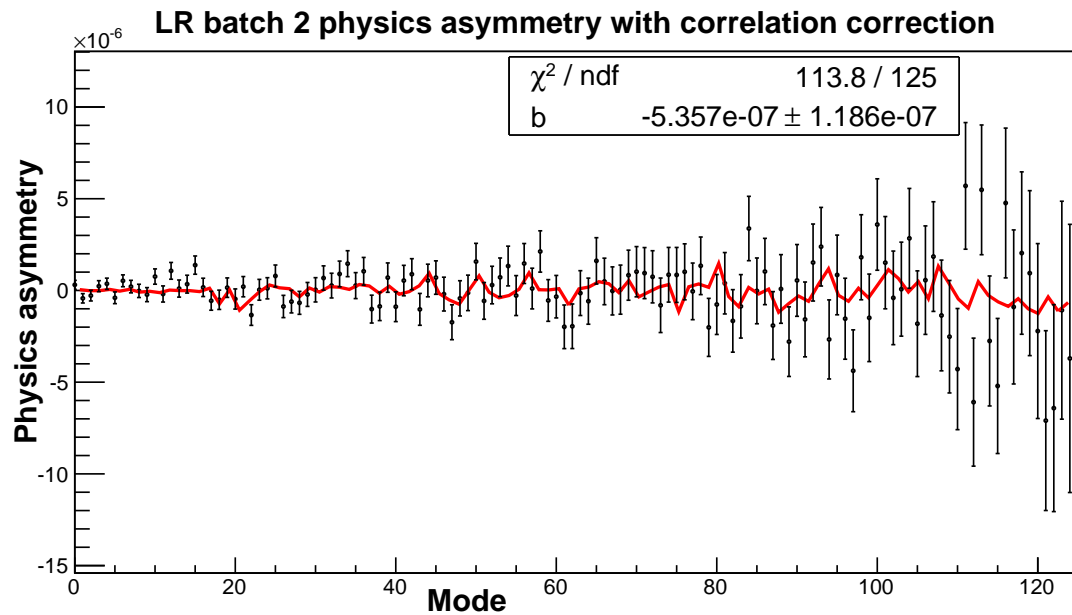


Figure D.1: Fit with covariance for LR batch-2 data. Alternative approach of the fit

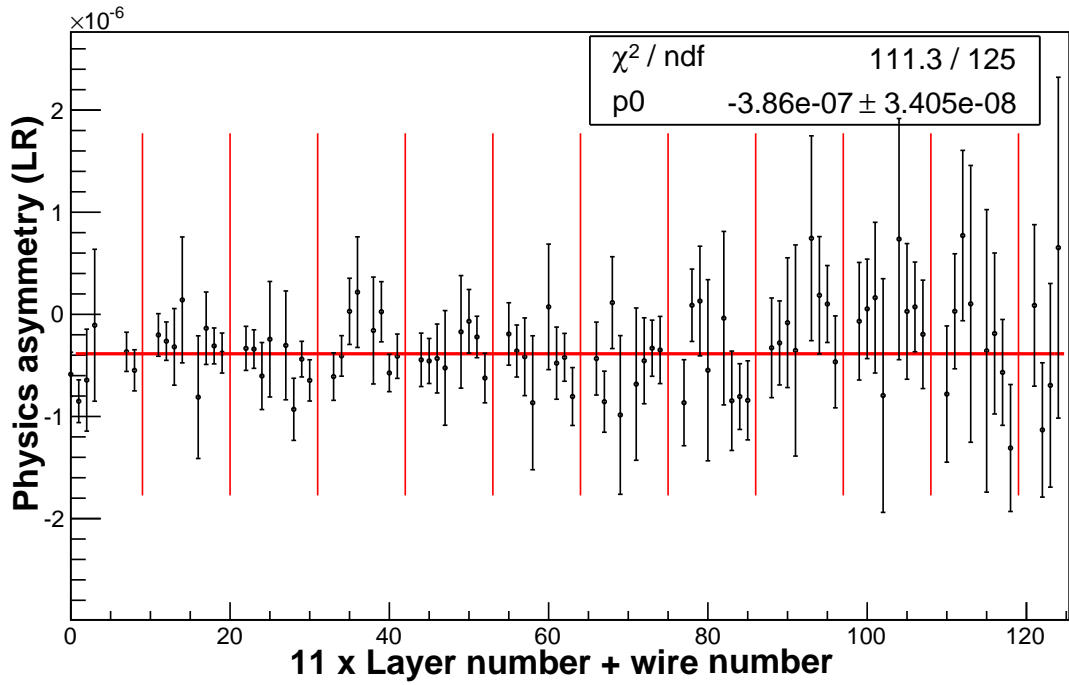


Figure D.2: LR physics asymmetry (uncorrected) considering all the runs in a single batch

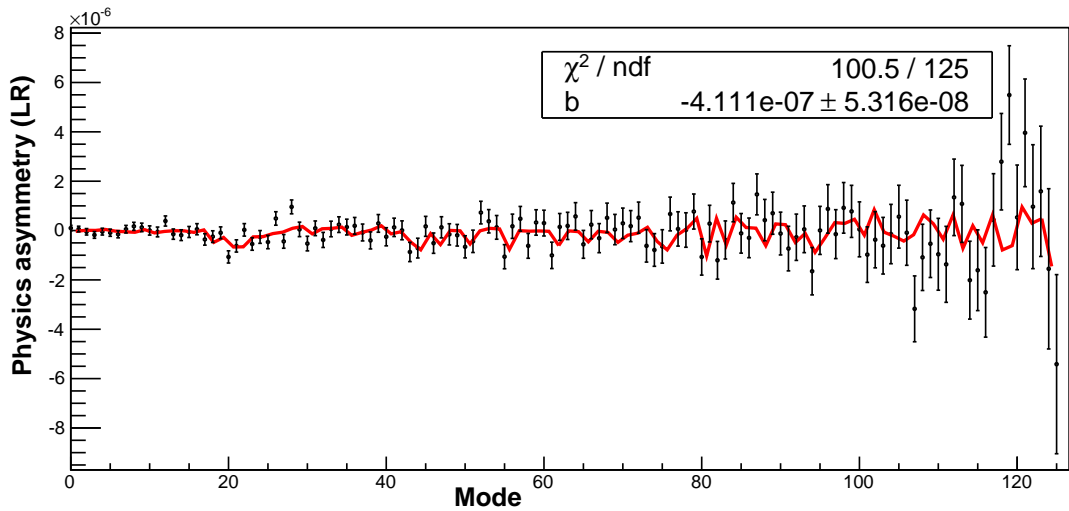


Figure D.3: LR physics asymmetry (corrected) using average wire asymmetry which is obtained by fitting over all the batches.

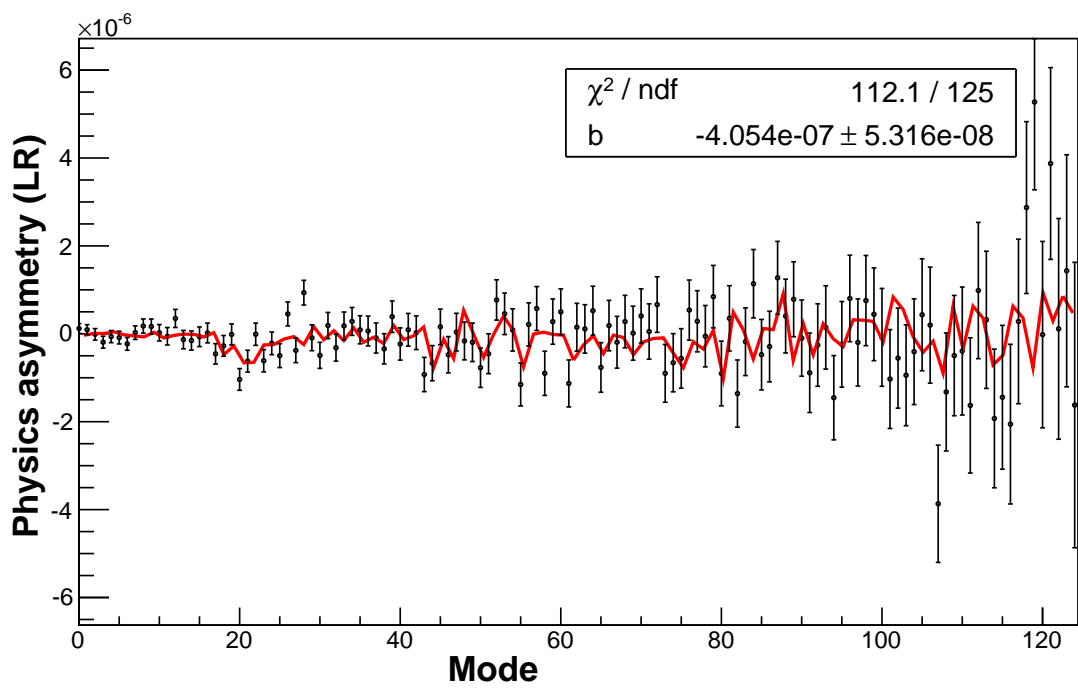


Figure D.4: LR physics asymmetry (corrected) considering all the runs in a single batch.

## D.2 Parity violating asymmetry

---

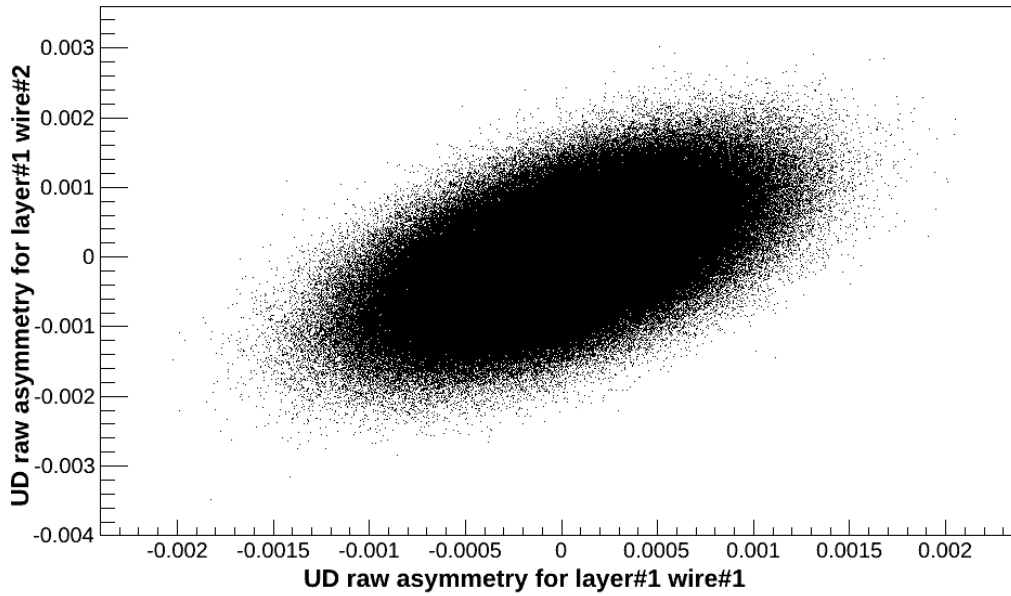


Figure D.5: Raw asymmetry correlation between wires. Here the correlation is presented between layer-1 wire-1 and layer-1 wire-2 raw asymmetries for UD case

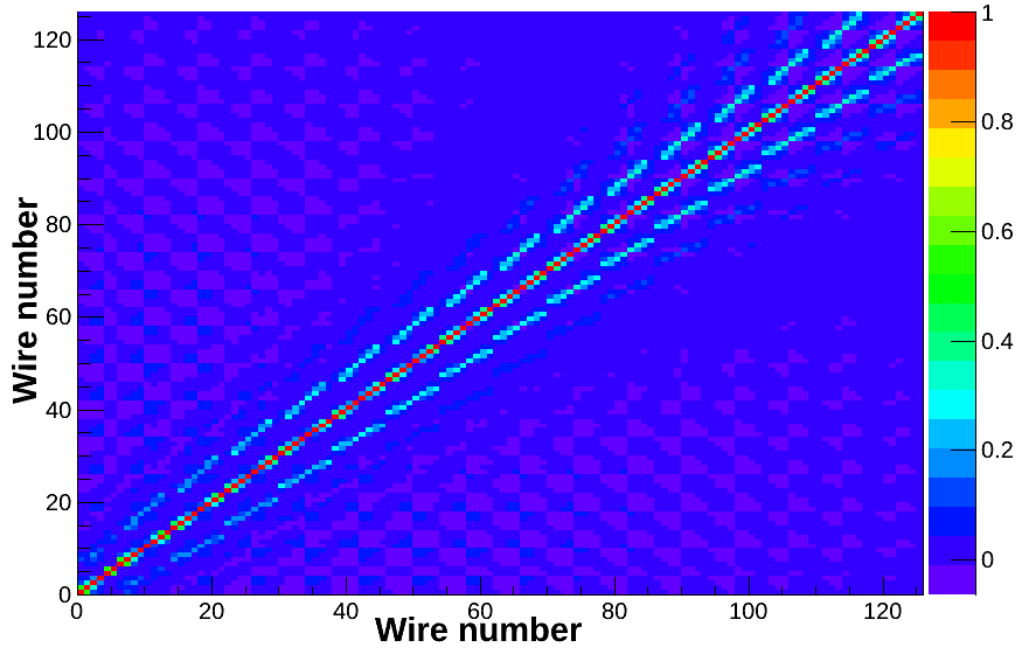


Figure D.6: Physics asymmetry correlation between wires from UD batch-1 data. The color represent the correlation coefficient  $\rho$  defined in Eq. 6.32. The labels “wire number” along the axes here actually represent  $8 \times \text{Layer number} + \text{wire number}$

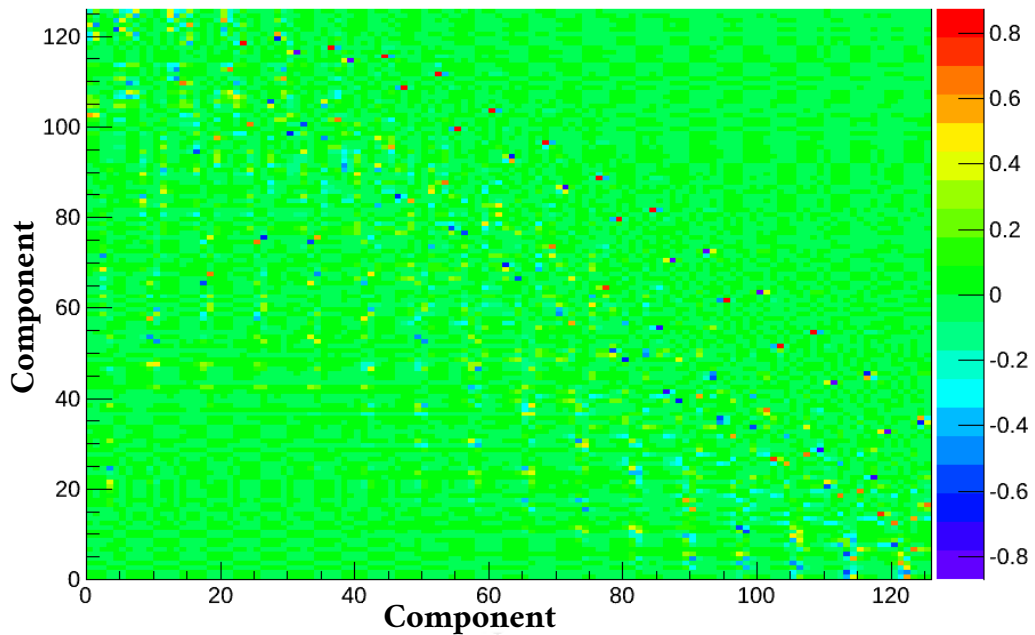


Figure D.7: The transformation matrix  $S$  for UD batch-2 data

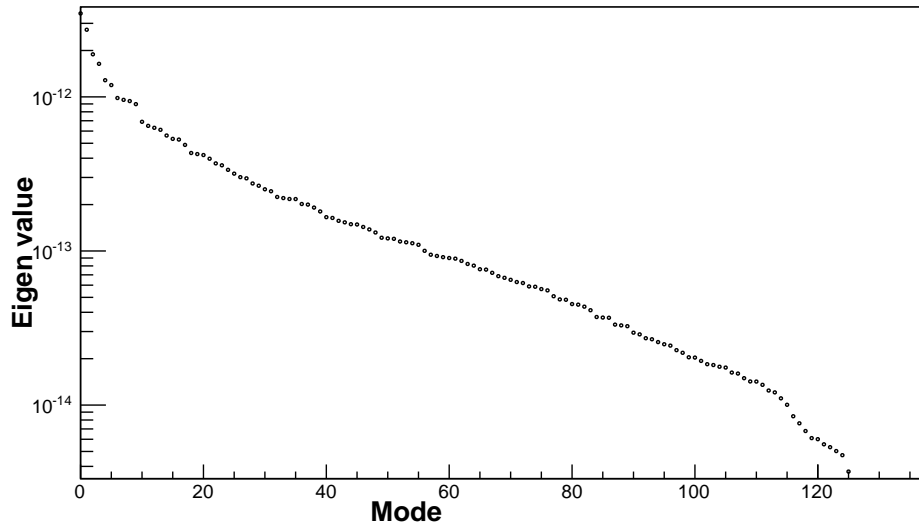


Figure D.8: The eigenvalues from UD batch-2 data

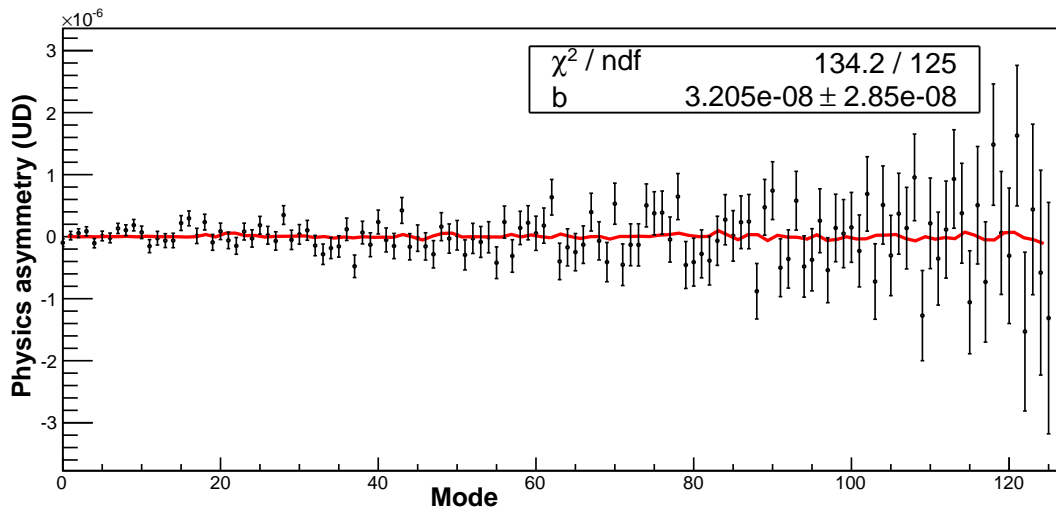


Figure D.9: UD physics asymmetry (corrected) for batch 2 using alternative fitting.

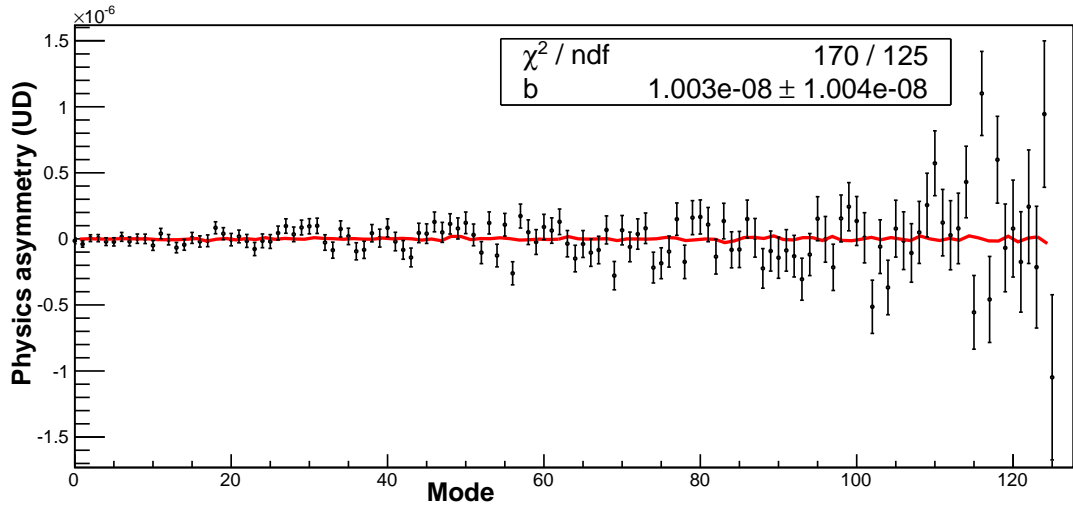


Figure D.10: UD physics asymmetry (corrected) calculated using average wire asymmetry obtained by fitting over all the batches.

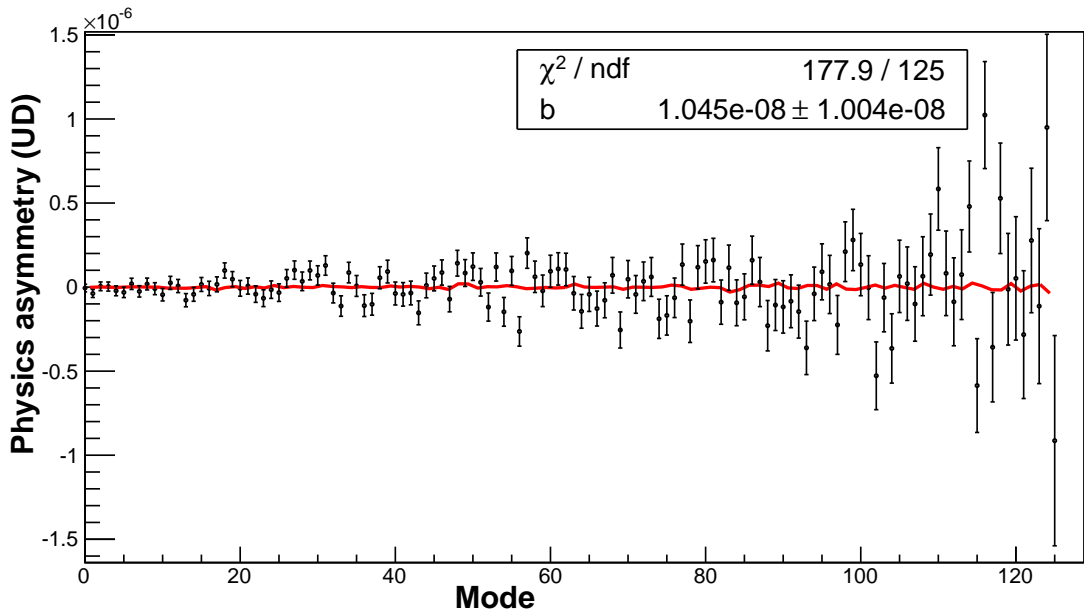


Figure D.11: UD physics asymmetry (corrected) considering all the runs in a single batch

# Bibliography

- [1] T. D. Lee and C. N. Yang *Physical Review* **104**, 254 (1956)
- [2] C.S. Wu *et al. Phys. Rev.* **105**(1957) 1413
- [3] R. L. Garwin, L. M. Lederman, & M. Weinrich, *Phys. Rev.* **105**, 1415 (1957).
- [4] N. Tanner, *Phys. Rev.* **107**, 1203
- [5] V. M. Lobashov *et al.*, *Phys. Lett. B* 25, **104** (1967)
- [6] R.P. Feynman and M. Gell-Mann, *Phys. Rev.* **109**, 193 (1958)
- [7] B. Desplanques, J.F. Donoghue and B.R. Holstein. *Annals of Physics*, **124**, 449(1980)
- [8] G. Barton, *Nuovo Cim.* **19**, 561 (1961)
- [9] E. G. Adelberger, W.C. Haxton, *Ann. Rev. Nucl. Part. SSci.* **35** 501-558
- [10] M. J. Ramsey-Musolf, S.A. Page, *Ann.Rev.Nucl.Part.Sci.***56**:1-52,2006
- [11] S. L. Zhu, C. M. Maekawa, B. R. Holstein, M. J. Ramsey-Musolf and U. van Kolck, *Nucl. Phys. A* **748**,. 435 (2005)
- [12] M. R. Schindler and R.P. Springer, *Progress in Particle and Nuclear Physics*, Volume **72**, 2013, 1-43
- [13] H. Rothe, Lattice gauge theories: An Introduction, *World Sci.Lect.Notes Phys.* 43 (1992) 1-381.
- [14] R. Gupta, Introduction to lattice QCD: Course. *arXiv:hep-lat/9807028*.
- [15] S. Beane, W. Detmold, K. Orginos, M. Savage, Nuclear Physics from Lattice QCD, *Prog.Part.Nucl.Phys.* **66** (2011) 1-40.
- [16] S. R. Beane, M. J. Savage, Hadronic parity violation on the lattice, *Nucl.Phys.* **B636** (2002) 291-304.
- [17] J Wasem, *PRC* **C85** (2012)
- [18] J. Dai, M. J. Savage, J. Liu, R. P. Springer, *Phys.Lett.* **B271** (1991) 403-409.
- [19] B. Tiburzi, *Phys.Rev.* **D85** (2012) 054020.



- [20] B. Tiburzi, *Phys.Rev.* **D86** (2012) 097501.
- [21] W. C. Haxton, B. R. Holstein, *Progress in Particle and Nuclear Physics*, **71** (2013) 185-203
- [22] P.D. Evershiem *et al.*, *Phys. Lett.* **B256**, 11 (1991).
- [23] D.E. Nagle *et al.*, *AIP Conf. Proc.* **51** (AIP, New York, 1978), p 224.
- [24] R. Balzer *et al.*, *Phys. Rev. Lett.* **44**, 699 (1980) and *Phys. Rev.* **C30**,1409 (1984); S. Kistryn *et al.*, *Phys. Rev. Lett.* **58**, 1616 (1987).
- [25] A. R. Berdoz *et al.*, *Phys. Rev. Lett.* **87**, 272301 (2001) and *Phys. Rev.* **C68** (2003) 034004.
- [26] J. F. Cavaignac, B. Vignon, and R. Wilson, *Phys. Lett.* **B67**, 148 (1977).
- [27] M. T. Gericke *et al.*, *Phys. Rev.* **C83**, 015505 (2011).
- [28] V. M. Lobashov *et al.* *Nucl. Phys.* **A197**, 241 (1972).
- [29] V. A. Knyaz'kov *et al.*, *Nucl Phys.* **A417**, 209 (1984).
- [30] M. Viviani *et al.*, *Phys, Rev.* **C82**, 044001 (2010).
- [31] K. M. Nollet *et al.*, *Phys. Rev. Lett.* **99**, 022502 (2007).
- [32] J. Lang *et al.*, *Phys. Rev. Lett.* **54**, 170 (1985); R. Henneck *et al.*, *Phys. Rev. Lett.* **48**, 725 (1982).
- [33] W.M. Snow *et al.*, *Phys. Rev.* **C83** 022501 (2011).
- [34] D.E. Nagle *et al.*, *AIP Conf. Proc.* 51 (AIP, New York, 1979) p. 24.
- [35] C. A. Barnes *et al.*, *Phys. Rev. Lett.* **40**, 840 (1978).
- [36] M. Bini *et al.*, *Phys. Rev. Lett.* **55**, 795 (1985).
- [37] G. Ahrens *et al.*, *Nucl. Phys.* **A390**, 496 (1982).
- [38] S. A. Page *et al.*, *Phys. Rev.* **C35**, 1119 (1987).
- [39] E. G. Adelberger *et al.*, *Phys. Rev.* **C27**, 2833 (1983).
- [40] K. Elsener *et al.*, *Nucl. Phys.* **A461**, 579 (1987); *Phys. Rev. Lett.* **52**, 1476 (1984).
- [41] K. A. Snover *et al.*, *Phys. Rev. Lett.* **41**, 145 (1978).
- [42] E. D. Earle *et al.*, *Nucl. Phys.* **A396**, 221 (1983).
- [43] P. Vetter *et al.*, *Phys. Lett.* **B74**, 2658 (1995).
- [44] N. H. Edwards *et al.* *Phys. Rev. Lett.* **74** 2654 (1995).
- [45] C.S. Wood *et al.*, *Science* **275**, 1759 (1997).
- [46] C. -P. Liu, *Physical Review C* **75**, 065501 (2007)

- [47] W. C. Haxton *et al.* *Phys.Rev.Lett.***86**.5247
- [48] Rob Mahurin and Chris Crawford, Opening angles for the SNS FnpB choppers  
*Unpublished technical note*
- [49] S. Agostinelli *et al.*, *Nuclear Instruments and Methods in Physics Research A* **506** (2003) 250-303
- [50] Rene Brun, Fons Rademakers, *Nuclear Instruments and Methods in Physics Research A* **389** (1997) 81-86
- [51] H. A. Bethe, *Ann. Physik* **5**,325 (1930)
- [52] F. Bloch, *Ann. Physik* **16**,285 (1933)
- [53] W. R. Leo, *Techniques for Nuclear and Particle Physics Experiments*, Eq.(2.14)
- [54] E. L. Plemons, *Installation and Alignment of the  $n$ -<sup>3</sup>He Experiment. Master's Thesis, University of Tennessee, 2015*
- [55] ADS1278 specification, *Texas Instruments ADS1278 specification sheet*
- [56] M. McCrea, *Parity violation and cold neutron capture: A study of the detailed interaction between hadrons, PhD Thesis, University of Manitoba, 2016*
- [57]  $n$ -<sup>3</sup>He Software,  *$n$ -<sup>3</sup>He Software Repository*
- [58]  $n$ -<sup>3</sup>He Analysis Tools,  *$n$ -<sup>3</sup>He Analysis Tools Repository*
- [59] C. B. Hayes, *Spin Flipper, Neutron Polarimetry, and Simulation, for the  $n$ 3He Experiment PhD Thesis, University of Tennessee, 2016*
- [60] S. Balascuta *et al.*, *Nuclear Instruments and Methods in Physics Research A* **671** (2012) 137-143
- [61] N. Fomin *et al.*, *Nuclear Instruments and Methods in Physics Research A* **773** (2015) 45-51
- [62] G. Charpak and F. Sauli, *Nuclear Instruments and Methods* **162** (1979) 405-428
- [63] P. -N. Seo *et al.*, *Phys. Rev. ST Accel. Beams* **11**, 084701 (2008)
- [64] J. D. Bowman *et al.* *The NPDGamma experiment at LANSCE proposal*
- [65] I. I. Rabi, N.F. Ramsey and J. Schwinger, *Rev. Mod. Phys.* **26**, 167 (1954)
- [66] Joel Tellinghuisen. On the Least-Squares Fitting of Correlated Data: Removing the Correlation. *Journal of Molecular Spectroscopy*, **165**:255-264, 1994.
- [67] D. Blyth, Derivation of a least-square solution for the NPDGamma result. *Unpublished technical note.*
- [68] R. Alarcon *et al.*, *Proposal for the  $n$ -<sup>3</sup>He experiment at SNS, March 16th, 2013*
- [69] J. D. Bowman *et al.*, *Proposal for the  $n$ -<sup>3</sup>He experiment at SNS, Nov 15th, 2007.*

- [70] S. Gardner *et al.*, *A New Paradigm for Hadronic Parity Nonconservation and its Experimental Implications*. *arXiv:1704.02617*
- [71] D. R. Phillips, D. Samart and C. Schat *Phys. Rev. Lett.* **114** no. 6, (2015) 062301
- [72] M. R. Schindler, R. P. Springer and J. Vanasse *Phys. Rev.* **C93** no.2, (2016) 025502
- [73] J. Fry *et al.*, *Hyperfine Interaction* **238** no. 1, (2017) 11

# Vita

---

Md Latiful Kabir was born and raised in Bangladesh. He received his B.S. in Physics and M.S. in Theoretical Physics from the University of Dhaka. He came to the U.S. in the fall of 2010 to join the University of Kentucky to pursue higher study in Physics. He received M.S. in Physics from the University of Kentucky in 2013. After successfully completing the course work, he moved to TN to be stationed at the Oak Ridge National Lab (ORNL) to actively participate his thesis experiment. He served as a Teaching Assistant in the department of Physics and Astronomy from 2010 to 2013. He was a research assistant under the same department and stationed at ORNL from 2013 to 2017.